

The Self-Organisation of Biological Soft matter Systems at Different Length-scales



A thesis submitted to the National University of Ireland in fulfilment of the requirements for the degree of

Doctor of Philosophy

By

Alice Blumlein, B. Sc.

Department of Chemistry

Maynooth University

February 2016

Research Supervisor: Dr. Jennifer McManus

Head of Department: Dr. John Stephens

*Dedicated to my children, William and Naomi,
and my parents, Christina and Desmond.*

Declaration

I hereby certify that this thesis has not been submitted before, in whole or in part, to this or any university for any degree and is, except where otherwise stated, the original work of the author.

Signed: _____

Date: _____

Acknowledgements

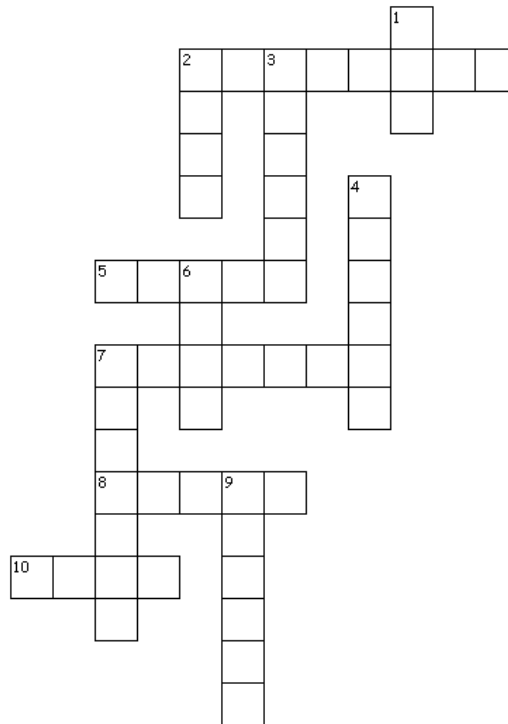
To Dr. Jennifer Mc Manus I owe you my deepest gratitude for your guidance and support. Without your perseverance, when mine was sorely lacking, this thesis would never have seen the light of day: I think I've used up my full allocation of your tissues. I am forever amazed by the depth of your knowledge and I admire the generosity with which you share it. I hope you remember some of my analogies – I'm particularly fond of the trampoline one.

In addition, I would like to thank Prof. John Lowry who was instrumental in securing my funding and Dr. John Stephens for allowing me the opportunity to carry out my research in the Department of Chemistry. Thanks to all the other members of the Chemistry department for your support and assistance. To Carol and Donna without whom this would never have been printed. To Noel – a special thanks – for all the hours we've spent drilling and soldering, I enjoyed our chats very much. To Ken for giving me the opportunity to demonstrate to the undergraduate students and starting me off on this journey. To Anne, I'm sorry you had to chase me down for grades so many times but hopefully I added something to your week too. I must especially thank Walter for rescuing me from the Bunsen water fountain. And to all the other staff for good-humoredly answering my random questions.

To my fellow Mc Manus group members past and present, only we will know what we've come to mean to each other. Ruth (the first-born), it is only now that I have come to realize how difficult the submission process is – *meā culpā*. But that doesn't mean I forgive you for all the frights you've given me. Susan (the fairest of them all), you have shown amazing dignity and strength of character. I am so glad that Dhruv and Febey are finally able to join you. Ula (celebrations to you too, very soon), I still can't believe you divided our desk space with a yellow (!) piece of tape – how childish. May we always have a spare room for one another. Michelle (my other child), my how we have grown together! I would especially like to thank you for your assistance in reading papers (some were even for journal club). Mark (the shy one), why and how you put up

with us, I'll never know. But I do know it makes you one heck of a tough guy – and don't you forget it.

Without coffee nothing is possible – I can't find a reference for that – but then again I don't have to! I've made a crossword for all my coffee buddies, for what good is coffee without a crossword.



Across

- 2. Red hot rodent sandwich (8)
- 5. Don't back down (5)
- 7. Nearly not out of disco biscuits (7)
- 8. A small change to a dark place, who's the fairest skinned of us all? (5)
- 10. Best not to go out in the mid-day sun (4)

Down

- 1. Orchard preserve (3)
- 2. Who's got a dirty lab coat? (4)
- 3. This little beast cried wee, wee, wee (6)
- 4. A mixed up little mermaid keeps happy (6)
- 6. He was never racist towards me (4)
- 7. Yes, I can almost (7)
- 9. Smile, it's a Kodak moment! (6)

To my family and friends to whom I owe a debt of gratitude; my children William, and Naomi, my mother and father, Christina and Des, Vernon, Doreen, Hazel, Linda, Gail and Paul. There is not enough I can say here to thank you all for your support and kindness. It's over – I'm finally free to idly have coffee, shop and chat once more. I look forward to spending a lot more time with you.

Papers arising from this thesis

Blumlein, A. & McManus, J.J., 2013. Reversible and non-reversible thermal denaturation of lysozyme with varying pH at low ionic strength. *Biochimica et biophysica acta*, 1834(10), pp.2064–70.

Blumlein, A. & McManus, J.J., 2015. Bigels formed via spinodal decomposition of unfolded protein. *J. Mater. Chem. B*, 3(17), pp.3429–3435.

Blumlein, A. & McManus, J.J., The mechanical properties of individual cell-bundles. In preparation

Abstract

Spontaneous self-organisation occurs in physical, chemical and biological systems throughout the natural world when the components of an initially unstructured system arrange to form ordered structures. Research into the mechanisms underlying these systems has led to exciting developments in materials chemistry where a bottom-up approach based on directed self-organisation has the potential to yield novel materials with a wide range of technological and scientific applications. Owing to their high specificity and potency, biopharmaceutical therapeutics are often favoured over small molecule drugs. However, protein based biopharmaceuticals are prone to degradation as a result of physical and chemical instability, a process leading to devastating financial and safety outcomes. Accordingly, understanding and quantifying the adverse effects of protein degradation is imperative. One such form of degradation is protein self-organisation in the form of aggregation. For certain solution conditions, aggregated unfolded protein leads to the formation of gels. Hydrogels are a class of gel formed from hydrophilic polymer chains capable of holding large amounts of water in their three dimensional network and have numerous medical and pharmaceutical uses. Self-organisation drives gel formation. Therefore, understanding the principles of self-organisation is a prerequisite in the development of novel hydrogels with increased functionality. At longer length-scales cells self-associate to form tissues. Spheroids are self-organised entities comprised of a single-cell type. They are the archetypal model for tumours and are an ideal system to study the biophysical phenomena associated with self-organisation. Unlike tissues, when a single cell type is used to form the spheroid, compositionally identical replicates can easily be grown. Furthermore, unlike with explants, other factors including age and the biochemical environment, which have been shown to alter the mechanical characteristics of cells and tissues can be rigorously controlled. Here, the experimental techniques of the wider soft matter field are used to investigate the biophysical properties of systems that span the biologically relevant spectrum of length-scales in which soft matter contributions are important.

Differential scanning calorimetry analysis was used to quantify the reversibility of unfolding following thermal denaturation of lysozyme. Solution conditions (pH, ionic

strength and the presence/absence of disaccharides) were varied to systematically alter the temperature at which the protein unfolds, T_m . The enthalpies of unfolding during successive heating and cooling cycles were compared to quantify the degree of reversible unfolding that occurs following thermal denaturation. The sugars were used to evaluate whether a disaccharide induced increase in T_m affects the reversibility of thermally induced denaturation. It was shown that there was considerable overlap between the T_m values where reversible and non-reversible thermal denaturation occurred. Indeed, at the highest and lowest T_m no refolding was observed whereas at intermediate values refolding occurred. Furthermore, similar T_m values had different proportions of refolded protein. Using this novel analysis, it was possible to quantify the degree to which protein is lost to irreversible aggregation and show that an increase in the melt transition temperature does not necessarily confer an increase in reversibility. This type of analysis may be a useful tool for the biopharmaceutical and food industries to assess the stability of protein solutions.

Bigels are an emerging class of tuneable soft materials composed of two discrete but interpenetrating networks, both of which contribute to the physical and mechanical properties of the material. A bigel network was formed from two proteins, BSA and gelatin. Thorough control of the solution conditions and kinetics ensured that the inter-species attraction between the two protein systems were weak compared to the intra-protein attraction, leading to bigel formation. The protein bigel was shown to have an elastic modulus four times greater than the combined elastic moduli of the parent gels. Furthermore, the elastic response was maintained over several deformation cycles and the gel is both thermo- and chemo-responsive. These gels have the potential to be used in drug delivery, for biomedical applications such as wound healing or as a biomimetic in tissue culture.

Cavitation rheology was used to show that for spheroids formed from HEK293 cells the interfacial tension was dominated by cortical tension at length-scales $< 30 \mu\text{m}$. It was found that the elastic modulus could be related quantitatively to the disruption of cell-cell adhesion molecules which facilitates the formation of the cavity. A cascade of cadherin-cadherin dissociation events, totalling a disrupted surface are equivalent to 3, 8 and 117 cells was calculated for 5, 10 and 30 μm needles, respectively, was calculate. Furthermore, the process involved was shown to be largely elastic and a mechanism

involving a rapid cycle of “unzipping” and “re-zipping” the cadherin bonds was proposed to account for this elasticity. Since changes in cortical tension and cell-cell adhesion are associated with the transition from healthy to malignant cells, CR may prove a useful addition to the oncologists’ toolbox.

Table of Contents

Declaration	i
Acknowledgements	ii
Papers arising from this thesis	v
Abstract	vi
Table of Contents	1
Chapter 1 Introduction	1
1.1 Self-organisation	2
1.2 Non-covalent forces responsible for self-organisation	3
1.2.1 Hydrogen bonds (H-bonds).....	5
1.2.2 Van der Waals interactions	6
1.2.3 Hydrophobic interactions	6
1.2.4 Electrostatic interactions	6
1.3 Thermodynamics of self-organisation	7
1.4 Soft matter.....	9
1.5 Biological Soft Matter.....	9
1.5.1 Protein structure	10
1.5.2 Higher-order assembly of proteins.....	11
1.5.2.1 The effects of pH on protein colloidal and structural stability.....	14
1.5.2.2 The effects of ions on protein colloidal and structural stability	15
1.5.2.3 The effects of co-solutes on protein colloidal and structural stability	16
1.5.3 Mechanisms of protein aggregation	18
1.5.3.1 Self-association of native monomers	18
1.5.3.2 Self-association of non-native conformers.....	19
1.5.3.3 Self-association following chemical modification.....	20
1.6 Protein Phase Diagrams	20
1.6.1 Spinodal decomposition.....	21
1.7 Gels.....	22

1.7.1	Physical gels.....	22
1.7.1.1	Polymeric physical gels	22
1.7.1.1.1	Colloidal physical gels	24
1.7.2	Covalently cross-linked gels	25
1.8	Cells and Tissues.....	26
1.8.1	The cytoskeleton	27
1.8.2	Cell adhesion & the extracellular matrix	29
1.8.2.1	Cell-Cell adhesion.....	29
1.8.2.1.1	Cadherins	30
1.8.2.1.2	Integrins	30
1.8.2.2	Cell adhesion to the extracellular matrix	31
1.8.2.2.1	Collagen	31
1.8.2.2.2	Elastin	32
1.8.2.2.3	Fibronectins and laminins	32
1.8.3	Surface tension effects in cells and tissues	33
1.8.3.1	Cortical tension	34
1.8.3.2	Adhesion tension.....	34
1.9	Thesis motivation.....	36
Chapter 2	Techniques used to Characterise Soft Matter	37
2.1	Methods used to determine Young's elastic modulus.....	38
2.1.1	Oscillating shear rheology	39
2.1.2	Microrheology.....	41
2.1.3	Atomic force microscopy (AFM).....	42
2.1.4	Cavitation Rheology	43
2.2	Methods of assessing protein unfolding.....	45
2.2.1	Fourier transform infrared spectroscopy	45
2.2.2	Circular dichroism spectroscopy.....	46
2.2.3	Fluorescence spectroscopy.....	46
2.2.4	Nuclear magnetic resonance spectroscopy.....	47
2.2.5	Differential Scanning Calorimetry (DSC)	47
2.3	Model proteins	50
2.3.1	Lysozyme.....	50

2.3.2	Bovine serum albumin (BSA).....	51
2.3.3	Gelatin.....	52
2.4	Spheroids as model systems.....	53
2.4.1	Hanging drop method of spheroid formation.....	54
2.4.2	Liquid overlay method of spheroid formation	55
2.4.3	Cell line HEK 293T/17	56
Chapter 3 Reversible and non-reversible thermal denaturation of lysozyme with varying pH at low ionic strength		57
3.1	Introduction.....	58
3.1.1	Aim of this study.....	62
3.2	Materials and methods	62
3.2.1	Phosphate buffer preparation	62
3.2.2	Lysozyme preparation.....	62
3.2.3	Determination of lysozyme concentration	63
3.2.4	Preparation of disaccharide solutions.....	63
3.2.5	Sample preparation	63
3.2.6	Differential Scanning Calorimetry (DSC) measurement	64
3.2.7	SDS-PAGE (Sodium Dodecyl Sulfate – Poly Acrylamide Gel Electrophoresis).....	65
3.2.7.1	Preparation of resolving gel (12.6 %)	66
3.2.7.2	Preparation of stacking gel (4 %).....	66
3.2.7.3	Preparation of the gel	67
3.2.7.4	Preparation of SDS samples.....	67
3.2.8	Intrinsic fluorescence	68
3.3	Results.....	68
3.3.1	Typical thermogram and baseline subtraction	68
3.3.2	Van't Hoff enthalpy	71
3.3.3	Confirmation of aggregation and return to natively refolded protein after heating and cooling.	72
3.3.4	Quantifying reversibility	75
3.3.5	Effect of solution conditions	78

3.4	The addition of disaccharide excipients.....	82
3.5	Discussion.....	83
3.6	Conclusion.....	87
Chapter 4	Bigels formed via spinodal decomposition of unfolded protein.....	89
4.1	Introduction.....	90
4.1.1	Aims of this study.....	96
4.2	Methods and materials.....	96
4.2.1	Reagents.....	96
4.2.2	Sample Preparation.....	97
4.2.3	Differential scanning calorimetry.....	97
4.2.4	Light microscopy.....	97
4.2.5	Environmental scanning electron microscopy (ESEM).....	98
4.2.6	Confocal Microscopy.....	98
4.2.7	Labelling proteins with fluorescent dyes.....	99
4.2.8	Fluorescence measurements.....	100
4.2.9	Cavitation rheology (CR).....	100
4.2.9.1	Calibration of cavitation rheology equipment.....	100
4.2.9.2	Typical cavitation rheology experiment.....	101
4.3	Results.....	101
4.3.1	Differential scanning calorimetry.....	101
4.3.2	Calibration of CR equipment.....	102
4.3.3	BSA only gels.....	104
4.3.4	Gelatin only gels.....	107
4.3.5	BSA and gelatin gels.....	108
4.3.5.1	Light microscopy of bigels.....	108
4.3.5.2	Cavitation rheology of bigels.....	109
4.3.5.3	Environmental Scanning Electron Microscopy of bigels.....	110
4.3.5.4	Confocal microscopy of bigels.....	111
4.3.5.5	Thermo-responsive behaviour of bigels.....	112
4.4	Discussion.....	113
4.5	Conclusions.....	119

Chapter 5	The Mechanical Properties of Spheroids	121
5.1	Introduction.....	122
5.2	Aims of this study	125
5.3	Sensor selection and implementation.....	126
5.3.1	Noise during analog to digital conversion (ADC)	126
5.3.2	Sensor selection.....	127
5.4	Methods and materials	128
5.4.1	Preparation of polyacrylamide gels (37.5:1 acrylamide:bis)	128
5.4.2	Preparation of gelatin gels.....	128
5.4.3	Silanization of glass surfaces	128
5.4.4	Cell culture.....	129
5.4.4.1	Growing cells from frozen stocks.	129
5.4.4.2	Sub-culturing and passaging of cells.....	130
5.4.4.3	Cryopreservation of culture	131
5.4.4.4	Spheroid culture	131
5.4.5	Light microscopy	131
5.4.6	Cavitation rheology.....	132
5.5	Results and discussion	133
5.5.1	Calibration.....	133
5.5.2	Investigation of 1-D confinement and “thickshell” limit.....	135
5.5.2.1	Effect of surface area	135
5.5.2.2	Effect of surface type	136
5.5.2.3	Maintaining volume and varying needle radius	137
5.5.3	Spheroid investigation.....	139
5.5.3.1	Mechanical properties of spheroids	141
5.5.3.2	What length-scales are begin measured?	141
5.5.3.3	Interpretation of the data	144
5.6	Conclusions.....	150
	Final conclusions	152
	References.....	153
	Appendix: Integration and automation of syringe pump.....	I

I.	Aim	I
II.	Brief outline of programming in LabView	I
III.	Software development.....	II
I.	Block diagram – Frames 1, 2 & 3	II
II.	Block diagram – Frame 4.....	IV
III.	Front Panel.....	VII
IV.	Conclusion	VIII

Chapter 1 Introduction

1.1 Self-organisation

Self-organisation occurs throughout the natural world in physical, chemical and biological systems when local, non-covalent, interactions between the components of an initially unstructured system spontaneously arrange to form ordered structures (Karsenti 2008). These self-assembly processes occur across nano, meso and macroscopic length-scales when nature transforms molecular systems (proteins, nucleic acids and lipids) into complex life forms by relying on the hierarchal quality of the self-assembly process (Gradišar & Jerala 2014). This field of research offers an exciting route for the development of materials using a bottom-up approach since the ability to direct this self-organisation has the potential to yield novel materials with a wide range of technological and scientific applications (Thiruvengadathan et al. 2013; Gradišar & Jerala 2014).

The formation of Bénard cells is an elegant example of self-organisation resulting from a physical phenomenon, convection, whereby a regular pattern of convection cells become established in a horizontal plane of fluid heated from below (Sugakov 1998), figure 1.1a. Chemical systems also display self-organisation. Belousov–Zhabotinsky reactions are complex redox reactions that exhibit spatial and temporal self-organisation. When observed in a glass dish, coloured spots appear in the solution and develop over time as an expanding series of concentric rings which disappear if stirred and spontaneously reappear (Sugakov 1998), figure 1.1b.

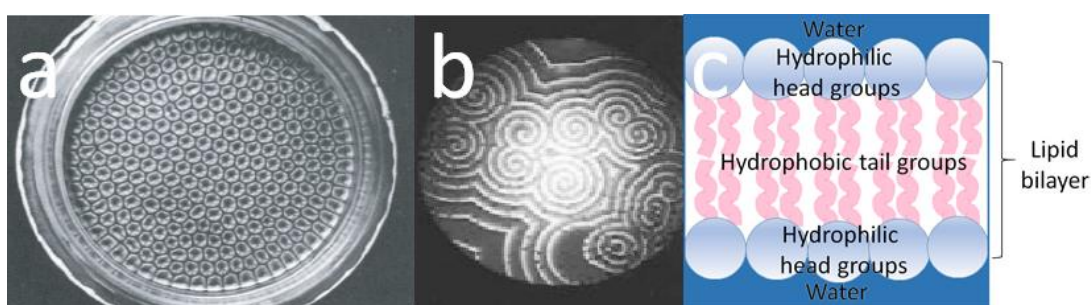


Figure 1.1 Self-organisation in physical, chemical and biological systems. (a) Bénard cells; modified from Koschmieder, 1993, (b) a Belousov–Zhabotinsky reaction; modified from (Epstein, Irving & Pojman, John 1998) and (c) schematic of a phospholipid bilayer.

Biomolecules, lipids, carbohydrates, nucleic acids and proteins, are not merely capable of, but must, self-organise. Without self-organisation there is no living organism and compartmentalisation is the most basic prerequisite; at a minimum a boundary must exist between the environment and the organism. This minimum boundary exists as a cell-membrane, a self-assembling bilayer composed mainly of phospholipids. These amphiphilic molecules are comprised of a hydrophilic head group and a hydrophobic tail region. In an aqueous environment, the hydrophobic tails interact with one another forming a hydrophobic centre and the hydrophilic head groups are organised so that they remain exposed to water. The resulting, spontaneously assembling structure, a lipid bilayer (figure 1.1c), is a universal feature of a cell membrane (Monnard & Deamer 2002). Carbohydrates and carbohydrate derivatives (glycolipids) play a fundamental role in the self-organisation of cells. Nucleic acids self-organise to replicate the genome and begin the process of protein synthesis and proteins also self-organise to form complex structural, signalling and catalytic assemblies (Reece et al. 2009). Furthermore, in viruses, proteins spontaneously assemble to form a capsid, a single-molecule-thick protein shell surrounding the nucleic acid (Cadena-Nava et al. 2012). Protein self-assembly is also a feature of numerous pathological states, some of which are known as amyloid diseases and include Alzheimer's disease, Huntington's disease, diabetes mellitus type 2 and Parkinson's disease (Ghahghaei & Faridi 2009).

In biological systems, non-covalent forces are responsible for self-organisation (Černý & Hobza 2007) and therefore an understanding of these interactions is essential both in the intelligent design of novel biomaterials and the appreciation of the biophysical properties of natural biological soft matter systems.

1.2 Non-covalent forces responsible for self-organisation

Covalent bond lengths are typically $< 2 \text{ \AA}$ and typical bond strengths are $\geq 100 \text{ kcal/mol}$ (Lodish et al. 2000). Conversely, non-covalent interactions do not involve the sharing of electrons, occur at greater distances ($> 2\text{-}10 \text{ \AA}$) and have bond strengths on the order of 1-5 kcal/mol (Lodish et al. 2000). These bond strengths are on an energy scale comparable with the average thermal energy at room temperature (kT). Thus, at room temperature ($\sim 25 \text{ }^\circ\text{C}$), the thermal energy is $\approx 0.6 \text{ kcal/mol}$, which is sufficient to break non-covalent bonds (Atkins 2014). Therefore, the non-covalent forces responsible for self organisation

are considered reversible and are often referred to as interactions rather than bonds. Furthermore, non-covalent interactions may be repulsive or attractive, strong or weak and occur over short or long length-scales, table 1.1.

Table 1.1 Types of non-covalent interactions between particles in aqueous solution^[a depends on pH and ionic strength]; modified from (Bryant & McClements 1998)

Type	Sign	Strength	Range
Hydrogen bonding	Attractive	Weak	Short
Van der Waals	Attractive	Weak	Short
Hydrophobic	Attractive	Strong	Long
Electrostatic	Attractive or Repulsive	Weak → Strong ^(a)	Short → long ^(a)
Hydration	Repulsive	Strong	Short
Steric repulsion	Repulsive	Strong	Short

The four principal types of non-covalent interaction are; hydrogen bonds, van der Waals interactions, hydrophobic interactions and electrostatic interactions, figure 1.2. Permanent, induced and instantaneous electrostatic interactions between atoms have been attributed to these various non-covalent interactions (Atkins 2014).

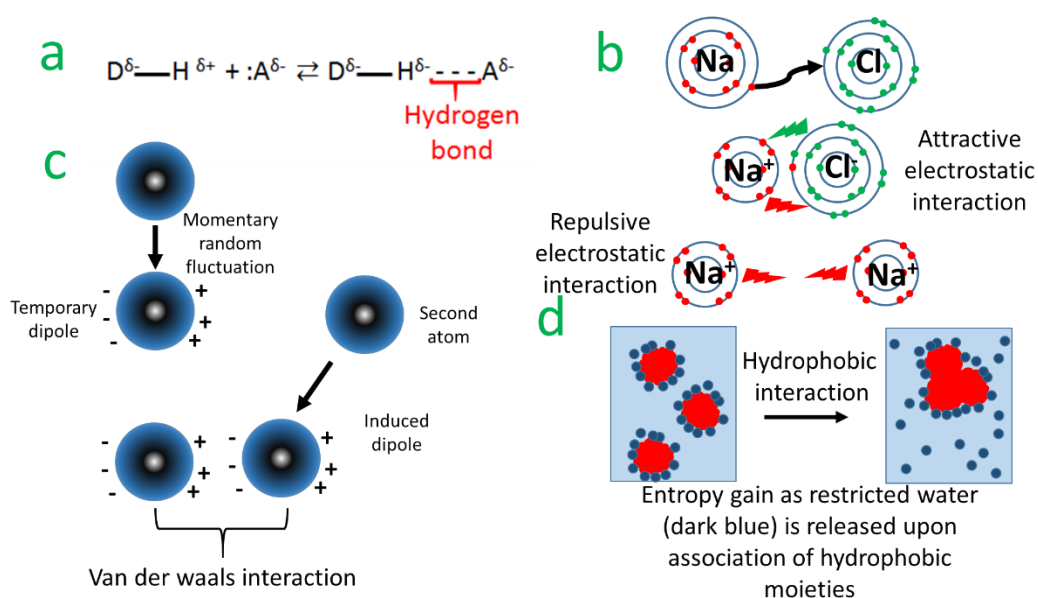


Figure 1.2 Four types of non-covalent interactions; (a) Hydrogen bond, (b) Electrostatic interaction, (c) van der Waals interaction and (d) Hydrophobic interaction.

Zeta potential (described below) is an important measure of the magnitude of the effective electrostatic interactions between protein molecules. In solution, an electrostatic double layer is formed by an increase in counter-ion concentration close to the particle surface; the stern layer of strongly bound counter-ions and a diffuse layer of less tightly bound counter-ions. The boundary between the diffuse layer and bulk solution is known as the slipping plane and the potential at this boundary is referred to as the zeta potential, figure 1.3.

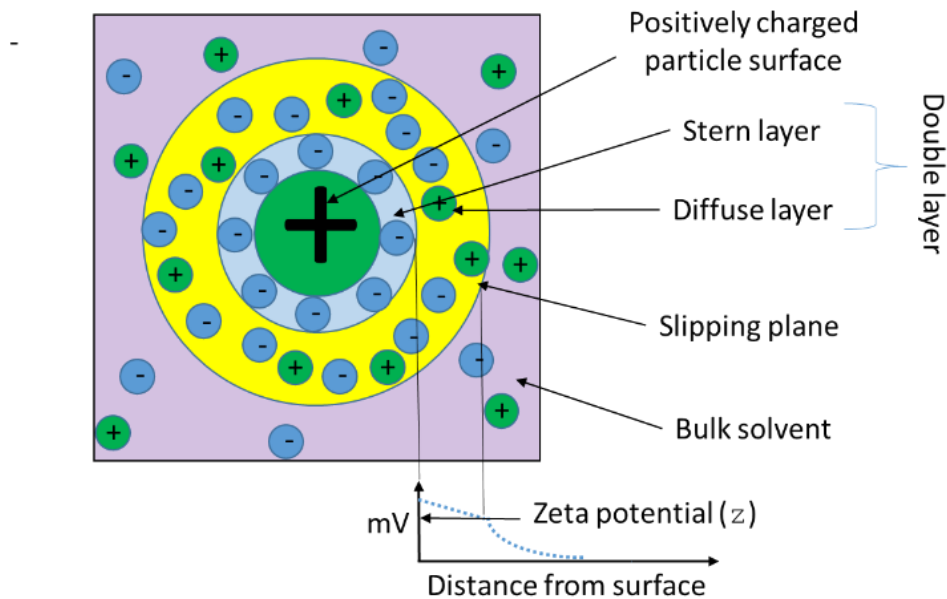


Figure 1.3 Illustration of electronic double layer and zeta potential.

1.2.1 Hydrogen bonds (H-bonds)

A hydrogen bond is an attractive interaction is a particular dipole-dipole (both permanent) interaction that involves a partially positive hydrogen atom and a highly electronegative atom (typically oxygen or sulphur) to which it is not covalently bound. The partially positive hydrogen atom is present due to an unequal distribution of electrons within a covalent bond between the hydrogen and what is termed the ‘donor’ atom with the electron density preferentially associated with the donor atom. The slightly positive hydrogen atom may then form an additional weak association with an acceptor atom, A. This weak association is termed a “hydrogen bond”, figure 1.2a. Usually, the strength of hydrogen bonds lies between 0.5 - 6kcal/mol (Sheu et al. 2003).

1.2.2 Van der Waals interactions

Van der Waals interactions are weak, nonspecific attractive interactions resulting from transient dipole formation when the momentary random fluctuations in the distribution of electrons produces a temporary uneven distribution of electrons. When two non-covalently bonded atoms approach each other, a transient dipole in one can induce an oppositely oriented transient dipole in the other, figure 1.2c. Van der Waals interactions occur at greater distances than covalent bonds (≈ 2 times greater) due to the electrostatic repulsion of the electrons in the valence shells. A carbon-hydrogen covalent bond ≈ 0.1 nm whereas a carbon-hydrogen van der Waals interaction ≈ 0.2 nm. The typical energy of a van der Waals interaction is approximately 1 kcal/mol (Miyamoto & Kollman 1993).

1.2.3 Hydrophobic interactions

Hydrocarbons are non-polar and are virtually insoluble in water, they do not become hydrated, and are termed hydrophobic, from the Greek meaning “water-fearing”. In an aqueous environment, hydrophobic molecules or the parts of a molecule that are hydrophobic, associate together to exclude water. This entropy driven process results in a decrease in free energy for the system by reducing the hydrophobic surface area and decreasing its restrictive interaction with water. The presence of non-polar molecules in an aqueous solution distorts the usual water structure since they cannot form hydrogen bonds with water. This restricts the number of orientations which the water molecules can adopt, decreasing the entropy of the water in the system. The association of hydrophobic molecules, reduces the number of water molecules thus restricted. Although the entropy of the hydrophobic molecules is decreased by hydrophobic interactions, the entropy of the system is increased as multiple water molecules become unrestricted by this process, figure 1.2d.

1.2.4 Electrostatic interactions

Atoms with very different electronegativity do not share electrons, rather the electrons are transferred to the more electronegative atom; i.e. the atoms become ionized with the more electronegative atom having a formal negative charge (anion) and the less electronegative atom having a formal positive charge (cation), figure 1.2b. Electrostatic interactions are attractive between oppositely charged ions and are repulsive between similarly ions.

1.3 Thermodynamics of self-organisation

Thermodynamics is the study of energy changes associated with chemical and physical transformations (Atkins 2014). Thermodynamics is concerned with the relationship between heat, work and the internal energy of the system. Energy, E [the capacity to do work] and work, W [and activity involving force (F) and distance (d)] are interrelated by;

$$W_{ad} = F \times d \quad (\text{Equation 1.1})$$

The first law of thermodynamics is concerned with the conservation of energy. In an adiabatic (closed) system, the quantity of work done (W_{ad}) is the increase in the internal energy of the system (ΔU);

$$W_{ad} = \Delta U = U_f - U_i \quad (\text{Equation 1.2})$$

and ΔU is the heat supplied (q) to the system minus work done by it (W);

$$\Delta U = q - W \quad (\text{Equation 1.3})$$

thus

$$q = W_{ad} - W \quad (\text{Equation 1.4})$$

and

$$\Delta U = \delta q + \delta u \quad (\text{Equation 1.5})$$

Enthalpy, H , is a key parameter in thermodynamics. It is the sum of the internal energy and the product of pressure (p) and volume (V);

$$H = U + pV \quad (\text{Equation 1.6})$$

when at constant pressure and with no non p, V work

$$\delta H = \delta q \quad (\text{Equation 1.7})$$

The second law of states that the sum of entropies (S) [a measurement of the degree of randomness of energy] in a system always increases. Entropy is related to work through;

$$\delta s = \frac{\delta q}{T} \quad (\text{Equation 1.8})$$

where T is temperature in Kelvin. Another key parameter in thermodynamics is Gibb's free energy (ΔG) which is the maximum amount of non-expansion work that may be performed by a thermodynamically closed system. No mass is exchanged, i.e. the number

of moles (n) remains constant, only energy is exchanged and the reaction conditions must be under constant temperature and pressure and (equation 1.7 holds. In addition the reaction must be reversible, thus by Hess's Law the total enthalpy change for a reaction is the sum of all changes;

$$\Delta H_{forward} = -\Delta H_{reverse} \quad (\text{Equation 1.9})$$

Using (equation 1.8

$$\Delta S_{surroundings} = \frac{\Delta q}{T} \quad (\text{Equation 1.10})$$

then

$$\Delta S_{surroundings} = \frac{\Delta H_{surroundings}}{T} \quad (\text{Equation 1.11})$$

and

$$\Delta S_{surroundings} = -\frac{\Delta H_{system}}{T} \quad (\text{Equation 1.12})$$

because

$$\Delta S_{universe} = \Delta S_{system} + \Delta H_{surroundings} \quad (\text{Equation 1.13})$$

so

$$\Delta S_{universe} = \Delta S_{system} + \frac{\Delta H_{system}}{T} \quad (\text{Equation 1.14})$$

and

$$-T\Delta S_{universe} = -T\Delta S_{system} + \Delta H_{system} \quad (\text{Equation 1.15})$$

if

$$\Delta G = -T\Delta S_{universe} \quad (\text{Equation 1.16})$$

then

$$\Delta G = \Delta H_{system} - T\Delta S_{system} \quad (\text{Equation 1.17})$$

A system is said to be in thermodynamic equilibrium when ΔG is zero. Some ordered systems such as crystal and lipid bilayers exist at thermodynamic equilibrium. Other ordered systems such as the Bénard cell and biological tissues exist under non-equilibrium conditions. When self-ordering occurs under non-equilibrium conditions this is referred to as a thermodynamically open (dissipative) system (Prigogine 1967; Prigogine et al. 1974). Such a system exchanges either energy or matter with an environment; Bénard cells require the addition of thermal energy whereas biological systems require electromagnetic (plants) or chemical energy (animals) to maintain ordered structures with the energy being dissipated through the system as adenosine

triphosphate (Karsenti 2008). Complex feedback loops (Castets et al. 1990), molecular diffusion (Glade et al. 2002) and symmetry breaking mechanisms (Nogales et al. 1999) have been shown to be central to biological self-organisation under non-equilibrium conditions. In biological self-organising systems, complex feedback loops arise from the cooperativity of non-covalent interactions which drive the self-assembly process (Escudero et al. 2010).

1.4 Soft matter

The seminal work of de Gennes, for which he received the Nobel Prize in Physics in 1991, paved the way for scientists to begin to investigate the field of soft matter, (de Gennes 1992). Soft matter (also referred to as; soft condensed matter, complex fluids, structured fluids) is concerned with the study of a variety of physical systems that can be deformed, by mechanical or thermal stress on the magnitude of thermal fluctuations (Kleman & Laverntovich 2007). The ease of deformation results from the non-covalent interactions that are responsible for the maintenance of these systems, these interactions are on an energy scale comparable with the average thermal energy at room temperature (kT). Included in this field are colloidal dispersions, polymers, foams, gels, surfactants and biological materials (Jones 2002).

1.5 Biological Soft Matter

Biological systems are, in essence, composed of soft matter; DNA is a stiff polymer (Manning 2006), cell membranes are composed of lipids which are essentially surfactants (Lee et al. 2009) and globular proteins behave as colloids, (Heinen 2011). DNA, found in the nucleus, is the genetic material of all living cells. This biopolymer is composed of a sugar-phosphate backbone and a base. There are four nucleotide bases; adenine (A), guanine (G), thymine (T) and cytosine (C), which become paired in a double stranded helix. A is complementary to T and C to G. The basepairs are held together by hydrogen bonds. A typical human cell contains 23 paired polymer strands, known as chromosomes, each strand being composed ~ 200 million nucleotides. From end-to-end a strand is ~5 cm long and must undergo a complex series of folds (around a histone protein) to form a condensed chromosome that can be accommodated within a cell ~ 10 μm , figure 1.4.

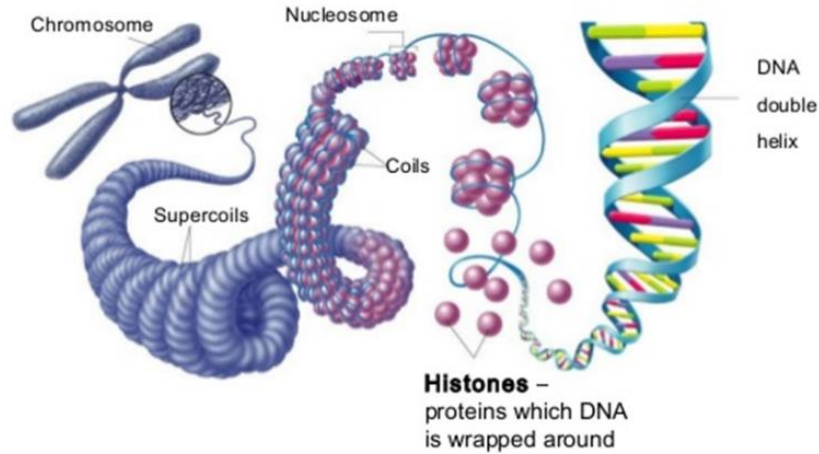


Figure 1.4 Schematic of DNA polymer strand folding around histones; modified from (Reece et al. 2009)

Lipids are amphiphilic molecules composed of a hydrophilic head group and a hydrophobic tail region. Lipids spontaneously assemble to form lipid bilayer when exposed to water, thus acting as surfactants, figure 1.1. Proteins perform many roles within biological systems including; structural (Strnad et al. 2016), mechanical (Merrifield 2016), enzymatic (Di Cera 2009) and signalling (Sedger & McDermott 2014). For many proteins, the function they perform is related to the three dimensional arrangement of the amino acids from which it is composed, (Reece et al. 2009).

1.5.1 Protein structure

The amino acid sequence of the protein is known as the primary structure which is composed of twenty commonly occurring amino acids that differ from each other due to the nature of their side chain (R), figure 1.5a & b. These side chains may be neutral, acidic, basic, hydrophobic or hydrophilic. Encoded within the primary sequence of amino acids is sufficient information for the protein to fold and become a functional protein which occurs through intermediate forms known as the secondary structures (Anfinsen, Haber et al. 1961). The most common secondary structures are alpha helixes and beta-pleated sheets (figure 1.5c). These structures, in-turn, interact to produce the three dimensional tertiary structure of the protein (figure 1.5d) (Anfinsen 1973). The three dimensional structure is further stabilised by electrostatically charged side chains forming salt bridges and disulphide bridges formed from paired cystines within the protein's core.

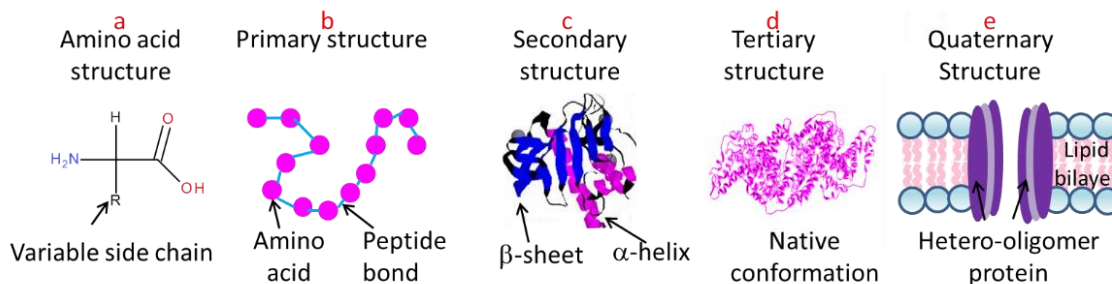


Figure 1.5 Hierarchy of protein folding from amino acid to native tertiary structure.

The time required for a protein to randomly sample all possible three dimensional arrangements, in order to settle on a thermodynamically favourable conformation, is not compatible with biological lifetimes, known as Levinthal's paradox. (Levinthal 1968). For some small proteins two states exist, folded and unfolded but for larger proteins, partially folded and molten globule (formed via hydrophobic collapse) intermediate states are known to exist along the folding pathway, (Rahaman et al. 2015), figure 1.6.

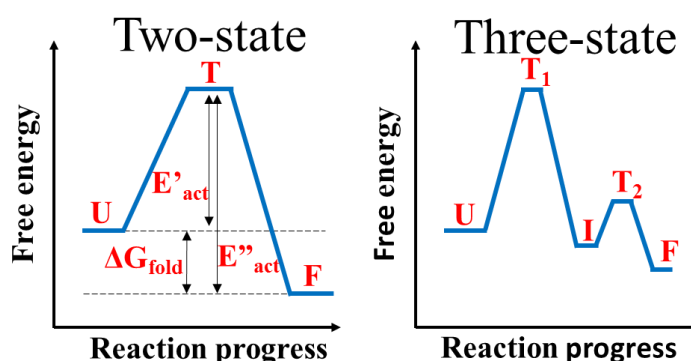


Figure 1.6 Reaction coordinate diagram (left) a two-state and (right) a three-state protein folding process. U = unfolded protein, F = folded protein, T = transition state, I = intermediate state, E'_{act} = activation energy for folding process, E''_{act} = activation energy for unfolding process, ΔG_{fold} = free energy difference between the unfolded and folded states.

1.5.2 Higher-order assembly of proteins

The natively folded tertiary structures may self-assemble into homo-dimers or higher order oligomeric complexes or form heteromers, protein complexes formed from chains with different amino-acid sequences (Zhanhua et al. 2005) or large amorphous aggregates (E. Y. Chi et al. 2003). In addition, proteins may self-organise intermolecularly with other classes of biomolecules such as nucleic acids and lipids forming for example transcription factors (Spitz & Furlong 2012) and ion channels (Kurachi & North 2004),

respectively, figure 1.5(e). Higher-order assemblies are not restricted to those formed by natively folded proteins (crystals, virus capsids, transcription factors, etc.), proteins may also assemble from partially unfolded monomers, which can result in the formation of amyloid fibers and amorphous aggregates.

In viruses, proteins spontaneously assemble to form a capsid, a single-molecule-thick protein shell surrounding the nucleic acid (Cadena-Nava et al. 2012). Virus capsid subunits interact with weak individual contact energies to form stable structures the majority of which are icosahedral or helical (Katen & Zlotnick 2009), figure 1.7. Like amyloid forming proteins, capsid proteins have conserved secondary structural motifs including an eight-strand antiparallel β -barrel (Rossmann & Johnson 1989) and a five-strand β -sheet flanked by two C-terminal alpha-helices (Golmohammadi et al. 1993). Since the capsid must be stable enough to protect the viral genome outside of the host, but weak enough to disassemble within the host (thereby allowing replication), the thermodynamic stability of virus capsids is studied as a potential route to developing novel anti-virals (Tsang et al. 2000).

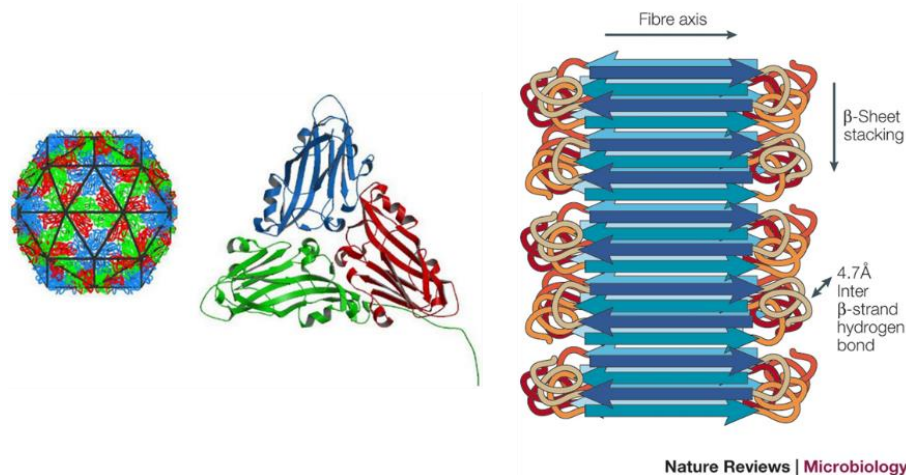


Figure 1.7 Higher order assemblies of proteins; (left) A virus capsid formed for protein subunits and (right) the assembly of an amyloid fibre from β -sheet strands. Modified from (Sömera et al. 2015) and (Gebbinck et al. 2005), respectively.

The formation of amyloid fibers is an important issue in medicine as these fibers have been linked with multiple diseases including Alzheimer's disease, Parkinson's disease, Huntington's disease and Type II diabetes (DeToma et al. 2012; McGowan et al. 2000). Amyloid fibers, are insoluble and proteolytic resistant and assemble from

normally soluble proteins (Rambaran & Serpell 2008) Amyloid fibers are thermodynamically stable and structural studies indicated that they are composed of β -sheet secondary structure in a cross- β conformation (Goldschmidt et al. 2010), figure 1.7.

Amorphous aggregates may be formed from folded or unfolded proteins and are structures without ordered intermolecular interactions. In addition to being the cause of some diseased states (Truscott 2005; Sugiyama et al. 2010), amorphous aggregates are a particular source of difficulty in the biopharmaceutical industry, (E. Chi et al. 2003).

The formation of higher-order protein assemblies is dictated by the colloidal stability of the monomer, be that folded or unfolded. Colloidal particles typically range in size between 1 nm and 10 μ m. When dispersed in a medium (the continuous phase), the behaviour (stability) of the colloids is dependent on the interaction potential between the particles. The colloid-colloid interaction potential is approximated as the interaction potential between two hard spheres and modelled using DVLO (Derjaguin, Verway, Landau and Overbeek) theory. DVLO theory links the effects of electrostatic repulsion, due to the double layer of counterions (see section 1.2) and the attraction due to van der Waals' forces. The electrostatic repulsion increases exponentially for particles at decreased separation and the van der Waals' attraction increases as an inverse power of separation. The additive force (interaction potential) is depicted below using a potential energy versus separation curve, figure 1.8. Where the interaction potential is positive, the particles are mutually repulsive and where the interaction potential is negative there is a net attraction between the particles. In general, the magnitude of the zeta potential (ζ) determines whether the system is colloidally stable; for stable colloidal solutions $-30 \text{ mV} < \zeta < +30 \text{ mV}$. The osmotic second virial coefficient, B_{22} , is a key parameter for the measurement of the propensity of proteins to self-associate; a negative value indicates protein-protein attraction, whereas a positive value indicates mutual repulsion (Mehta, White et al. 2012).

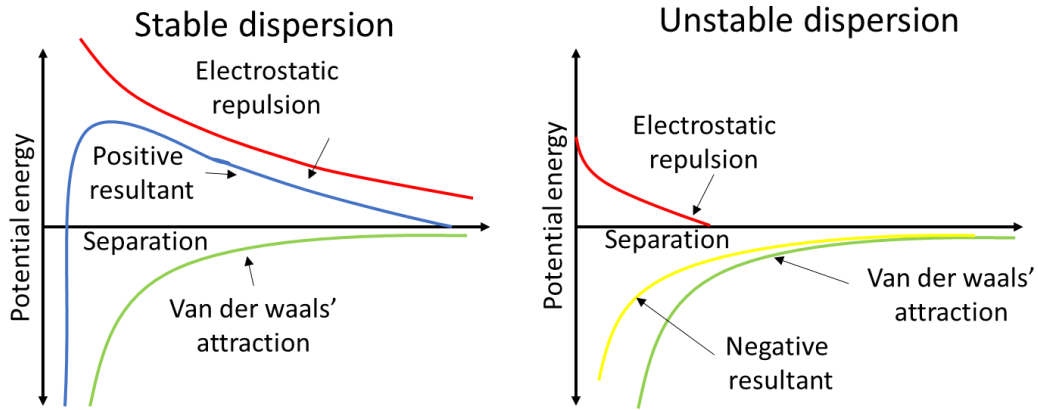


Figure 1.8 Schematic diagram showing the resultant interaction potential with particle separation for a suspension with (a) a high zeta potential (b) low zeta potential

Small globular protein molecules have a radius of gyration in the region of 1-2 nm (García De La Torre et al. 2000) and a solution of proteins may therefore be considered as a colloidal fluid. Protein stability is used to refer to both/either the structural stability of the protein or the solution (colloidal) stability. Here, structural stability refers to is the resistance of the protein to unfolding i.e. the maintenance of the native conformation whereas colloidal stability refers to the ability of the molecules to exist as monomers in solution for a defined set of solution conditions.

The temperature at which thermal denaturation of proteins occurs is often used as an indicator of how structurally stable a protein is (Cooper 1999), and the temperature at which unfolding occurs changes depending upon the solution conditions such as protein concentration, pH, ionic strength (Eisenberg and Schwert 1951), presence of co-solutes (Iser-Vincentelli and Leonis 1964) and ion type (Von Hippel and Wong 1965), discussed below. Differential scanning calorimetry is a useful technique used to determine the temperature at which denaturation occurs and the thermodynamic parameters associated with this event. This technique will be discussed in detail in section 2.2.5.

1.5.2.1 The effects of pH on protein colloidal and structural stability

At a particular pH known as, the isoelectric point (pI), a protein molecule has no net electrical charge. The amino acid constituents of a protein each have their own individual pKa's and the sum of these determines the overall charge on a protein at a given pH. As the pH of a solution is lowered the carboxyl and amine groups become protonated whereas at higher pH, these groups become deprotonated. The pH at which

protonation/deprotonation occurs is the pKa. Thus, altering the pH of a protein solution alters the overall charge on a protein. The higher the net charge on a protein, the greater the electrostatic repulsion between the molecules and the less likely the proteins are to associate. At certain concentrations, salt can screen charges and reduce the effect of the electrostatic repulsion. At the isoelectric point (or when sufficient salt is present) the colloidal stability of a protein is compromised and the protein molecules may aggregate (McUmber et al. 2015).

The pH also affects the structural stability of the protein through its ability to form intramolecular salt bridges (Anderson, Becktel et al. 1990). In addition, changes in pH produce perturbations in the strength of the hydrogen bonds in alpha helices and beta pleated sheets (Johnson 1988). These secondary structural elements of the native protein are critical to the overall structural stability.

1.5.2.2 The effects of ions on protein colloidal and structural stability

That ions effect the secondary and tertiary structure of protein has been studied since the early twentieth century beginning with the seminal work of Hofmeister and remains an active field of investigation up to the present day (Rembert, Paterová et al. 2012). The Hofmeister series is a categorization of ions based on their ability to salt out (a decrease in solute solubility with an increase in salt concentration) or salt in (increased solute solubility with an increase salt concentration) proteins, with anions having a greater effect than cations, figure 1.9

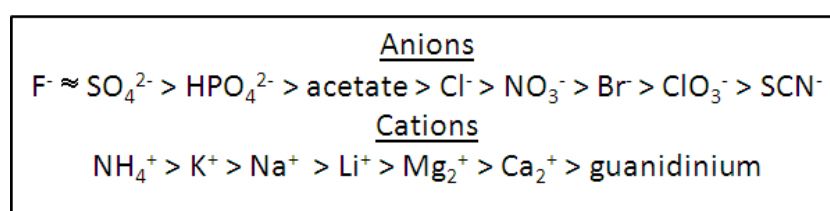


Figure 1.9 Hofmeister series showing the ranked ability of ions to salt in and out proteins.

The effect of ionic strength and ion type on protein structural stability is ascribed to free energy of the interaction between the protein and solvent. The Hofmeister series classifies ions according to their effects on protein solubility; kosmotropic ions increase in the stability of water–water interactions and whereas chaotropic ions decrease the water

structure. The process by which ions stabilise proteins is not fully understood but is thought to be mediated by both specific and non-specific interactions between the ions and proteins and between the ions and water by affecting the free energy of the water (Zhang and Cremer 2006, Kameoka, Masuzaki et al. 2007).

1.5.2.3 The effects of co-solutes on protein colloidal and structural stability

The solution conditions to which a protein is subjected during purification, processing and storage e.g. harsh pH, raised temperature or shear, are often detrimental to its structural and colloidal stability. In particular, unfolding and aggregation of protein based pharmaceuticals can have a negative impact on the product effectiveness and safety; a native conformation must be maintained for the protein to have a therapeutic benefit, the non-native conformation may be immunogenic (De Groot and Scott 2007, Weiss, Young et al. 2009). Furthermore, aggregation may result in the fouling and blockage of production or dispensing devices (Schoenitz, Grundemann et al. 2015). The solvent environment may be modified to mitigate these unfavourable conditions by the addition of co-solutes, which decrease aggregation by stabilizing the native conformation (Ohtake, Kita et al. 2011). Sugars, polyols and amino acids are common co-solutes used in biopharmaceutical formulations. (Chi, Krishnan et al. 2003).

Sugars may form covalent bonds with proteins, by the reduction of an amino group within the protein by the aldehyde group on the sugar, figure 1.10. This reaction occurs between 140 and 165 °C is known as the Maillard reaction. This is important in the browning of foods during the cooking process (Martins, Jongen et al. 2000). Non-reducing sugars, such as the disaccharides maltose and trehalose, do not have an aldehyde group and are unreactive to proteins under standard processing conditions.

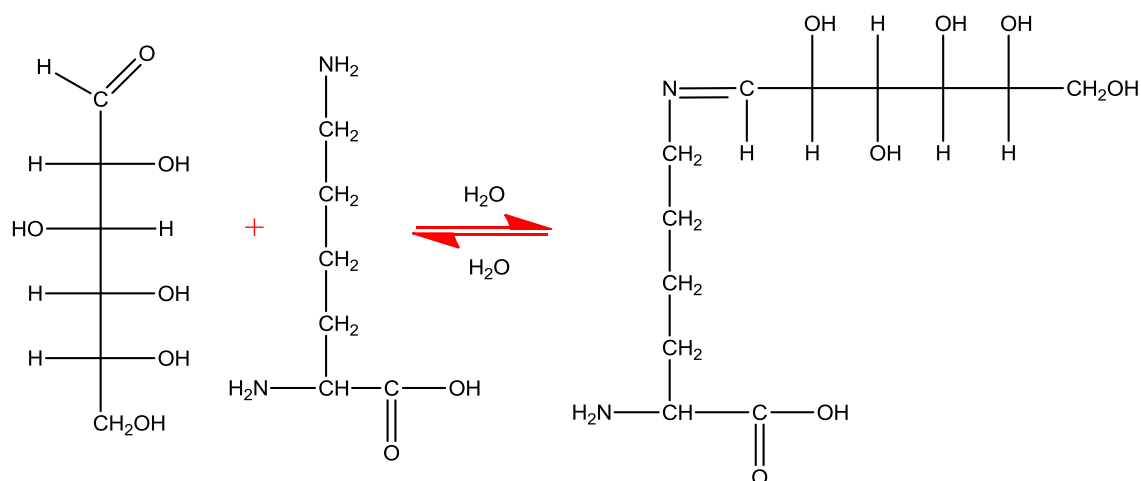


Figure 1.10 Maillard reaction; reducing sugar glucose binds to amino acid lysine.

The mechanism by which disaccharides stabilise the native conformation is an area of intense interest to biopharmaceutical companies since the melt transition temperature of proteins is often increased in the presence of sugars (Chi, Krishnan et al. 2003, Kamerzell, Esfandiary et al. 2011, Ohtake, Kita et al. 2011). The mechanism that has gained the most widespread acceptance is that of a preferential exclusion effect (Lee and Timasheff 1981). The source of this preferential exclusion effect has been variously attributed to the effect of sugars on interfacial tension (Lin and Timasheff 1996), water structure (Jain and Roy 2009), the sugars inherent hydrophobicity (Liu and Bolen 1995) and an excluded volume effect (Ebel, Eisenberg et al. 2000), figure 1.11. In an earlier study, the McManus group showed that enhancement of colloidal stability in the presence of sugars only correlates with an increase in the structural stability when the solution behaviour is not dominated by stabilising electrostatic interactions (James & McManus 2012).

In the presence of excipients that have preferential exclusion behaviour, the unfolding of protein from the native conformation is thermodynamically unfavourable since unfolding increases the volume of the excipient free water which is associated with an unfavourable decrease in entropy for the system, figure 1.11.

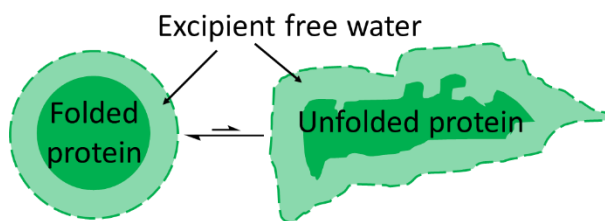


Figure 1.11 Schematic of excluded volume effect and preferential exclusion. The unfolded protein is associated with an increased volume of excipient free water. The resultant loss of entropy thermodynamically favours the native structure.

1.5.3 Mechanisms of protein aggregation

Protein aggregation is a collective term which encompasses the solid-like, condensed phases of proteins. Aggregates may form from natively folded proteins (Minton 2005) or may develop from unfolded or partially unfolded conformations (Fields, Alonso et al. 1992, Gupta, Hall et al. 1998, Wang 1999, Finke, Roy et al. 2000, Cellmer, Bratko et al. 2007). The process may be reversible (Arakawa and Timasheff 1985, Arakawa, Bhat et al. 1990) or irreversible (Kendrick, Cleland et al. 1998) and the attachments between the components may be physical, electrostatic or covalent. Furthermore, the aggregate may be classified by size or structure e.g. amorphous aggregate or amyloid-type fibril (Narhi, Schmit et al. 2012). Whatever the classification used, the type of aggregate formed depends on the intrinsic biophysical properties of the protein and on the solution conditions (Philo and Arakawa 2009). There are five principal mechanisms of protein aggregation including; reversible association of the native monomer, aggregation of conformationally-altered monomer, aggregation of chemically-modified product, nucleation-controlled aggregation and surfaced induced aggregation. These pathways are not mutually exclusive and may even occur concurrently within a solution (Philo & Arakawa 2009). Once assembly has begun, higher order oligomers may assemble in a stochastic manner via the formation of an aggregation nucleus or at a surface (where denaturation was as a result of protein-interface interactions). The morphology of protein aggregates depends on the mechanism via which it is formed.

1.5.3.1 Self-association of native monomers

Self-association of protein monomers may occur due to non-specific (colloidal-like) and specific interactions. For this mechanism, no conformational change is required for the monomer to self-associate and from small oligomers and these are generally reversible.

Sometimes, these originally reversible associations become irreversible due to the formation of covalent, intermolecular disulphide bonds (Alford, Kwok et al. 2008). The surface of a folded protein is inherently anisotropic due to the varied chemical nature of the amino acids on the surface and it is these regions that may be specifically attractive between protein monomers. The oligomers which form may follow many different growth patterns due to the many possible combinatorial arrangements available owing to the variability and amount of the surface patches, figure 1.12.

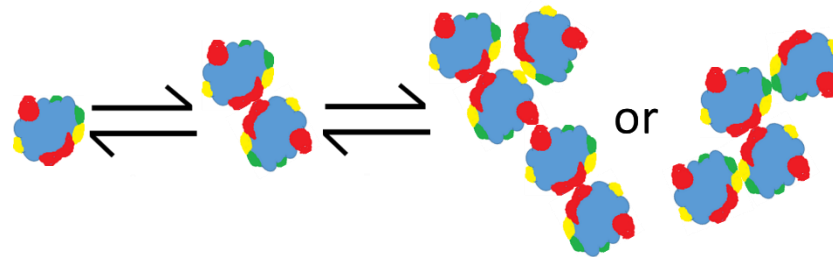


Figure 1.12 Schematic of self-association of native monomers.

Two reversible association mechanisms have been proposed. Eisenberg suggested a mechanism for the aggregation of glutamate dehydrogenase;



where N is native monomeric state and N_n is the oligomer with length n (Reisler & Eisenberg 1970). Later Thusius proposed a “random association mechanism” which included the possibility of both monomeric and polymeric association;



whereby any two native units, N_i or N_j of any size (i and $j = 1, 2, \dots, \infty$) can associate together (Thusius et al. 1975).

1.5.3.2 Self-association of non-native conformers

A conformational change may be induced due to changes in solution conditions such as in pH, ionic strength or temperature. The non-native monomer has an increased propensity to self-associate due to the presence of exposed hydrophobic patches (Zhang, Lu et al. 2008). This entropy driven process results in a decrease in free energy for the

system by reducing the hydrophobic surface area and decreasing its restrictive interaction with water. As with the aggregation of native monomers, these initially reversible associations may become irreversible following the formation of covalent bonds.

1.5.3.3 Self-association following chemical modification

Chemical modification via oxidation, deamidation or proteolysis creates changes to the chemical structure of the protein. These changes may result in a change in electrostatic or the covalent bonding capability of the protein. Changes to electrostatics will affect the interaction potential. The most common covalent protein-protein crosslinking is via the formation of intermolecular disulfide bonds. The formation of such novel intermolecular bonds (from free cysteine and re-pairing of cystine residues) results in the formation of irreversible aggregates (Trivedi, Laurence et al. 2009).

1.6 Protein Phase Diagrams

A protein phase diagram describes the physical state of a protein in two or three dimensions, e.g. temperature, volume fraction, pH or salt concentration. Small globular protein molecules have a radius of gyration in the region of 1-2 nm (García De La Torre et al. 2000) and a solution of proteins may therefore be considered as a colloidal fluid. Colloidal particles in solution may exist as a colloidal fluid, coacervates or a condensed phase. The condensed phase may have a regular structure, in the case of crystals, or amorphous structure, in the case aggregates (Asherie et al. 1996). The structure of the phase diagram is determined by the range of the attraction between the particles in the system (Daanoun et al. 1994) and the thermodynamic forces which drive the transition of a protein from one phase to another is the sum of the interactions occurring between protein and solvent molecules (Dumetz et al. 2008). A two dimensional phase diagram might typically map a solution condition variable (pH, the concentration of a co-solute or temperature) as a function of volume fraction, figure 1.13. The liquid-liquid, coexistence or binodal line, signifies the transition from single phase consisting of a uniformly dispersed colloidal solution to condition where two distinct phases, co-exist; one protein-rich and one protein-poor. The different phases occur due to the concentration fluctuations at temperatures less than the critical temperature for phase separation. The spinodal line (within the bounds of the bimodal) separates the biphasic region into a metastable and unstable region. Liquid-liquid phase separation has been observed for γ -

crystallins (a family of proteins found in the eye lens) (McManus et al. 2007) and lysozyme (an anti-microbial protein found in tears and egg white) (Muschol & Rosenberger 1997).

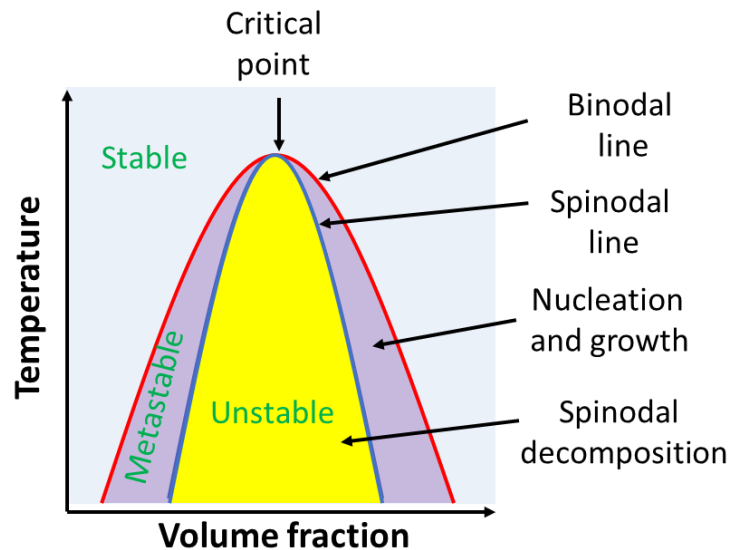


Figure 1.13 A hypothetical phase diagram in the temperature-density plane in the temperature- showing the different phases

1.6.1 Spinodal decomposition

During spinodal decomposition, protein molecules begin to cluster together leading to the formation of micro-regions which are either protein-rich or protein-poor (Varrato et al. 2012). In a process referred to as coarsening, these clusters coalesce and grow until a single protein-rich and a single-protein-poor phase is present (Atkins 2014). However, spinodal decomposition may become dynamically arrested and complete de-mixing does not occur. For certain quench temperatures and at certain quench rates, colloidal solutions begin to liquid-liquid phase separate via the spinodal decomposition method, however, during coarsening, the formation of space spanning clusters causes ‘jamming’ and prevents the formation of a single colloid-rich and a single colloid-protein-poor phase (Lu et al. 2008). Arrested spinodal decomposition has been shown to be a mechanism for the formation of nucleic acid and protein gels at intermediate values of inter-particle interaction strength (U_a) and volume fraction (Φ) (Blumlein & McManus 2015; Zaccarelli 2007).

1.7 Gels

The term gel has been defined in many ways but in all cases, refers to a system consisting mostly of solvent but demonstrating a solid-like consistency, with the solid character derived from a three dimensional cross-linked network (Flory 1941). The formation of this network is referred to as the gel-sol (a liquid mixture of solute particles suspended in solvent) transition and is associated the emergence of a finite shear modulus and an infinite zero-shear viscosity (Chambon 1987)(see section 2.1). Where water is the solvent, these gels are termed hydrogels. Gels formed from proteins are often referred to as natural gels in contrast with synthetic gels, the terms reflecting the origin of the constituent polymer. Regardless of the source of the polymer, the physiochemical properties of a gel are conferred by the chemistry of the polymer and the physical and chemical conditions underwhich gelation occurs. Gels may form via physicals interactions (Ward 1954, Morris, Rees et al. 1980, Blandino, Macías et al. 1999, Zaccarelli 2007, Varrato, Di Michele et al. 2012), chemical crosslinking (Laemmli 1970, Abraham, Brahim et al. 2005, Bayramoglu, Bitirim et al. 2013) or a combination of these mechanism (Havea, Carr et al. 2004, Sun, Zhao et al. 2012).

1.7.1 Physical gels

Physical gels are also referred to as reversible gels. These are held together by molecular entanglements, depletion interactions, ionic, hydrogen bonding and hydrophobic interactions or a combination thereof. These interactions are reversible and the gel may be transformed to the sol state by an alteration in the physical conditions e.g. pH, temperature, pressure. These gels may form from either polymers or colloids.

1.7.1.1 Polymeric physical gels

For polymer gels the long polymer chains no longer act as individual components but as a single unit. These networks are formed either in the molten state or in solution when critical entanglement molecular weight (M_c) is reached (Wool 1993)(Equation 1.20).

$$M_c = C_\infty M_o / \alpha^2 j \quad (\text{Equation 1.20})$$

where C_∞ is the characteristic ratio (the ratio between the actual unperturbed dimensions of real chain and that of a conceptually freely jointed chain), M_o is the monomer molecular weight, j is the number of backbone bonds per monomer. The α factor is

$$\alpha = \frac{C}{bzj} \quad (\text{Equation 1.21})$$

where C is the C-axis dimension of the unit cell, b is the bond length and z is the number of monomers per C-axis length (equation 1.21).

Ionic cross-linked gels, such as those formed by alginates or gellans, are a very important class of physical hydrogels with many biomedical applications (Lee and Mooney 2012, Osmalek, Froelich et al. 2014). Alginate gels are formed by the ionic cross-linking of this anionic polymer by divalent cations. Alginates are naturally occurring polysaccharides that are harvested from seaweed and commercially available as, water soluble, sodium alginate, which are unbranched binary co-polymers composed of 1-4-linked- β -D-mannuronic acid (M) and α -L-guluronic acid (G) (Rinaudo 2008). The distribution and proportion of repeat units (MM, GG, GM) vary depending on the source, and this can affect the physico-chemical properties of the gels (Martinsen, Skjåk-Bræk et al. 1989). In solution, alginates adopt a flexible coil structure, however, they form gel structure when cross-linked by divalent cations due to complex formation between calcium and the oxygen atoms of guluronic acid on two different polymer strands (Li, Fang et al. 2007)(figure 1.14). The thermo-reversible protein based gels formed from gelatin also belong to this class of gel as do the polysaccharide agarose gels which are used in cell culture.

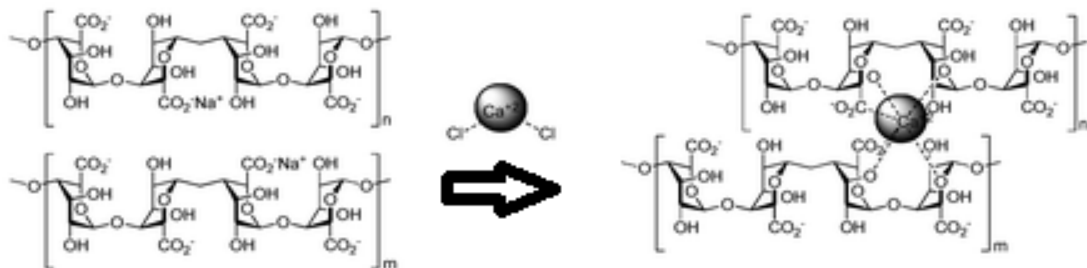


Figure 1.14 Reversible gelation of alginate by complexation of α -L-guluronic acid moieties from separate polymer strands with divalent calcium ions to form a junction. Modified from (Delaney, Liberski et al. 2010).

1.7.1.1.1 Colloidal physical gels

Colloidal gels form where the attraction between particles is strong but short range. The particles aggregate to form clusters that have an open, branched and tenuous network with a small number of particles occupying a large volume (Lu & Weitz 2013). Colloidal particles which also include proteins, form both non-equilibrium and equilibrium gels. Three different routes to gelation have been proposed; (1) non-equilibrium gelation occurring as the result of arrested spinodal decomposition, (2) equilibrium gels formed as a result of competition between short range attraction and long range repulsion and (3) equilibrium gels formed from patchy particles: the different gel states arising out of different inter-particle potentials (Zaccarelli 2007). For colloidal gels, bonds can be deemed to have formed between a pair of particles when the particles are closer than the range of attraction. It should be noted that, for physical gels, percolation does not necessarily signify gelation due to the finite bond lifetimes (Zaccarelli 2007). The gel structure can endure for long periods (Ruzicka et al. 2011) if gravitational or self-generated stress is lower than the yield stress of the gel (Tanaka 2013).

For colloidal gels two limits of aggregation exist, diffusion-limited cluster aggregation (DLCA) and reaction-limited cluster aggregation (RCLA) (Lu & Weitz 2013), figure 1.15. For DLCA the particles stick irreversibly to each other and the system's behaviour (and therefore morphology) is governed by the diffusion of the particles. Gels formed by DLCA have a low fractal dimension of ~ 1.8 (Dinsmore & Weitz 2002). During RCLA the particles must overcome a repulsive barrier prior to bonding and multiple attempts are required to form an inter-particle bond which leads to the formation of more compact clusters with higher fractal dimensions (Weitz et al. 1985).

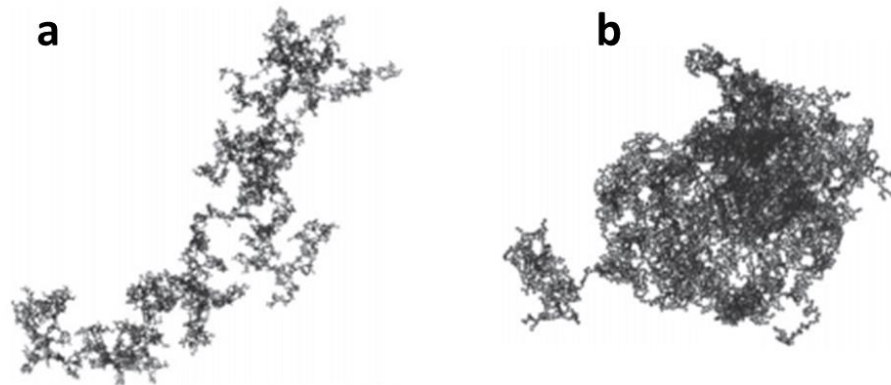


Figure 1.15 Transmission electron micrograph of typical clusters of gold colloids formed by a) diffusion-limited and b) reaction-limited cluster aggregation; modified from (Lu & Weitz 2013)

The solvent has been shown to play a critical role during gelation. When hydrodynamic interactions (HI) are included in numerical simulations, the volume fraction required for gelation was reduced by a factor of 1.75 (Royall et al. 2015). Here it was shown that the inclusion of HI within the simulations led to the formation of highly anisotropic threads which promote an open gel network. In the absence of HI compact clusters (~ 10 particles) were formed, however with the inclusion of HI the particles were mainly arranged as four-member tetrahedral or five-member triangular bipyramids, which are minimally mechanically stable. This is an important observation since the mechanical properties of gels are dependent on the structure of the gel (Valadez-Pérez et al. 2013; Kroy et al. 2004) and the authors suggest that where the concentration of the gelling agent is important, it is prudent to include HI within the simulations rather than solely relying on Brownian dynamical simulations.

1.7.2 Covalently cross-linked gels

Chemical gelation is described in terms of percolation theory. The mean-field theory of percolation was first developed by Flory (Flory 1941) and refined by Stockmayer (Stockmayer 1943). Two basic assumptions underpin the theory; (1) no intramolecular bonds occur i.e. no loops are allowed and (2) each reactive unit is equally reactive. Here, the monomers occupy a position in a lattice with a probability of p , and the probability of a bond between occupied lattice points is b . At high p or b an infinite cluster (percolated network) is formed. The degree of bonding required for the formation of a percolated network is given by (equation 1.22);

$$P_c = \frac{1}{Z-1} \quad (\text{Equation 1.22})$$

here P_c is the critical bond probability, z is the number of functional groups on the monomer. For example, for $P_c = 1/2$, a percolated network will form when half the possible bonds have been made. Above P_c a gel is formed, figure 1.16.

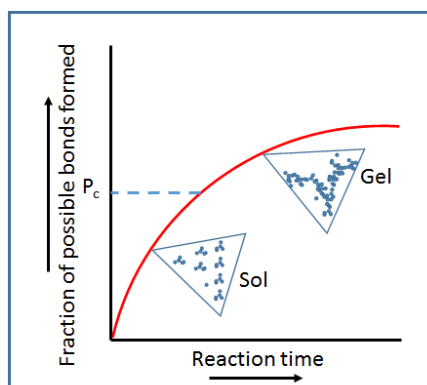


Figure 1.16 Schematic showing percolation and gel formation above the critical bond probability.

Polyacrylamide gels are a classic example of a covalently cross-linked hydrogels. The polymer is formed from acrylamide subunits ($\text{CH}_2\text{CHCONH}_2$) and the polymer chains $[-\text{CH}_2\text{CHCONH}_2-]_n$ are cross-linked, typically, using $\text{N,N}'$ -methylenebisacrylamide (bis-acrylamide), figure 1.17.

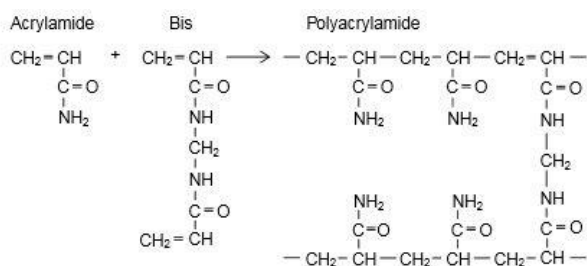


Figure 1.17 Polymerisation of polyacrylamide.

1.8 Cells and Tissues

Cells and tissues exist under non-equilibrium conditions in a thermodynamically open system where energy is exchanged with the environment (Rastogi 2008; Prigogine et al. 1974). Mammals belong to the eukaryote domain, therefore cells are bound by a cell

membrane and contain a membrane bound nucleus and other membrane bound organelles along with fluid known as cytoplasm within which there is an extensive network of protein filaments and tubules that are responsible for maintaining the cell's shape and transportation within the cell. These filaments are also involved in cell signalling, division and migration. This cytoskeleton is connected to proteins embedded in the cell membrane which are in turn connected to the extracellular matrix [an intricate network of glycoproteins and polysaccharides secreted by cells which provides a physical scaffold for cells within tissues and is also involved in initiating important biochemical and biomechanical cues involved in tissue morphogenesis, differentiation and homeostasis (Frantz et al. 2010)]. The cytoskeleton participates in both the intra-cell and inter-cell contributions to the mechanical properties of tissues (Reece et al. 2009), figure 1.18.

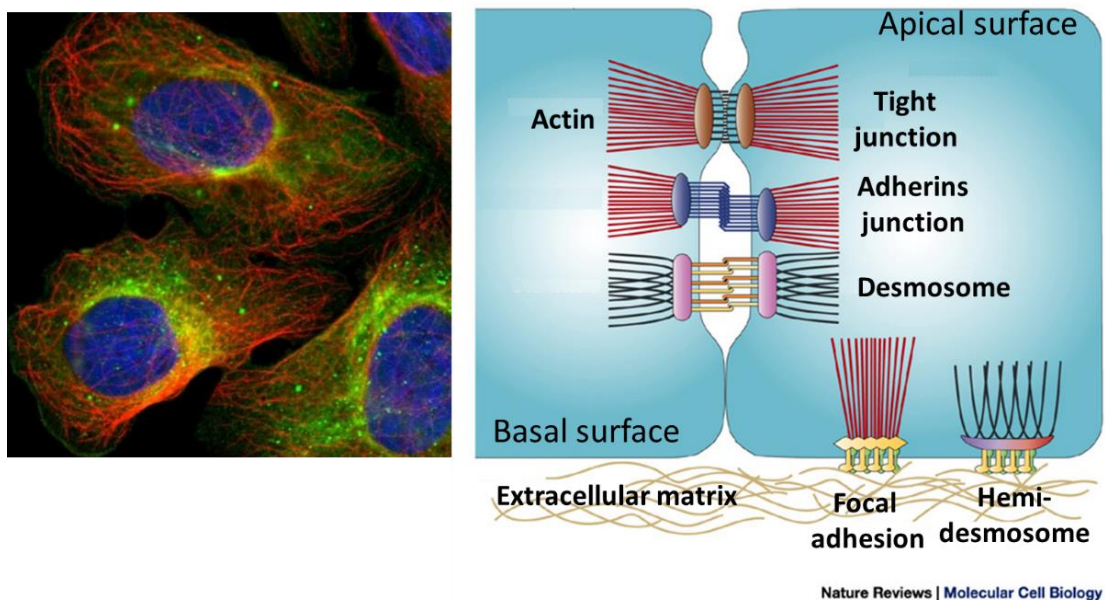


Figure 1.18 Mammalian cell and tissue architecture; (left) fluorescence microscopy image of a cells shows nucleus (blue) and an extensive cytoskeleton (red) and (right) a schematic of the cell-cell adhesion molecules and cell-extracellular adhesion molecules; images from Novus Biologicals and (Jefferson et al. 2004), respectively.

1.8.1 The cytoskeleton

The cytoskeleton has three major components; microfilaments - a multimer of the protein actin; microtubules - a multimer of the protein tubulin and intermediate filaments - a hetero-oligomer composed of multiple proteins (Wickstead & Gull 2011). The

cytoskeleton is not rigid, it is dynamic and many proteins have been found that bind to and alter the cytoskeleton for example, in motile cells, such as leukocytes (immune system cells), a macromolecular complex of proteins known as WAVE promotes the fabrication of actin microfilaments in the direction of movement (Weiner et al. 2007; Chen et al. 2014; Blanchoin et al. 2014).

The mechanical stiffness of the cytoskeleton polymers differs considerably, as measured by their persistence lengths: intermediate filaments are the most flexible (0.5 μm), actin filaments less so (13.5 μm) and microtubules are the most rigid (5,000 μm) (Brangwynne 2006; Gittes et al. 1993; Fletcher & Mullins 2010). The three polymer networks of the cytoskeleton are linked together in a complex manner and this super-network both responds to and exerts mechanical forces into the microenvironment of the cell. The mechanisms involved in the transmission of compressive or tensile forces may be non-specific, from steric hindrance, entanglement, or specific through the action of proteins that act as linkers. This interconnectivity means that internal or external forces can be distributed throughout the cell through continuous mechanical coupling (Fletcher & Mullins 2010).

The cytoskeleton behaves as a semi-flexible polymer. The elasticity of the cytoskeleton has both an entropic and enthalpic contribution. Entropic elasticity results from the reduction in number of configurations available to the fibers upon stretching – providing a restorative force. While the enthalpic contribution is due to changes in the cytoskeleton molecules (MacKintosh et al. 1995). The architecture of the network appears to determine the influence of each mechanism to the overall mechanical properties.

In response to shear stress the cytoskeleton has been shown to undergo shear stiffening as a result of filament entanglement and entropic elasticity (Storm et al. 2005). To demonstrate the importance of entropic elasticity in networks without specific filament orientation, shear stress was applied to randomly organised actin filaments and the elastic modulus was shown to increase significantly when crosslinkers (scruin and filamin A) were added to the fibers (Gardel et al. 2004; Koenderink et al. 2009; Tharmann et al. 2007). Where the filaments show a more highly organised architecture, the enthalpic bending of the filaments rather than the entropic stretching has been shown to be the more

dominant elastic component (Chaudhuri et al. 2007). The mechanical properties of the cytoskeleton has also been shown to depend on the properties (rigidity, length and density) of the crosslinking proteins (Wagner et al. 2006).

Two other influences must also be considered with respect to the intra-cell mechanical response; the displacement of fluid and the deformation of the cell membrane. The resistance of the fluid-like cytosol to flow around the cytoskeleton, organelles and macromolecules (poroelasticity) can affect the propagation of stress through the cell, which is slow compared to the direct mechanical coupling through the cytoskeleton network (Charras et al. 2005; Moeendarbary et al. 2013; Fletcher & Mullins 2010). In addition, since the cytoskeleton is connected to the cell membrane via attachment proteins, the mechanical properties of the cell membrane also affect the overall intra-cell contribution to the mechanical properties of tissues (Herant et al. 2005).

The cell membrane is a composite structure which is mainly composed of phospholipids and also contains proteins and carbohydrates and other lipids, figure 1.1 (Reece et al. 2009). The properties of the cell membrane affects the overall mechanical properties directly and indirectly. The elasticity of the membrane is affected by the membrane thickness which is dependent upon the chain length and the number of saturated hydrocarbons in the component phospholipids, with poly-cis unsaturated chain bilayers being thinner and more flexible than saturated or monounsaturated chain bilayers (Rawicz et al. 2000). Furthermore, there is a dynamic interplay between the components of the membrane and the actin cytoskeleton, in particular phosphoinositides have been shown to play a key role in regulating the actin filaments by acting as a platform for the recruitment of proteins that trigger signalling cascades which direct the organisation and polymerisation of the filaments (Saarikangas et al. 2010).

1.8.2 Cell adhesion & the extracellular matrix

1.8.2.1 Cell-Cell adhesion

In tissues, one cell is connected to the cytoskeleton of its neighbours and to the extracellular matrix through an array of multi-protein complexes. The proteins involved are termed cell adhesion molecules. Three important classes of cell adhesion molecules

are cadherins, claudins and integrins. Cell-cell complexes are mediated primarily by cadherins and claudins whereas integrins are associated with cell-extracellular matrix complexes. There are three principle classes of cell-cell junctions; anchoring junctions, tight junctions and gap junctions. Gap junctions are regulated, porous structures that are primarily involved in the exchange of ions, second messengers (e.g. cAMP) and small metabolites between cells. Unlike anchoring junctions and tight junctions, gap junctions are not connected to the cytoskeleton and do not appear to have a mechanism to dissipate mechanical stress (Meşe et al. 2007).

There are a plethora of anchoring and tight junctions, desmosomes, hemidesmosomes, focal adhesions and adherens junctions, figure 1.18b. Adherens junctions provide a strong mechanical attachments between neighbouring cells. Through a multi-protein complex they connect the actin filaments of adjacent cells. In mature cells a linear bundle of actin filaments form a circumferential actin belt inside the cell membrane and the cytoplasmic domain of cadherins associates with these actin filaments (Takeichi 2014).

1.8.2.1.1 *Cadherins*

Cadherins are transmembrane proteins, with an extracellular Ca^{2+} binding domain, that forms homodimers with cadherins from neighbouring cells (Maître & Heisenberg 2013). Desmosomes are also linked via cadherins but are bound to intermediate filaments within the cell (Desai et al. 2009). Tight junctions regulate the flow of ions across the paracellular space. Here, a multi-protein complex connects to actin filaments and a family of transmembrane proteins called claudins. The mechanism by which claudins interact in the extracellular space is not yet fully elucidated, but studies indicate that homotypic cell-cell adhesion, mediated by a complimentary hydrophobic interaction, may be responsible. (Anderson & Van Itallie 2009).

1.8.2.1.2 *Integrins*

Integrins are the major family of transmembrane proteins that link the cytoskeleton, through hemidesmosomes and focal adhesions complexes to the extracellular matrix. Integrins are heterodimeric, having an alpha and beta strand; with a multiplicity of subtypes available for each strand. Binding specificity to the various

components extracellular matrix (fibronectin, collagen and laminin) is conferred by the combination of strand subtypes and how they bind to specific motifs within the extracellular proteins. (Huttenlocher & Horwitz 2011) Integrin binding to the extracellular matrix is dependent on divalent cations (Ca^{2+} , Mg^{2+} and Mn^{2+}) (Campbell & Humphries 2011).

1.8.2.2 Cell adhesion to the extracellular matrix

The extracellular matrix (ECM) provides a physical support for cells and a regulatory role in cell differentiation by means of providing mechanical and biochemical cues. Fibroblasts are cells that specialise in the production and secretion of ECM proteins and polysaccharides but ECM proteins are also expressed, though less profusely, by other cells. ECM composition varies in both a spatial and temporal manner and is mainly composed of proteins (elastin) and glycoproteins (collagen). The ECM undergoes dynamic reconstruction in response to mechanical stimuli emanating from both cells and the environment. The components of the ECM have evolved innate biophysical properties that facilitate their self-organisation into large homo- and heteropolymeric fibers; which interact with one another with the result that the ECM displays a highly organised architecture that provides a physical support to the cells of the tissue. The individual ECM macromolecules self-organise into supramolecular structures that vary in composition and in a tissue specific manner. Two essential properties of the ECM are strength and elasticity which are established by fibers themselves and by the structured network which they form. Collagen fibers primarily provide strength whereas elastin fibers primarily provide elasticity. (Mouw et al. 2014)

1.8.2.2.1 Collagen

Collagen, from which gelatin is derived, is the most abundant protein in the ECM and collagen fibers may be composed of hetero- or homotrimers held together by hydrogen bonds along the body of the fiber and a covalent aldol crosslink between lysine or hydroxylysine residues at the C-terminus of one molecule to two similar residues on the N-terminus of an adjacent strand (Shoulders & Raines 2009). Collagen fibers vary in thickness; type I fibers are heterotrimers of 50 nm in diameter and collagen type II and type III fibers are homo-polymers 80 nm and 30-130 nm in diameter, respectively. These three are the major collagen types in most adult tissue [type I (80%) and type III (10%)]. Collagen fibers are arranged as a right-handed triple helix of polypeptides with a repeating

Gly-X-Y amino-acid motif; where X and Y are any amino acid, but where X is frequently proline and Y is frequently hydroxyproline. Collagen molecules are post-translationally modified by glycosylation prior to their transfer into the extracellular environment. (Koláčná et al. 2007) The Young's modulus of single collagen fibrils [ordered bundles of ~ 500 nm in diameter, which assemble from the triple helix] has been determined, using atomic force microscopy, to range between ~ 0.5 and 5.4 GPa (Wenger et al. 2007; Kontomaris et al. 2012). The Young's modulus and ultimate tensile strength of hydrated cartilage samples (from the knee) with a dry weight collagen content of ~ 90% were determined to range between 22 to 26 MPa and 15 to 25 MPa, respectively (Eleswarapu et al. 2011). Tendons which are designed to transfer mechanical force from muscle to bone, show great variation in the elastic moduli depending on the source and age of the specimens. Reported values range from ~ 200 mPa to > 1,000 mPa (LaCroix et al. 2013). Taken together, these reports show that collagen fibers provide stiffness (large elastic modulus) and strength (large tensile strength) to the extracellular matrix.

1.8.2.2.2 *Elastin*

Elastin fibers are composed of molecules that are rich in hydrophobic amino acid residues. These fibers self-organise from monomers with a series of beta turns, which in turn organise via hydrophobic folding into beta-spirals that further assemble, hydrophobically, into twisted filaments 0.5 -1 μm in diameter. The strands are covalently cross-linked at intervals at modified lysine residues. Elastin fibers deform reversibly without losing energy and show large deformations under small stress. Increased entropy in the relaxed state versus the stretched state is the source of elasticity in these fibers. The elastic modulus of elastin fibers has been shown to range from 0.1 to 1.2 MPa with yield strength ranging from 0.2 to 2 MPa (Thiriet 2011; Lillie & Gosline 2002; Pollock & Shadwick 1994). Thus, elastin fibers contribute elasticity but not strength to the extracellular matrix.

1.8.2.2.3 *Fibronectins and laminins*

Fibronectins and laminins are two other important non-collagenous glycoproteins of the ECM. These ECM components bind to the integrins found in hemidesmosomes and focal adhesin complexes; thereby joining the ECM to the cytoskeleton.

Due to the mechanical coupling described above, the elastic modulus of cells in tissues, is related the cell's intrinsic elastic modulus, the elastic modulus of the mechanical properties of the ECM and adhesion molecules and it has been shown that the cytoskeleton of cells in tissues subjected to stress has been shown to re-orientate in response to that stress (Birukov et al. 2002). The elastic modulus of tissues varies widely from ~ 20 GPa for cortical bone (Rho et al. 1993) to ~ 1 Pa for the aortic arch (Isnard et al. 1989). For unconfined, non-adherent cells the elastic modulus is solely a property of the individual cell.

1.8.3 Surface tension effects in cells and tissues

Recently, the importance of a surface tension contribution to the self-ordering and mechanical properties of tissues had been appreciated and investigated (Manning et al. 2010; Foty & Steinberg 2005; David et al. 2014; Brasch et al. 2012). In liquids, surface tension is due to an imbalance of intermolecular forces, with the net force tending to draw surface molecules towards the bulk. In the same way that surface tension results in the rounding of liquids, interfacial tension has been used to explain the rounding of cells undergoing cytokinesis (Stewart et al. 2011; David et al. 2014) and the rounding of explanted tissues (Ninomiya & Winklbauer 2008; Foty et al. 1996). The energy required (δE) for a change in surface area (δs) is related to surface tension (σ) by (equation 1.23);

$$\Delta E = \sigma \delta s \quad (\text{Equation 1.23})$$

Surface tension endows cells and tissues with apparent mechanical stiffness with which they resist mechanical stress; tension values for tissues have been measured at ~ 1.6 to 20 mNm^{-1} (Guevorkian et al. 2010; Mgharbel et al. 2009; Foty et al. 1996; Manning et al. 2010) while those of individual cells range from 10^{-3} to 10^{-5} mNm^{-1} (Hochmuth 2000; Peukes & Betz 2014; Evans & Yeung 1989; Chaigne et al. 2015).

Two theories regarding the origin of tissue surface tension have been proposed; the differential adhesion hypothesis (DAH) (Foty & Steinberg 2005) and the differential interfacial tension hypothesis (DITH) (Graner 1993; Brodland 2003; Harris 1976). DAH considers tissues analogous to conventional fluids and surface tension is proportional to the adhesive energy between the component cells. Indeed it has been determined experimentally that a linear relationship between expression levels of adhesion molecules

and tissue surface tension exists (Foty & Steinberg 2005). More recently, however, AFT (Krieg et al. 2008) and tissue surface tensiometer experiments suggest a contribution of cortical tension to surface tension (Manning et al. 2010) which is consistent with the DITH, as DITH recognises that a cell's mechanical energy changes with cell shape, thus a role for cortical tension is acknowledged. Accordingly, two principal components of surface tension have been identified; cortical tension and adhesion tension and that it is the ratio of adhesion tension to cortical tension that determines the overall surface tension (Manning et al. 2010). Cortical tension (from the cell cortex) is the largest component of tension in isolated cells and contract free regions of tissues. Adhesion tension results from the negative contribution of adhesion molecules to the surface tension. (Manning et al. 2010)

1.8.3.1 Cortical tension

Unlike liquids, the interior of the cell is not composed of the same material as the cell surface and a change in surface area cannot be achieved by a straightforward addition of molecules from the bulk to the surface. However, the membrane is creased and folded, and this amounts to a reservoir of molecules which are available to change the cell's apparent surface area and therefore its area of contact with other cells. Thus, the surface tension of a cell is a dynamic property dependent on the apparent surface area (Peukes & Betz 2014). The cell shape and surface area is dependent on the actomyosin cortex. Cortical tension is generated by the actomyosin cortex, a specialised layer of cytoskeleton found inside the plasma membrane, to which it is attached (Fischer-Friedrich et al. 2014). This dense, actin rich layer provides mechanical stiffness to the cell. Due to the mechanical coupling of the cortex and membrane, the effective cortical tension involves a contribution from both structures (Peukes & Betz 2014). When two cells are in contact the shape of cells changes such that they are no longer spherical, analogous to soap bubbles in a foam, figure 1.19a-b. This change in shape is opposed by cortical tension, figure 1.19c. Therefore, since cell surface tension is related to area and cell area (shape) is related to cortical tension, cell surface tension is related to cortical tension. (Lecuit & Lenne 2007)

1.8.3.2 Adhesion tension

The increase in the cell-cell contact area, mediated by adhesion proteins, signifies a reduction in interfacial tension (Maître & Heisenberg 2013). Cadherins are an important

class of proteins found in large protein complexes involved in cell-cell adhesion (Reece et al. 2009). The extracellular domain of these transmembrane proteins contains multiple Ca^{2+} binding domains which need to be occupied to maintain the native structure of the protein (Kim et al. 2011). Cell-cell attachment occurs when the EC1 domains of cadherins from opposing cells substitute for each other a tryptophan residue in their folded structure; this process is known as trans-dimerization (Cailliez & Lavery 2005). For cadherin type II, cis-dimerization also occurs (Maître & Heisenberg 2013). Here two cadherins from the same cell engage in residue swapping and this appears to be an important mechanism whereby cadherins are recruited to cell-cell junctions (Brasch et al. 2012) In addition to establishing a mechanical contact, the formation of these trans-bonds also influences cell-cell self-organisation by reducing local interfacial tension, figure 1.19d. Interfacial tension is reduced directly through adhesion tension and indirectly through signalling to the cytoskeleton which reduces the cortical tension and thus interfacial tension. (Maître & Heisenberg 2013).

Adhesion tension originates from the formation of the trans-dimers, which is energetically favourable. Following binding, other cadherins are recruited to the cell-cell contact site where they become stabilised by trans-bonding. It is thought that cadherin accumulation increase cell-cell contact expansion in a number of ways including zippering and protein crowding leading to lateral pressure.

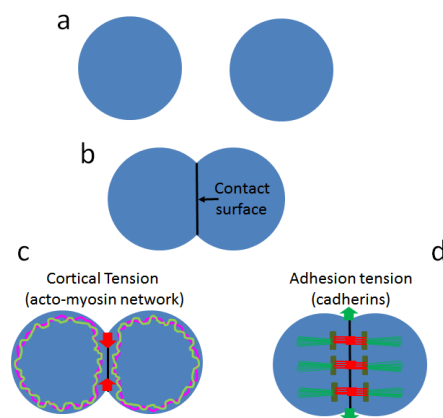


Figure 1.19 Cell surface tension is related to cortical tension and adhesion tension. (a) Two cells not in contact will take the shape of a sphere. (b) Upon contact, a contact surface is established and the shape of the cells changes from spherical (c) This change in shape is opposed by cortical tension (d) Adhesion molecules, cadherins increase the contact surface.

1.9 Thesis motivation

The motivation for this work was to further our understanding of the mechanisms of self-organisation in biological soft matter systems at different length-scales. In biological systems, self-organisation occurs over a range of length-scales from the molecular level to that of an entire organism. The interactions responsible for this self-organisation are on an energy scale comparable to that of the average thermal energy at room temperature (kT). Here, the experimental techniques of the wider soft matter field are used to investigate the biophysical properties of these systems. Research into the mechanisms underlying these systems provides a route to exciting developments in materials chemistry where a bottom-up approach based on directed self-organisation has the potential to yield novel materials with a wide range of technological and scientific applications.

The first part of this work aims to understand the mechanisms involved in molecular-level interactions that govern the aggregation process of proteins following thermal denaturation. In the second chapter, the model proteins BSA and gelatin, were used to assess if the self-organisation behaviour of proteins could be used to generate a novel biomaterial. The third chapter explores self-association at the cellular length scale. Here an attempt is made to relate the mechanical behaviour of tissues to cell-cell self-organisation.

Chapter 2 Techniques used to Characterise Soft Matter

2.1 Methods used to determine Young's elastic modulus

Biological tissues behave as gel-like materials in response to external stress, they store (elastic response) and dissipate (viscous response) energy. Following deformation induced by an applied force, a Hookean elastic material will revert to its initial shape and size when that force is removed as long as the stress is below the elastic limit of the material. In a viscoelastic material the original shape and size are not restored by the removal of the applied force, figure 2.1 (Atkins 2014). On short time scales biological tissues behave as elastic solids whereas on long time scales viscous fluid-like behaviour is exhibited (Fung 2013). In chick fibroblast, elastic forces have been shown to dominate for short time scales (seconds) whereas viscous behaviour was apparent at intermediate time scales (minutes) (Thoumine & Ott 1997).

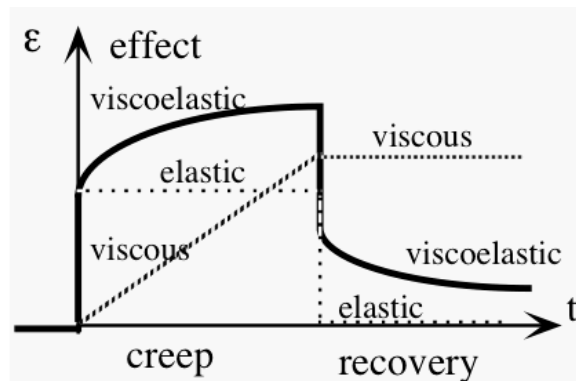


Figure 2.1 The relationship between strain (ϵ) and time in elastic, viscous and viscoelastic materials. Adapted from (Lakes 2009)

Young's modulus (longitudinal elasticity), E , is a measure of the inherent stiffness of a material; it is the force (per unit area) needed to stretch or compress a material (Giambattista 2010), given by;

$$E = \frac{\sigma}{\epsilon} \quad \text{Hooke's Law (Equation 2.1)}$$

where σ is tensile stress and ϵ is extensional strain. Other measures of elasticity include the bulk modulus (which measures the response to uniform compression) and the shear modulus (which measures the response to shear). Methods to test elastic moduli include static and dynamic methods such as; active microrheology (e.g. optical tweezers), atomic force microscopy, image based passive microrheology (e.g. particle tracking) and rheometer based macrorheology (Chen, Wen et al. 2010). The choice of method will

depend on the size of the sample available for testing, the length-scale at which the modulus is to be determined, the expected elastic modulus of the material, whether the sample is in-vivo, the throughput rate required and the cost, figure 2.2.

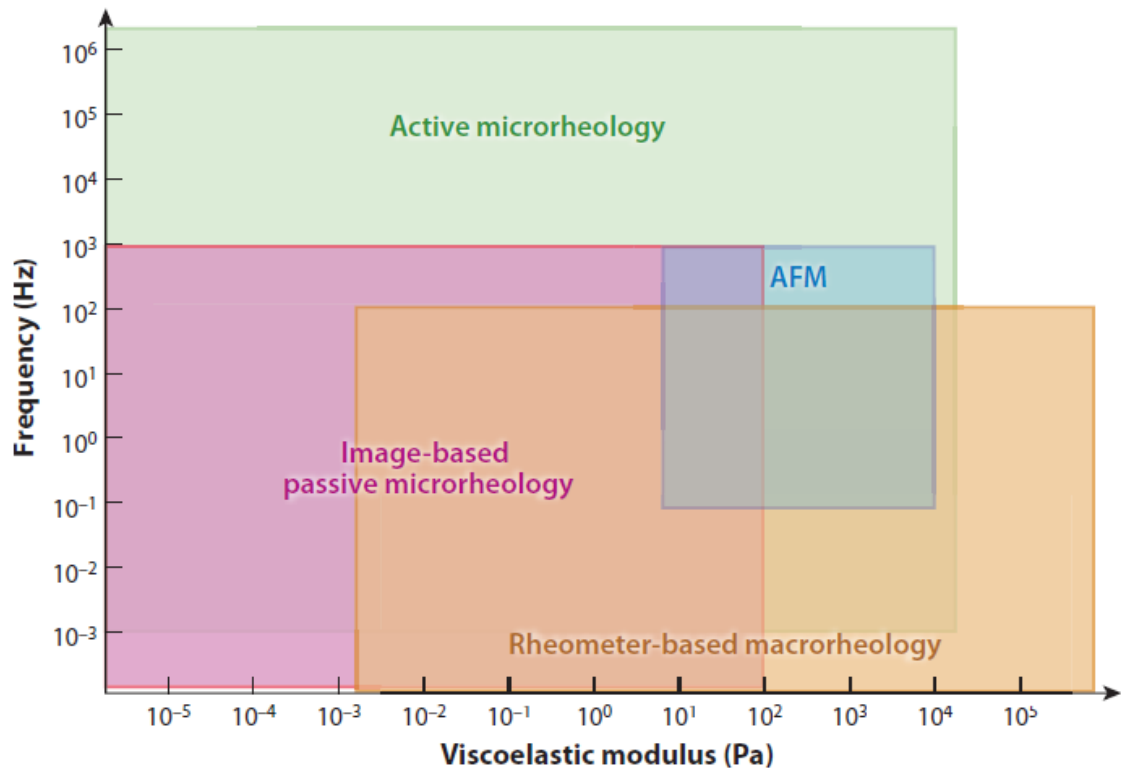


Figure 2.2 Methods to determine the viscoelastic modulus of soft materials. Modified from (Chen, Wen et al. 2010)

2.1.1 Oscillating shear rheology

Cone and plate shear rheometers (operated in oscillating mode) are often used to measure the elastic modulus of macroscopic volumes of soft materials, figure 2.3. Here, the material is placed between two plates and the lower plate is sinusoidally oscillated about its axis at a fixed frequency and strain rate and the top plate is attached to a torsional strain measuring device which measures the strain and the phase difference between the upper and lower plates. For a Hookean elastic solid, the force (F) is proportional to the displacement (γ);

$$F = K\gamma \quad (\text{Equation 2.2})$$

where K is the Hookean constant. For sinusoidal displacement;

$$\gamma = \gamma_0 \sin \omega t \quad (\text{Equation 2.3})$$

$$F = F_0 \sin \omega t \quad (\text{Equation 2.4})$$

where ω is the frequency and t is the time. For a perfect fluid the force exerted by the fluid is proportional to the rate of deformation (dy/dt);

$$F = \eta \frac{dy}{dt} \quad (\text{Equation 2.5})$$

where η is the Newtonian viscosity. Thus, for sinusoidal displacement;

$$F = F_0 \cos \omega t \quad (\text{Equation 2.6})$$

$$\frac{dy}{dt} = \gamma_0 \cos \omega t \quad (\text{Equation 2.7})$$

Hence, in a perfect fluid, the deformation oscillations proceed the displacement by 90 degrees. For viscoelastic materials the phase difference is in the range 0 to 90 degrees and the force is given by;

$$F = F_0 \sin \omega t + \delta \quad (\text{Equation 2.8})$$

where δ is the phase difference. By manipulation and expansion;

$$F = F_0 \cos \delta \sin \omega t + F_0 \sin \delta \cos \omega t \quad (\text{Equation 2.9})$$

Since the phase difference is a constant, the first term is in phase with the deformation and is related to the solid behaviour of the material while the second term is out of phase by 90 degrees and is related to the liquid behaviour of the material. The complex modulus G^* of a viscoelastic material is determined by dividing the force by the strain, yielding

$$G' = G' \sin \omega t + G'' \cos \omega t \quad (\text{Equation 2.10})$$

where G' is the elastic or storage modulus and G'' is the viscous or loss modulus. Where $G' > G''$ the material is said to be more solid than liquid and vice-versa. (Menard 2008).

In a typical experiment, an amplitude sweep is performed to ensure that subsequent experiments are performed in the linear viscoelastic region, then a frequency sweep is performed. For isotropic, incompressible, elastic materials the shear modulus can be transformed into the Young's modulus. The limitation of cone and plate rheology is that a sample size in excess of 0.5 ml, is required e.g. Wells-Brookfield Cone and Plate Rheometer, Brookfield Engineering Laboratories, MA, USA.

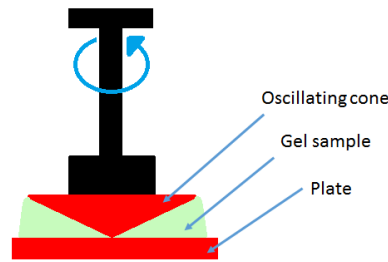


Figure 2.3 Schematic of a cone and plate rheometer

2.1.2 Microrheology

Over the past two decades, microrheology has emerged as the leading technique to probe the local elasticity and viscosity in biomaterials (Zhao et al. 2015; Baker et al. 2010; Daniels et al. 2010; Robert et al. 2012; Cicuta & Donald 2007; Ziemann et al. 1994; Hoffman & Crocker 2009; Menard 2008). Microrheology is an umbrella term used to cover a variety of techniques (video-particle tracking, laser tweezers and magnetic tweezers) which measurement of the mean square displacement (MSD) of a probe embedded within a sample (Mansel et al. 2013). Microrheology may either be passive or active. In passive microrheology the embedded tracker particles move due to the thermal energy (kT) whereas an external force such as a magnetic field gradient is used to actively manipulate the probes in active microrheology (Cicuta & Donald 2007). In a purely viscous material, the MSD of the embedded particles increases linearly with time (a logarithmic plot with a slope of one), whereas in a purely elastic material the MSD of the embedded particle will not increase over time (a logarithmic plot with a slope of zero), the particle's position merely fluctuating about an equilibrium position. Viscoelastic materials yield a logarithmic plot of MSD versus time with a slope somewhere between 0 and 1. Furthermore, since viscoelastic materials may behave as elastic solids or viscous fluids on different time-scales, the slope of such a plot can change during the experimentally observed time range and measuring the MSD over a range of time

intervals is equivalent to probing the viscoelastic properties as a function of frequency. (Mansel et al. 2013) Microrheology is a particularly useful technique since the frequency range can be extended to higher values than traditional rheology and the microscopic scale samples volumes required for analysis are much smaller. Furthermore, the properties can be determined at micrometre length-scales (Cicuta & Donald 2007). The recent development of x-ray photon correlation spectroscopy (XPCS) removes a previous limitation that the sample must be somewhat transparent to light (Leheny 2012). Recently, it has been suggested that the use of passive microrheology may be limited by the active interaction of certain nanoparticle tracers with proteins in biomaterials, resulting in a nonequilibrium state whereby the fluctuation-dissipation theorem, upon which passive microrheology is based, is no longer valid (Lesniak et al. 2012).

2.1.3 Atomic force microscopy (AFM)

Atomic force microscopy (AFM) has been used to measure the elastic modulus of cells and tissues (see table 5.1). The technique detects the forces acting between a probe and the surface of a sample, figure 2.4. A cantilever, with a known spring constant, is lowered to the surface of the sample. At the start height, the cantilever is straight, as the cantilever is merely in resting on the sample surface. As the cantilever is lowered, the tip of the cantilever bends in response to the mechanical properties of the sample. Bending is greater for stiff samples than for soft samples. The degree of bending is converted to a force value and the elasticity of the material is calculated.

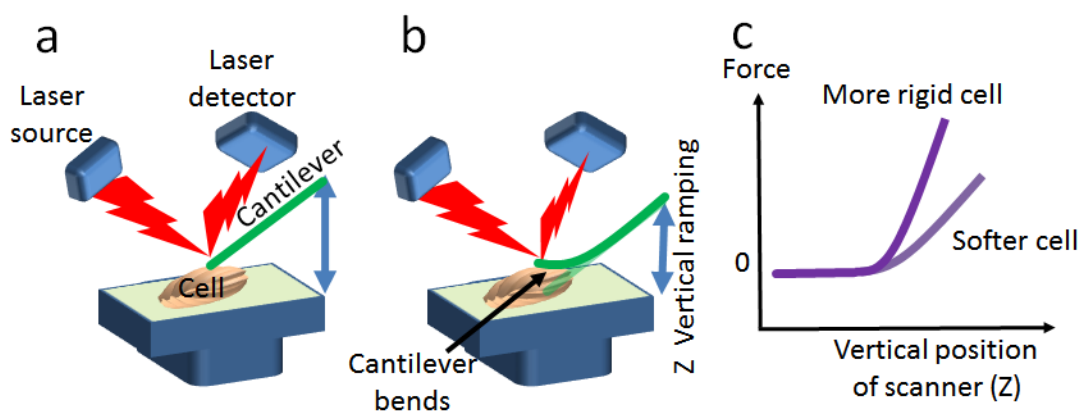


Figure 2.4 Atomic Force Microscopy. (a) A cantilever (with known spring constant) is brought in contact with a cell for which the position is detected by a laser (b) The cantilever is lowered and the degree to which the cantilever bends is measured (c) The degree of bending is converted to force.

As the cantilever is lowered more force (bending) is measured for rigid cells than soft cells.

2.1.4 Cavitation Rheology

Cavitation rheology (CR) has been shown to measure the Young's modulus of biological and non-biological soft materials, including polyacrylamide gels, the eye lens and vitreous (Kundu & Crosby 2009; Zimmerlin et al. 2010; Cui et al. 2011; Zimmerlin et al. 2007; Chin et al. 2013). During cavitation rheology, a cavity is induced within a soft material and the critical pressure at the onset of this mechanical instability is measured. This critical pressure is related to the elastic modulus of the material.

A typical cavitation rheology apparatus is shown in figure 2.5. The equipment consists of a personal computer, needle, syringe, syringe pump, pressure transducer and tubing to connect the needle, syringe and pressure transducer. The system is closed, thus, at constant temperature, a change in the volume of system results in a change in the pressure of the system as per Charles Law;

$$P \propto \frac{1}{V} \quad \text{(Equation 2.11)}$$

where pressure, P is indirectly proportional to volume, V . A typical cavitation rheology experiment begins with the insertion of a blunt ended needle into the sample. The plunger is depressed, at a constant rate, using a syringe pump. The pressure in the system is monitored using a pressure sensor from which data is sent to a personal computer for collection, analysis and viewing. Since the system is closed, the depression of the plunger decreases the system volume with a concomitant increase of the pressure in the system. At a critical pressure cavitation occurs. Due to the geometry of the blunt needle tip a spherical cap develops, the formation of which was previously resisted by two forces, the elastic restoring force of the sample and the surface tension between the cavitating medium and the sample.

The pressure required to grow a cavity in a viscoelastic network is the sum of both the surface energy and the elastic restoring energy of the network. The pressure required to form a bubble (P) into a Newtonian liquid follows the relationship of;

$$P = \frac{2\gamma}{r} \quad \text{(Equation 2.12)}$$

where γ is the surface tension and r is the radius of the bubble.

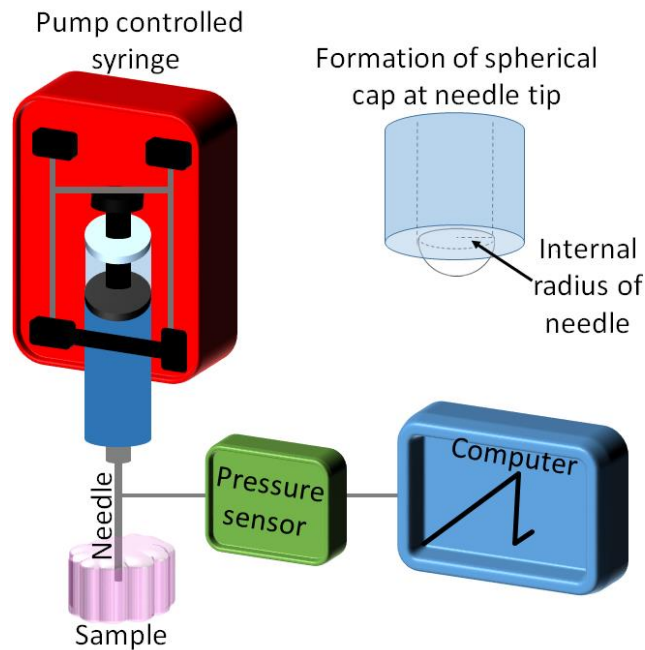


Figure 2.5 Cavitation rheology. A needle is placed in the sample and the plunger is depressed. The pressure in the system is measured using a pressure sensor. The formation of a cavity at the tip of the needle results in a rapid decrease in pressure. The critical pressure is the maximum pressure before cavitation.

The elastic component is described using the neo-Hookean strain energy function to relate the inflation pressure, P to the elastic modulus, E ;

$$P = \frac{5E - 4\lambda^{-1} + \lambda^{-4}}{6} \quad (\text{Equation 2.13})$$

where λ is the cavity expansion ratio, the ratio of the radius of the bubble (R_c) to the inner radius of the needle, R_i . Gent and co-workers have shown that the pressure in natural rubber elastomers has an asymptote at a value of $5/6E$, consistent with (Equation 2.13, (Gent & Lindley 1959). **Thus, the first approximation of the pressure-growth relationship for a spherical void in a viscoelastic material then becomes;**

$$P_c = \frac{5E}{6} + \frac{2\gamma}{r} \quad (\text{Equation 2.14})$$

where P_c is the critical pressure, the maximum inflation pressure, figure 2.6.

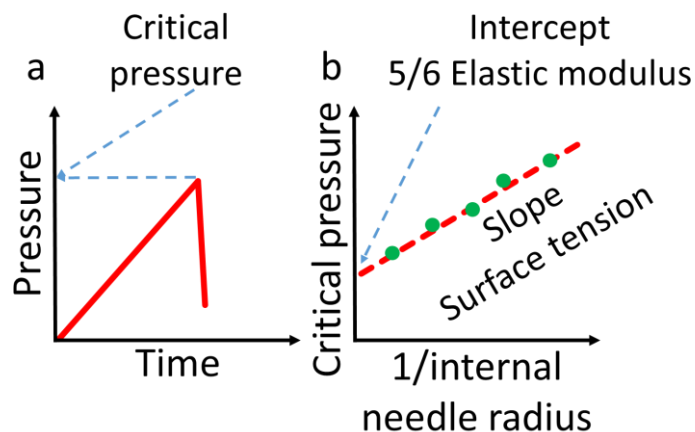


Figure 2.6 (a) A typical pressure plot during a cavitation rheology experiment. (b) Elastic modulus and surface tension is determined from a plot of $1/\text{radius}$ versus critical pressure.

Cavitation rheology has several advantages over other forms of rheology. CR does not require that the material be transparent. The formation of the cavity does not need to be visualised since a rapid decrease in pressure within the closed system (due to the increase in the system volume upon the expansion of the cavity) signals that cavitation has occurred (Zimmerlin et al. 2007). Furthermore, since the local elastic modulus is measured, CR is capable of detecting heterogeneities within the probed material which is not possible using macroscopic shear rheology (Zimmerlin et al. 2007). In addition, the elastic modulus of specimens as small as $1\mu\text{l}$ have been determined for semi-dilute polymer solutions (Pavlovsky et al. 2014).

2.2 Methods of assessing protein unfolding

In addition to differential scanning calorimetry (see below), protein folding can be assessed by a variety of spectroscopic methods including Fourier transform infrared spectroscopy (FTIR), circular dichroism spectroscopy (CD), fluorescence spectroscopy and nuclear magnetic resonance spectroscopy (NMR).

2.2.1 Fourier transform infrared spectroscopy

FTIR provides information on the degree to which the alpha helical and beta sheet secondary structure of a protein molecule is modified during the unfolding process. The absorbance of Amide I (1700cm^{-1} - 1600cm^{-1}) associated with the stretching vibrations of the C=O bond of the protein peptide back-bone is measured. Intensity and frequency are

determined by the character of the hydrogen bonding along the backbone which reflects the secondary structure of the protein (Jackson and Mantsch 1995).

2.2.2 Circular dichroism spectroscopy

CD is a spectroscopic technique which measures the difference in absorption of left or right hand circularly polarised light as it passes chiral (optically active) molecules over a range of wavelengths and is widely used to protein folding/unfolding. Proteins, are optically active due to the asymmetric environment of the three dimensional secondary structure and CD is widely used to evaluate the presence of alpha-helix and beta-sheet structures present in a sample, i.e. it may be used to monitor the decrease in signals associated with specific secondary structure components with a change in environmental conditions, e.g. during unfolding (Kelly et al. 2005).

2.2.3 Fluorescence spectroscopy

Fluorescence occurs when molecules absorb light of a particular wavelength and emit light at a higher wavelength; the difference between the two wavelengths being known as the Stokes shift, figure 2.7. Upon the absorption of a high energy photon, electrons are promoted from the ground state to the excited state. Relaxation to the ground state may occur via either radiative or non-radiative decay. The maximum excitation wavelength ($\lambda_{\text{max ex}}$) is the wavelength at which the molecule absorbs the most light and the maximum emission wavelength ($\lambda_{\text{max em}}$) is the wavelength where the maximum light emitted.

Fluorescence spectroscopy takes advantage of the intrinsic fluorescence of proteins due to the presence of the aromatic amino acid residues, phenylalanine, tyrosine and tryptophan. The emission spectra are dominated by tryptophan and tyrosine since their quantum yield is considerably greater than that of phenylalanine. Both tryptophan and tyrosine are excited at 280 nm whereas excitation at 295 nm excites only tryptophan. The emission spectra is sensitive to the solvent/environment of the aromatic residues, and thus changes to the proteins three dimensional organization due to unfolding are manifested in the data (Lakowicz 2006). Other fluoresce techniques including fluorescence recovery after photobleaching (FRAP) and fluorescence resonance energy transfer (FRET) have also been used to investigate protein unfolding (Costantini & Snapp 2013; Schuler & Eaton 2008).

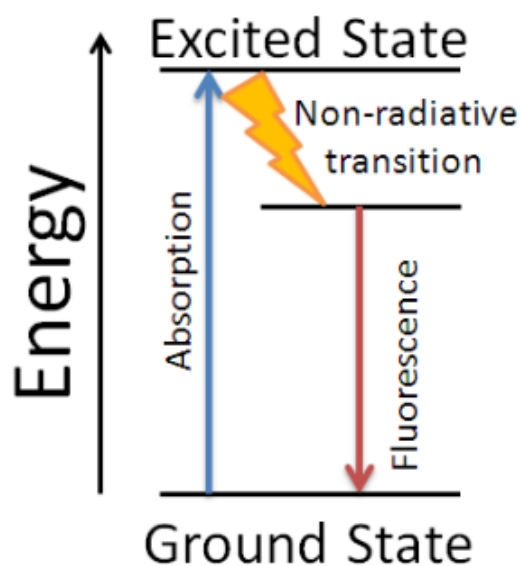


Figure 2.7 Jablonski diagram. An electron absorbs a high energy photon, the system relaxes and fluoresces at a longer wavelength

2.2.4 Nuclear magnetic resonance spectroscopy

During an NMR experiment the protein is subjected to a magnetic field causing the nuclei absorb and re-emit electromagnetic radiation. The frequency of absorbed electromagnetic radiation for a particular nucleus (such as ^1H or ^{13}C) depends on the molecular environment of the nucleus. NMR can therefore be used to determine how atoms are linked chemically, how close atoms are in space and how rapidly they move with respect to one another (Atkins 2014). Due to the abundance of hydrogen atoms in a protein, it is difficult to assign the individual nuclei from a ^1H NMR spectrum of a protein, however, secondary and tertiary structural elements can be identified (Kumari & Dorai 2013). Protein unfolding is fast compared to the time-scale of an NMR experiment, however, multidimensional analysis and advanced techniques such as the temperature-jump and stopped-flow methods, have increased NMR's usefulness as a tool to monitor protein unfolding (Waudby et al. 2013).

2.2.5 Differential Scanning Calorimetry (DSC)

Differential scanning calorimetry is a powerful technique used to determine the melt transition temperature (T_m) and thermodynamic parameters associated with protein denaturation. A schematic of a DSC instrument is shown in figure 2.8. A sample is

heated or cooled at a constant rate and the differences in heat energy uptake required to maintain an equal temperature between the sample and reference cells is measured. Where the sample has a known mass, the excess heat flow (usually in milliwatt (mW)), can be converted to a molar heat capacity, C_p , ($\text{kcal mol}^{-1} \text{K}^{-1}$).

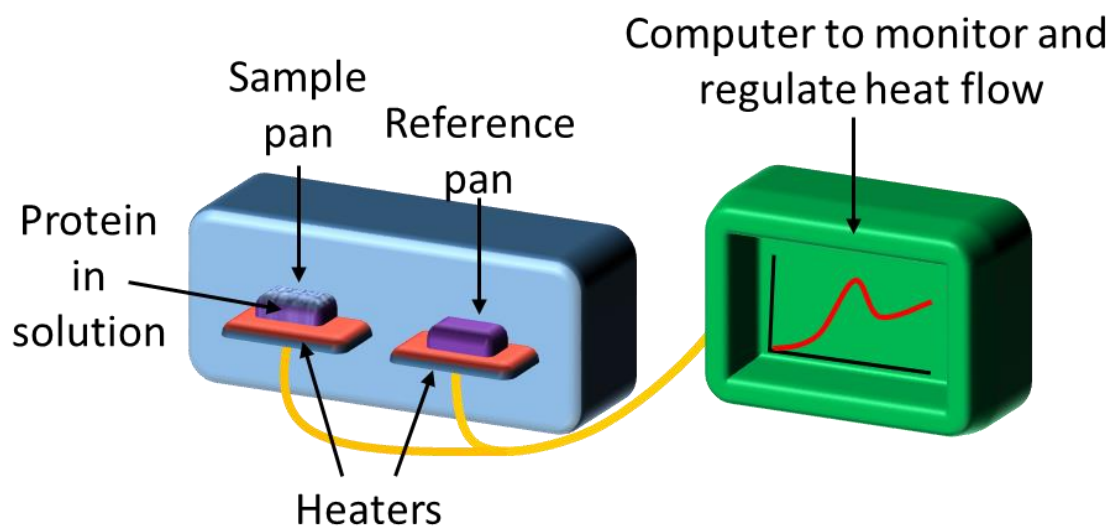


Figure 2.8 Schematic of Differential Scanning Calorimetry instrument

A typical DSC thermogram of a protein solution during a heating cycle is composed of three regions: the pre-transition baseline, the endothermic unfolding transition, and the post-transition baseline a schematic of which is shown in figure 2.9. The pre-transition baseline indicates the difference in heat capacity between the natively folded protein and the solvent. For aqueous protein solutions the protein has a lower heat capacity than water and thus the excess heat flow will have a negative value. Furthermore, the slope of this baseline will be lightly positive, indicative of a gradual increase in heat capacity with increasing temperature, typical of organic molecules (Cooper et al. 2000). When the protein begins to unfold an increase in excess heat capacity (C_p) is registered which reaches a maximum at approximately the mid-point for an ideal two-state, reversible, first-order endothermic processes. The post-transition baseline indicates the difference in heat capacity between the unfolded protein and the solvent.

Unfolding is a thermodynamic process with both enthalpic, S and entropic, H components contributing to free energy, G minimisation (Equation 2.15);

$$\Delta G = \Delta H - T\Delta S \quad (\text{Equation 2.15})$$

where T is temperature in Kelvin. Unfolding is an endothermic process, $\Delta H > 0$. The enthalpic contribution is due to the absorption of the energy required to break the bonds that maintain the native structure (Baldwin 2007). Whereas, the entropic contribution is due to the interaction of the protein with the solvent. In aqueous systems the strength of hydrogen bonds decreases with increased temperature, therefore the entropic gain from burying the non-polar amino-acid side-chains is no longer present, instead, at elevated temperatures entropy is gained by allowing conformational freedom of the primary amino-acid sequence. After baseline subtraction, the calorimetric enthalpy (ΔH_{cal}) is the integrated area under the thermogram;

$$\Delta H_{cal} = \int_{T_1}^{T_2} \Delta C_p dt \quad (\text{Equation 2.16})$$

and calorimetric entropy (ΔS_{cal}) is given by;

$$\Delta S_{cal} = \int_{T_1}^{T_2} \frac{(\Delta C_p)}{T} dt \quad (\text{Equation 2.17})$$

During thermal denaturation many of the complex enthalpic and entropic events cancel each other out energetically and the free energy change associated with thermal denaturation is relatively small, on the order of 100 kJ mol^{-1} (Baldwin 2007).

The van't Hoff enthalpy (ΔH_{VH}) is an alternative measure of the enthalpy of the denaturation process. Here the area underneath the C_p peak at a given temperature is divided by the total area to measure the fraction of unfolding that has occurred at that temperature. Comparing the two enthalpy values yields information about the denaturation process. Where $\Delta H_{cal} = \Delta H_{VH}$ the unfolding process is a first order, two-state, reversible transition (Cooper 1999).

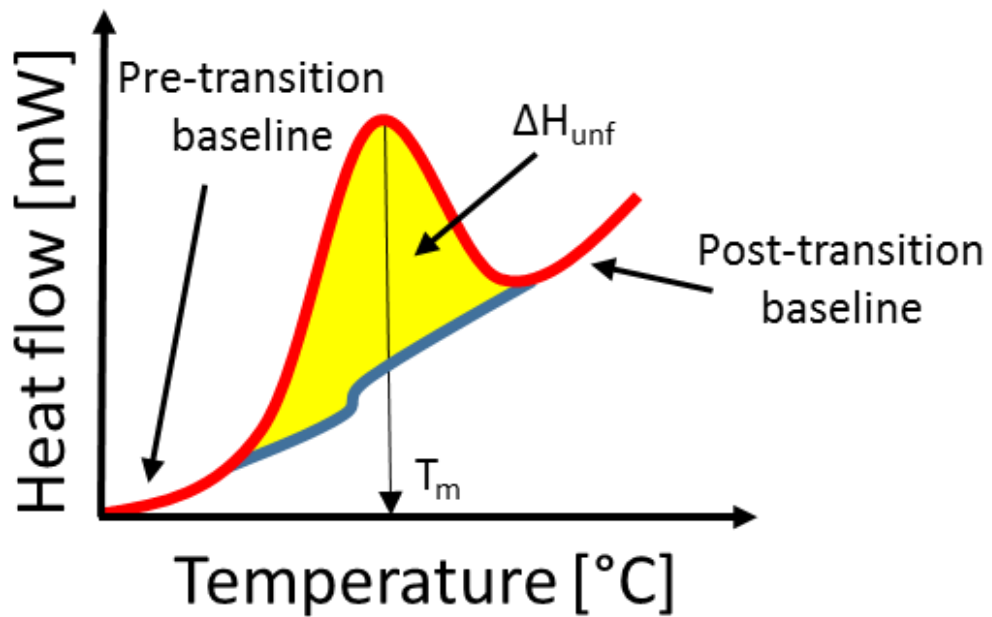


Figure 2.9 Idealised plot from DSC

2.3 Model proteins

Because of their relative abundance, ease of purification and early established structures and sequences, hen egg white lysozyme (HEWL), bovine serum albumin (BSA) and gelatin have been used in many studies to investigate the biophysical behaviour of proteins (Steiner 1964; Blake et al. 1965; Ogashara & Hamaguchi 1967; Sun et al. 1989; Velev et al. 1998; Liu et al. 2011; R. Swaminathan et al. 2011; Vasita & Katti 2012).

2.3.1 Lysozyme

The lysozyme family of enzymes (muramidases) catalyse the hydrolysis of polysaccharides found in bacterial cell walls. These bactericidal proteins are found in many body secretions including, tears, saliva and milk. Hen egg white lysozyme (HEWL) is a small (14.3 kilodaltons) monomeric protein comprised of 129 amino acids that acts as anti-bacterial agent in chicken eggs. The crystal structure and amino acid sequence of HEWL were among the first to be determined (Canfield 1963; Blake et al. 1965). HEWL is comprised of two domains, alpha (residues 1-35 and 85-129) and beta (residues 36-84), containing five alpha helical and five beta sheet regions in total. These secondary structures are joined together by random coils that make up the remainder of the polypeptide backbone which is covalently linked with four disulphide bridges, figure

2.10. The isoelectric point of lysozyme is 11, which makes the protein charged at physiological pH (Alderton and Fevold 1946).

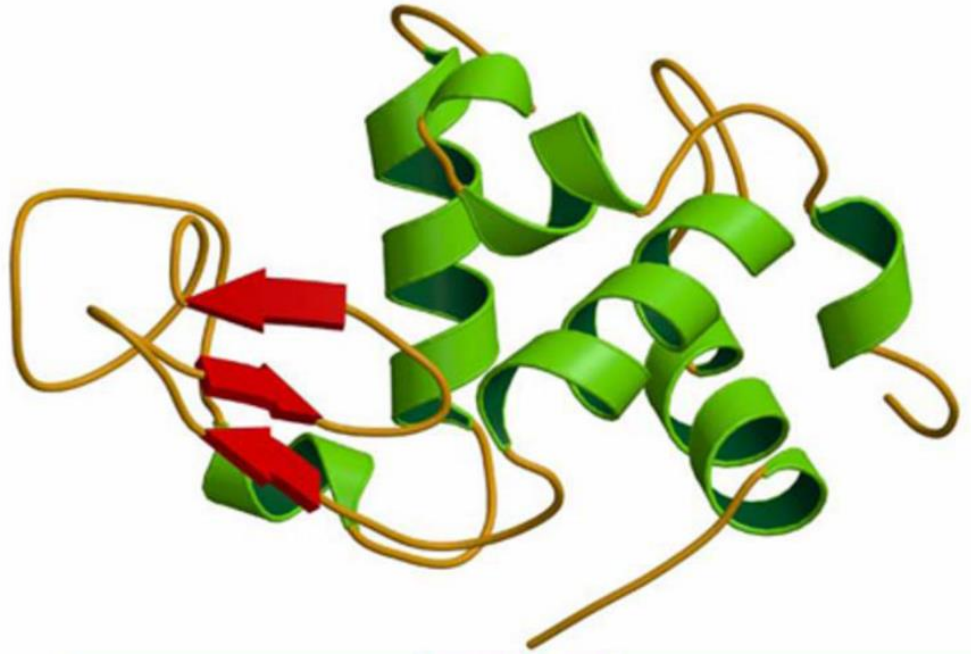


Figure 2.10 Ribbon representation of the crystal structure of lysozyme (PDB code: 3LZT) reproduced from Protein Data Bank

2.3.2 Bovine serum albumin (BSA)

BSA, otherwise known fraction V, belongs to the albumin family of globular proteins found in abundance in mammalian blood. BSA is produced in the liver and plays an important role in maintaining osmotic pressure and the transportation of metabolites (Cohn 1941). The mature protein contains 583 amino acids, has a molecular weight of 66.5 kilodaltons (Cohn 1941), and an isoelectric point of 4.7. (Ge, Kojio et al. 1998) BSA is a heart shaped monomeric protein consisting of three homologous domains (I, II & III). Each domain is made up of two subdomains (A and B) and these share common structural motifs. (Huang, Kim et al. 2004) The protein is stabilised by 35 cysteine residues that form 17 disulphide bridges, leaving one free cysteine at position 34. The secondary structure is composed mainly of alpha helices with some beta sheet and disordered regions (figure 2.11)(Murayama and Tomida 2004).

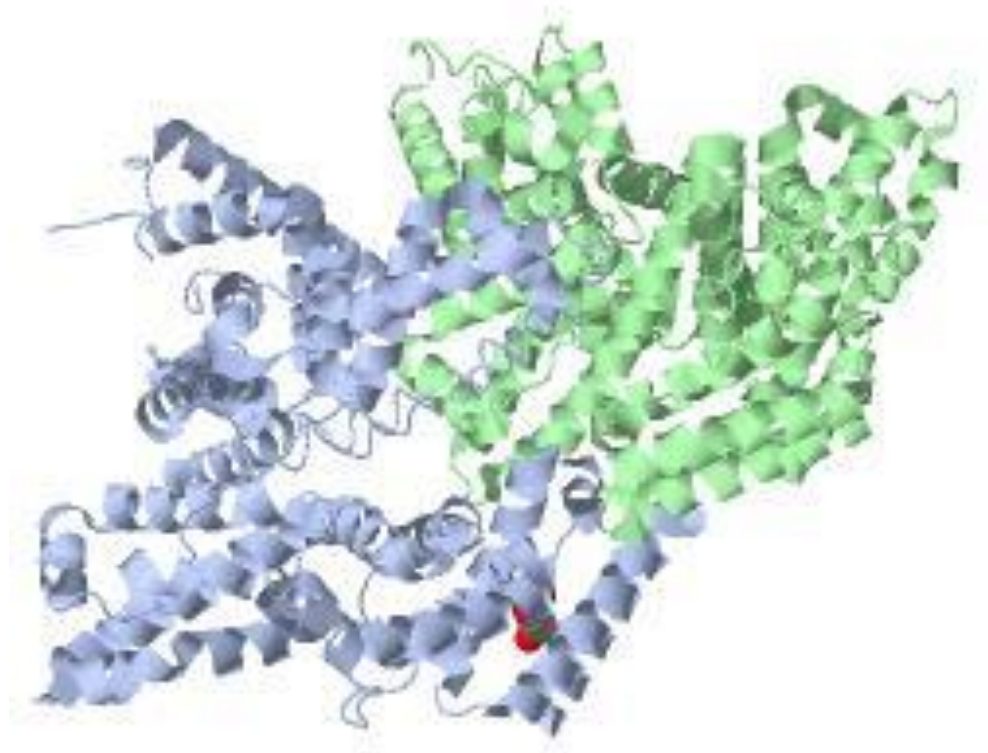


Figure 2.11 Cartoon representation of the crystal structure of BSA rendered using Jmol (PDB ID: 4f5s).

2.3.3 Gelatin

The hydrolysis of collagen results in the formation of gelatin, a mixture of peptides and protein fragments. Gelatin type A is formed by acidic hydrolysis whereas gelatin type B is formed under basic conditions. The isoelectric point of (IEP) Type A is 7.0 – 9.0 while the IEP of type B is lower, 4.7 -5.2. Above gelatin's melt transition temperature, T_m , the peptides adopt a random coil secondary structure, whereas below T_m the secondary structure is helical. Thermoreversible gels are formed by the physical entanglement of strands upon cooling (figure 2.12)(Bhattacharjee and Bansal 2005). Commercially, the strength of a gelatin gel is referred to by the Bloom number. This is measured (for a stipulated concentration) by an industry specific penetrometer and measure of the force required to displace an area of gel by a distance of 4 mm (Gelatin Manufacturers Institute of America 2013). The higher the bloom number, the stronger the gel with the bloom number being proportional to the average molecular mass of the component strands (Lai 2009).

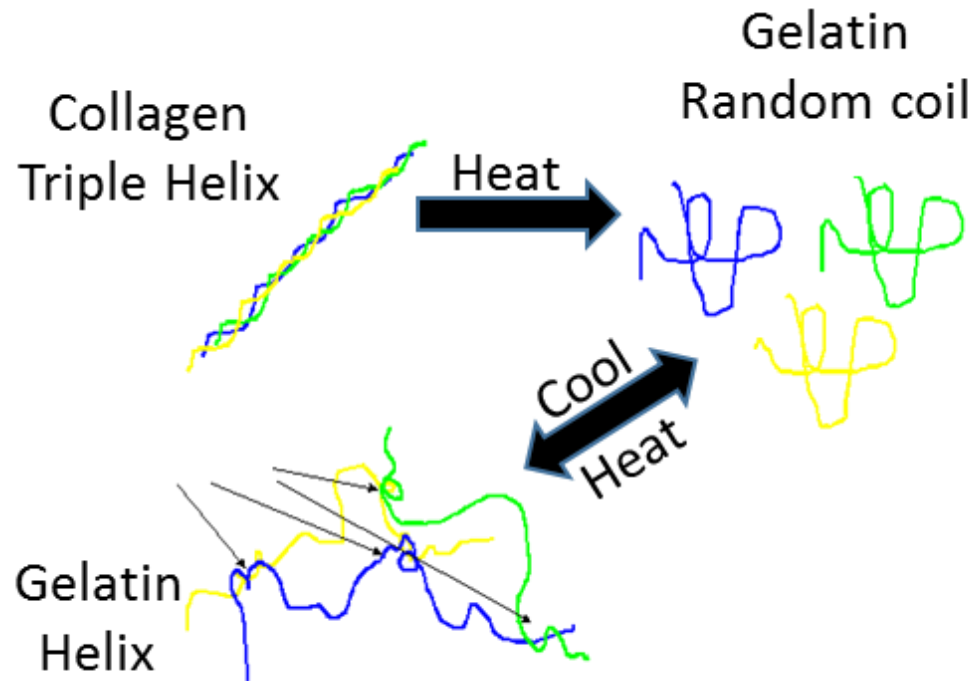


Figure 2.12 The formation of gelatin by hydrolysis and the reversible coil to helix transformation upon cooling.

2.4 Spheroids as model systems

Spheroids are microscale, spherical cell clusters which grow free of foreign material (Fennema et al. 2013). Spheroid cell cultures are three dimensional (3D) and the cells secrete an extracellular matrix, thus they mimic the physiological environment of cells in organisms more accurately than monolayer cultures (Fennema et al. 2013). The behaviour of cells in a 3D environment is materially different from cells grown as a monolayer in a two dimensional monolayer. Both phenotypic (Von Der Mark et al. 1977) and metabolic (Li et al. 2010) differences have been observed and these alterations have been linked to changes in cell-cell and cell-matrix interactions (Mahmood et al. 2004; Schooley et al. 2012). Spheroids have become a classic model for tumours as the avascular cellular bundle simulates the gradient of nutrients, waste and oxygen concentrations found in the physiological environment of human tumour tissue (Weiswald et al. 2015; Chandrasekaran 2012), figure 2.13. By simulating the cell-cell interactions and the interactions between the cell and the extracellular matrix, the morphology and biochemistry of the cells within the spheroid more closely resemble

those of a tumour and are therefore used as models to develop and evaluate the efficacy of anti-cancer drugs and treatments (Weiswald et al. 2015).

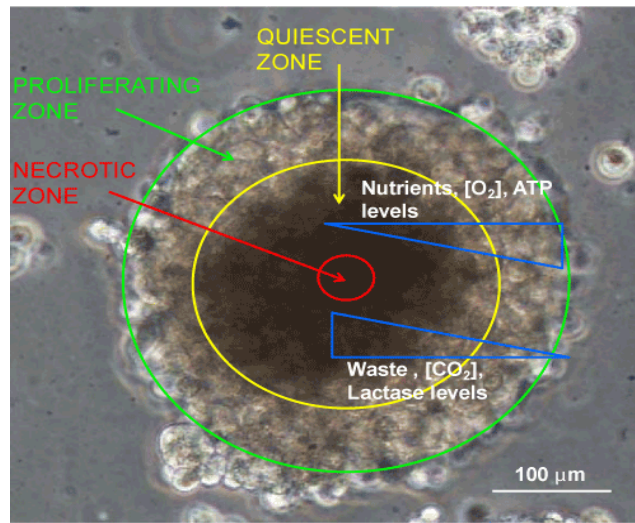


Figure 2.13 Gradient of gases, nutrients and waste in spheroids from (Chandrasekaran 2012).

Spheroids are an ideal model system to study the biophysical phenomena associated with the self-organisation of cells. Pathological changes in tissues are often associated with an increase in stiffness of the tissue affected (Cross et al. 2007; V. Swaminathan et al. 2011; Xu et al. 2012). An increased understanding of these biomechanics will aid in the early detection of cancer (i.e. prior to metastasis) and improves patient outcome, decreases mortality and reduces morbidity and economic costs of treatment (Fan et al. 2014; Zhang et al. 2015). Furthermore, increasing our understanding of the biophysical principles underpinning cell self-organisation will aid in the development of successful strategies to replace or regenerate injured tissue. Spheroids may be grown from human cells using a variety of culture methods including the hanging drop method liquid-overlay culture, spinning flasks and microfluidic devices (Yamada & Cukierman 2007; Abbott 2003; Ungrin et al. 2008; Kim et al. 2013; Tekin et al. 2010; Hsiao et al. 2009).

2.4.1 Hanging drop method of spheroid formation

A schematic of specialised 96-well plate (Perfecta3D®, 3D Biomatrix, MI, USA) that is often used for the hanging drop method to produce spheroids, is shown in figure 2.14. The cell suspension is dispensed into a hole to create the hanging drop. Gravity causes

the cells to accumulate at the bottom of the drop and the cells adhere to each other, due to the absence of substrate, to form a spheroid. The dimension of the spheroid is defined by the geometry of the drop.

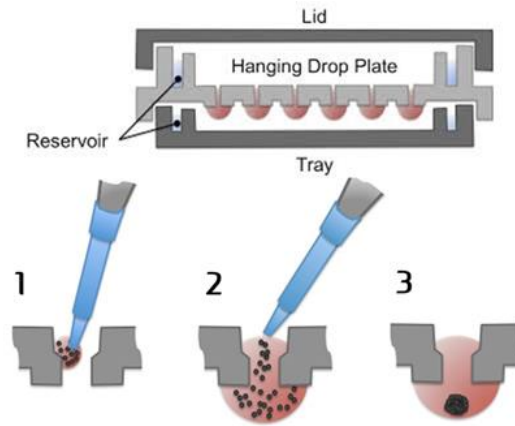


Figure 2.14 Schematic of Perfecta3D® hanging drop plate

2.4.2 Liquid overlay method of spheroid formation

Alternatively, cell substratum adhesion may be eliminated by coating the bottom of a normal culture vessel with a layer of material to which the cell will not form an attachment, such as agarose (Metzger et al. 2011). A thin film of 1 % agarose is commonly used to coat the surface. Agarose is a hydrophobic hydrogel which inhibits the attachment of cells in direct and indirect manner. The attachment of cell to a matrix is modulated by proteins known as integrins. Due to the hydrophobicity of the agarose, these proteins are either prevented from attaching to or denatured by the hydrogel. Thus the signalling cascade required for proliferation is not initiated.

Due to the difference in surface tension between the hydrogel and the polystyrene of the culture vessel, a concave surface develops in the material used to coat the chamber prior to gelation. For a fixed culture vessel type, the geometry of the surface is dependent upon the volume (and concentration) of agarose added. As with the hanging drop method gravity causes the cells to accumulate at the bottom of the concave surface and the cells adhere to each other, due to the absence of substrate and then, to form a spheroid, figure 2.15. The dimension of the spheroid is defined by the geometry of the agarose surface.

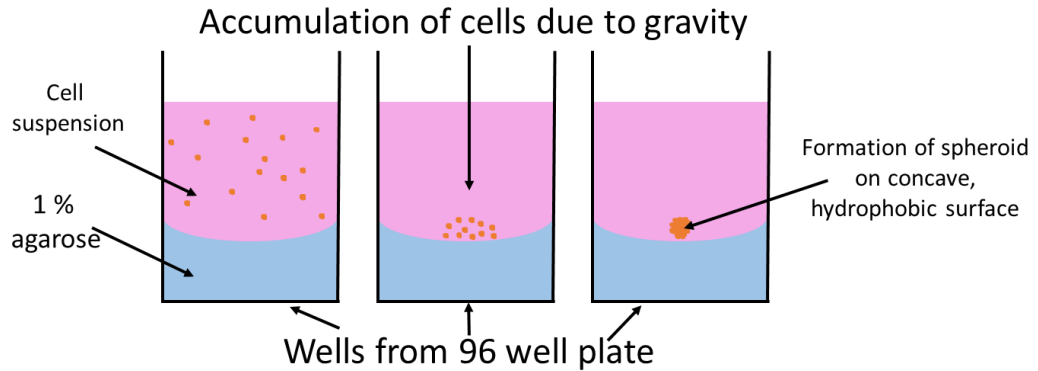


Figure 2.15 Schematic of liquid overlay method of spheroid culture

2.4.3 Cell line HEK 293T/17

Lot #6084069 of a cell line known commercially as ATTC ® CRL-11268™ was purchased from American Type Culture collection, VA, USA and used to form spheroid cultures. These Human Embryonic Kidney (HEK) 293 cells were originally cultured in the van der Eb laboratory by transformation of HEK cell by the introduction of a viral gene (adenovirus, E1 gene) that deregulates the cell cycle, which thereby establishing an immortal cell line HEK 293 (Graham & van der Eb 1973). This cell line was further transformed using the large T antigen of simian virus 40 (HEK 293T) which controls viral genome replication and further dis-regulates the host cell cycle by inactivating the tumour suppressing protein, p53, thus this cell line can be grown for long periods in vitro. Clone 17 was chosen for its high transfectibility (HEK 293T/17). This cell line has an adherent growth habit and is generally grown in tissue-culture treated vessels to allow cell adhesion and spreading.

Chapter 3 Reversible and non-reversible thermal denaturation of lysozyme with varying pH at low ionic strength

3.1 Introduction

Since the launch of recombinant human insulin in the early 1980's, biopharmaceutical production has grown to become a global multi-billion euro industry (Mitragotri et al. 2014). Due to their high specificity and potency, biopharmaceutical drugs are often favoured over small drugs (Morrow & Felcone 2004). However, these proteins-based therapeutics are prone to aggregation and these aggregates are a practical problem for clinicians (Aguzzi & O'Connor 2010) and in the biopharmaceutical industry (E. Chi et al. 2003). It has been shown both in-vitro (Neudecker et al. 2012) and using computation studies (Cellmer et al. 2007) that non-native folding intermediates are a significant source of protein aggregates. Protein folding is under thermodynamic regulation, however the native conformation is only marginally more energetically favourable than the unfolded state, ~ 5 -10 kcal/mol (Xu et al. 2014; Pace 1990). The processes involved in purifying and concentrating proteins require adjustments to pH, ion type, ionic strength and temperature and these physiochemical conditions are often not favourable to maximum protein structural stability (Wang 2005). Aggregation may reduce the shelf life and the therapeutic capacity of the product (Weiss et al. 2009). Furthermore, aggregated proteins may induce an immunogenic response resulting in compromised product safety (De Groot & Scott 2007) or the solution viscosity may increase enough to hinder the parenteral administration of the product (Amin et al. 2014). Thus, it is both a financial and safety imperative to understand and quantify the effect of solution conditions on the structural stability of proteins.

The structural stability of a protein is sometimes assessed by measuring the temperature at which thermal denaturation occurs (Cooper 1999), and is dependent upon solution conditions such as protein concentration, pH, ionic strength, presence of co-solutes and ion type (Chi, Krishnan et al. 2003). Thermal denaturation, which may lead to the formation of aggregates, may be unavoidable, or occur inadvertently, during the processing of proteins (Mulvihill and Donovan 1987, Kamerzell, Esfandiary et al. 2011). On the other hand, thermal denaturation may be the objective of some processes, for example cow milk proteins in their native states are potential allergens for infants with a milk allergy, thus the milk is heat treated to denature whey proteins to produce a formula with low allergenicity (Lee 1992). Therefore, when the temperature returns to below the melt transition temperature, it is important to quantify, for different solution conditions,

the amount of protein that refolds back to the native conformation and the amount of protein that forms aggregates.

An extensive amount of both in-vitro (Arakawa and Timasheff 1985, Fields, Alonso et al. 1992, Finke, Roy et al. 2000) and in-vivo (Gupta, Hall et al. 1998, Cellmer, Bratko et al. 2007) studies have shown that many aggregates are formed from non-native folding intermediates. Where the native monomer does not form aggregates but the non-native monomer does, the non-native form must have a more attractive net interaction potential than the native form, thus indicating that the structural stability of a protein is intimately related to the colloidal stability. Thus, consideration must be given to the mechanisms by which solution conditions affect both intramolecular and intermolecular self-organization.

The denatured monomer has an increased propensity to self-associate compared to the native protein, largely due to the exposure of hydrophobic amino acid residues (Zhang, Lu et al. 2008). Hydrophobic mediated self-association is an entropy driven process which decreases the free energy of a system by reducing the hydrophobic surface area exposed to water and thereby decreasing its restrictive interaction with water. As with the aggregation of native monomers, these initially reversible associations may become irreversible following the formation of covalent bonds. This mechanism appears to be a significant source of aggregate formation during the production and processing of therapeutic proteins (Weiss et al. 2009). Aggregates may form regular structures such as amyloid type fibrils or irregular structures referred to as amorphous aggregates. The physicochemical characteristics of a protein and the solution conditions dictate the type of aggregate formed. Amorphous aggregates tend to form at low net charge, close to the pI of the protein, whereas fibrillar aggregates are observed at high net charge (Krebs, Devlin et al. 2009). Protein aggregates range in size from nanometres to structures visible to the naked eye (> 100 μ M) and range in composition from dimers through to protein complexes consisting of more than a million subunits.

Changes in pH result in switching on and off of charges at particular residues as the pKa of that residue is crossed. Intramolecularly, the native conformation may be perturbed by the disruption of salt bridges, or structures that were stabilized by like charge repulsion may no longer be possible, in addition, hydrogen bond interactions (and their

stabilizing effects) can be perturbed by changes in pH (Talley and Alexov 2010). Intermolecularly, changes to the protein structure, the ionization state and H-bonding ability of residues affect the colloidal stability. Two mechanisms in particular have an effect on colloidal stability. Firstly, if hydrophobic residues become exposed, an increase in the attractive part of the interaction potential will occur. Secondly, as pH deviates from the isoelectric point of a protein, the overall charge on the protein increases. An overall increase in charge results in an increase in colloidal stability due to greater electrostatic repulsion between the molecules.

The processes by which ion type and ionic strength effect protein stability are complex and not fully elucidated. At present specific and non-specific interaction between the ion and the proteins and the ions and water are both thought to contribute to the effect (Zhang and Cremer 2006, Kameoka, Masuzaki et al. 2007) . Classically ions have been ranked in what is known as the Hofmeister series according to how they affect protein solubility (Hofmeister 1888).

Here, the concentration of the lysozyme was fixed at 100 mg/ml. This protein concentration was selected since is typical of the final concentration of many biopharmaceutical formulations (Wang 2005) and is consistent with the total protein level in serum (Putignano, Kaltsas et al. 2000). In an earlier study, the McManus group showed that for lysozyme, T_m is pH dependent (James and McManus 2012), however that study used different buffer salts to obtain the desired pH (i.e. sodium phosphate for pH 7.0 and sodium acetate for pH 4.5). In this study, a single buffer type is conserved over the full pH range (pH 5 to pH 9) to eliminate a buffer-specific effect. Co-solutes, such as sugars, polyols and amino acids are frequently used in biopharmaceutical formulation (Chi, Krishnan et al. 2003) to decrease aggregation by stabilising the native conformation (Ohtake, Kita et al. 2011), a process thought to occur as a consequence of preferential exclusion of disaccharides from the surface of proteins (Sola-Penna and Meyer-Fernandes 1998, Hedoux, Willart et al. 2006). Here, two sugars, trehalose and maltose were used to investigate if an increase in T_m induced by the presence of these disaccharides would have an impact on whether the unfolded protein refolded to the native state or had aggregated when the temperature was returned to below the melt transition temperature. Thus, the solution conditions were chosen with the expectation of systematically modifying the structural and colloidal stability of the protein.

Lysozyme has been used in many studies to investigate the biophysical behaviour of proteins (Blake et al. 1965; Liu et al. 2011; Steiner 1964; Sun et al. 1989), indeed the crystal structure and amino acid sequence of HEWL were among the first to be determined (Canfield 1963, Blake, Koenig et al. 1965). For this reason, this 14.7 kDa globular protein was selected for use in this study. Although, lysozyme is not of commercial interest, it is used here to demonstrate the utility of the approach.

DSC is a classical method used to evaluate protein thermodynamic parameters including the enthalpy of unfolding, ΔH_{unf} and heat capacity, C_p . The temperature at which denaturation occurs, T_m , is widely considered as a measure of protein stability (Cooper 1999, Zhang and Cremer 2009). DSC was selected to quantify the reversibility of thermal unfolding since other methods, such as spectroscopy, are not amenable to the study of the reversibility of thermal unfolding; the formation of aggregates would produce light scattering effects and thereby prevent the determination of the proportion of protein that refolded to the native structure.

While differential scanning calorimetry has previously been used to assess reversibility, however, in a recent perspective, Pethica remarked on lack of data on second (and subsequent) DSC scans in the literature (Pethica 2010). Several recent reviews and papers examine protein stability and aggregate formation using DSC (Johnson 2013; Sasahara & Goto 2012). In DSC experiments where samples were pre-incubated with stirring, a sharp decrease in heat capacity was observed that was assigned to the heat flow associated with the conversion from an ‘aggregation-competent’ lysozyme species to amyloid fibrils (Sasahara et al. 2007). Lou et. al. performed a series of interruption-incubation DSC experiments and established a method to distinguish between two-state and non-two-state thermal denaturation for lysozyme and bovine serum albumin, respectively (Luo et al. 2011). Using temperature-modulated scanning calorimetry in combination with Raman spectroscopy, a two-stage process for the thermal denaturation of lysozyme has been proposed whereby an initial change in the tertiary structure occurs without any change to the secondary structure is followed by an unfolding of the secondary structure (Hedoux, Ionov et al. 2006).

3.1.1 Aim of this study

In this study, the aim is to evaluate whether T_m is related to the degree of aggregation following thermal denaturation. Thermograms from consecutive heating and cooling cycles are compared to determine what proportion of thermally denatured protein refolds to the native state and therefore, indirectly, what proportion forms irreversible aggregates. Thus, the study considers whether T_m , a thermodynamic parameter to express the structural stability of a protein is sufficient to describe the stability of a protein solution or does quantifying the reversibility of that unfolding provide a more useful analysis.

3.2 Materials and methods

3.2.1 Phosphate buffer preparation

Sodium phosphate buffers at concentrations from 5 mM-1 M were prepared using analytical grade monosodium phosphate monohydrate and disodium phosphate heptahydrate. 100 ml of 1M solutions were prepared as shown in table 3.1, which were then diluted as necessary to the required concentration.

Table 3.1 Preparation of 1M phosphate buffers (100 ml)

pH	NaH ₂ PO ₄ ·H ₂ O (137.99 g/mol) g	Na ₂ HPO ₄ ·7H ₂ O (268.07 g/mol) g
5	13.62	0.36
6	12.14	3.22
7	5.84	15.45
8	0.94	24.97
9	0.10	26.61

3.2.2 Lysozyme preparation

Chicken egg white lysozyme was purchased from Calbiochem and used without further purification. The lysozyme was dissolved in buffer at \approx 4 mg/ml. Co-precipitated acetate salts were removed by concentrating the sample washing repeatedly with the desired buffer by ultrafiltration for 5 minutes using Amicon Ultra-4 MWCO 10 kDa (Merck Millipore, Darmstadt, Germany) centrifugal devices at 4,000 x g. When the pH of the lysozyme solution matched the buffer pH a final spin at 7,000 x g for approximately 10 minutes was used to concentrate the sample.

3.2.3 Determination of lysozyme concentration

Protein concentration may be determined by absorption of ultraviolet light at 280 nm. This absorption is primarily due to the presence of amino acid residues; tyrosine, tryptophan and phenylalanine. According to the Beer-Lambert law, the protein concentration, c , is related to the absorption, A , though;

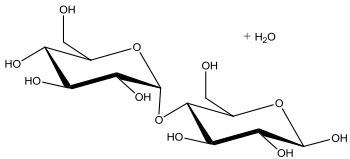
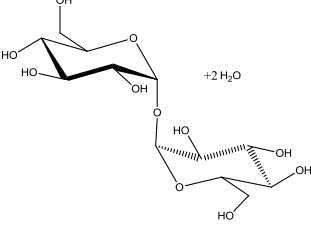
$$A = \varepsilon cl \quad (\text{Equation 3.1})$$

where ε , the extinction coefficient and l , the path length. Lysozyme concentrations were determined by UV absorbance using an extinction coefficient of $2.64 \text{ ml mg}^{-1} \text{ cm}^{-1}$ (Sophianopoulos, Rhodes et al. 1962). The final concentration was adjusted using the appropriate buffer, to 200 mg/ml and fresh solutions were prepared for each DSC experiment directly before use.

3.2.4 Preparation of disaccharide solutions

Maltose monohydrate and trehalose dihydrate were purchased from Calbiochem and used without further purification. 1 mL of each sugar was prepared in the same buffer as the protein solution to a final concentration of 40% (v/v) as shown in table 3.2.

Table 3.2 Preparation of 40 % v/v disaccharide solutions (1mL)

	Maltose monohydrate	Trehalose dihydrate
Empirical formula	$\text{C}_{12}\text{H}_{22}\text{O}_{11} \cdot \text{H}_2\text{O}$	$\text{C}_{12}\text{H}_{22}\text{O}_{11} \cdot 2\text{H}_2\text{O}$
Structure		
Molecular weight (g/mol)	360.31	387.33
Density (g/cm ³)	1.54	1.58
g/ml (40% v/v)	0.616	0.632

3.2.5 Sample preparation

Samples were prepared for DSC by mixing the lysozyme solutions in a 50/50 ratio with either the appropriate buffer or a sugar solution. The final concentration of lysozyme was

therefore 100 mg/ml protein and the final concentration of sugar was 20% (v/v), where present.

3.2.6 Differential Scanning Calorimetry (DSC) measurement

Differential calorimetry was used to determine the enthalpy of unfolding, ΔH_{unf} and the melt transition temperature, T_m , of a protein. DSC determines these thermodynamic parameters by measuring the change in heat flow as the sample is heated at a constant rate. Briefly, the sample is heated or cooled and the heat capacity is monitored as a change in heat flow. The unfolding of a protein is an endothermic process due to the rearrangement of the protein from the native to the unfolded conformation as a consequence of the reassignment of non-covalent bonds. Such an endothermic process is associated with an excess of heat being absorbed by the sample with respect to a reference. Where the sample has a known mass, the heat flow, milliwatt (mW), can be converted to molar heat capacity, C_p , ($\text{kcal mol}^{-1} \text{K}^{-1}$). The conversion from mW to $\text{kcal mol}^{-1} \text{K}^{-1}$ for the samples used herein is presented in table 3.3. When a suitable baseline is subtracted from a plot of C_p versus temperature, the area underneath the curve corresponds to ΔH_{unf} and the mid-point of the transition denotes the melt transition temperature.

Table 3.3 Conversion from heat flow to molar heat capacity

Concentration of lysozyme	100 mg/ml
Volume of sample	55 μl
Mass of lysozyme per sample	55 mg
Moles of lysozyme per sample (M.W. 14.7 kDa)	3.74×10^{-7} moles
mW \Rightarrow joules s^{-1}	/1000
joules $\text{s}^{-1} \Rightarrow$ kcal s^{-1}	* 0.239/1000
Heating rate	$1 \text{ K min}^{-1} = 0.0167 \text{ ks}^{-1}$
kcal $\text{s}^{-1} \Rightarrow$ kcal/K	/0.0167
kcal/K \Rightarrow Kcal $\text{mol}^{-1} \text{K}^{-1}$	/ 3.7×10^{-7}
1 mW \Rightarrow Kcal $\text{mol}^{-1} \text{K}^{-1}$	$1 \Rightarrow 38.33$

A Perkin Elmer Pyris-6 Differential Scanning Calorimeter (Perkin Elmer, Ireland) was used to conduct the DSC measurements (Ju, Hettiarachchy et al. 2001, Roux, Notario et al. 2011). A 55 μl sample was prepared and weighed into a large volume stainless steel capsule (Perkin Elmer, Ireland) which was then sealed and analysed. The sample was equilibrated at 25° C for five minutes before the temperature was increased from 25° C

to 95° C at a scan rate of 1° C/min. The scan rate was maintained throughout subsequent scans and the sample was cooled from 95° C to 40° C whereupon heating to 95° C and cooling to 40° C was repeated twice more. Thus, three heating and cooling cycles were completed. Baseline subtractions and data analysis were executed using OriginPro version 9.0 software (Origin-Lab Corporation, Northampton, MA).

3.2.7 SDS-PAGE (Sodium Dodecyl Sulfate – Poly Acrylamide Gel Electrophoresis)

1 ml samples were prepared in Eppendorf tubes in the same manner as for DSC analysis. Following thermal denaturation, the samples were centrifuged to sediment the aggregates. SDS-PAGE was used to determine if low-molecular weight aggregates, which would not sediment during centrifugation, were present in the supernatant. Since the relative molecular mass of a protein can be determined using SDS-PAGE, the presence and relative abundance of dimers and higher order molecular weight aggregates may also be detected using this technique.

The Laemmli method involves separating the proteins by subjecting them to an electric field (electrophoresis) in a discontinuous polyacrylamide gel in which the proteins are denatured using sodium dodecyl sulfate (SDS) (Laemmli 1970). The difference in pH, ionic strength and acrylamide concentration facilitates the concentration of the protein within the stacking gel while within the resolving gel, the protein migrates towards the anode on the basis of their molecular mass. The negatively charged SDS binds to the polypeptide chain, in proportion to the relative molecular mass, and disrupts the native structure and intrinsic charge of the protein. Thus the protein becomes negatively charged and linear and migrates towards the positively-charged anode, through the polyacrylamide gel. The mesh structure of the polyacrylamide gel retards the migration of larger proteins with respect to smaller proteins and since the SDS-denatured proteins have the same charge-to mass ratio, the outcome is that the proteins separate based on their relative molecular mass. In a reference lane, a mixture of protein standards known as a molecular weight or protein marker, is used to determine the molecular mass of the proteins in the sample. Coomassie Blue is commonly used to visualise the migrated proteins embedded within the gel following SDS-PAGE. A schematic of an SDS-PAGE is shown in figure 3.1.

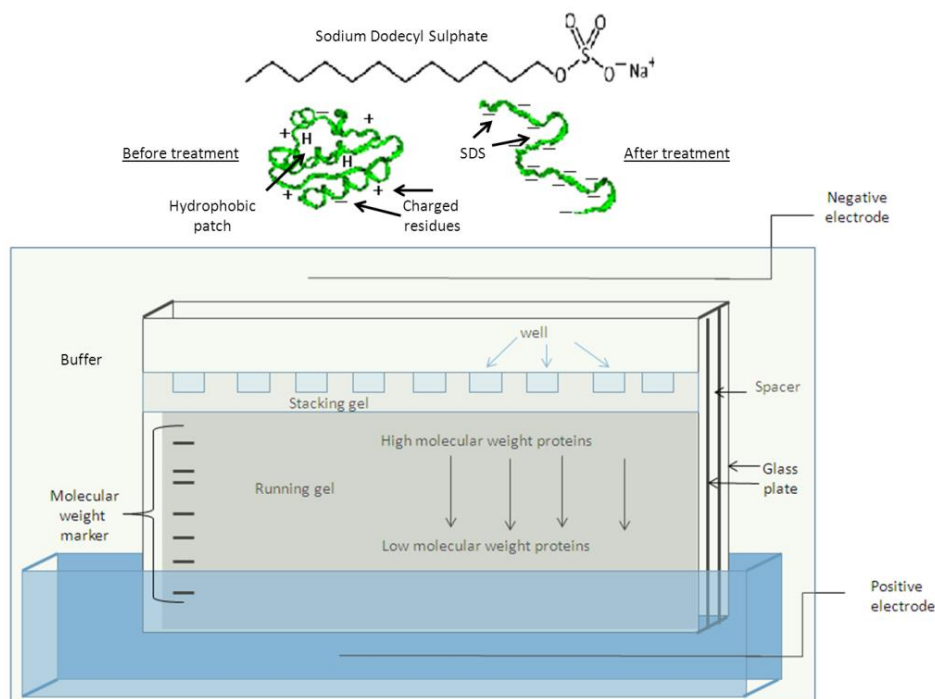


Figure 3.1 Schematic of SDS-PAGE

3.2.7.1 Preparation of resolving gel (12.6 %)

The resolving gel was prepared by the addition of the reagents found in table 3.4. These components were mixed together and degassed for 15 minutes. 50 µl of, freshly prepared, 10% ammonium persulphate (Riedel-de-Haën, Germany) and 5 µl of TEMED (tetramethylethylenediamine) (Thermo Scientific, IL, USA) were then added.

Table 3.4 12.6% SDS-PAGE resolving gel

MilliQ water	3.15 ml
1 M Tris-HCl pH 8.8 (Merck, Germany)	2.5 ml
10 % w/v SDS (Riedel-de-Haën, Germany)	100 µl
Acrylamide/Bis 29:1 (30% stock) Bio-Rad (Hercules, CA, USA)	4.2 ml

3.2.7.2 Preparation of stacking gel (4 %)

The stacking gel was prepared by the mixing the reagents found in table 3.5. These components were mixed together and degassed for 15 minutes. 25 µl of freshly prepared, 10% ammonium persulphate and 5 µl of TEMED were then added.

Table 3.5 4% SDS-PAGE stacking gel

MilliQ water	3.05 ml
0.5M Tris-HCl pH 6.8	1.25 ml
10 % w/v SDS	50 μ l
Acrylamide/Bis 29:1 (30% stock)	0.65 ml

3.2.7.3 Preparation of the gel

The resolving gel mixture was poured into a Bio-Rad (Hercules, CA, USA) mould leaving approximately 1 cm for the addition of the stacking gel. The gel was covered with a little tert-amyl alcohol to exclude oxygen in order to promote the polymerisation of the acrylamide. The gel was allowed to set for 35 minutes. The tert-amyl alcohol was poured off and the top of the gel was rinsed with MilliQ water and blotted dry. The stacking gel mixture was added and the comb, which had been wiped with a little tert-amyl alcohol, was inserted. The gel was allowed to set for 25 minutes.

3.2.7.4 Preparation of SDS samples

Sample buffer was prepared by the addition of the reagents in table 3.6. Lysozyme samples were prepared in Eppendorf tubes in a similar manner as for DSC. Two 1 ml aliquots were pipetted into 1.5 ml Eppendorf tubes which were sealed. The samples were then heated to 95 °C and allowed to cool to 23 °C. One of the samples was heated for a second cycle. Thus, the DSC conditions were simulated. The sample was centrifuged at 13,000 x g using a VWR Galaxy D, microcentrifuge to separate the aggregate from the supernatant. The protein concentration in the supernatant was determined using UV absorbance. The samples were diluted to 1 mg/ml. 30 μ l of protein was added to 30 μ l of sample buffer and both were boiled at 95 °C for 5 minutes. 30 μ l of sample was pipetted into the appropriate well. A Thermo Scientific PageRuler Plus pre-stained protein ladder (Thermo Scientific, IL, USA) was used to determine the molecular weight of the lysozyme band. The gel was run at 200 mV for 50 minutes followed by Coomassie Brilliant Blue (Bio-Rad, Hercules, CA, USA) staining and de-staining solution (30 % methanol, 10 % acetic acid, 60 % MilliQ water).

Table 3.6 SDS-PAGE sample buffer

MilliQ water	4 ml
0.5 M TRIS-HCl pH 6.5	1 ml
Glycerol (Sigma, USA)	0.8 ml
10 % w/v SDS	1.6 ml
Bromophenol blue (Sigma, Germany)	0.5 mg

3.2.8 Intrinsic fluorescence

Intrinsic fluorescence was used to determine whether the protein had refolded to the native conformation upon cooling. The intrinsic fluorescence of a protein is a combination of the fluorescence from the aromatic amino acid residues, tryptophan and tyrosine (and to a lesser extent phenylalanine), found in the polypeptide chain. Both tryptophan and tyrosine absorb maximally ($\lambda_{\max \text{ abs}}$) at 280 nm where the contribution of tryptophan is approximately five times that of tyrosine whereas at 295 nm tryptophan absorption is ~ 30 times absorption of tyrosine, thus absorption at 295 nm is considered effectively to be that of tryptophan only. Due to the difference in molecular symmetry the wavelength of tryptophan fluorescence is more strongly dependent on the solvent type and degree of exposure than tyrosine, shifting to shorter wavelengths and increasing in intensity as the polarity of the solvent increases.

The samples were prepared in the same manner as for SDS page. A Molecular Devices SpectraMax M2^e (Molecular Devices, USA) was used to conduct intrinsic fluorescence measurements. Fluorescence intensity (F. I.) and maximum emission wavelength ($\lambda_{\max \text{ em}}$) were measured following excitation at 280 nm and 295 nm for samples at 1 mg/ml lysozyme concentration.

3.3 Results

3.3.1 Typical thermogram and baseline subtraction

During the DSC experiments, the temperature was increased (or decreased) at 1 °C per minute while the change in heat capacity of the sample was measured. The excess heat flow of the aqueous protein solution was measured to have a negative value, since protein molecules have a lower heat capacity than water. Additionally, the overall slope of the baseline was slightly positive, indicating a gradual increase in heat capacity with

increasing temperature typical of protein and other organic molecules (Cooper et al. 2000).

During the heating cycle a temperature is reached where the protein begins to unfold. Unfolding is an endothermic event and is registered as an increase in excess heat capacity. The maximum excess heat capacity is at approximately the mid-point of this peak, for an ideal two-state, reversible, first-order endothermic processes. During the cooling cycle some of the protein refolded to the native conformation. Folding is an exothermic event and is therefore recorded as a reduction in excess heat capacity. The heat capacity of the sample did not return to the original value due to a difference in heat capacity between the natively folded protein and the aggregated form (Salveti et al. 2002).

Irreversible denaturation and aggregation may sometimes cause the deformation of the DSC transition (Cooper et al. 2001). However, the thermograms recorded here were qualitatively consistent with those of Salveti et al. and did not show any such distortion. Thus, for this protein and for these solution conditions neither irreversible denaturation nor aggregation contributed significantly to the apparent heat capacity measured. A baseline was subtracted and the calorimetric enthalpy (ΔH_{cal}) was determined by integrating the area under the thermogram. The data was fitted using a cubic baseline subtraction, performed in OriginPro 9.0. All baseline corrections inevitably introduces some minor distortion into the DSC analysis (Cooper et al. 2001), however, any bias introduced by baseline subtraction was later eliminated during the calculation of the proportion of refolded lysozyme. A typical DSC trace is shown in figure 3.2 showing the apparent C_p prior to baseline subtraction and baseline determined by cubic interpolation using OriginPro 9.0.

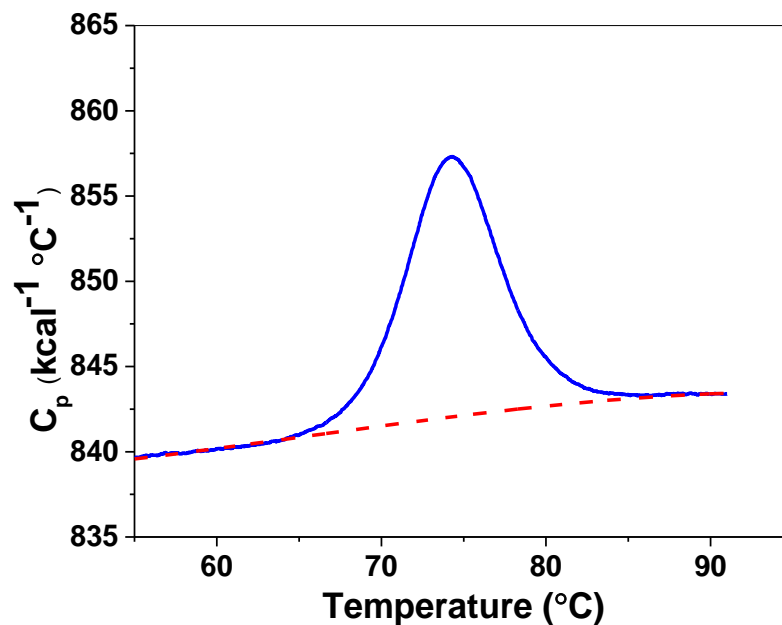


Figure 3.2 DSC trace for 50 mM sodium phosphate, pH 6 showing apparent C_p prior to baseline subtraction (blue) and baseline determined by cubic interpolation using OriginPro 9.0 (red).

Each DSC experiment included three heating and three cooling cycles. Figure 3.3 shows a typical, baseline subtracted DSC thermogram over the course of an experiment. H1-H3 chart the three heating cycles whereas C1-C3 chart the three cooling cycles.

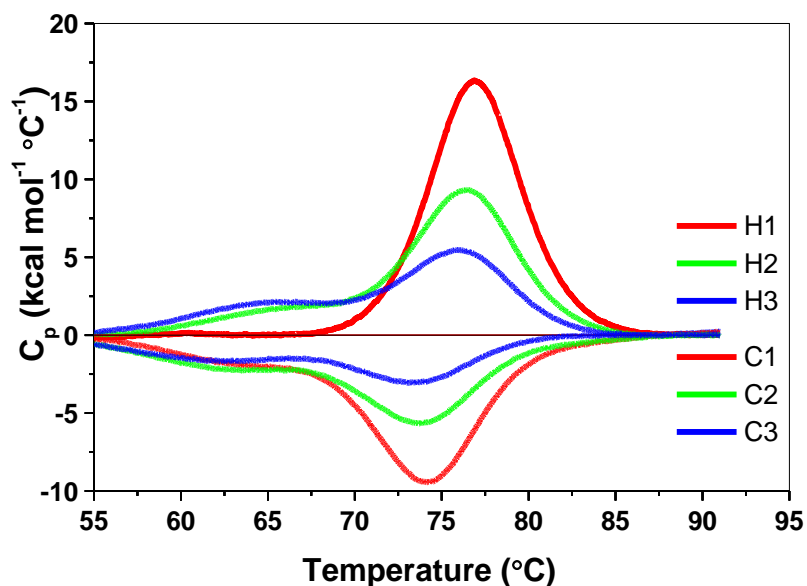


Figure 3.3 The normalised and baseline subtracted DSC thermogram for lysozyme (100 mg/ml) in 0.01 M sodium phosphate buffer, pH 5 in the absence of sugar during three heating (H1-H3) and three cooling cycles (C1-C3)

3.3.2 Van't Hoff enthalpy

The van't Hoff enthalpy (ΔH_{VH}) is an independent measure of the enthalpy of unfolding (Jackson & Brandts 1970; Sturtevant 2003). This analysis depends on the shape of the endotherm and assumes a two-state mode. For van't Hoff analysis the area under the C_p peak at a given temperature is divided by the total area, thus the extent of unfolding that has occurred at that temperature is measured figure 3.4. The equilibrium constant K_{unfold} is defined as;

$$K_{unfold} = \frac{f_{unfolded}}{f_{folded}} \quad (\text{Equation 3.2})$$

where $f_{unfolded}$ is the fraction unfolded and f_{folded} is the fraction folded.

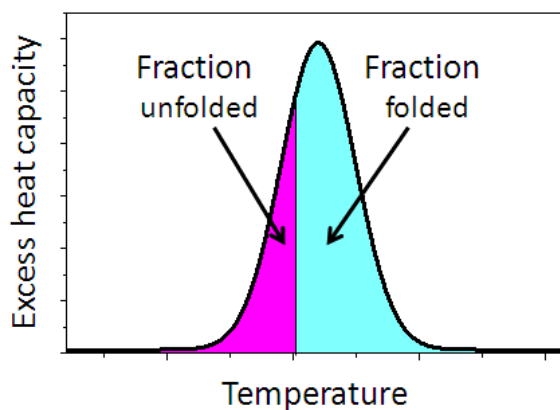


Figure 3.4 Van't Hoff analysis using area under the C_p peak at a given temperature to determine fraction of unfolded protein.

The temperature variation of the fraction of unfolded protein is related to the apparent enthalpy of the process using the van' Hoff equation;

$$-RT \ln K = \Delta H^0 - T\Delta S^0 \quad (\text{Equation 3.3})$$

then

$$\ln K = \frac{-\Delta H^0}{RT} + \frac{\Delta S^0}{R} \quad (\text{Equation 3.4})$$

and

$$\frac{d(\ln K)}{d(1/T)} = -\frac{\Delta H^0}{R^0} \quad (\text{Equation 3.5})$$

where K is area unfolded/total area. R is the universal gas constant, T is temperature in Kelvin. Therefore, a plot of $\ln K$ vs $1/T$ gives a line with a slope equal to the van't Hoff enthalpy divided by R . Van't Hoff enthalpy was calculated at $\Delta H_{VH} = 118 \text{ kcal mol}^{-1}$, figure 3.5.

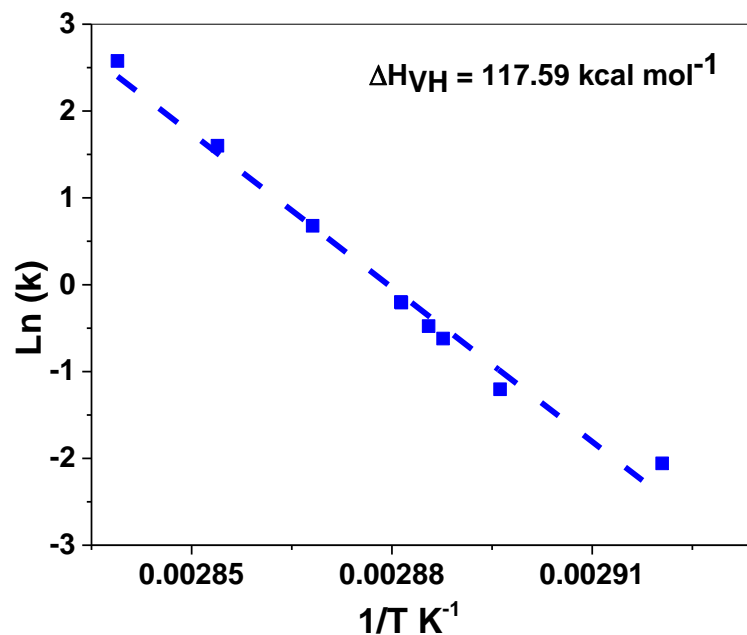


Figure 3.5 Calculation of Van't Hoff enthalpy, which assumes a two-state process.

3.3.3 Confirmation of aggregation and return to natively refolded protein after heating and cooling.

Since the DSC analysis required the samples to be crimp sealed into sample pans the samples were therefore not available for further visual examination. Instead, sample preparation was replicated and the samples were placed into 1.5 ml Eppendorf tubes and subjected to the same heating conditions.

Visual inspection of the samples revealed that a single heating and cooling cycle resulted in a change in the appearance from a clear to a turbid solution. This is consistent with the formation of aggregates above 1 μm in diameter. The samples were centrifuged at 13,000 $\times g$ to separate the aggregate from the supernatant containing soluble protein.

The supernatant was removed by aspiration and analysed using SDS PAGE and intrinsic fluorescence methods.

Exposure to high temperatures can lead to the rupture of the covalent bonds between the amino acids constituents of protein molecules and the resulting fragments are unable to refold to the native conformation (Cournoyer, Pittman et al. 2005). An SDS-PAGE was run with three samples; a sample which was not heated, a sample heated for one cycle and a sample heated for two cycles. No such fragments were detected using SDS PAGE in any of the samples, indeed the presence of non-fragmented, monomeric lysozyme was detected as a single band at ~14.3 kDa, figure 3.6.

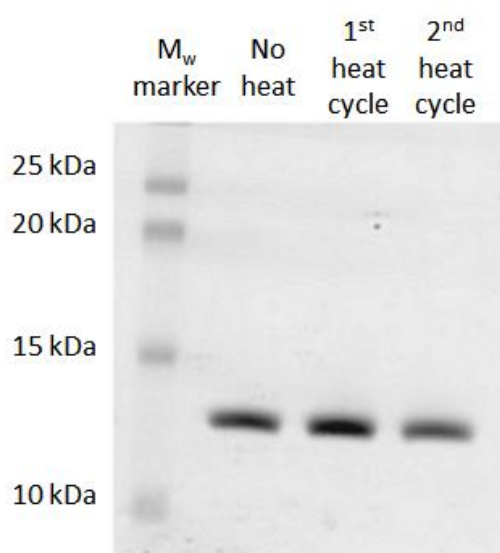


Figure 3.6 Lysozyme samples (50 mM sodium phosphate, pH 6) resolved in 12.6 % SDS PAGE

Intrinsic fluorescence was used to determine whether the protein had refolded to the native conformation upon cooling. Following centrifugation, a supernatant sample from one heating and cooling cycle, previously shown to contain monomeric lysozyme using SDS PAGE, was probed using intrinsic fluorescence. The fluorescence emission spectra from this sample were compared with those of unheated lysozyme. Fluorescence intensity (F. I.) and maximum emission wavelength ($\lambda_{\text{max em}}$) were measured following excitation at 280 nm and 295 nm for samples at lysozyme concentration of 1 mg/ml. Following excitation at 280 nm, the emission spectra for both the heated and unheated samples showed considerable overlap as did the emission spectra for the samples excited at 295 nm, figure 3.7. The overlap of the emission spectra indicates that the monomeric

protein in the supernatant had the same conformation as the unheated sample, thus indicating that upon cooling the protein has refolded to the native conformation.

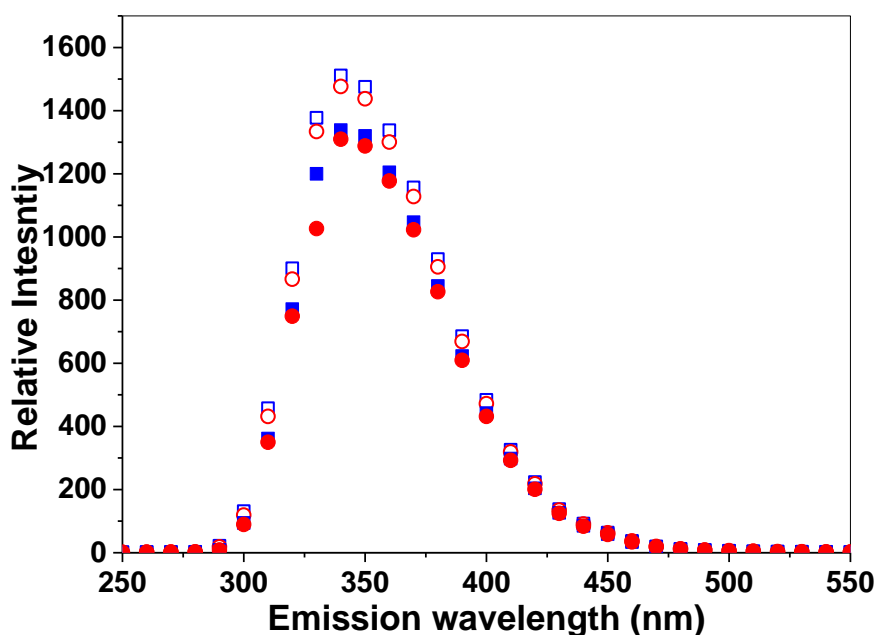


Figure 3.7 Intrinsic fluorescence; relative intensity and λ max. Open symbols - excitation at 295nm; Closed symbols - excitation at 280nm. Blue symbols - no heat treatment, Red symbols - one heating cycle (50 mM sodium phosphate, pH6)

From visual observation and inspection of some samples with a blunt probe it was determined that some of the samples had a gel-like consistency following heat treatment. The DSC thermogram for these samples did not have a second unfolding event. For these samples it was not possible to separate soluble lysozyme from the aggregated phase by centrifugation.

Where refolding was observed, a second, broad, exothermic, overlapping transition appeared in the thermogram during the first cooling cycle. During the second and subsequent heating cycles, this broad transition manifested as a second endotherm. A comparable low-temperature shoulder was reported in previous studies, however no attempt was made to characterise this peak (Salveti, Tombari et al. 2002, Rembert, Paterová et al. 2012). To determine whether this broad transition was associated with the refolded soluble lysozyme or the aggregate a modified DSC procedure was devised. In a 1.5 ml Eppendorf, samples were prepared and heated for one cycle under the same conditions as for the DSC measurements. The samples were centrifuged to separate the

soluble protein from the aggregate. The supernatant was then placed in a DSC pan and then subjected to a second heating cycle. There was only one endothermic peak observed during this second heating cycle, figure 3.8. Thus the elimination of the aggregated material from the first heat cycle resulted in the elimination of the broad peak observed during the second heat cycle. Indeed, the melt transition temperature for the soluble lysozyme from the supernatant was 74.6 °C which is consistent with the T_m observed during a standard DSC experiment, 74.1 °C, for the same solution conditions (100 mM sodium phosphate, pH 6); which is additional verification that the supernatant contained lysozyme that had refolded to the native conformation upon cooling.

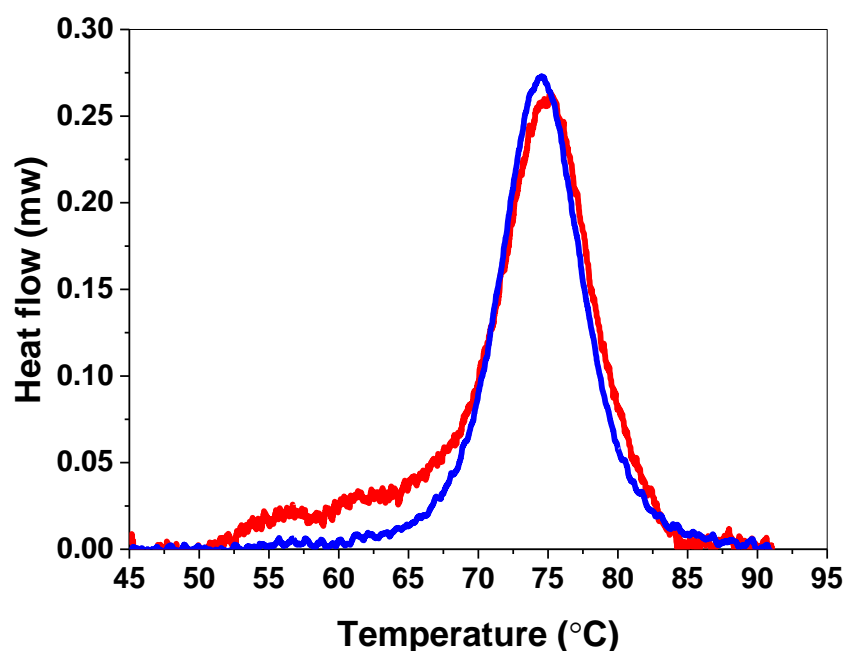


Figure 3.8 Second heating cycle (100 mM sodium phosphate, pH 6) Red line shows aggregate and soluble protein (standard DSC experiment) Blue line aggregate removed by centrifugation only soluble fraction remains.

3.3.4 Quantifying reversibility

The crimped pans and the flow of nitrogen in the test chamber ensure that the system remains closed during the course of the DSC experiment; there is no loss or gain of material through evaporation or condensation. Following thermal denaturation some unfolded molecules irreversibly aggregate and do not refold to the native state upon cooling. Therefore, for second and subsequent heating cycles, an apparent decrease in

ΔH relative to the first heating cycle is due to fewer natively folded lysozyme molecules undergoing thermal denaturation. A refolding index (RI) was calculated to determine the proportion of reversible unfolding following thermal denaturation, using;

$$RI = \frac{\Delta H_{me}(n+1)}{\Delta H_{me}(n)} \quad \text{(Equation 3.6)}$$

where, ΔH_{me} is the integrated area under the unfolding peak from the melt transition temperature, T_m to the end of the endothermic transition, T_e , during an unfolding event, n .

Table 3.7 Reversibility Index (R.I. = $\Delta H_{me2}/\Delta H_{me1}$) in the presence and absence of disaccharide

Solution conditions	pH 5		pH 6		pH 7		pH 8		pH 9	
	T_m	R.I	T_m	R.I	T_m	R.I	T_m	R.I	T_m	R.I
0 mM phosphate (MilliQ)	-	-	75.2 ★	0.6 4	-	-	-	-	-	-
5 mM phosphate	-	-	75.3 ■	0.3 3	-	-	-	-	-	-
10 mM phosphate	76.8 ○	0.5 8	75.1 ●	0.3 0	72 ↔	0.0 0	71.5 ←	0.0 0	70.2 ↔	0.0 0
10 mM 20% v/v maltose	81.9 △	0.5 9	82.3 ▲	0.6 6	79.7 ⇒	0.2 1	77.7 ⇒	0.0 0	-	-
10 mM 20% v/v trehalose	83.8 ▽	0.6 4	80.1 ▼	0.4 2	80.7 ↑	0.0 7	79.7 ↑	0.0 0	-	-
50 mM phosphate	76.8 ▷	0.5 5	74.3 ◆	0.2 0	71.4 ↓	0.0 0	70.1 ↓	0.0 0	70.1 ▷	-
50 mM 20% v/v maltose	83.5 □	0.5 6	79.7 ◀	0.3 5	77.4 ↖	0.0 0	74.3 ↖	0.0 0	-	-
50 mM 20% v/v trehalose	85.1 ◇	0.5 6	81.0 ▶	0.2 7	77.6 ↗	0.0 0	76.4 ↗	0.0 0	-	-
100 mM phosphate	76.7 ▽	0.5 1	74.1 ●	0.1 7	71.3 ↔	0.0 0	70.7 ↔	0.0 0	69.9 ↔	0.0 0
200 mM phosphate	-	-	73.9 ◆	0.0 0	-	-	-	-	-	-
500 mM phosphate	-	-	73.9 ◎	0.0 0	-	-	-	-	-	-
750 mM phosphate	-	-	74.8 ★	0.0 0	-	-	-	-	-	-
1 M phosphate	-	-	76.1 ●	0.0 0	-	-	-	-	-	-

Further DSC experiments were completed to confirm the accuracy of the *RI* value. Lysozyme solutions were prepared at concentrations of 20, 25 and 50 mg/ml in 50 mM sodium phosphate buffer at pH 6. The ΔH_{cal} values at each concentration are shown in table 3.8. An *RI* value of 0.20 is the equivalent of saying that following thermal denaturation of a solution containing of 100 mg/ml, 20% of the lysozyme (20 mg/ml) refolds to the native conformation. Thus, a lysozyme solution at a concentration of 20 mg/ml should have the same ΔH_{cal} value for its first heating cycle as a 100 mg/ml sample during the second heating cycle, if the *RI* value is 0.20.

Table 3.8 Area associated with lysozyme unfolding at different protein concentrations. Where the initial protein concentration of 100 mg/ml is thermally denatured and an R.I. value of 0.20 is measured this is consistent with the area of an equivalent 20 mg/ml solution

Lysozyme concentration (mg/ ml)	Area T_m-T_e
100	55.5
50	29.1
25	18.6
20	12.4
RI = 0.20	11.7

Where *RI* > 0 following the first heat treatment, a second *RI* value was determined to quantify the degree of reversibility following a second heat treatment. These data are shown in table 3.9.

Table 3.9 Reversibility Index (R.I. = $\Delta H_{me3}/\Delta H_{me1}$) in the presence and absence of disaccharide

Solution conditions	pH 5	pH 6	pH 7
0 mM phosphate (MilliQ)	-	0.31	-
5 mM phosphate	-	0.17	-
10 mM phosphate	0.37	n/a	-
10 mM 20% v/v maltose	0.37	0.45	0.00
10 mM 20% v/v trehalose	0.37	0.20	0.00
50 mM phosphate	0.38	0.00	-
50 mM 20% v/v maltose	0.28	0.11	-
50 mM 20% v/v trehalose	0.41	0.00	-
100 mM phosphate	0.36	0.08	-

3.3.5 Effect of solution conditions

In this study, a single buffer type is conserved to eliminate a buffer-type effect. The pH, ionic strength and presence/absence of disaccharides were varied to determine their effect on, the melt transition temperature during the first DSC heating cycle, T_{m1} . The lysozyme purchased from Calbiochem had been precipitated from an acetate buffer, therefore it was necessary to remove any co-precipitated salts prior to experimentation since these salts could affect pH, ionic strength and the buffer salts present in the final samples. The acetate salts were removed at the start of sample preparation by washing the lysozyme repeatedly by ultrafiltration, with the appropriate buffer.

Figure 3.9 shows the decrease in T_{m1} as pH was increased from pH 5 to pH 9. Between pH 5 and pH 6 for 50 mM and 100 mM buffers there was a sharp decrease in T_m ($\Delta T_m = 2.9$ °C and 2.6 °C, respectively) whereas a slightly more gradual decrease was observed for the 10 mM buffer, $\Delta T_m = 1.7$ °C. Between pH 6 and pH 7 the decrease in T_m was sharp for all three buffers ($\Delta T_m = 3.1$ °C, 2.9 °C and 2.8 °C, respectively). Between pH 7 and pH 9 a more gradual decrease in T_m was observed for all three buffers ($\Delta T_m = 1.3$ °C, 0.0 °C and 0.8 °C, respectively). Regardless of ionic strength the T_m values converge at pH 5 and pH 9.

Given that the melt transition temperature was shown to be dependent upon both ionic strength and pH, the range of ionic strengths was extended to between 5 and 1000 mM for pH 6 and further DSC analysis was performed figure 3.10.

These experiments were performed at pH 6 since this was the pH of the lysozyme solution (measured in-situ) following extensive desalting washes with deionised MilliQ water. T_m in the absence of sodium phosphate was 75.2 °C. The T_m dependence on ionic strength was observed to be bi-modal. As ionic strength increased from 0 to 200 mM there was a decrease in T_m . Between 200 and 500 mM T_m reached a minimum at 73.9 °C. T_m began to increase again between 500 and 750 mM and exceeded T_m in the absence of buffer salts at 1000 mM.

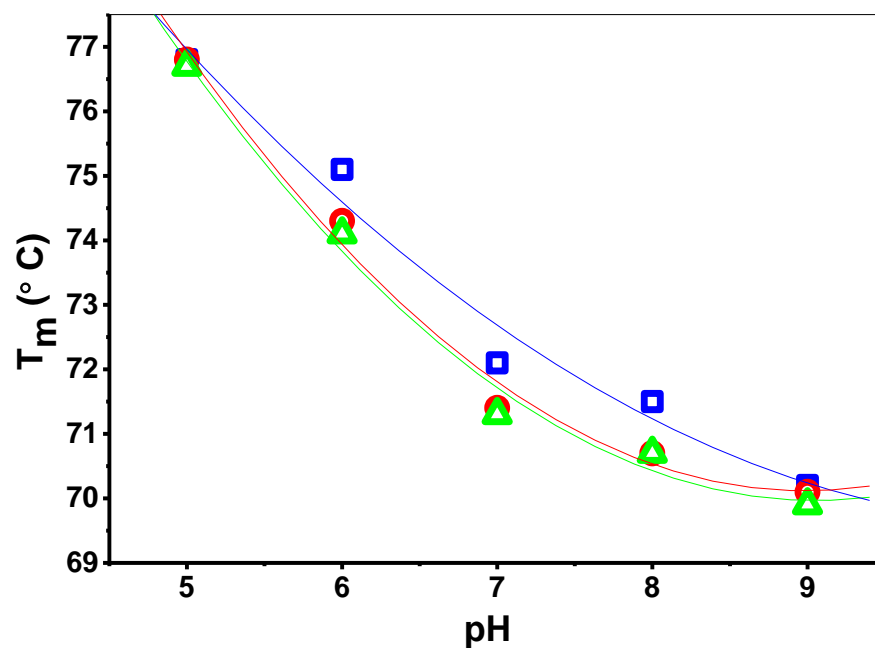


Figure 3.9 The pH and ionic strength dependence of the melt transition temperature, T_{m1} , during the first DSC heating cycle. Blue 10 mM, Red 50 mM, Green 100 mM.

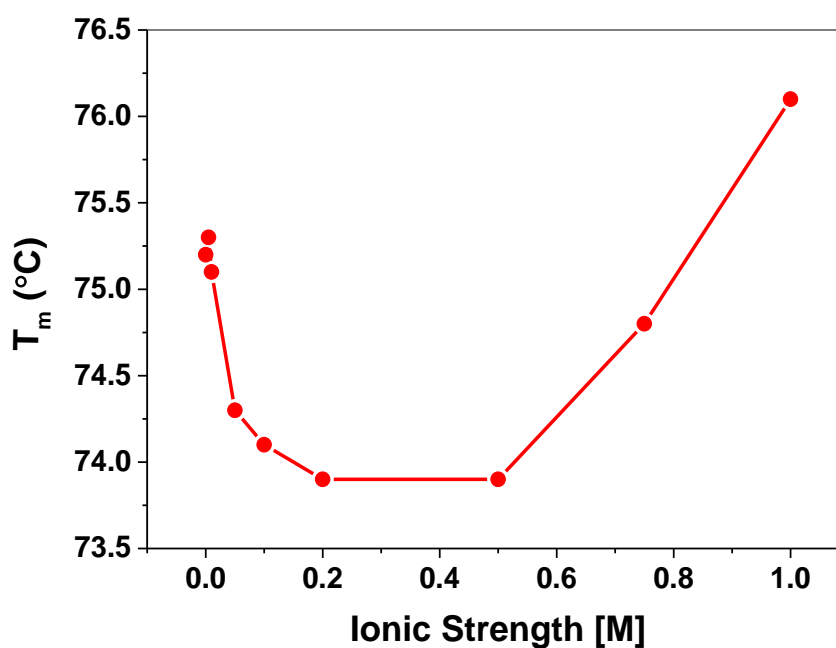


Figure 3.10 The ionic strength dependence of T_m at pH 6.

Figure 3.11 shows the dependence of the refolding index, RI , on pH and ionic strength. The proportion of protein that successfully refolded to the native state decreased as pH increased and at $pH \geq 7$ no refolding was observed. At pH 5 and pH 6 more refolding was observed for 10 mM than for either 50 or 100 mM, where RI value was the same for both.

Figure 3.12 shows the ionic strength dependence of the refolding index for the extended range of ionic strengths at pH 6. In deionised MilliQ water (i.e. in the absence of sodium phosphate) a maximum value was observed for RI, 0.64. As ionic strength increased, reversibility decreased when the concentration reached 200 mM and above, no refolding was observed.

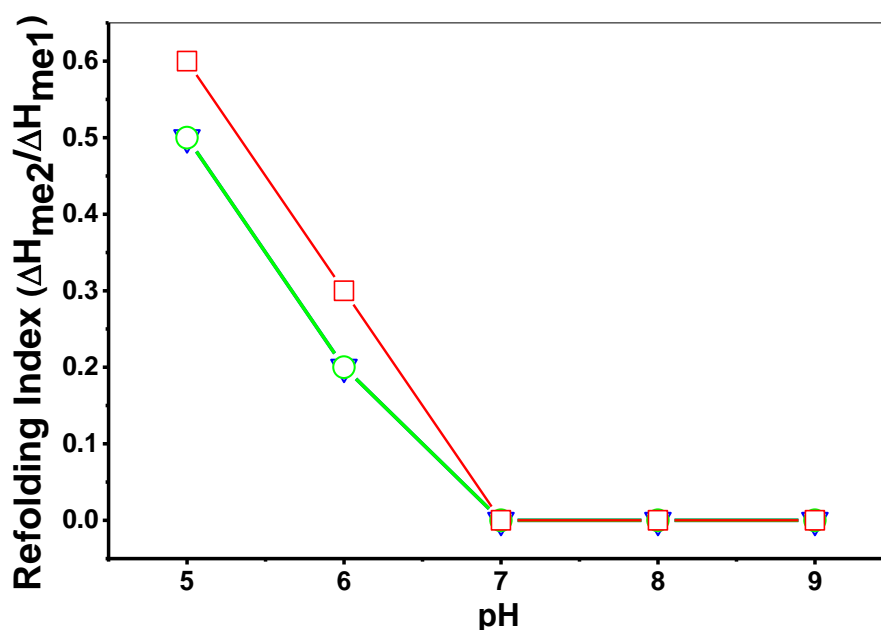


Figure 3.11 The pH and ionic strength dependence of the refolding index, $\Delta H_{me2}/\Delta H_{me1}$, after the first DSC heating cycle. Red 10 mM, Green 50 mM, Blue 100 mM.

There is a complex relationship between the thermal stability of lysozyme, as measured by T_m , and the extent of refolding to the native conformation. In figure 3.11 refolding was observed at pH 5 and pH 6 but was absent at pH 7 and higher. In addition, the melt transition temperatures where refolding was observed were greater than those at pH 7 and above. However, refolding behaviour is not predicated on T_m . There was considerable overlap between T_m values where reversible and non-reversible thermal denaturation occurred; refolding was observed at T_m values between 74.1 °C and 80.7 °C while no refolding was observed at T_m values between 69.9 °C to 79.7 °C, figure 3.13.

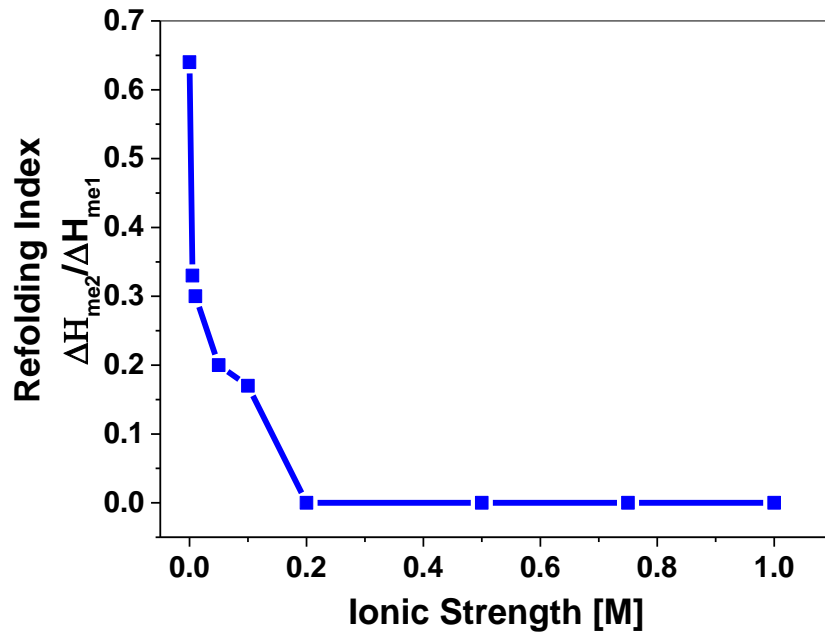


Figure 3.12 The ionic strength dependence of the refolding index, $\Delta H_{me2}/\Delta H_{me1}$, after the first DSC heating cycle at pH 6.

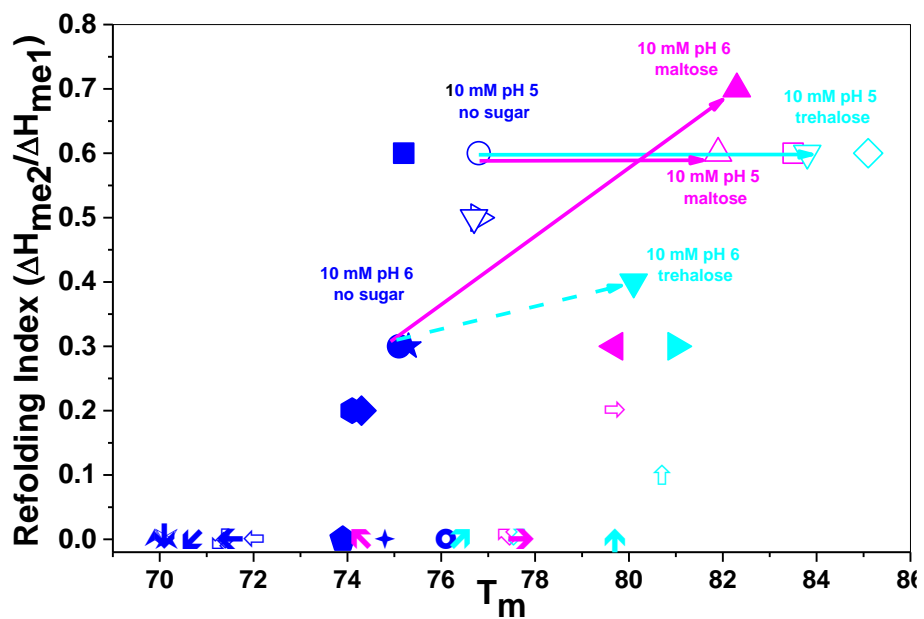


Figure 3.13 The T_m dependence of the refolding index. For key see Table 3.7.

For the extended range of ionic strengths investigated at pH 6 no refolding was observed at either the highest or lowest T_m , however, refolding was observed for intermediate values. Furthermore, similar T_m values were associated with different proportions of refolded protein, figure 3.14.

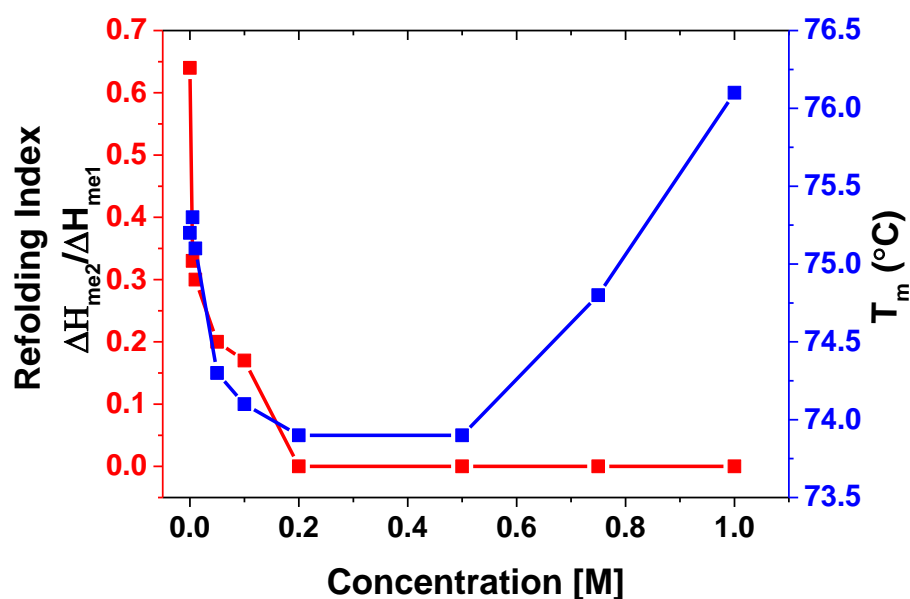


Figure 3.14 The ionic strength dependence of the refolding index and melt transition temperature at pH 6. ■ T_m ■ Refolding Index.

3.4 The addition of disaccharide excipients

Previous studies have shown that disaccharide excipients increase T_m (Sola-Penna and Meyer-Fernandes 1998). DSC experiments were repeated in the presence of either 20 % v/v trehalose or maltose, in order to determine whether the increase in T_m associated with these co-solutes had an influence on the extent of refolding to the native conformation following thermal denaturation, table 3.9. For all solution conditions examined, T_m was increased in the presence of the disaccharide co-solutes. The proportion of protein refolded was not increased at pH 5. The proportion of protein refolded at pH 6 was increased for all solution conditions examined. The proportion of protein refolded at pH 7 was only increased for 10 mM solutions. The proportion of protein refolded was not increased at pH 8. Thus, no direct correlation between T_m and RI was observed nor was any correlation observed between ΔT_m and ΔRI , table 3.10.

Table 3.10 Increase in the melt transition temperature, ΔT_m , and the change in reversible unfolding, ΔRI , associated with the addition of sugar co-solutes.

	pH 5		pH 6		pH 7		pH 8	
Solution conditions	ΔT_m	ΔRI	ΔT_m	ΔRI	ΔT_m	ΔRI	ΔT_m	ΔRI
Sodium phosphate buffer								
10 mM 20% v/v maltose	5.1	0.01	7.2	0.36	7.7	0.21	6.2	0
10 mM 20% v/v trehalose	7	0.06	5	0.12	8.7	0.07	8.2	0
50 mM 20% v/v maltose	6.7	0.01	5.4	0.15	6	0	4.2	0
50 mM 20% v/v trehalose	8.3	0.01	6.7	0.07	6.2	0	6.3	0

3.5 Discussion

Differential scanning calorimetry was used to quantify the degree of reversible unfolding following thermal denaturation of lysozyme. A decrease in the change in apparent heat capacity, associated with the unfolding of the native conformation of lysozyme, was observed between the initial heating cycle and the ensuing heating cycles. Replicate experiments performed in Eppendorf tubes rather than DSC pans indicated that two distinct protein phases were present after heat denaturation. The visibly aggregated protein was separated by centrifugation from a supernatant containing soluble, natively folded, non-fragmented monomers which were characterized using SDS PAGE and intrinsic fluorescence spectroscopy. Where the replicate samples were observed to be gel-like, natively folded lysozyme could not be separated by centrifugation. The formation of irreversible aggregates from thermally denatured lysozyme reduces the quantity of monomeric protein available to refold to the native conformation upon cooling and therefore the quantity of natively folded monomers available to unfold during a second heating cycle. This reduction or total depletion of natively folded lysozyme is consistent with the decrease or absence of the unfolding endotherm during subsequent heating cycles (Salveti, Tombari et al. 2002).

Aggregation manifests as an exotherm during a DSC heating cycle while unfolding is an endothermic process. Therefore, consideration must therefore be given to the impact that this opposing energy flow might have on the unfolding endotherm. For the sample analyzed herein, the unfolding endotherm was neither followed by, nor appreciably foreshortened by a competing energy flow associated with aggregate formation. Where aggregation occurs, the enthalpy cannot be unambiguously calculated. Nevertheless, the calorimetric enthalpy (ΔH_{cal}) was calculated by integrating the area

under the peak and was found to be in agreement with previously published values; $\Delta H_{\text{cal}} = 111 \text{ kcal mol}^{-1}$ for 50 mM at pH6 and van't Hoff enthalpy was calculated for the same solution conditions at $\Delta H_{\text{VH}} = 118 \text{ kcal mol}^{-1}$. Comparison of the van't Hoff enthalpy with calorimetric enthalpy gives information about the validity of the two state assumption. For an ideal, two-state, reversible transition $\Delta H_{\text{VH}} = \Delta H_{\text{cal}}$, however, the solution conditions chosen for these experiments were such that a fully reversible unfolding was not expected. Nonetheless, $\Delta H_{\text{VH}}/\Delta H_{\text{cal}}$ was determined to be ≈ 1 , a value which indicates that the unfolding endotherm is not significantly distorted by the competitive heat flow associated with aggregation (Escudero et al. 2010), under the conditions used.

To exclude any kinetic effects during unfolding process within these DSC experiments, a scan rate of $1 \text{ }^\circ\text{C}/\text{min}$ was chosen, a value which is commonly used for lysozyme since slower scan rates do not affect T_m (Ferreira, Hofer et al. 1997, Wu, Luo et al. 2011). However, some hysteresis ($T_m > T_f$) was observed upon cooling, due to the kinetics of refolding. In order to allow the refolding to reach an equilibrium state, the refolding index values were calculated based on the second unfolding rather than the first refold. Since the rate at which the scans were executed was held constant, $1 \text{ }^\circ\text{C}/\text{min}$, this means that the protein in solutions with lower T_m values was unfolded for longer than the protein in solutions with higher T_m values. And from figure 3.13 it can be seen that there were very different amounts of refolding associated with protein solutions with very similar T_m values. Therefore, a kinetic component to the aggregation process was precluded.

It has long since been understood that solution conditions such as pH, ionic strength and ion type influence the self-organisation of proteins and the influence on the melt transition temperature, in particular, has been the subject of much investigation (Hofmeister 1888, Sophianopoulos, Rhodes et al. 1962, Tanford 1968). The solution conditions chosen herein deliberately exploit these effects in order to systematically vary the T_m of the protein. To the best of our knowledge, such a comprehensive set of data for lysozyme is unavailable in the literature. Thus, these data may be considered in their own right.

From figure 3.9 it is clear that the decrease in T_m was not linear. This was due to the deprotonation of amino acid residues that play an important role in stabilizing the tertiary structure of lysozyme. Between pH 5 and pH 7 the pKa of two residues is crossed; His 15 and Glu 35 at pKa 5.4 and 6.2, respectively (Inoue, Yamada et al. 1992, Ohmura, Ueda et al. 1997). In addition to this residue specific effect, varying pH also alters the hydrogen bonding network within the protein's secondary structural units in a non-specific manner, which, in turn, alters thermal stability (Mutter, Gassmann et al. 1991). For ionic strength ranging from 10 mM to 100 mM T_m values decrease. These values converged at pH 5 and pH 9 regardless of ionic strength. An extended range of ionic strengths were probed at pH 6, figure 3.10 and a bimodal response was observed. The addition of salt decreased the melt transition temperature for concentration ≤ 200 mM. Further addition of salt resulted in a recovery in the melt transition temperature. These results indicate that it is possible to use ionic strength to regulate lysozyme T_m between pH 5 and pH 9, but beyond these limits, T_m is not sensitive to sodium phosphate ionic strength at these low salt concentrations.

Following thermal denaturation no refolding to the native conformation was observed in the DSC thermograms above pH 7, indicating that all the protein had aggregated. This conclusion was upheld by visual inspection and centrifugation. Aggregate formation is promoted by attraction due to van de Waal's forces and hydrophobic effects and opposed by electrostatic repulsion between the molecules. The isoelectric point of lysozyme is 11 (Alderton and Fevold 1946), thus as the pH increased the solution approached the isoelectric point and the net electrical charge on the protein was decreased. As the repulsive electrostatic interaction decreases the attractive interaction becomes dominant, leading to the formation of aggregates at $\text{pH} \geq 7$.

The refolding of thermally denatured lysozyme was studied in the absence and presence of salts at pH 6 (0 to 1000 mM). Refolding was greatest in the absence of salt (i.e. in MilliQ water) and no refolding was observed at salt concentrations ≥ 200 mM. Ion specific effects on the aggregation behavior of proteins are more complex and is mediated by both specific and non-specific interactions between the ions and proteins and between the ions and water (Zhang and Cremer 2006, Kameoka, Masuzaki et al. 2007). Anions, at low concentration, have been shown to bind to amino acids with positive side chains. As a consequence the negative electrostatic charge is neutralised and repulsion

between the protein molecules is reduced. Once this electrostatic binding saturation point is reached, the polarizability of the anion governs the degree to which the anion interacts with hydrophobic binding sites on the proteins (Rembert, Paterová et al. 2012). The reversibility index data shown in figure 3.14 is supported by these studies. With respect to melt transition temperature, preferential partitioning of the phosphate anions accounts for the observed behavior. Initially, the phosphate anions accumulate at the protein surface and this salting-in behavior is expected to decrease T_m . When the positive amino acid residues become neutralised, the phosphate anions being to preferentially accumulate in the bulk, a salting-out process becomes dominant and an increase in T_m is anticipated. With respect to aggregation, the initial binding of the anions to the positive amino acid residues decreases electrostatic repulsions, leading to increasing aggregation. Above the saturation concentration, the exclusion of the highly polarised phosphate anion from the hydrophobic binding sites increases interfacial tension, which is subsequently minimised by aggregation.

Although melt transition temperature is widely used as a measure of protein stability (Cooper 1999, Pantoliano, Petrella et al. 2001, Zhang and Cremer 2009) our results show that T_m provides no indication of the reversibility of unfolding once thermal denaturation has occurred figure 3.13. Indeed, there was considerable overlap between the T_m values where non-reversible and reversible thermal denaturation occurred. The results for pH 6 clearly demonstrate this point; at both the lowest and highest T_m values no refolding was observed whereas refolding was observed for intermediate values. Furthermore, protein solutions with similar T_m values had dissimilar amounts of refolded protein upon cooling.

Disaccharide excipients are commonly used to increase the T_m in protein formulations (Sola-Penna & Meyer-Fernandes 1998; Kamerzell et al. 2011). Dynamic light scattering from the McManus group show that although saccharides consistently increase T_m , colloidal stability was observed to only increase when the interaction potential was not dominated by electrostatic repulsion (James and McManus 2012). Here we have shown that, although the presence of 20% v/v trehalose or maltose resulted in an increase in T_m values, this increase in thermal stability was not necessarily accompanied by an increase in the proportion of refolded lysozyme. Indeed, no quantifiable relationship between the increase in T_m , due to the presence of disaccharide excipients and

the extent of refolding following thermal denaturation could be determined. For example, for 10 mM phosphate at pH 5 the addition of maltose and trehalose resulted in an increased T_m of 5.1 and 7.0 °C, respectively, with virtually no increase in the proportion of refolded protein. Whereas, at pH 6, T_m increased in the presence of maltose and trehalose by 7.2 and 5.0 °C, respectively, with a concomitant increase in refolding of \approx 40 % and 10 %, respectively.

Therefore, using DSC, a method was developed to quantify the reversibility of unfolding following thermal denaturation and these results show that where melt transition temperatures are exceeded, deliberately or inadvertently, during protein purification, processing or handling, T_m provides no indication of the potential reversibility of that thermal denaturation.

3.6 Conclusion

The aim of this study was to evaluate whether T_m is related to the degree of aggregation following thermal denaturation. Systematically, a set of solution conditions were selected to alter the melt transition temperature of lysozyme; by varying pH, ionic strength and the addition of disaccharides. DSC thermograms from consecutive heating and cooling cycles were compared to determine what proportion of thermally denatured protein that refolds to the native state and thus, indirectly, what proportion forms irreversible aggregates. The proportion of reversible thermal denaturation was then measured and compared with T_m . Furthermore, protein solutions with similar T_m values had dissimilar amounts of refolded protein upon cooling. Reversibility was shown to be dependent both on ionic strength and pH; with the greatest proportion of refolded protein at pHs furthest from the isoelectric point. These results show that when the concentration of sodium phosphate is increased a decrease in extent of refolding is observed. Disaccharides excipients were shown to increase the melt transition temperature without necessarily increasing the proportion of refolded protein.

A method was established to measure the degree of reversible unfolding following thermal denaturation. This study shows T_m is not related to the degree of aggregation following thermal denaturation of lysozyme. Thus, solution conditions that promote intramolecular self-organisation of proteins do not necessarily prevent the intermolecular

self-organisation of thermally denatured proteins. This type of analysis may prove useful in assessing the stability of proteins in both the biopharmaceutical and food industries.

Chapter 4 Bigels formed via spinodal decomposition of unfolded protein

4.1 Introduction

Hydrogels are a class of gels formed from hydrophilic polymer chains capable of holding large amounts of water in their three-dimensional network. These gels have been used in numerous medical applications, especially in the area of tissue engineering, prosthetics and wound healing (Dou, Liow et al. 2014, Lisman, Butruk et al. 2014). In addition, hydrogels have been employed within the pharmaceutical industry as environment-sensitive implantable delivery systems (Zhang, Chan et al. 2013, Dou, Liow et al. 2014). Because of their extensive cross-linked structure and high water content, hydrogels are used in cell culturing as a surrogate for the extracellular matrix. Here the hydrogel provides a template for directed cell growth, a scaffold to induce mechanically stimulated cell differentiation and via the water filled pores, a diffusive network to deliver nutrients and remove waste (Van Vlierberghe et al. 2011). A wide variety of hydrogel systems are currently available, each with its own advantages and shortcomings e.g. brittleness and low elastic moduli (Tibbitt & Anseth 2009). Ultimately, more sophisticated hydrogels are needed to satisfy the complex demands required for advanced applications. To develop improved products and treatments, medics, tissue engineers and pharmaceutical companies need hydrogels with increased functionality, with tunability and with bioactivity; an inert and biologically compatible hydrogel is no longer sufficient. Thus, the development of such biomimetics is the focus of intense research (Lavine, Frisk et al. 2012, Verhulsel, Vignes et al. 2014).

Various methods have been used to enhance the properties of hydrogels including, combining synthetic and biologic (natural) hydrogels to form hybrids (Tibbitt & Anseth 2009), sophisticated covalent crosslinking of components (Okumura & Ito 2001), nanocomposition (Haraguchi & Takehisa 2002) and bigelation ((J.-Y. Sun et al. 2012; Buehler & Ackbarow 2008; Varrato et al. 2012). The term bigel or double network gel has been used to refer to a variety of different types of material. The Mahdy group referred to the emulsion obtained from a mixture of a hydrogel and an organogel as an oleo-hydrogel and a bigel (Ibrahim, Hafez et al. 2013). The Zhou group applied the term to a macroscopically heterogeneous construct, comprised of two unique gel strips bonded together (Zhang, Wu et al. 2012). The Foffi group used the term to refer to a binary, interpenetrating colloidal gel (Varrato, Di Michele et al. 2012). In addition, the term double network gel has been used to describe gels formed from the interpenetration but

unconnected networks formed from polymeric gels. The Osada group used sequential covalent cross-linking to produce a mechanically strong double network hydrogel, which yields after the application of a fracture stress of 17.2 MPa (Gong, Katsuyama et al. 2003). In 2012, the Suo group reported a double network gel that had fracture energies of $\sim 9,000 \text{ Jm}^{-2}$ which could be stretched to 20 times its initial length and maintained considerable mechanical strength when notches were present. These double network gels were formed from covalently cross-linked polyacrylamide and alginate, a polymeric physical gel (Sun, Zhao et al. 2012). Here, the term bigel refers to a gel formed from two percolated, interpenetrating but discrete networks, regardless of the nature of the bond type within the network, figure 4.1. Thus, the bigels of the Mahdy and Zhou group are excluded whereas the bigels of Foffi and double-network gels of Osada and Suo are included.

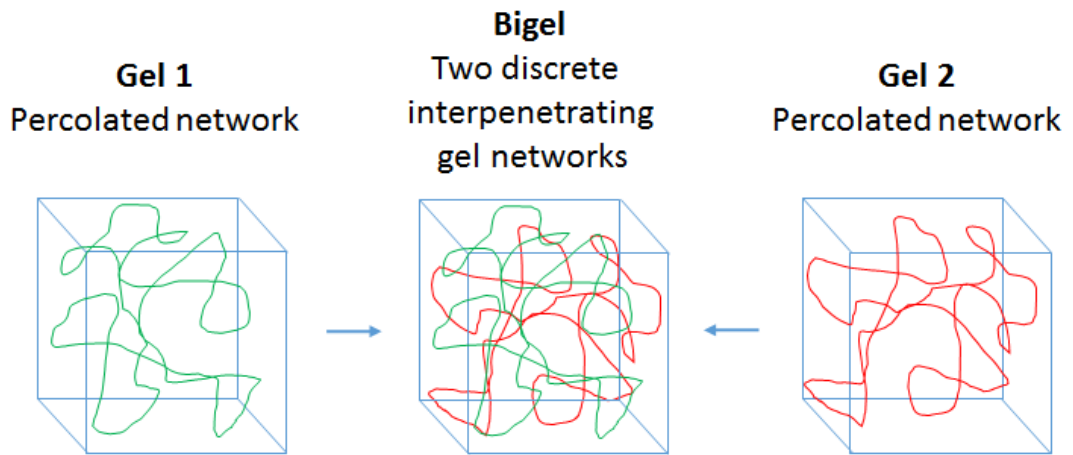


Figure 4.1 Schematic of a bigel, formed from two discrete interpenetrating gel networks.

The mechanical properties of hydrogels, in particular their lack of toughness and elasticity, restrict the range of potential application (Calvert 2009). However, bigels, show great potential for further applications due to their enhanced mechanical properties (Sun, Zhao et al. 2012, Di Michele, Fiocco et al. 2014, Zhao 2014). Since both networks contribute to the physical and mechanical properties of the bigel and these features can be tuned, bigelation increases the functionality of hydrogels (Sun, Zhao et al. 2012, Varrato, Di Michele et al. 2012).

In 2012, the Foffi group functionalised polystyrene particles with DNA and used that system to demonstrate the validity of their numerical simulations and showed that arrested spinodal decomposition leads to the formation of a bigel (Varrato, Di Michele et al. 2012), figure 4.2. Later, in 2014, the mechanical and structural properties of their bigel was studied (Di Michele, Fiocco et al. 2014). In this numerical study, the particles were allowed to reach a free energy minimum following quenching. Then, the configuration of the particles was deformed by displacing particles slightly and the free energy was minimised for the deformed conditions. Thus a stress-strain relationship was simulated from which it was shown that the arrested phase of the bigel yields at a higher shear stress than a single-component gel at the same volume fraction (for $\phi_{\text{total}} = 0.1$ the stress at the yield point is about four times larger for a bigel than for the gel).

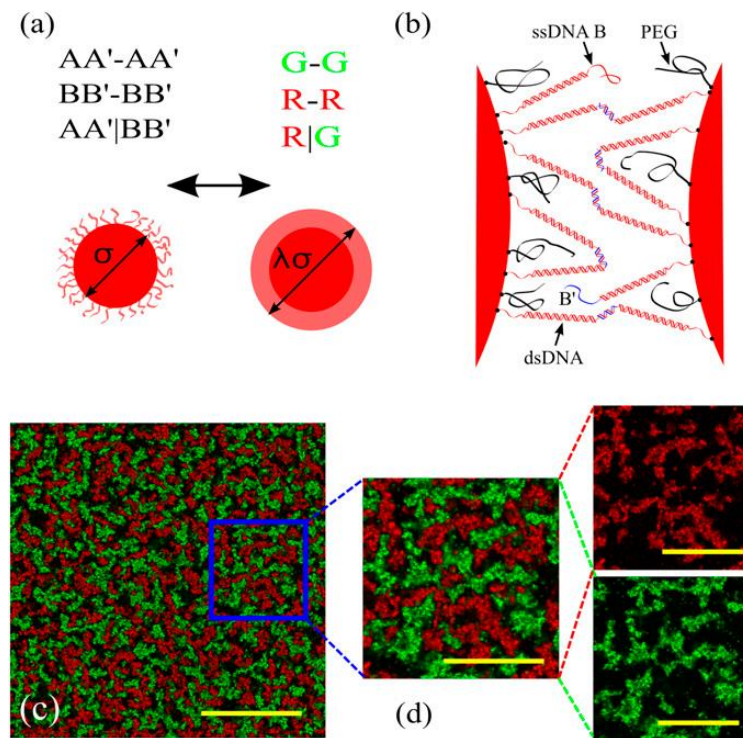


Figure 4.2 (a) Schematic of DNA coated polystyrene colloids showing only intra-species attraction for colloid radius σ (500 nm) and attractive range $\lambda\sigma$. (b) Schematic of the gap between two interacting R colloids. Red double helices indicate dsDNA spacers; red and blue strands indicate B and B' sticky ends, red-blue double helix indicates the hybridization of complementary sticky ends forming bridges. Black strands indicate inert PEG polymers. (c) Confocal image of the demixed bigel showing R and G colloids (d) Detail of image (c). Modified from (Foffi 2012).

The seminal work of the Osada group produced double-network gels with extremely high mechanical strength by sequential covalent cross-linking of two polymers (Gong, Katsuyama et al. 2003). The mechanical properties of a gel prepared from poly(2-acrylamido-2-methylpropanesulfonic acid), PAMPS, and poly(acrylamide), PAA_m, in a molar ratio of 1:2 with crosslinking densities of 4% and 0.1%, respectively, was extensively characterised. The first gel network was prepared in the usual manner and this gel was subsequently immersed in an aqueous solution containing acrylamide which was then polymerised. A stress-stain curve of this double-network gel under compression is shown in figure 4.3. The single network component gels (PAMPS and PAA_m) break at stresses of 0.4 and 0.8 MPa, respectively, whereas the double networks breaks at 17.2 MPa. The stress-strain curve of the double-network gels overlaps with that of PAMPS at strains < 40 %, suggesting that the PAMPS contributes to the response to the applied elastic stress while the PAA_m contributes to the strain. The authors show that the optimal molar ratio was 1:2 and that the most notable increase in mechanical strength was observed when the 1st network was highly cross-linked (4%) and the second network was loosely cross-linked (0.1%). The proposed yielding mechanism for these gels included the formation of PAMPS clusters at the damage zone, figure 4.4. Importantly, both polymers were miscible in water and do not chemically interact with one another. Thus the increase in mechanical strength was neither induced by phase separation, molecular interaction nor simple physical entanglement (since maximum strength is observed at low cross-linking density for the second network). Double-network gels of this style have been developed with hardness (elastic modulus of 0.1–1.0 MPa), strength (failure tensile stress 1~10 MPa, strain 1000–2000%; failure compressive stress 20–60 MPa, strain 90–95%), and toughness (tearing fracture energy of 100–1000 J m⁻²)(Gong 2010). Thus, the fundamental requirements for mechanically strong double-network gels are; (a) two contrasting polymers gels to be used (a rigid polyelectrolyte as the first network and a ductile neutral polymer as the second network), (b) an excess molar concentration for the second network and (c) the second network to be loosely cross-linked.

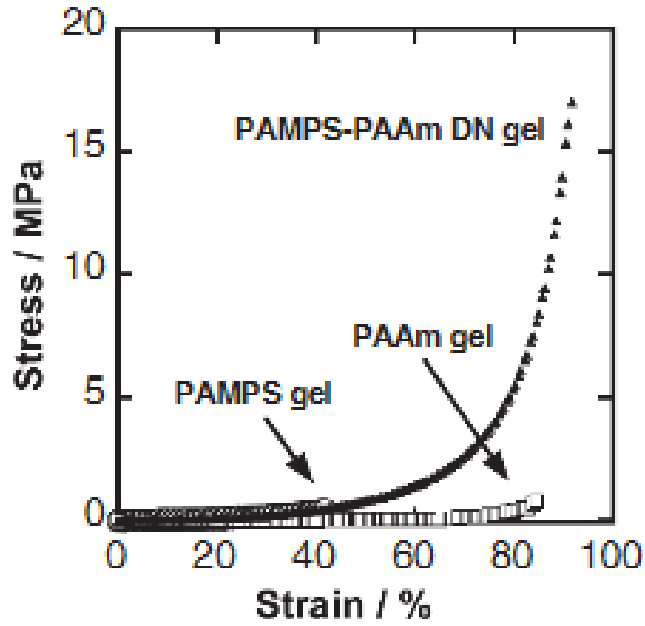


Figure 4.3 A compressive stress-strain curve for the single component and double-network gels of the Osada group. Modified from (Gong, Katsuyama et al. 2003).

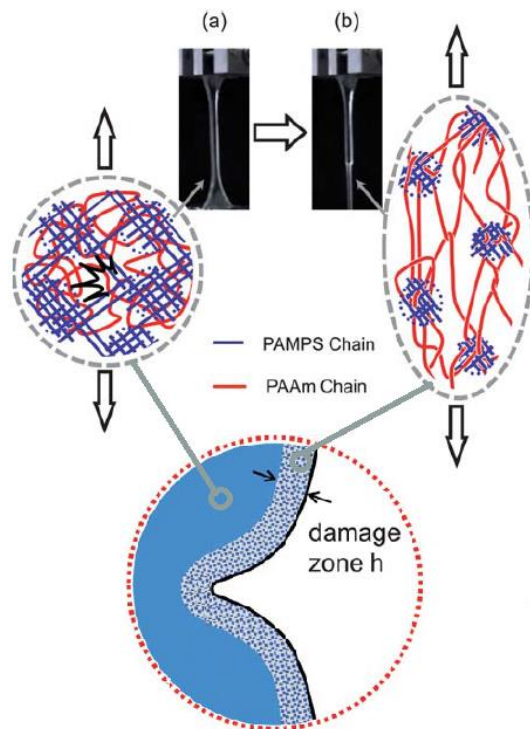


Figure 4.4 Schematic of proposed yielding mechanism in double-network gel; (a) unperturbed gel, (b) formation of PAMPS clusters in damage zone, h. Modified from (Gong 2010).

To account for the yielding zone, the Brown-Tanaka model was proposed and the fracture energy, G , expressed as (Equation 4.1);

$$G_0 = G_0 + \sigma_c \varepsilon_c h \quad (\text{Equation 4.1})$$

where G_0 is the intrinsic fracture energy, σ_c is yielding stress, h is the size of the softening zone and ε is the strain where the necking zone finishes. Gong observed that the limitation of the double-network gels lies in their lack of fatigue resistance, owing to irreversible fracture of chemically cross-linked gels and suggested that the double-network principle could be applied to other ‘self-healing’ materials (Gong 2010).

Physical gels, are reversible or ‘self-healing’ gels which are held together by molecular entanglements, depletion interactions, ionic, hydrogen bonding and hydrophobic interactions or a combination thereof. These interactions are reversible and the gel may be transformed to the sol state by an alteration in the environmental conditions e.g. pH, temperature, pressure. In 2012, the Suo group produced a remarkable double network gel composed of physical polymeric gel, alginate and a covalently cross-linked gel, polyacrylamide (Sun, Zhao et al. 2012). These gels were capable of being stretched more than 20 times their initial length and were notch-insensitive; samples containing notches stretched to more than 17 times their initial length. In addition, these gels were extremely tough with fracture energies of $\sim 9,000 \text{ Jm}^{-2}$. Allowing a 24 hour recovery period, at 80 °C, these gels showed a 74% recovery of original rupture strength. The strength of this gel relies on the polyacrylamide network bridging a crack which stabilises deformation while unzipping of the alginate network over a large region of the gel dissipates energy and the increased fatigue resistance stems from the reformation of the alginate – Ca^{2+} network.

Synthetic materials such as poly(glycolic acid), poly(lactic acid) and poly(acrylic acid) are often used in scaffolds for tissue engineering and drug delivery. The inherent biocompatibility and biodegradability of natural polymers, such as proteins, make them ideal components for biomimetic hydrogels; indeed particular protein epitopes may be incorporated to control the release of drugs (Zhu & Marchant 2011; Zhang et al. 2014). The release of drugs from hydrogels is often diffusion limited and fast release requires small, thin sections, however, traditional hydrogels lack mechanical stability and thus are

not always suitable delivery devices (Qiu and Park 2001). Furthermore, tough hydrogels with high fracture energies and extensionality are crucial for strain bearing biomedical applications such as replacement cartilage and bone grafting (J.-Y. Sun et al. 2012). For bigels, the mechanical properties of each component gel works synergistically to endow the gel with mechanical properties beyond those of the parent gels (Sun, Zhao et al. 2012). The development of a tough, protein-only bigel would satisfy the mechanical and biocompatibility shortcomings of traditional hydrogels.

Cavitation rheology (CR) has been shown to measure the modulus of biological and non-biological soft materials, including polyacrylamide gels, the eye lens and vitreous (Kundu & Crosby 2009; Zimmerlin et al. 2010; Cui et al. 2011; Zimmerlin et al. 2007; Chin et al. 2013). Additionally, the cavitation and fracture behaviour of polyacrylamide gels was probed using CR; whereby the network chains can either deform elastically to accommodate a cavitation event or rupture to form via fracture (Kundu & Crosby 2009). Thus, CR is an ideal method to investigate the material properties of a bigel.

4.1.1 Aims of this study

The aim of this study is to use BSA and gelatin to form an all protein bigel; consisting of a discrete network of thermally denatured BSA which has undergone spinodal decomposition and an interpenetrated but discrete second network formed from randomly organised, physically entangled linear gelatin filaments.

4.2 Methods and materials

4.2.1 Reagents

Gelatin B (from bovine skin) and polyethylene glycol 20,000 were purchased from Sigma-Aldrich (St. Louis, MO, USA) and bovine serum albumin was purchased from Fisher Scientific. Solutions of hydrochloric acid, calcium chloride and sodium chloride were prepared using analytical grade reagents purchased from Fisher scientific. Fluorescein isothiocyanate (FITC) and Dylight 633 were purchased from Thermo Scientific. Polyethylene glycol (PEG) 20,000 was purchased from Sigma-Aldrich. All reagents were used without further purification.

4.2.2 Sample Preparation

BSA and gelatin samples ranging in concentration from 10 mg/ml to 200 mg/ml were prepared as outlined below for all experiments with the exception of confocal microscopy. For single protein gels, solutions were made up to the desired final concentration and for double protein gels, stock solutions were made at twice the desired final concentration and mixed in a 50:50 ratio to obtain the desired final concentration. To dissolve the gelatin, the samples were heated to 80 °C (above the melt transition temperature, T_m) for 10 minutes in a water bath. The gelatin was allowed to cool, and was then mixed with the appropriate concentration of BSA. The samples were sealed and placed in a water bath at 80 °C for 1 hour, following which they were cooled at room temperature for 1 hour. Since BSA and gelatin gels are known to cure (form additional bonds over time) it was necessary to ensure that the gels were aged in the same fashion (Tobitani and Ross-Murphy 1997, Tosh, Marangoni et al. 2003). The gels containing PEG were prepared using the same procedure. For the controlled release experiment and swelling/shrinking experiments, sections of gels were cut (7 x 3 mm). These disks were incubated at the indicated temperature in 5 ml of MilliQ water. For the controlled release experiments FITC was added to a final concentration of 0.03 µg/ml during sample preparation, prior to heating.

4.2.3 Differential scanning calorimetry

DSC was used to determine the melt transition temperature of BSA and separately, gelatin. A Perkin Elmer Pyris-6 Differential Scanning Calorimeter (Perkin Elmer, Ireland) was used to conduct the DSC measurements. A 55 µl sample (100 mg ml⁻¹) was prepared and weighed into a large volume stainless steel capsule (Perkin Elmer, Ireland) which was then sealed and analysed. For BSA, the sample was equilibrated at 25 °C for five minutes before the temperature was increased from 25 °C to 95 °C at a scan rate of 1 °C/min. For gelatin, the sample was held at 50 °C for 10 minutes then cooled to 15 °C at 1 °C/min and reheated to 80 °C at the same rate.

4.2.4 Light microscopy

Light microscopy was performed on an Olympus BX61 microscope, equipped with a digital imaging system was used to examine the gels at 100× magnification. Cell^F

software was used to view and record the images and all image analysis was done using ImageJ software (Schneider, Rasband et al. 2012).

4.2.5 Environmental scanning electron microscopy (ESEM)

Standard scanning electron microscopy is used to generate a three-dimensional image of the surface of a specimen. An electron beam is scanned across the surface of the specimen and the image is achieved by detection of the secondary electrons. Since the SEM works under vacuum, biological samples need to be dried prior to analysis otherwise the sample will collapse in the vacuumed chamber. As the freeze drying or lyophilisation of samples is likely to produce artefacts in the gels (Nordestgaard & Rostgaard 1985) environmental SEM was selected rather than conventional SEM. ESEM uses specialised electron detectors and a series differential pumping systems which allows a gaseous environment to be accommodated within the specimen chamber, thereby permitting the imaging of hydrated samples by electron microscopy.

ESEM images were obtained for the parent 90 mg/ml BSA and 100 mg/ml gelatin, and for the 9:10 bigel. The images were obtained using a FEI Quanta 3D FEG DualBeam (FEI Ltd, Hillsboro, USA) at the Nano Imaging and Material Analysis Centre, University College Dublin, Ireland.

4.2.6 Confocal Microscopy

Confocal microscopy uses point illumination and a pinhole conjugate to the focal point, a confocal pinhole, to limit the exposure of the sample to the excitation light and eliminate the emitted light which is out of focus, respectively. Thus, as only fluorescence close to the focal plane is detected, the optical resolution of the image, especially in the depth direction, is greatly enhanced over traditional fluorescence spectroscopy, (Nwaneshiudu et al. 2012). Horizontal and vertical resolutions of 0.2 μm and 0.5 μm , respectively, are achievable using confocal microscopy. (Prasad et al. 2007).

Confocal Microscopy images were obtained for bigels formed from 90 mg/ml BSA and 100 mg/ml gelatin using a Zeiss LSM 710 NLO at the Royal College of Surgeons, Dublin, Ireland.

4.2.7 Labelling proteins with fluorescent dyes

Dylight 633 was used to fluorescently label the BSA (the protein appears red) and fluorescein isothiocyanate (FITC) was used to label the gelatin (protein appears green). FITC and DyLight 333 are both reactive to primary amines. In proteins, primary amines are found at the α -amino group of the N-terminal amino acid and the ϵ -amino group of lysine. A stable amide bond is formed by the conjugation of the dye to the amine, figure 4.5.

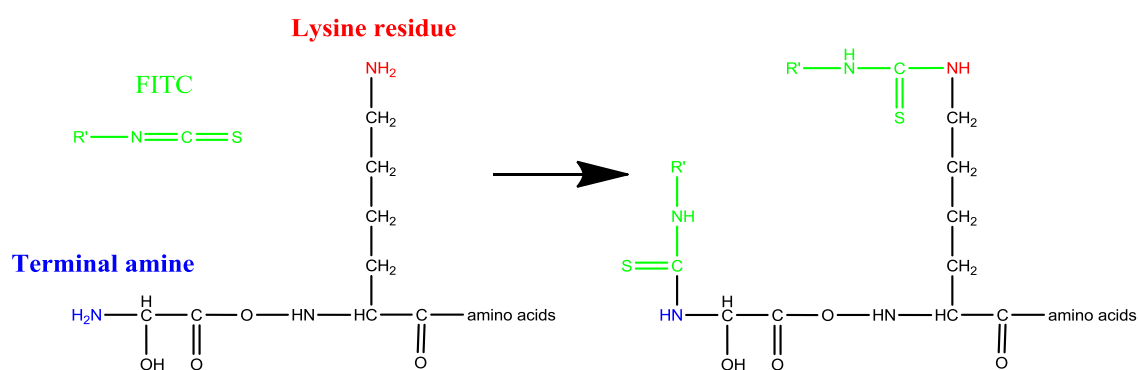


Figure 4.5 Conjugation of FITC to primary amine

A 10 mg/ml, stock solution of FITC was prepared by dissolution of the dye in dimethylformamide (Sigma, St. Louis, MO, USA). 100 μ l of 1 mg/ml gelatine was added to 8 μ l of 0.67 M sodium borate buffer, pH 5.8 (Sigma, St. Louis, MO, USA) and 2 μ l of FITC stock solution. The solution was incubated for 1 hour at room temperature in the dark.

A Dylight 633 NHS Ester Labeling Kit was used to fluorescently label the BSA. 100 μ l of 1 mg/ml BSA was added to the reagent vial and gently pipetted up and down to mix. The vial was centrifuged for 30 seconds to collect the sample at the bottom of the tube. The mixture was allowed to incubate for 1 hour in the dark at room temperature.

The labelled proteins were repeatedly washed by ultrafiltration for 5 minutes, using Amicon Ultra-4 MWCO 10 kDa centrifugal devices at 4,000 x g, until no unbound fluorophore was detected in the filtrate. A final spin at 7,000 x g for 10 minutes was used

to concentrate the protein and the entire sample was used with the addition of unlabelled protein to prepare bigels as indicated above.

4.2.8 Fluorescence measurements

FITC has maximum excitation and emission wavelengths of 495 nm and 519 nm, respectively. DyLight 633 has maximum excitation and emission wavelengths of 638 nm and 658 nm, respectively. Fluorescence measurements were made using a Molecular Devices SpectraMax M2e (Molecular Devices, USA) and Hellma Analytics fluorescent precision cells.

4.2.9 Cavitation rheology (CR)

The cavitation rheology apparatus was set up as in figure 2.5. The cavitation rheology instrument was built in-house and comprises of a syringe pump (New Era) regulating a syringe (Hamilton GASTIGHT®), connected to a pressure sensor (Omega Engineering) and blunt end needles (Fisher scientific). The syringe pump was controlled from a personal computer using a custom written programme using LabVIEW software (National Instruments), which also recorded pressure at the needle tip during the experiments.

4.2.9.1 Calibration of cavitation rheology equipment

The omega pressure transducers (sensors) were calibrated using a hydrostatic method. Hydrostatic pressure is the pressure exerted by a column of fluid (water) due to pressure. The pressure increase is in proportion to the height of the column because of the increasing weight of the fluid exerting downward force from above. This pressure is often measured in pounds per square inch (psi); which can be readily converted to Pascals. A column of water was connected to the sensor as shown in figure 4.6. The height of the column of water was adjusted and the voltage associated with the pressure was recorded.

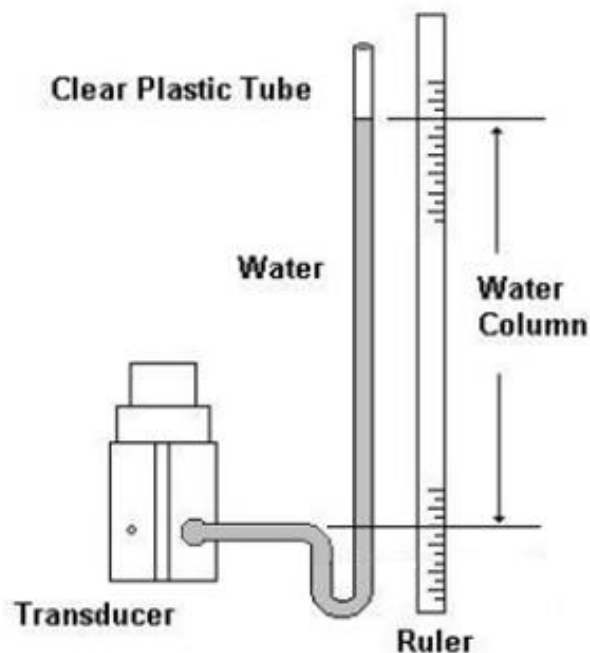


Figure 4.6 Hydrostatic calibration – Known pressure values are induced by a column of water and the response voltage is recorded

4.2.9.2 Typical cavitation rheology experiment

During cavitation rheology a syringe is inserted into the sample and a cavity is formed at the tip by increasing the pressure of the medium within the syringe. The sample was placed on a translation stage, which was adjusted until the needle tip was at the centre of the sample. Compression of the medium within the syringe was then induced at a rate of $400 \mu\text{l min}^{-1}$ when air was used as the cavitation medium and $50 \mu\text{l min}^{-1}$ when water was used for cavitation. The syringe pump was run for multiple pressurization and depressurization cycles to determine the degree of elasticity remaining in the material following deformation.

4.3 Results

4.3.1 Differential scanning calorimetry

Differential scanning calorimetry was used to determine the melt transition temperature (T_m) of BSA. The melt transition temperature was measured at 77.5°C and a sharp exotherm (associated with aggregation) was observed following the denaturation of the protein, figure 4.7. Differential scanning calorimetry was also used to determine the melt transition temperature (T_m) of gelatin. The melt transition temperature was measured at $\sim 27^\circ\text{C}$, figure 4.8

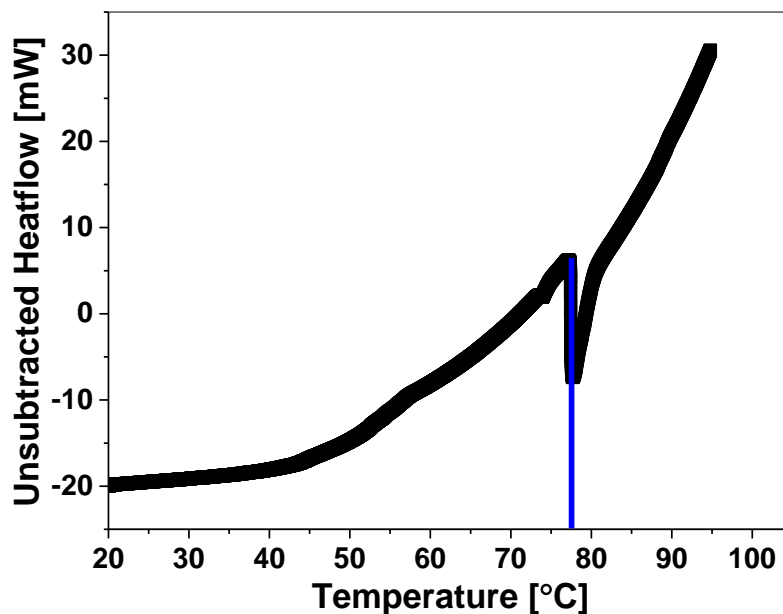


Figure 4.7 DSC of BSA showing T_m of 77.5 °C and a sharp exotherm associated with aggregation following denaturation

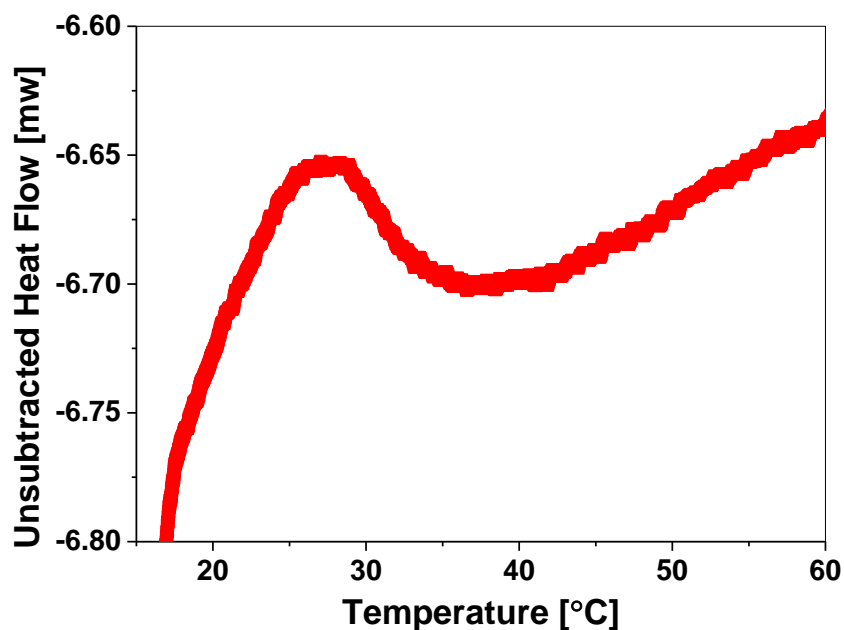


Figure 4.8 DSC of gelatin showing T_m of ~27 °C

4.3.2 Calibration of CR equipment

The omega PX26 series sensors were calibrated using the hydrostatic method. The height of the column of water was adjusted (pressure) and the voltage was recorded. The conversion factor from voltage to pressure is given by the slope of the standard curve.

Thus the conversion factors were 0.003, 0.375 and 0.593 mV/kPa for the Omega 0-10 psi, 0-5 psi and 0-1 psi sensors, respectively (figure 4.9).

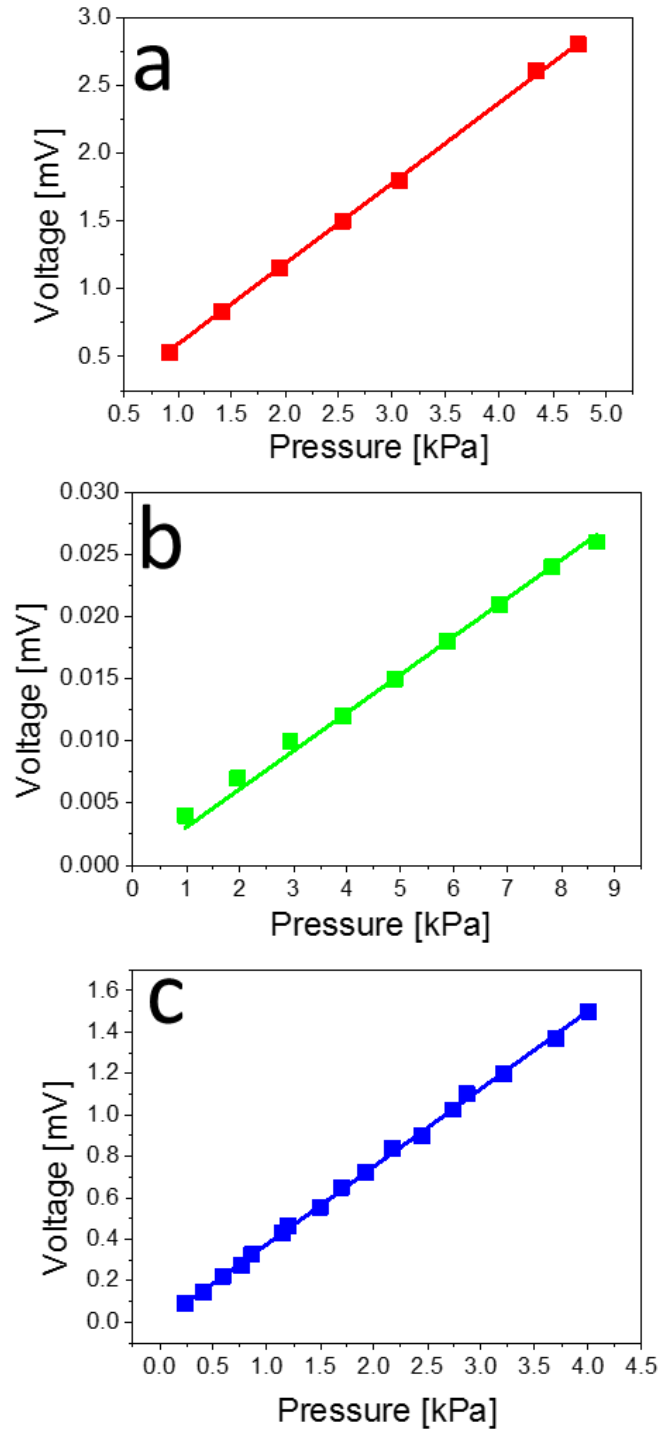


Figure 4.9 Calibration graphs for sensors used for cavitation rheology. a) Omega 0-1 psi b) Omega 0-5 psi c) Omega 0-10 psi

The calibration was validated using a 30 gauge needle; where the internal radius = 0.08 mm and $1/r = 12500 \text{ m}^{-1}$. Since, water is not elastic, the critical pressure (P_c) is related only to the surface tension (γ) and radius (r) of the needle, (Equation 4.2).

$$P_c = 2\gamma / r \quad (\text{Equation 4.2})$$

The surface tension of water at 20 °C is 0.073 mNm^{-1} , (Atkins 2014) and the pressure at which an air bubble should form in water, for this needle radius is 1.82 kPa. Cavitation occurred at 0.0057 mV or 1.9 kPa.

4.3.3 BSA only gels

Single component BSA gels were prepared, over a range of protein concentrations from 10 to 190 mg/ml. Given that the partial specific volume of BSA is $0.73 \text{ } \mu\text{l mg}^{-1}$, these gels had a BSA volume fraction (ϕ_{BSA}) ranging from 0.007 to 0.139 (Brown et al. 2011). Below a volume fraction of 0.059, the gels were transparent and very weak with elastic moduli in the region of 1 kPa, table 4.1.

Table 4.1 Table of elastic moduli for gels formed from various concentration of BSA and gelatin.

% Gelatin	E_{gelatin} [kPa]	% BSA	E_{BSA} [kPa]	E_{bigel} [kPa]
0	-	< 9	~1	-
0	-	9	3.2	-
0	-	11	3.4	-
0	-	13	10.1	-
0	-	19	52.2	-
10	2.8	0	-	-
19	10.5	0	-	-
10	2.8	9	3.2	24.3

At higher protein concentrations, $\phi_{\text{BSA}} = 0.066$, more stable gels formed and the elastic modulus increased to $\sim 3.2 \text{ kPa}$, figure 4.10. An increase in the error bars was observed as the r value decreased, which may be related to network anisotropy at these length-scales. As the concentration increased above $\phi = 0.118$ opaque gels formed, figure 4.11. At volume fractions of $\phi_{\text{BSA}} = 0.139$ (190 mg/ml), gels with an elastic modulus of 52.2 kPa were observed, figure 4.12.

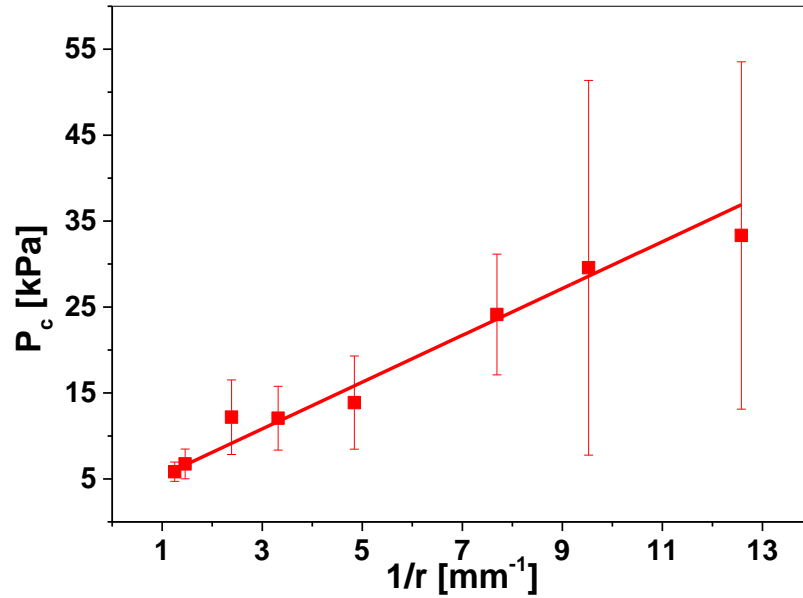


Figure 4.10 The elastic modulus $\phi_{\text{BSA}} = 0.066$ (90 mg ml^{-1} BSA) was found to be 3.2 kPa, using cavitation rheology

As the concentration increased above $\phi = 0.118$ opaque gels formed, figure 4.11.

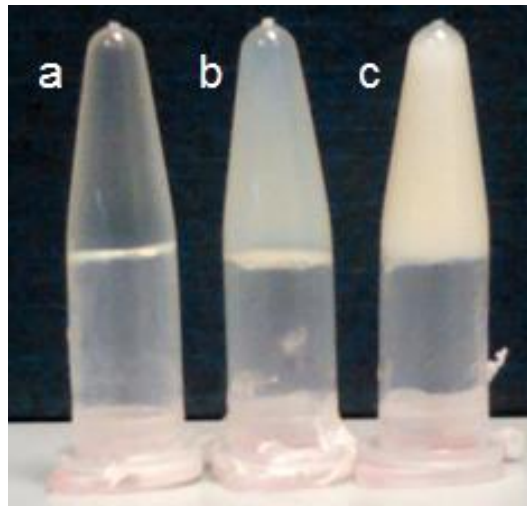


Figure 4.11 BSA gels transition from being transparent at a) $\phi_{\text{BSA}} = 0.066$ (90 mg ml^{-1}) to opaque at b) $\phi_{\text{BSA}} = 0.118$ (160 mg ml^{-1}) and this opacity increases with increasing BSA concentration, c) $\phi_{\text{BSA}} = 0.133$ (180 mg ml^{-1}).

At volume fractions of $\phi_{\text{BSA}} = 0.139$ (190 mg/ml), gels with an elastic modulus of 52.2 kPa were observed, figure 4.12. Visual observation indicated that fracture had occurred.

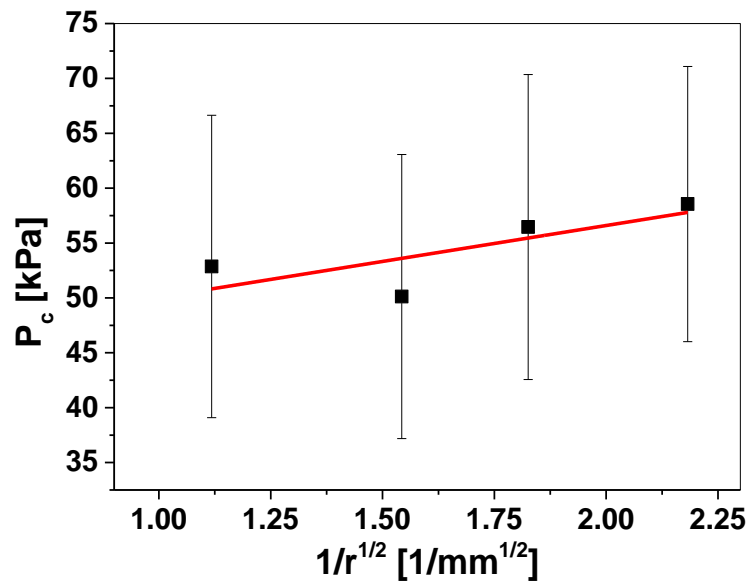


Figure 4.12 The elastic modulus $\phi_{\text{BSA}} = 0.139$ (190 mg ml^{-1} BSA) was found to be 52.2 kPa. P_c scaled linearly with $r^{-1/2}$, indicative of the primary mechanism for deformation occurring due to fracture

Cavitation rheology has previously been used to investigate the elasticity and fracture behaviour of synthetic hydrogels (Kundu & Crosby 2009). Elastic deformation (cavitation) may be differentiated from fracture by monitoring the critical pressure over several successive pressurization and depressurization cycles. Furthermore, where the deformation process proceeds via fracture propagation, the critical pressure scales linearly with $r^{-1/2}$. In addition, cavitation rheology can be used to characterise the properties of a hydrogel over a range of length scales, ranging from μm to mm . For 90 mg/ml BSA gels ($\phi = 0.066$), partial reversibility of the cavitation process (60 – 70%) was measured for larger needle radii ($r = 0.42 \text{ mm}$ and 0.17 mm) during the second pressurisation cycle (figure 4.13) although the P_c did decrease further with subsequent cycles. For gels formed at $\phi_{\text{BSA}} \geq 0.111$ the deformation mechanism proceeded by irreversible fracture rather than cavitation, as shown by the scaling relationship in figure 4.12.

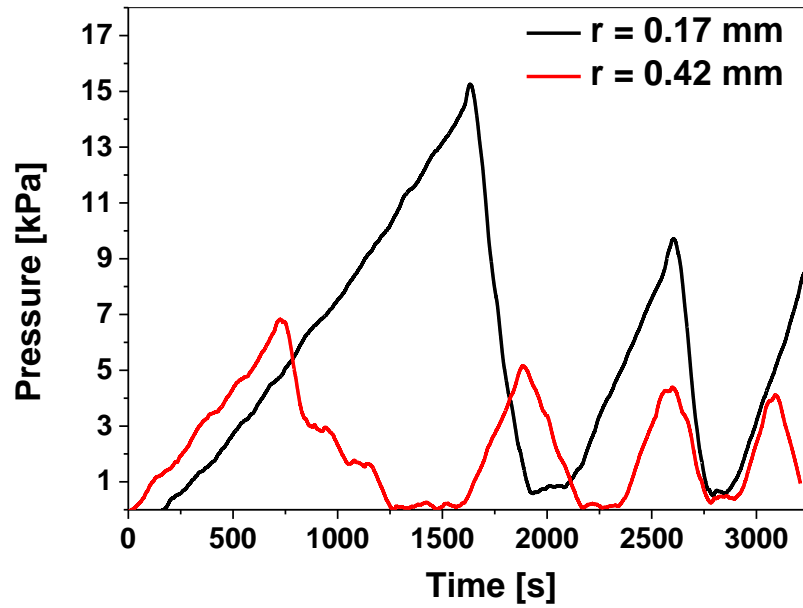


Figure 4.13 Cavitation rheology $\phi_{\text{BSA}} = 0.139$ (190 mg ml^{-1} BSA) shows the deformation process is partially (60-70 %) reversible, ϕ = Volume fraction

4.3.4 Gelatin only gels

Gels were formed from gelatin type B over a range of concentrations $\phi_{\text{gelatin}} = 0.029$ to $\phi_{\text{gelatin}} = 0.139$ (40 to 190 mg ml^{-1}). At $\phi_{\text{gelatin}} \leq 0.022$ (30 mg ml^{-1}) the solution remained liquid-like. All the gelatin only gels were transparent. The elastic moduli of the gels were measured to range from 2.8 to 10.5 kPa ($\phi_{\text{gelatin}} = 0.073$ to $\phi_{\text{gelatin}} = 0.139$, respectively), which is consistent with previous work, (Djabourov 1988) and shown in, figure 4.14 and table 4.1. For these gels, the critical pressure scaled linearly with $r^{-1/2}$, indicating that the deformation proceeds by irreversible fracture, figure 4.14.

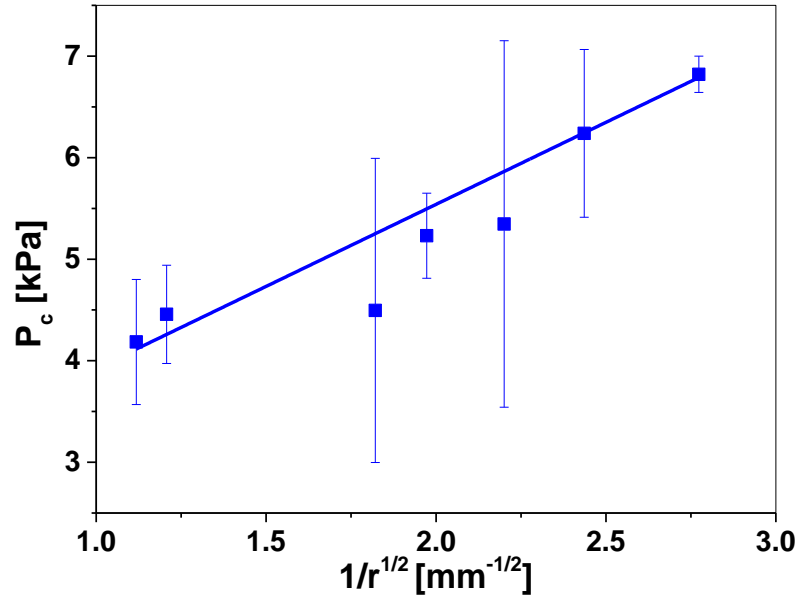


Figure 4.14 The elastic modulus of $\phi_{\text{gelatin}} = 0.073$ (100 mg ml⁻¹ gelatin) was found to be 2.8 kPa, using cavitation rheology.

4.3.5 BSA and gelatin gels

4.3.5.1 Light microscopy of bigels

Gels were formed from mixtures of BSA and gelatin; the concentration of gelatin was fixed at $\phi_{\text{gelatin}} = 0.073$ (100 mg ml⁻¹) and the BSA concentration was varied between $\phi_{\text{BSA}} = 0.007$ to 0.066 (10 to 90 mg ml⁻¹). All bigels were turbid. At lower BSA concentrations, $\phi_{\text{BSA}} = 0.007$ (10 mg ml⁻¹), light microscopy of these gels showed clusters of spherical aggregates; these transitioned to a percolated network at $\phi_{\text{BSA}} = 0.029$ (40 mg ml⁻¹), figure 4.15.

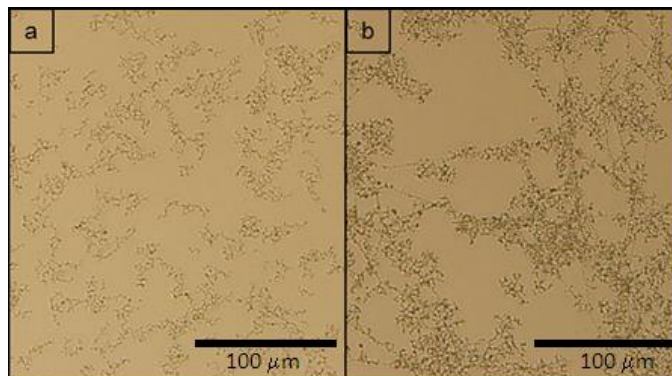


Figure 4.15 Light microscopy image of gels formed from $\phi_{\text{gelatin}} = 0.073$ (100 mg ml⁻¹) and a) $\phi_{\text{BSA}} = 0.007$ (10 mg ml⁻¹), b) $\phi_{\text{BSA}} = 0.029$ (40 mg ml⁻¹) showing the transition from clusters to a percolated network of spherical aggregates.

4.3.5.2 Cavitation rheology of bigels

Using cavitation rheology, the elastic modulus of these gels were determined, table 4.1. The most robust gels formed at a 9:10 BSA/gelatin weight ratio and these gels were further probed to examine their mechanical properties and microstructure. Using cavitation rheology, the elastic modulus of these gels was determined to be 24.3 kPa, figure 4.16. To determine whether the enhanced mechanical properties were simply as a result of the increased total volume fraction, gels containing BSA and PEG 20,000 were prepared in the same manner and in the same proportions (9:10), $\phi_{BSAPEG} = 0.141$. These gel were transparent and had no significant increase in elastic modulus compared to the BSA only gel, $\phi_{BSA} = 0.066$ (90 mg ml⁻¹ BSA).

To probe the mechanical properties of the 9:10 BSA:Gelatin gels further ($\phi_{Bigel} = 0.141$), the deformation process was investigated using successive pressurization and depressurization cycles. These measurements indicate that the deformation process is predominantly elastic. In fact, the critical pressure returns to 60-70% of the original value during the second and subsequent (up to 4) pressurisation cycles, figure 4.17.

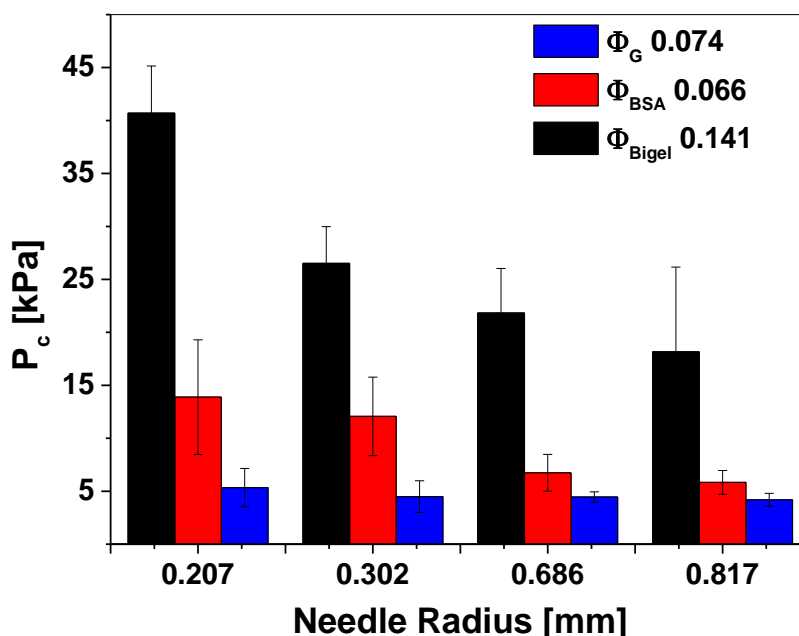


Figure 4.16 Comparison of the critical pressure for $\phi_{gelatin} = 0.073$ (100 mg ml⁻¹ gelatin), $\phi_{BSA} = 0.066$ (90 mg ml⁻¹ BSA) and $\phi_{Bigel} = 0.141$ (9:10 BSA:Gelatin) for different needle radii.

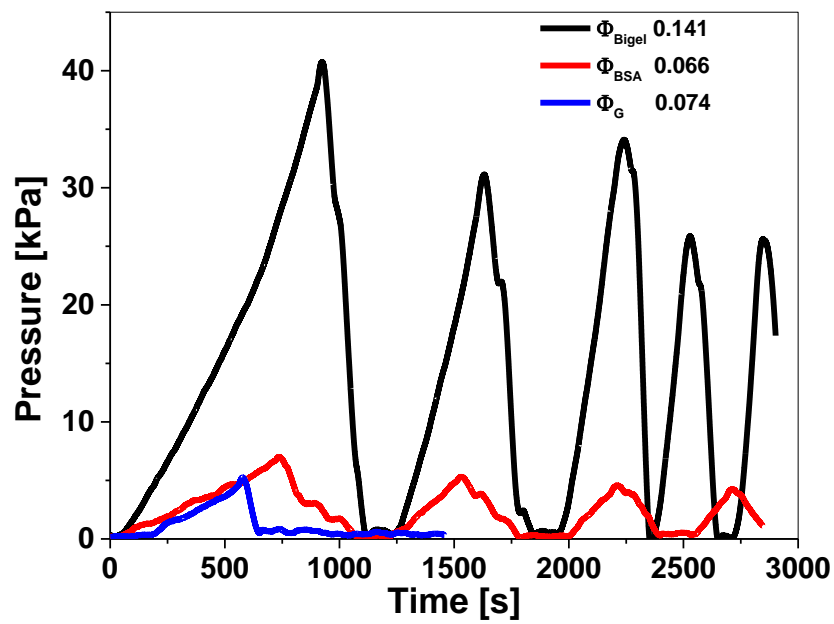


Figure 4.17 Cavitation rheology of bigel show the deformation process is partially (60-70 %) reversible.

4.3.5.3 Environmental Scanning Electron Microscopy of bigels

ESEM was used to examine the microstructure of these gels. The ESEM images indicate that the gel surface consists of a percolated network of spherical structures of $\sim 1 \mu\text{m}$ in diameter, figure 4.18, consistent with the sizes observed by light microscopy, figure 4.15.

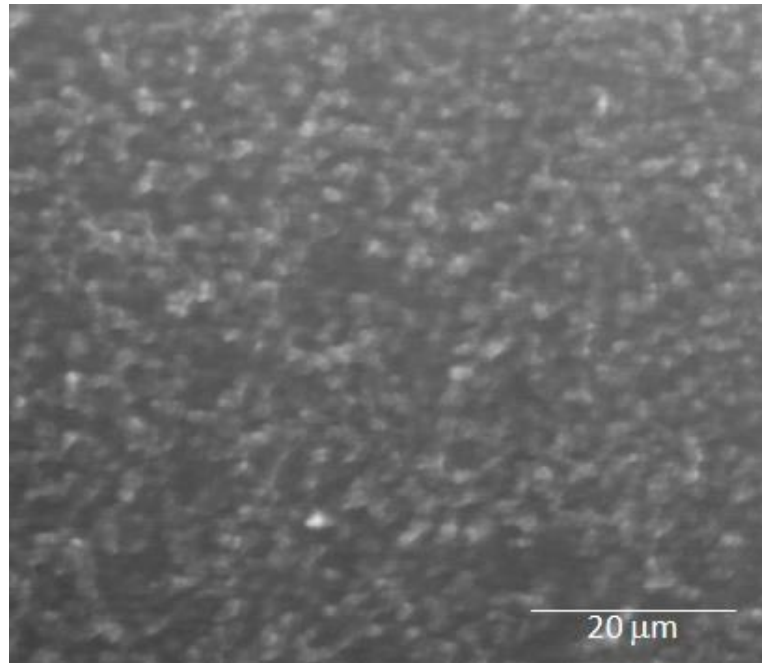


Figure 4.18 Environmental scanning electron micrograph of gel formed from $\phi_{\text{Bigel}} = 0.141$ [$\phi_{\text{gelatin}} = 0.073$ (100 mg ml⁻¹ gelatin), $\phi_{\text{BSA}} = 0.066$ (90 mg ml⁻¹ BSA)] showing a surface composed of 1-2 μm spheres.

4.3.5.4 Confocal microscopy of bigels

Confocal microscopy was also used to examine the microstructure of these gels. For the confocal images, the gelatin was labelled with fluorescein isothiocyanate, FITC, and the BSA was labelled with Dylite 633. Thus, the gelatin appears green and the BSA appears red. The BSA network appears as a branched structure of connected spherical aggregates, figure 4.19 a and d. Whereas for the gelatin gel no distinct structural features were observed, figure 4.19 b and e. When the confocal images of BSA and gelatin were overlaid, a discrete spatial distribution of the two protein networks was observed, figure 4.19 c and f. A fracture point was captured in the confocal images. The BSA particle gel bridges the gap at the fracture point, whereas the gelatin component of the gel is irreversibly fractured, figure 4.19 bottom d, e and f.

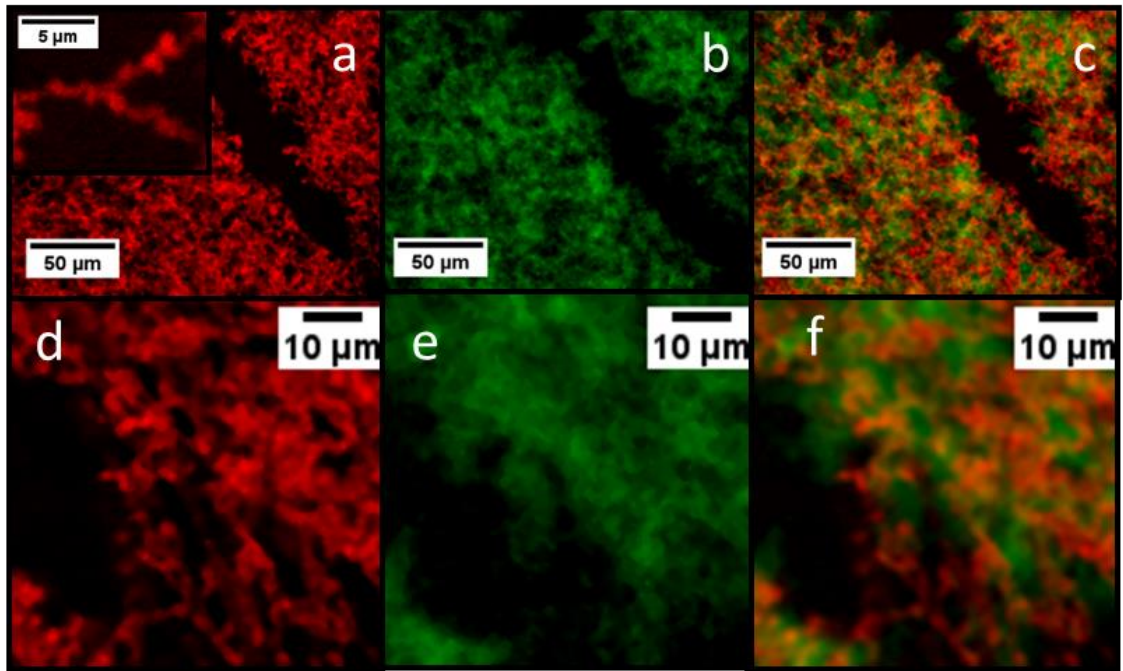


Figure 4.19 Confocal micrograph 20x magnification $\phi_{\text{Bigel}} = 0.141$ [$\phi_{\text{gelatin}} = 0.073$ (100 mg ml⁻¹ gelatin), $\phi_{\text{BSA}} = 0.066$ (90 mg ml⁻¹ BSA)]. Gelatin labelled with FITC appears green, BSA labelled with Dylight 633 appears red. Insert in panel 1 is at 100x magnification. The overlay of the two images indicates that the gel networks are discrete but interpenetrating.

4.3.5.5 Thermo-responsive behaviour of bigels

The thermo-responsiveness of the bigels was investigated by comparing the swelling of these gels in excess water at room temperature, 4 °C and 37 °C. At 4 °C and at room temperature, the gels swell in the presence of excess liquid, figure 4.20. However, at 37 °C, there is a remarkable transition to shrinking behaviour.

The temperature controlled release experiments showed that FITC release was greatest at 37 °C and least at 4 °C. An intermediate amount was released at room temperature (~ 23 °C). The release was sustained over a 48 hour period, figure 4.21.

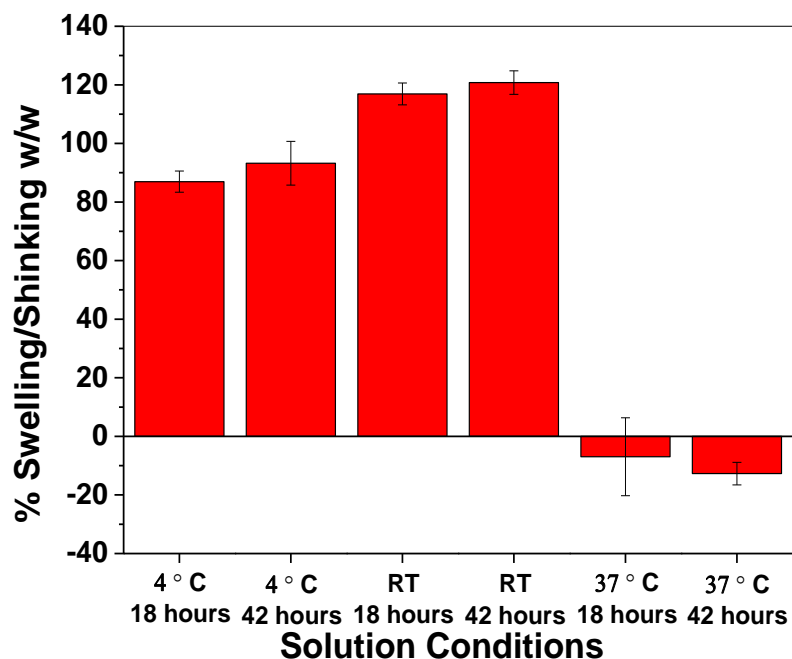


Figure 4.20 Swelling/shrinking behaviour of $\phi_{\text{Bigel}} = 0.141$ [$\phi_{\text{gelatin}} = 0.073$ (100 mg ml⁻¹ gelatin), $\phi_{\text{BSA}} = 0.066$ (90 mg ml⁻¹ BSA)] in response to heat treatment over 18 and 2 hours.

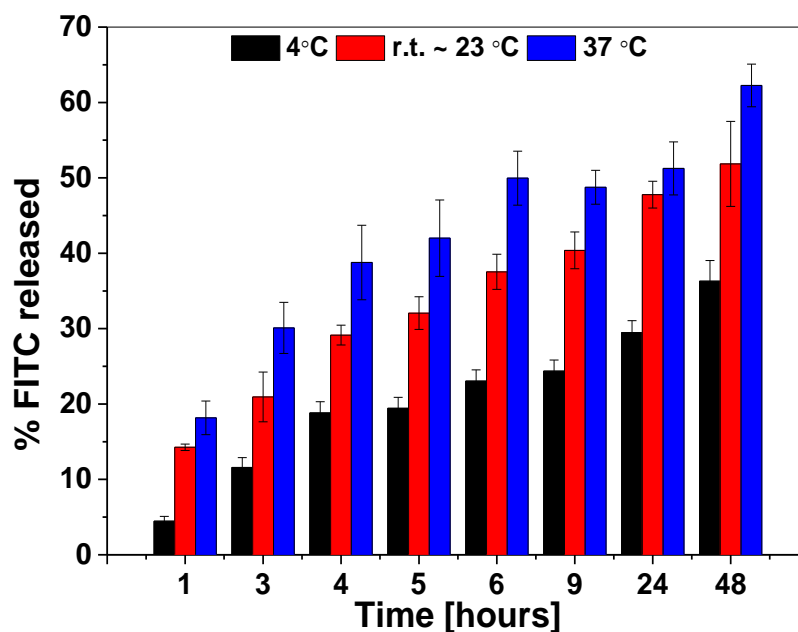


Figure 4.21 FITC release profile for the $\phi_{\text{Bigel}} = 0.141$ [$\phi_{\text{gelatin}} = 0.073$ (100 mg ml⁻¹ gelatin), $\phi_{\text{BSA}} = 0.066$ (90 mg ml⁻¹ BSA)] indicating improved release of FITC at physiological temperature.

4.4 Discussion

Cavitation rheology was used to investigate the mechanical properties of the various gels. Stable, transparent, single component BSA gels only formed at $\phi_{\text{BSA}} \geq 0.066$ (90 mg ml⁻¹

¹). These gels had an elastic modulus of ~ 3.2 kPa and the deformation induced in these gels was 60-70% elastic. As the concentration of BSA was increased to $\Phi_{\text{BSA}} = 0.118$, the gels became somewhat opaque and this opacity increased with further increases in concentration. In addition, as the BSA concentration increased, the strength of the gels increased and at $\Phi_{\text{BSA}} = 0.139$ (190 mg/ml) an elastic modulus of 52.2 kPa was measured. The deformation process for these gels proceeded by a fracture (only) mechanism.

In addition, the elastic modulus of gelatin was probed. As with BSA, increasing the volume fraction of gelatin, increased the elastic modulus of the gelatin gels. Below a volume fraction of 0.059, the gels were transparent and very weak with an elastic modulus the region of 1 kPa, table 4.1. These gels were transparent and the deformation proceeded by a fracture mechanism. Thus, although stronger gels were made from higher volume fraction BSA as a single component, the gels were brittle which is an undesirable characteristic for hydrogels where a strain bearing application requires extensionality or elasticity.(J.-Y. Sun et al. 2012).

The mechanical properties of each component gel within a bigel have been shown to work synergistically to endow bigels with mechanical properties beyond those of the parent gels (Sun, Zhao et al. 2012). The development of a tough, protein-only bigel would satisfy the mechanical and biocompatibility shortcomings of traditional hydrogels. BSA and gelatin type B were selected as the proteins from which to make the bigel. These proteins have an isoelectric point of 4.7 and 4.7-5.2, respectively (Ge et al. 1998; Bhattacharjee & Bansal 2005). Therefore, there is no charge attraction between the two components in solution; a necessary prerequisite since the two networks within the bigel must remain discrete. Above the melt transition temperature for gelatin, ~27 °C, the peptides adopt a random coil secondary structure, whereas below T_m the secondary structure is helical. Thermoreversible gels are formed by the physical entanglement of strands upon cooling (Bhattacharjee and Bansal 2005). Above the melt transition temperature of BSA, 77.5 °C, the protein is unfolded and hydrophobic residues become exposed to the solvent, water.

At a certain temperature and concentration, liquid-liquid phase separation will occur in order to minimise the free energy of the system. When the free energy barrier is low, this phase separation proceeds via spinodal decomposition, occurring rapidly and

uniformly throughout the initial phase (Gibaud & Schurtenberger 2009). At certain quench rates and for certain quench temperatures, spinodal decomposition may become dynamically arrested, resulting in the formation of a gel composed of space-spanning clusters (Zaccarelli 2007).

By heating the gelatin above its melt transition temperature and mixing this with a BSA solution (below its melt transition temperature), a homologous, two-protein solution is prepared. Light microscopy, ESEM and confocal microscopy all indicate that a percolated network of spherical BSA aggregates about 1-2 μm in diameter is formed upon heating this mixture to 80 $^{\circ}\text{C}$, above the melt transition temperature of BSA. This is consistent with the length scale of dynamically arrested clusters formed by the arrested spinodal decomposition of lysozyme solutions (Gibaud & Schurtenberger 2009). Thus upon heating to 80 $^{\circ}\text{C}$ a gel composed of a percolated network of BSA is formed. Upon cooling, the gelatin peptides transition from a coil to a helix conformation, forming a second, discrete, physical entangled gel around the BSA gel. The independent nature of the gelatin gel is confirmed by the discrete spatial distribution of the gelatin gel in the confocal images. Thus, an all-protein, bigel composed of two discrete interpenetrating networks was formed by spinodal decomposition of unfolded protein, figure 4.22.

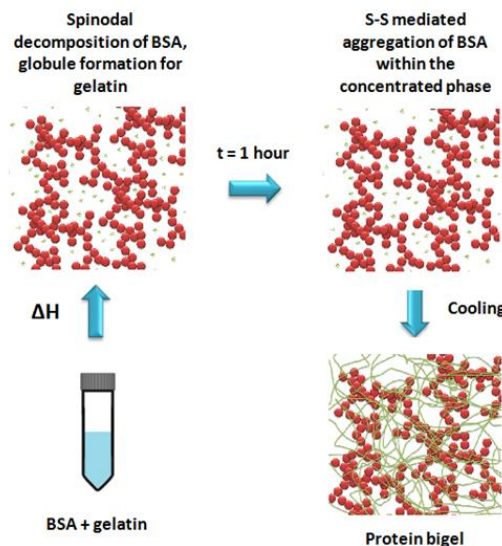


Figure 4.22 The proposed mechanism for the formation of a protein bigel. The two component proteins are mixed and the BSA gels are formed by the arrested spinodal decomposition of BSA, above its melt transition temperature, T_m . Upon cooling, a second, discrete, interpenetrating gel is formed by the gelatin around the BSA gel.

Mixtures of BSA and gelatin were prepared where the concentration of gelatin was held constant at $\Phi_{\text{gelatin}} = 0.073$ (100 mg ml⁻¹) and the concentration of BSA was varied from $\Phi_{\text{BSA}} = 0.007$ to 0.66 (10 to 90 mg ml⁻¹). All of the gels were turbid. The microstructure of these gels was probed using light microscopy. Clusters of spherical aggregates were observed for mixtures of $\Phi_{\text{gelatin}} = 0.073$ (100 mg ml⁻¹ gelatin) and $\phi_{\text{BSA}} \leq 0.029$ (40 mg ml⁻¹ BSA). When the concentration of gelatin was increased beyond this value, the clusters formed a percolated network. The most robust gels ($E = 24.3$ kPa) were formed at $\phi_{\text{Bigel}} = 0.141$ [$\Phi_{\text{gelatin}} = 0.073$ (100 mg ml⁻¹ gelatin), $\phi_{\text{BSA}} = 0.066$ (90 mg ml⁻¹ BSA)]. This is significantly higher than the elastic modulus of either parent gel at their individual concentration and four times greater than their combined elastic moduli.

The deformation process was investigated by measuring successive pressurization and depressurization cycles using CR. Surprisingly, these measurements indicate that the deformation process has a significant elastic contribution of between 60 and 70% and this elasticity was maintained for up to four pressurisation cycles. Gelatin $\phi_{\text{gelatin}} = 0.073$ (100 mg ml⁻¹) is subject to irreversible fracture following a cavitation event across the full range of needle radii that were probed. BSA only gels with $\phi_{\text{BSA}} = 0.066$ (90 mg ml⁻¹) exhibited partial reversibility, but these gels were much weaker than the bigel (3.4 kPa and 24.3 kPa, respectively). Therefore the protein bigel exhibited both improved resistance to deformation and a superior retention of elasticity following multiple deformation cycles.

The confocal images may point to the origin of these enhanced mechanical properties. At a fracture point in the bigel, only the gelatin has fractured. The structure of the BSA particle gel remains intact, bridging the gap between the fractured portions of the bigel. This is reminiscent of the double network gel produced by the Suo group from alginate and polyacrylamide, (J. Y. Sun et al. 2012). These gels rely on the polyacrylamide network bridging a crack which stabilises deformation while unzipping of the alginate network over a large region of the gel dissipates energy.

Following the initial cavitation event in the bigel, which irreversibly fractures the gelatin component, a BSA particle gel structure remains with an estimated elastic

modulus of ~ 17 kPa, which is greatly in excess of that for the single component gel at the same concentration (~ 3.4 kPa). These results follow the numerical simulations from the Foffi group whereby a bigel network formed from colloidal particles functionalised by single stranded DNA indicates that bigels can withstand increased stress compared to single component gels (Di Michele et al. 2014). It appears that the enhanced mechanical properties of the protein bigel may be due to a change in the behaviour of the BSA particle gel in the presence of gelatin.

In an attempt to identify the source from which the enhanced mechanical properties are derived, additional gels were prepared at the same volume fraction as the bigel, $\phi_{\text{bigel}} = 0.141$. In the first mixture the gelatin was replaced by polyethylene glycol with a molecular weight of 20,000 g/mol (PEG 20,000). PEG 20,000 was selected to replace gelatin since the gelatin type B used in these experiments had a bloom value of 70. Given that the bloom number is proportional to the average molecular mass of the component strands (Lai 2009), a bloom value is equivalent to a molecular weight of between 20,000 and 25,000 g mol⁻¹. In addition, the melting point of PEG 20,000 is between 63 and 66 °C, below the melting point of BSA, as is required for the first step of forming a homologous binary solution. The BSA-PEG gels were transparent and the elastic modulus was not increased with respect to the elastic modulus of the BSA only gel. Therefore, the enhanced mechanical properties of the BSA/gelatin bigel was not simply due to the increased overall volume fraction. A second gel was prepared at $\Phi = 0.141$ and contained only BSA. While these gels had a higher elastic modulus than the BSA/gelatin gels at the same volume fraction, the deformation is not elastic and the gels fracture irreversibly upon deformation.

The bigels exhibited a potentially useful, thermo-responsive behaviour. At and below room temperature the gels swell in the presence of excess water whereas, at 37 °C there is a dramatic transition to shrinking behaviour figure 4.20. A potential use as a drug delivery agent could therefore be envisaged. FITC was used as a model, hydrophobic small molecule drug. The FITC was loaded into the gel during formation and a temperature induced release profile was generated figure 4.21. A higher concentration of FITC is released at physiological temperatures.

Since a bigel is formed from two percolated, interpenetrating but discrete networks, it follows that the inter-species attraction must be negligible compared to the intra-molecular interactions between the component species. Experimentally, this was elegantly achieved for colloids which were coated with single stranded DNA (Varrato et al. 2012). The single stranded DNA coatings were designed such that pairings could only take place between particular colloids. When using proteins as the bigel components, this selective interspecies attraction needs to be considered, to ensure that the bigelation conditions are realised. Here, this is achieved through the specific chemistry of each protein, the solution conditions and the kinetics of the reaction.

The solution conditions were chosen such that gelatin is close to its isoelectric point – resulting in a net charge close to zero for the gelatin component. Some residual charge remained for the BSA ($pI = 4.7$) preventing its self-aggregation in the initial solution. When the solution was heated above the melt transition temperature the BSA abruptly unfolds, deep within the spinodal region of its phase diagram. Spinodal decomposition arrests and a percolated network is formed. This was observed for $\phi_{\text{bigel}} \geq 0.102$ where $\phi_{\text{gelatin}} = 0.073$ and $\phi_{\text{BSA}} \geq 0.029$. The homogeneity in the BSA gel particle size strongly suggests that spinodal decomposition is the mechanism producing the BSA gel. Since spinodal decomposition occurs rapidly and uniformly throughout the initial phase, the particle size should be homogenous, unlike the broad distribution in particle size associated with a nucleation and growth mechanism. Furthermore, spinodal decomposition must precede BSA self-aggregation in the unfolded state to ensure that this homogeneous particle size distribution occurs. If amorphous aggregate formation occurred first, then a heterogeneous structure would result.

The question is then why gelatin, which is in a molten globular state under these conditions, does not associate with the BSA at this point. Previous studies have shown that unfolded BSA forms irreversible aggregates via covalent inter-molecular disulphide bonds (Havea et al. 2004) and it is proposed that within the BSA clusters, formed by arrested spinodal decomposition, irreversible aggregation occurs. Gelatin does not have cysteine residues and will not form covalent, disulphide bonds with the BSA. Furthermore, gelatin is primarily hydrophilic, both above and below its melt transition temperature and therefore inter-species attraction driven by hydrophobic amino acids is

minimised. (Bhattacharjee & Bansal 2005). In addition, the bigel becomes opaque at 80 °C before the gelatin network forms, which indicates that spinodal decomposition of the BSA is complete before gelatin gel formation. Once the BSA gelation is complete and upon cooling, the gelatin is free to form a discrete and interpenetrating network around the pre-existing BSA network. Given these conditions, there is a definite mechanism by which bigelation can occur and this is supported by the experimental evidence from the confocal images and cavitation rheology data. The confocal images show a discrete spatial distribution of the two proteins components including a separation of the networks at a fracture tip and the cavitation rheology data shows the same scaling in mechanical behaviour as the previously described DNA bigels (Di Michele et al. 2014). Furthermore, the density at which bigel formation occurs ($\phi_{\text{Bigel}} = 0.141$), and composition of the material ($\phi_{\text{BSA}}/\phi_{\text{Bigel}} = 0.47$), are within the region of the phase diagram in which two dynamically arrested interpenetrating gels are predicted to form (Varrato et al. 2012).

4.5 Conclusions

BSA and gelatin were used to form an all protein bigel; consisting of a discrete network of thermally denatured BSA which has undergone spinodal decomposition and an interpenetrated but discrete second network formed from randomly organised, physically entangled, linear gelatin filaments. Cavitation rheology was used to demonstrate the enhanced mechanical properties of the bigel in comparison with the individual gels from which it was composed, with the bigel being stronger than either of the parent gels and remaining mechanically elastic over successive deformation cycles. Confocal images suggest this is due to the synergistic interactions between the two networks. In addition, this biocompatible material was shown to have thermo-responsive behaviour that has clear applications for the material to be used as a drug delivery vehicle as demonstrated by the release of FITC at 37 °C, over a sustained period. The gel may be placed in a solution of bioactive molecules to allow the uptake of the molecules, then placed in vivo where there is release of the drug due to the shrinking of the gel and the ejection of the molecules into the surrounding tissue.

Upon heating above the melt transition temperature, the BSA unfolds (or partially unfolds) leading to the exposure of hydrophobic amino acid that are normally buried within the folded structure. This leads to increased attractive hydrophobic interactions

between the protein molecules and the formation of amorphous (non-amyloid) aggregates. The unfolded protein displays an inverse solubility with temperature and exhibits a lower critical solution temperature (LCST) not unlike that of poly (N-isopropylacrylamide), often used a protein proxy due to the peptide bonds on its side chains (Algaer & van der Vegt 2011; Du et al. 2010). This behaviour has been shown to be driven by entropic restriction of the solvent exposed hydrophobic residues in the heat denatured conformation (Heskins & Guillet 1968; Cardinaux et al. 2007).

Thus, it has been shown that by adjusting the solution conditions to promote selective interspecies attractions between proteins an all protein bigel was formed. The confocal microscopy images confirm bigel formation and an energy dissipation mechanism which accounts for the enhanced rheological properties of the bigel, as originally suggested by Sun *et. al.* for synthetic double network gels (Sun, Zhao et al. 2012).

Chapter 5 The Mechanical Properties of Spheroids

5.1 Introduction

How cells form living tissues and organisms has been a central issue in science for many centuries; indeed, our understanding of embryogenesis has moved on considerably from preformation theory, where organisms were thought to develop from miniature versions of themselves, to neof ormation or epigenesis, where the organism develops gradually from an undifferentiated mass of cells (Gardner et al. 2003). It is now known that in order to form mature tissues and organisms, cells must grow, differentiate and self-organise in both a spatial and temporal manner and these processes have been shown to be regulated by changes in cell adhesion (Barone & Heisenberg 2012), interfacial tension (Manning et al. 2010), the mechanical properties of the microenvironment of the cell (Banerjee et al. 2009) and signalling molecules (Stratman et al. 2011). Tumorigenesis, on the other hand, occurs when these control mechanisms become dysregulated (Weinber 2013). Furthermore, it has also been shown that biomechanics are strongly influential in the processes of tissue degeneration and repair (Chang & Buehler 2014; Amiel et al. 2009). Therefore, it is important to understand the fundamental biophysical phenomena involved in these processes, at multiple length-scales, since strategies to replace or regenerate injured or diseased tissue are limited by and incomplete understanding to the mechanical properties of normal tissues (Schiele et al. 2015).

The bulk biophysical properties of tissues emerge in a complex manner from the properties of the individual components and the interplay between these components, across multiple length scales, (Muiznieks & Keeley 2013). The biophysical properties of the cytoskeleton and cell membrane determine the mechanical properties of individual cells in isolation, while the material properties of multicellular aggregates and tissues arise through complex associations of cell adhesion molecules with each other, the cytoskeleton and the extracellular matrix, (Marturano et al. 2013; Schiele et al. 2015). For example, Kuo and co-workers recently conducted experiments on embryonic chick tendons and demonstrated that the elastic modulus increases as a function of developmental stage (Marturano et al. 2013). Furthermore, it was demonstrated (using atomic force microscopy) that while crosslinking of the collagen fibers in the extracellular matrix contribute significantly to the elastic modulus during late embryonic stages, this is not the case in the early embryonic stages where a well-organised actin cytoskeleton increases the elastic modulus (Marturano et al. 2013; Schiele et al. 2015).

Recent advances in embryogenesis suggests that the interfacial tension between cells provides a significant contribution to the overall mechanical properties of cellular materials (Manning et al. 2010; Foty & Steinberg 2005; David et al. 2014; Brasch et al. 2012). Two theories regarding the origin of tissue surface tension have been proposed; the older, differential adhesion hypothesis (DAH) (Steinberg 1963; Foty & Steinberg 2005; Harris 1976) and the more recent, differential interfacial tension hypothesis (DITH) (Graner 1993; Brodland 2003; Manning et al. 2010). Whereas, DAH considers only the relationship between adhesive energy and surface tension, DITH also recognises a contribution from cortical tension (the ratio of adhesion tension to cortical tension ((tension conferred by a layer of actin beneath the cell membrane)) that determines the overall surface tension. The cortical tensions of individual cells have been reported to range between 10^{-3} and 10^{-5} mNm⁻¹ (Cartagena-Rivera et al. 2015; Hochmuth 2000; Peukes & Betz 2014; Evans & Yeung 1989; Chaigne et al. 2015) while tissue interfacial tensions have been measured at ~ 1.6 to 20 mNm⁻¹ (Foty et al. 1996; Guevorkian et al. 2010; Mgharbel et al. 2009; Manning et al. 2010). Measurements of the elastic modulus for a variety of cell types have also been determined, using methods such as such as Atomic Force Microscopy (AFM) and Micropipette Aspiration. For epithelial cells Young's modulus values range from 150 to 10,000 Pa, depending on the method used, the cell type and the region of the cell probed (whole cell, cytoplasm or nucleus) and the experimental conditions, table 5.1.

Understanding the role of cortical and adhesion tension during embryogenesis is the first step towards tuning these interactions (Stirbat et al. 2013) and opens the door to the directed self-organisation of cells in artificial tissues (Athanasίου et al. 2013; Stirbat et al. 2013). Changes in the expression of adhesion proteins and the resulting change in cortical tension have been associated with the progression of cancer and metastasis, the dissociation of cancer cells from a primary tumour (Brodland & Veldhuis 2012; Logue et al. 2015; Bose et al. 2010; Bendas & Borsig 2012). Thus, the ability to measure cortical tension and adhesive energy could lead to advances in a number of different but interrelated fields.

Table 5.1 Young's elastic modulus measurements for different cell types

Cell type	Method	Young's Modulus (Pa)	Reference
Human aortic endothelial cell	AFM	1,000 – 5,000	(Costa et al. 2006)
Porcine/murine cerebral capillary endothelial cells	AFM	5,000	(Schrot et al. 2005)
Human umbilical vein endothelial cell	AFM	5,000-10,000	(Sato et al. 2004)
Human umbilical vein endothelial cell	AFM	1,400 (near edge) 6,800 (nucleus) 3,000 (in between)	(Mathur et al. 2007)
Bovine aortic endothelial cell	AFM	1,700-7,000	(Sato et al. 2000)
Rabbit aortic endothelial cell	AFM	600-10,000	(Miyazaki & Hayashi 1999)
Human umbilical vein endothelial cell	Magnetic twisting cytometry	400	(Feneberg et al. 2004)
Bovine thoracic aortic endothelial cell	Micropipette aspiration	400 (nucleus)	(Deguchi et al. 2005)
Porcine aortic endothelial cell	Micropipette aspiration	150	(Sato et al. 1990)
Bovine aortic endothelial cell	Micropipette aspiration	300-800	(Theret et al. 1988)
Bovine aortic endothelial cell	Compression between microplates	300-700 (cytoplasm) 4,000-8,000 (nucleus)	(Caille et al. 2002)
Schlemm's canal endothelial cells	AFM	1,000-3000	(Zeng et al. 2010)
Breast epithelial cancer cells	AFM	500-2,000	(Dokukin et al. 2013)
Chondrogenic progenitor cells	Micropipette aspiration	180-350	(Maeda et al. 2014)

Cavitation rheology can be used to determine both the interfacial tension and the elastic modulus of cellular materials (Cui et al. 2011; Zimmerlin et al. 2010; Chin et al. 2013). With appropriate needle selection, these biophysical properties may be determined at intracellular, cellular and intercellular length-scales. Spheroids are an ideal system in which to measure these properties. Unlike tissues, when a single cell type is used to form the spheroid, compositionally identical replicates can easily be grown. Furthermore, unlike with explants, other factors including age and the biochemical

environment, which have been shown to alter the mechanical characteristics of cells and tissues can be rigorously controlled (Sonmez et al. 2013; Rodier & Campisi 2011; Watters et al. 1985).

The relationship between the critical pressure and the elastic modulus measured using CR, is only valid in the “thickshell” case, where the sample volume is large relative to the radius of the expanding cavity i.e. when the outer boundary of the material is sufficiently far from the cavity origin to remain unperturbed by the cavity formation (Gent 2005). However, as the sample volume decreases the radius of the deformation (which scales with the needle radius) may begin to approach the “thickshell” limit. Spheroids are small (<1 mm) and the bubble growth may begin to approach the outer boundary of the spheroid and exceed the “thickshell” limit required for CR. Using the synthetic hydrogel, 4 % poly (ethylene oxide), Solomon and co-workers performed finite element simulations of cavitation in finite volumes (1 μ l) and obtained a modified relationship between the critical pressure and the elastic modulus:

$$P_c = \frac{5E}{6} \left[\frac{6a}{5} \left(\frac{R_i + H}{R_i} \right)^b + 1 \right] + 2\gamma/r \quad (\text{Equation 5.1})$$

where a and b are fitting parameters, equal to -0.8558 and -0.6547, respectively and H is the thickness of the elastic shell (Pavlovsky et al. 2014). Here, a bead of gel was pipetted onto a glass surface for experimentation. However, spheroids need to be examined in cell culture medium and are inclined to float away from the needle during insertion, such that it is necessary to “trap” the spheroid against the side of the container to prevent translocation. If the growth of the bubble within a trapped spheroid is beyond the “thickshell” limit then a 1-D confinement effect may also affect the critical pressure since.

5.2 Aims of this study

Spheroids are the archetypal model for tumours and are an ideal model system to study the biophysical phenomena associated with self-organisation. In this study, the aim is to determine, at various length-scales, the elastic modulus and interfacial tension of spheroids using cavitation rheology. To achieve this, a new sensor type, with reduced signal to noise ratio is to be selected and integrated into the CR apparatus.

Since spheroids are small (< 1 mm) and must be held in place (contained) to perform the CR experiments and as such any influence of confinement on the elastic modulus should be considered. Therefore there is a need to understand both the limits to which the material volume vs needle size can be employed and also any confinement effects (even if small), which may occur due to the “entrapment” of the spheroid to facilitate CR measurements (i.e. 1D confinement). A 1D confinement effect will not materialise without a breach of the “thickshell” limit i.e. the perturbations caused by the bubble do not reach the container wall. Two approaches to examine this 1D confinement effect (and thereby the “thickshell” limit) were used. Firstly, the radial dimensions of a container holding a sample gel was varied (with a fixed needle radius) and secondly the diameter of the container was fixed and the radius of the needle was increased to approach the radius of the container.

5.3 Sensor selection and implementation

5.3.1 Noise during analog to digital conversion (ADC)

The original cavitation rheology apparatus included an analog Omega PX26 series pressure transducer. The analog output (mV) from these sensors was not sufficient to be detected by the Peripheral Component Interconnect (PCI) device of the personal computer without the addition of a gain device. Inherent error introduced during digital to analog conversion, noise from the gain device and noise from the additional wiring required to connect the devices meant that these sensors were unsuitable for accurate detection of the critical pressure during cavitation rheology for materials with very small critical pressures (i.e. materials with a modulus less than 0.5kPa).

During analog to digital conversion a continuously variable signal, the analog signal, is converted to a multi-level signal, the digital signal: i.e. conversion involves the quantization of the input (Pelgrom 2010). The entire analog signal is not converted, rather the input is sampled. The result is a sequence of digital values that have been converted from a continuous-time, continuous-amplitude signal to a discrete-time, discrete-amplitude signal, figure 5.1. Both the sampling and the quantization processes introduce error into the system. The higher the sampling rate the more accurately the analog signal will be represented by the digital data. However, very high sampling rates generate large

amounts of data, and data storage can be problematic. The Nyquist frequency is the minimum rate at which the signal can be sampled without introducing errors. The Nyquist frequency is twice the frequency of the highest frequency present in the signal. Quantization noise is introduced during the process is due to rounding error between the analog input voltage and the digitised value, figure 5.1. Quantization noise may be reduced by increasing the number of quantization levels.

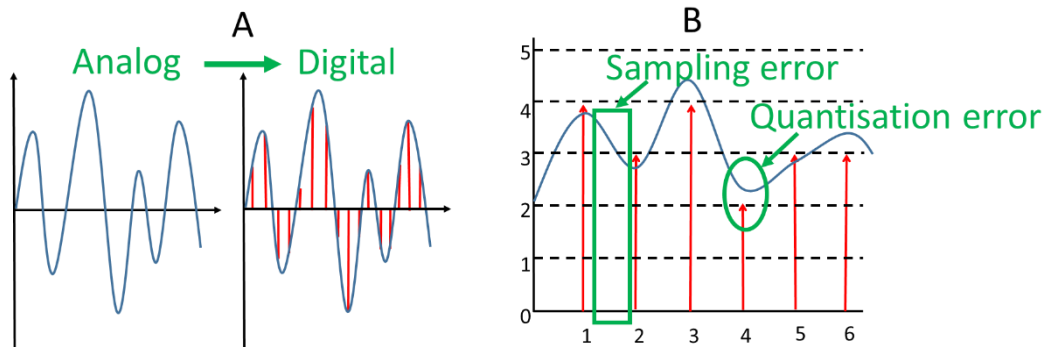


Figure 5.1 Schematic of analog to digital conversion. (A) a time-continuous, amplitude-continuous signal is transformed into a time-discrete, amplitude-discrete signal and (B) sources of error.

5.3.2 Sensor selection

Cavitation rheology involves the formation of a cavity in the material under investigation by the pressurised medium at the tip of the needle. The medium may be gaseous (typically air) or liquid (typically water), therefore the new pressure sensor must be capable of handling both liquid and gas. In addition, the ability of the sensor to connect to a USB (Universal Serial Bus) would be an advantage since a USB also supplies power to drive the device, thus eliminating the auxiliary power supply used in the standard device. In addition, many devices which connect via USB are supplied with free device driver software, eliminating the need to purchase a licence from e.g. National Instrument for the use of their software. These free software interfaces do not require extensive programming skills from the user and an engineer is not required to connect the sensor through a PCI to the computer which eliminates the time expenses associated with both these processes.

The HCS (High Accuracy Silicon Ceramic) series of pressure sensors by Honeywell was chosen to replace the Omega sensors. A selection of sensors across a

range of pressures (6.89 kPa to 1034 kPa) are available and are suitable for cavitation rheology of soft materials. They are available as either a dry-gas sensitive or a non-corrosive liquid sensitive transducer. In addition, both I²C and SPI digital output options are suitable to mount to USB connector device. These sensor are autocalibrated and have a total error $\pm 1\%$ and are temperature compensated across a 0 °C to 50 °C temperature range.

5.4 Methods and materials

5.4.1 Preparation of polyacrylamide gels (37.5:1 acrylamide:bis)

To adjust the acrylamide:bis ratio of a 30 % stock solution from 29:1 to 37.5:1, 425 μ l of acrylamide was added to 5 ml of the original stock solution. The concentration of the 37.5:1 solution was therefore 35.5%. Polyacrylamide gels were prepared at 3% (w/v) by the addition of 0.845mls of the 37.5:1 solution to 0.91 mls of MilliQ water. These components were mixed and degassed for 15 minutes, following which 50 μ l of freshly prepared 10% ammonium persulphate (Riedel-de-Haën, Germany) and 5 μ l of TEMED (Thermo Scientific, IL, USA) were added to each solution. 300 μ l of this solution was pipetted into 1.5 ml polypropylene microcentrifuge tubes and also into the wells of a polystyrene 96 well plate. The gels were allowed to set at room temperature for 15 hours.

5.4.2 Preparation of gelatin gels

Gelatin type B and phosphate buffered saline (PBS) were purchased from Sigma-Aldrich (St. Louis, MO, USA). Gels were formed from at 10% w/v (100 mg/ml) by the addition of gelatin to 1 x PBS solution. To dissolve the gelatin, the solutions were heated in a water bath at 80 °C for 10 minutes and stirred, to ensure that the solution was homogenous and then heated in the water bath for a further 10 minutes. 300 μ l of the gelatin solution was pipetted into the wells of a polystyrene 96 well plate, 1.5 and 0.5 ml polypropylene microcentrifuge tubes and to both untreated and silianized (*vida infra*) glass vials. The gels were allowed to cool on the bench overnight.

5.4.3 Silanization of glass surfaces

Borosilicate glass vials were silanized using dichlorodimethylsilane. All steps were conducted in the fume hood. The glassware was placed in a desiccation chamber with 3

ml of dichlorodimethylsilane in an open glass container. The chamber was connected to a vacuum pump and evacuated until the silane started to boil. The chamber was sealed to maintain the vacuum and the pump was switched off. During the process of silanization the evaporated silane becomes deposited on the surface of glassware and polymerises, figure 5.2. After 3 hours the desiccator was opened and any remaining fumes were allowed to disperse into the fume hood. The glassware was rinsed with MilliQ water to remove the reactive end of the polymer.

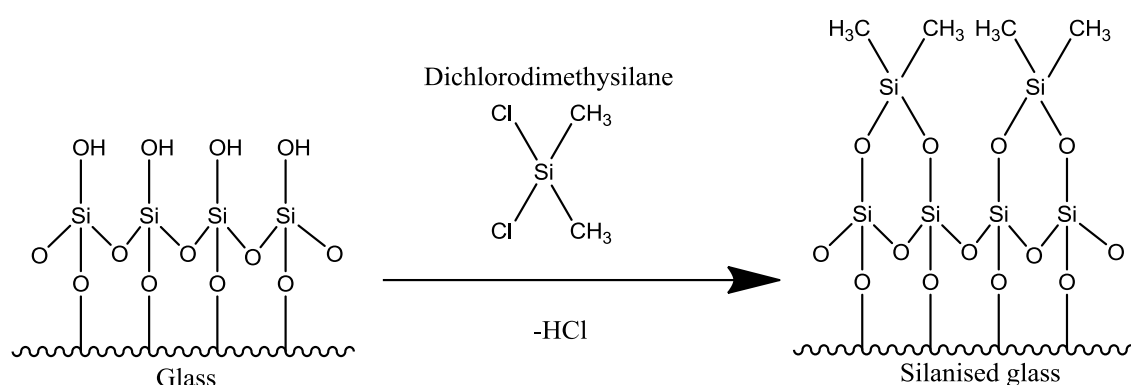


Figure 5.2 Silanization of glassware using dichlorodimethylsilane

5.4.4 Cell culture

HEK293 cells were grown in a Memmert INCO 153 (Schwabach, Germany) CO₂ incubator. Unless otherwise stated, the incubator was operated at 5% CO₂, 90 % relative humidity and 37 °C. Complete growth medium (CGM) was prepared from Dulbecco's Modified Eagles Medium (DMEM) as shown in table 5.2.

5.4.4.1 Growing cells from frozen stocks.

Complete growth medium (CGM) was warmed to 37 °C in a water bath for 15 minutes. The cells were thawed in their transportation vial in the water bath at 37 °C for 2 minutes. Both were transferred into the biological safety cabinet (SafeFast Classic, Faster S.r.l., Italy) and all operations were carried out under aseptic conditions. The vial contents were transferred into a 15 ml centrifuge tube containing 9 ml of CGM and were centrifuged for 7 minutes at 125 x g. The supernatant was discarded and the cells were resuspended in 15 ml fresh CGM and transferred into a pre-warmed T 75 cell culture flask (Corning, NY,

USA). The culture was placed in an incubator for 4 days. On day 5, 10 ml of CGM was removed from the flask and replaced with 20 ml of fresh pre-warmed CGM. On day 6 the cells reached 90 % confluence and were sub-cultured from passage 17 (original passage) to passage 18.

Table 5.2 Cell culture medium

Component	Source	Volume (ml)
HyClone ® DMEM/HIGH GLUCOSE + 4.00 mM L-Glutamine + 4,500 mg/ml L-Glucose - Sodium Pyruvate	Thermo Scientific (Utah, USA)	500
Bovine Calf Serum (Heat inactivated @ 56 °C for 45 minutes)	Sigma-Aldrich (St. Louis, MO, USA)	50
Penicillin (10,000Units) Streptomycin (10 mg/ml) Final concentration 0.5 %	Sigma-Aldrich (St. Louis, MO, USA)	2.5

5.4.4.2 Sub-culturing and passaging of cells

The cultures were maintained by refreshing the CGM every 2-3 days as necessary; indicated by a change in colour of the CGM from pink to orange as the pH of the CGM changed due to the metabolism of the cells. When the cultures reached 90 % confluence, the cells were passaged in the following manner; quantities used here are for culture in a T75 flask (a polystyrene flask with a vented lid and a growth surface area of 75 cm²). The volumes were adjusted proportionally for other flask sizes. The medium was removed and the cells were rinsed with 1 x Phosphate Buffered Saline (PBS) (Sigma-Aldrich, Saint Louis, MO, USA). The PBS was discarded and replaced with 3 ml of trypsin-EDTA (500 mg/L porcine trypsin, 200 mg/L EDTA.4Na, 1x PBS) solution (Sigma). The flask was returned to the incubator for 10 minutes. 10 ml of CGM was added and the cells were harvested by gently aspirating the medium to dislodge the cells from the wall of the flask. The cells were transferred into a centrifuge tube and spun at 125 x g for 10 minutes. The supernatant was discarded and the cells were resuspended 2 x 10⁵ cells/ml in a T75 flask (final volume 15 ml).

5.4.4.3 Cryopreservation of culture

Stocks of cells were frozen at a cell density of 3×10^6 cells/ml by resuspending the cells in cryopreservation medium (95% CGM, 5% Diethyl Sulfoxide). The vials were stored in liquid nitrogen vapour.

5.4.4.4 Spheroid culture

The liquid overlay method was used to generate cell spheroids. A thin film of 1 % agarose (Fisher, New Jersey, USA) was used to coat the bottom of a 96 well plate. 200 mg of agarose was added to 20 ml of MilliQ water in a 50 ml bottle and the solution was autoclaved (121 °C, 150 kPa for 20 minutes) to sterilise the agarose. The bottle was transferred to a water bath to equilibrate to 70°C (agarose melting point = 35-45 °C) and kept sterile at all times. In the biosafety cabinet, 75 µl of agarose was dispensed into the interior wells of a 96-well plate to form a concave surface. The outermost wells were filled with 200 µl of sterile water. The plate was allowed to cool for one hour. When HEK293 cell cultures reached 90 % confluence the cells were rinsed with 1 x PBS. The PBS was then discarded and replaced with 3 ml of trypsin-EDTA solution. The flask was returned to the incubator for 10 minutes after which 10 ml of CGM was added and the cells were harvested by gently aspirating the medium to dislodge the cells from the wall of the flask. The cells were transferred into a centrifuge tube and spun at 125 x g for 10 minutes. The supernatant was discarded and the cells were resuspended at a final concentration of 7.5×10^3 cells/ml. 200 µl of cell suspension was added per well, thus each well contained 1.5×10^3 cells. The plates were placed in the incubator and the spheroid cultures were maintained by refreshing the CGM after 4 days. To avoid disruption to the spheroid, 150 µl of medium was gently aspirated from the wells and replaced with an equal volume of fresh medium which was gently pipetted along sidewall of the well. The spheroids were harvested on day 7.

5.4.5 Light microscopy

Light microscopy was performed to monitor the growth of the spheroids. An Olympus CRX31 inverted microscope, equipped with a digital imaging system was used to view and record the images and all image analysis was done using ImageJ software (Schneider, Rasband et al. 2012). A grid with known partition dimensions was used to measure spheroid sizes.

5.4.6 Cavitation rheology

The cavitation rheology apparatus, built in-house was set up as shown in figure 2.5 and comprises a syringe pump (New Era) regulating a syringe (Hamilton GASTIGHT®), connected to a High Accuracy Silicon Ceramic pressure sensors (Honeywell) for the spheroid experiments and a PX26 series pressure sensor (Omega Engineering) for the polyacrylamide and gelatin gels. Blunt end needles were purchased from Fisher scientific and World Precision Instruments. A custom written programme recorded pressure at the needle tip during the experiments.

The PX26 series sensor was calibrated hydrostatically. The autocalibration and sensitivity of the Honeywell sensor was validated using a range of needles (internal radii from 1.2 mm to 0.028 mm) to experimentally determine the surface tension of water. The surface tension of 5 M NaCl (Fisher Scientific), 10% Ethanol (VWR, France) and total cell culture medium was determined in the same manner.

The elastic modulus of polyacrylamide and gelatin gels was determined as described for a typical cavitation rheology experiment (in 4.2.9.2). For spheroid measurements, the spheroid was removed from the well of a 96 well plate by aspiration of the spheroid and surrounding medium using a P1000 Gilson pipette (Middleton, WI, USA), the tip being sufficiently large to allow the free passage of the spheroid. The spheroid was then transferred into a glass capillary, along with a sufficient amount of medium to bathe the spheroid. The needle was attached to a custom built micro-manipulator. The needle was adjusted until the tip of the needle was inserted into the spheroid, at which time the cavitation rheology experiment began. The insertion process was monitored using cameras (with magnification) to ensure the correct placement of the needle tip (and to prevent through penetration). Front and side views of the needle were monitored and in doing so ensuring that the needle did not penetrate the spheroid on the vertical axis, figure 5.3.

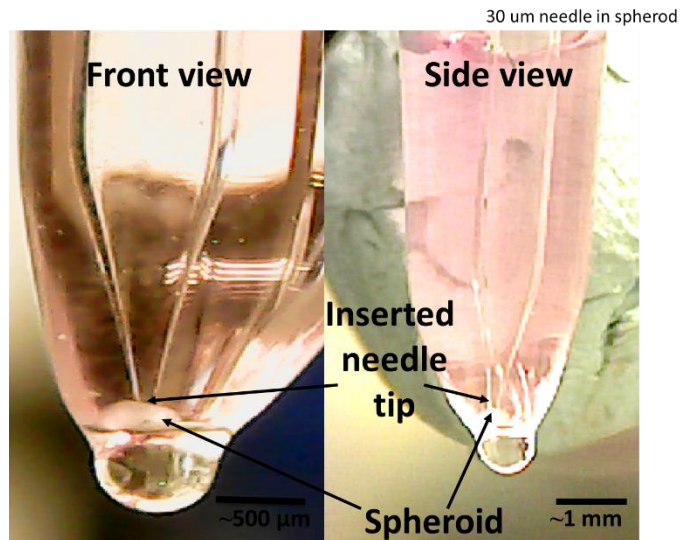


Figure 5.3 Insertion of a 30 μm needle into a spheroid - view from both horizontal axes.

5.5 Results and discussion

5.5.1 Calibration

The autocalibration of the Honeywell sensor was tested by experimentally determining the surface tension of water, figure 5.4. Using the cavitation rheology apparatus, the surface tension between air and water was determined to be 73 mNm^{-1} which is in good agreement with the previously determined value, (Atkins 2014).

The surface tension between air and solutions of 10% ethanol, 5 M NaCl and total cell culture medium was also determined. The addition of 5 M NaCl increased the surface tension to 82 mNm^{-1} which is consistent with the literature values for similar solutions (82.5 mNm^{-1} for 6M NaCl (Atkins 2014)). The surface tension of total cell culture medium and bovine calf serum were found to be 70 mNm^{-1} and 68 mNm^{-1} , respectively, which is only slightly lower than that of water, figure 5.5.

The elastic modulus of the 3% (w/v) polyacrylamide gels formed overnight in 1.5 ml polypropylene microcentrifuge tubes was measured at 2.9 kPa (figure 5.6), in good agreement with previously published values (Kundu & Crosby 2009). Therefore, it was demonstrated the cavitation rheology equipment was correctly mounted and calibrated.

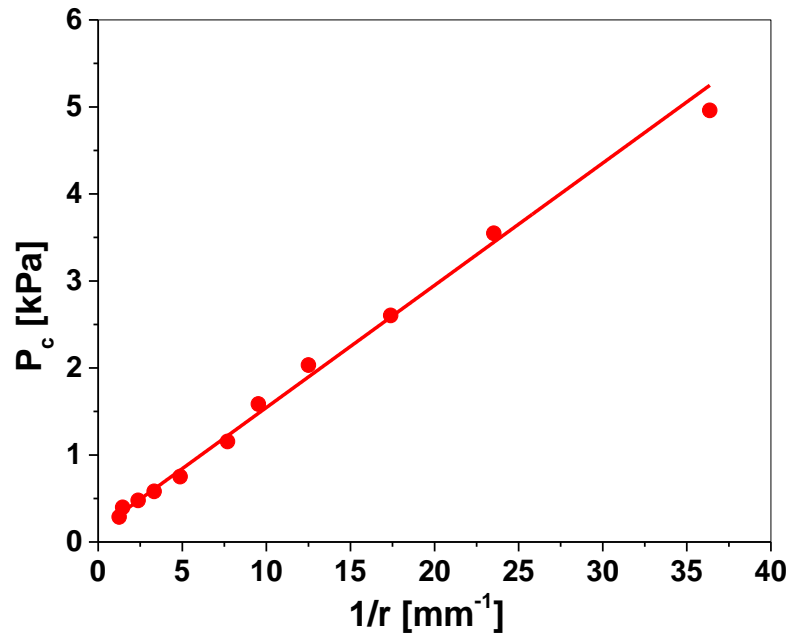


Figure 5.4 Testing the autocalibration of the Honeywell sensor. At 23.5 °C, the surface tension between air and water was determined to be 73 mNm⁻¹.

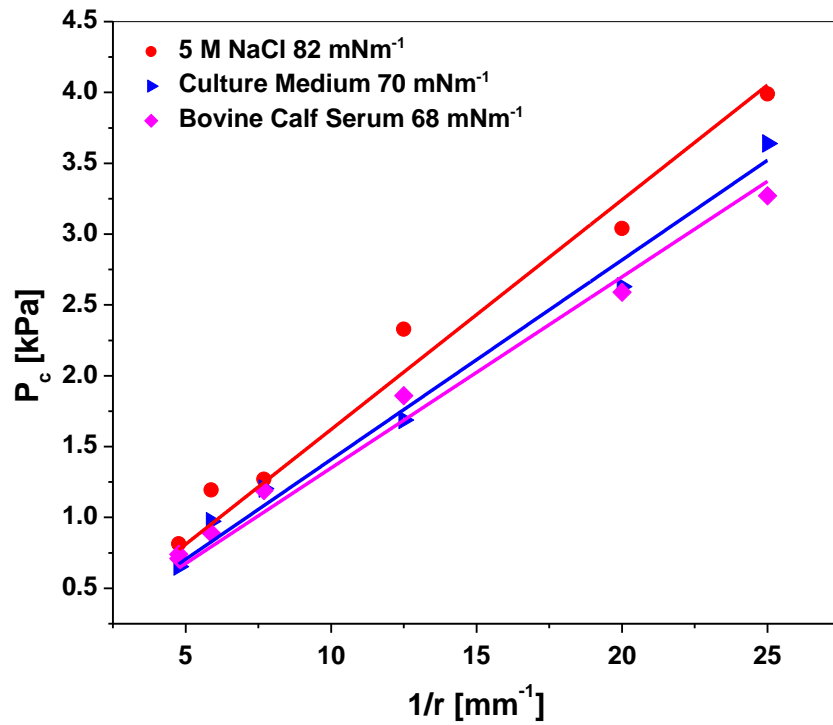


Figure 5.5 Surface tension between air and ● 5 M NaCl, ▶ Total cell culture medium, and ◆ Bovine calf serum

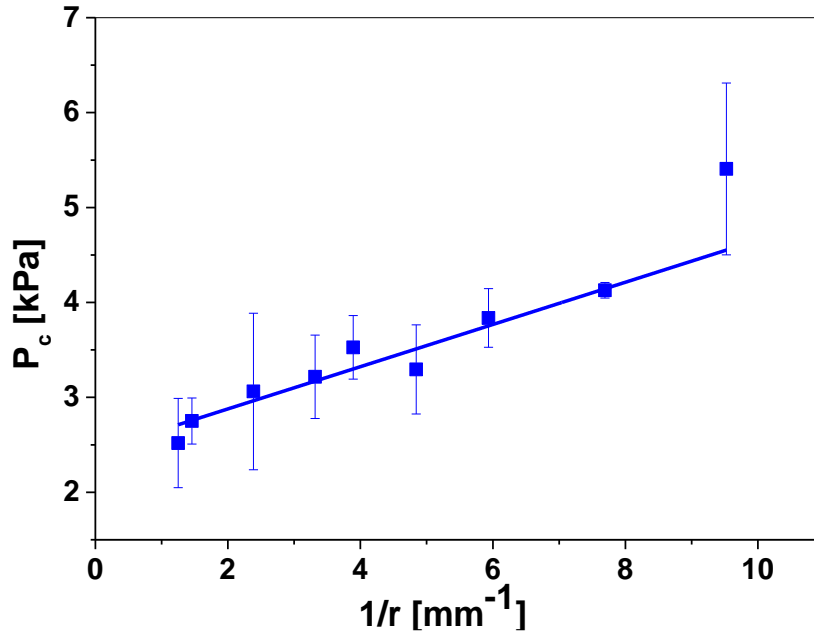


Figure 5.6 Elastic modulus of 3% w/v polyacrylamide gels formed in 1.5 ml microcentrifuge tubes, E= 2.9 kPa

5.5.2 Investigation of 1-D confinement and “thickshell” limit

10% w/v gelatin (in PBS) was selected to investigate the 1D confinement effect (and thereby the “thickshell” limit). No single container type was available over the range of diameters needed. Therefore, it was necessary to investigate the effect on the elastic modulus of; the container material, the surface area to volume ratio and surface hydrophobicity. 300 μ l samples were used throughout.

5.5.2.1 Effect of surface area

To investigate the effect of surface area of the mould in contact with the gelatin solution, gels were formed in 1.5 ml and 0.5 ml polypropylene centrifuge tubes, figure 5.7. Given the shape of the microcentrifuge tubes the surface area was calculated by the addition of the surface area of a cylinder [$2\pi r h_{cy} + 2\pi r^2$] to the surface area of a cone [$\pi r (r + (h_{co}^2 + r^2)^{1/2})$] with an adjustment made for the common surface area [$-2\pi r^2$], where r is the radius of the tube and h_{co} is the height of the cone at the tip of the tube and h_{cy} is the height of the column of gel formed above the cone tip. The surface area for a 300 μ l gel in a 1.5 ml and 0.5 ml microcentrifuge was 230 mm² and 180 mm² respectively and the surface area to volume ratios were 1:1.30 and 1:1.67, respectively. The elastic modulus for the samples was found to be 4.3 kPa in the 0.5 ml tubes and 5.3 kPa in the 1.5 ml tubes.

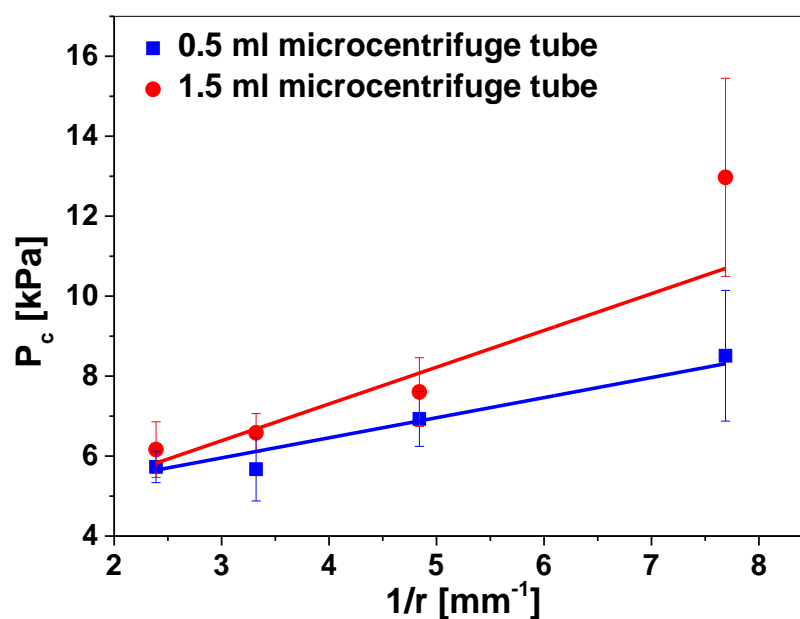


Figure 5.7 The elastic modulus of 10% w/v gelatin in PBS cast in 0.5 ml and 1.5 ml polypropylene microcentrifuge tubes, $E = 4.3$ kPa and 5.3 kPa, respectively.

5.5.2.2 Effect of surface type

To investigate the effect surface type and hydrophobicity of that surface on the elastic modulus of the gelatin gels, additional gels ($300 \mu\text{l}$) were cast in a polystyrene 96 well plate and in untreated glass vials and glass vials that were silanized. The elastic moduli were determined to be, $E = 10.5$ kPa, 6.4 kPa and 7.8 kPa, respectively, figure 5.8.

Thus, the surface area, container material and the hydrophobicity of the container were all demonstrated to affect the gelation process, which is consistent with the previous studies (K. Abraham Vaynberg et al. 1999; Murphy & Marvin 1974). Using x-ray reflectometry, differential adsorption of gelatin onto hydrophobic and hydrophilic surfaces was reported (K. Abraham Vaynberg et al. 1999) and differential adsorption was also reported for glass and polystyrene surfaces, (Murphy & Marvin 1974). Weaker gels formed at larger surface to volume ratios. Since these effects could not be decoupled from decreasing the radii of the container, this approach was discounted as a method to investigate the effects of confinement.

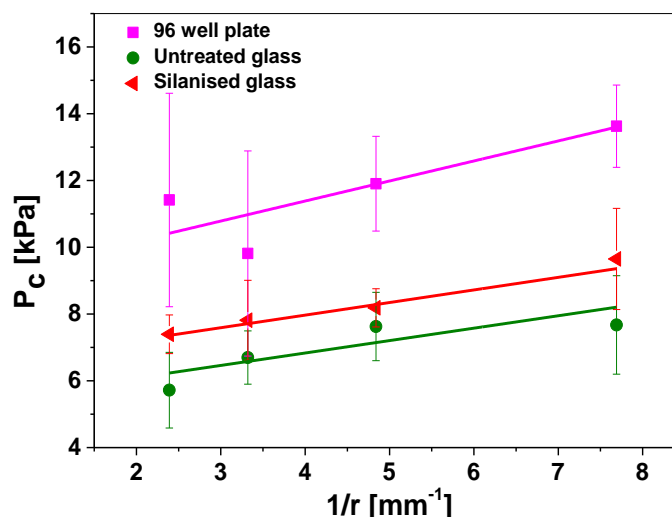


Figure 5.8 The elastic modulus of 10% w/v gelatin in PBS cast in a polystyrene 96 well plate and in glass vials which were (a) untreated and (b) silanized, $E = 10.5$ kPa, 6.4 kPa and 7.8 kPa, respectively.

5.5.2.3 Maintaining volume and varying needle radius

The second approach was to keep the radius of the container constant and to systematically increase the radius of the needle, figure 5.9. In doing so, the radius of the deformation (which scales with the needle radius) begins to approach the outer boundary of the material (both radially and vertically) and a confinement effect may be observed. Gels ($300 \mu\text{l}$) were formed in a 96 well plate where the diameter of the well (D_c) was 6.96 mm, yielding a cylindrical gel with radius 3.48 mm and height 7.89 mm. A range of needle diameters (D_n) were used (0.6 mm to 3.0 mm) and the needle was inserted into the sample at a depth of approximately one third the height of the gel. The critical pressure values were determined. A plot of critical pressure versus the ratio of needle diameter to container diameter (D_n/D_c) showed that the critical pressure was not affected by radial confinement in the regime studied, where $0.09 < D_n/D_c < 0.43$, figure 5.10.

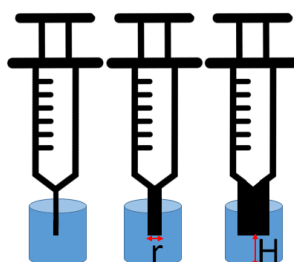


Figure 5.9 Schematic of method used to investigate vertical 1-D confinement

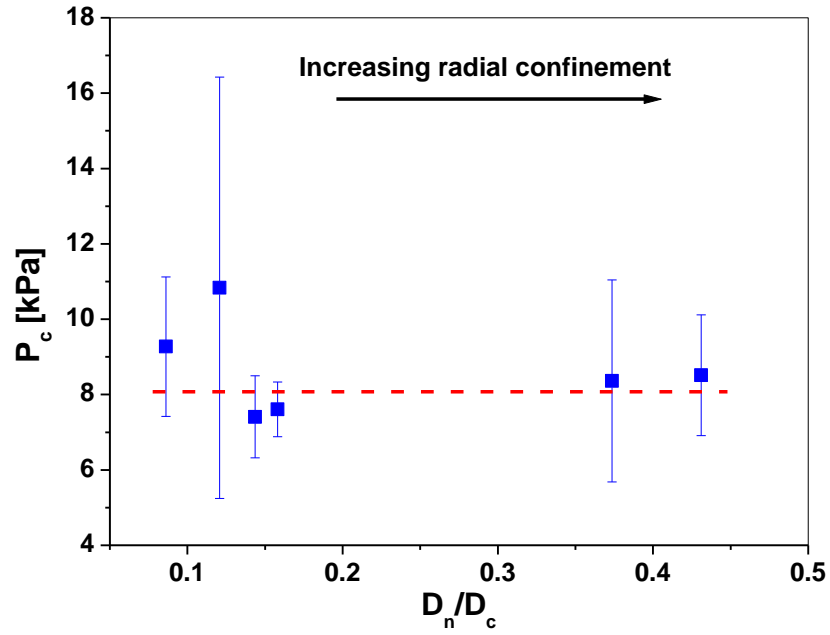


Figure 5.10 Plot of the critical pressure (P_c) for 10% w/v gelatin in PBS cast in a polystyrene 96 well plate against the ratio of the needle diameter to the diameter of the well (6.96 mm). The dashed line shown is used as a guide to the eye.

Since the vertical axis is primary axis along which the cavity expands, consideration must also be given to any vertical confinement effect since it is along this axis that the “thickshell” limit is more likely to be breached. Using finite element analysis, Solomon and co-workers obtained a modified relationship between the critical pressure and the elastic modulus:

$$P_c = \frac{5E}{6} \left[\frac{6a}{5} \left(\frac{R_i + H}{R_i} \right)^b + 1 \right] + \frac{2\gamma}{R_i} \quad (\text{Equation 5.2})$$

where a and b are fitting parameters, equal to -0.8558 and -0.6547, respectively and H is the thickness of the elastic shell (Pavlovsky et al. 2014). For large volumes $[(R_i+H)/R_i \sim 20]$ it was shown that the critical pressure reaches an asymptotic limit of $\sim 5E/6$ consistent with (Equation 2.14). Whereas for finite volumes $[(R_i+H)/R_i \sim 5]$ and $[(R_i+H)/R_i \sim 1.5]$ the critical pressure was significantly lower, indicating that in this regime (Equation 2.14) may not be valid.

For these gelatin confinement studies, a vertical confinement effect was not observed, figure 5.11. These results may indicate the limits of the “thickshell” boundary may depend on the material being studied.

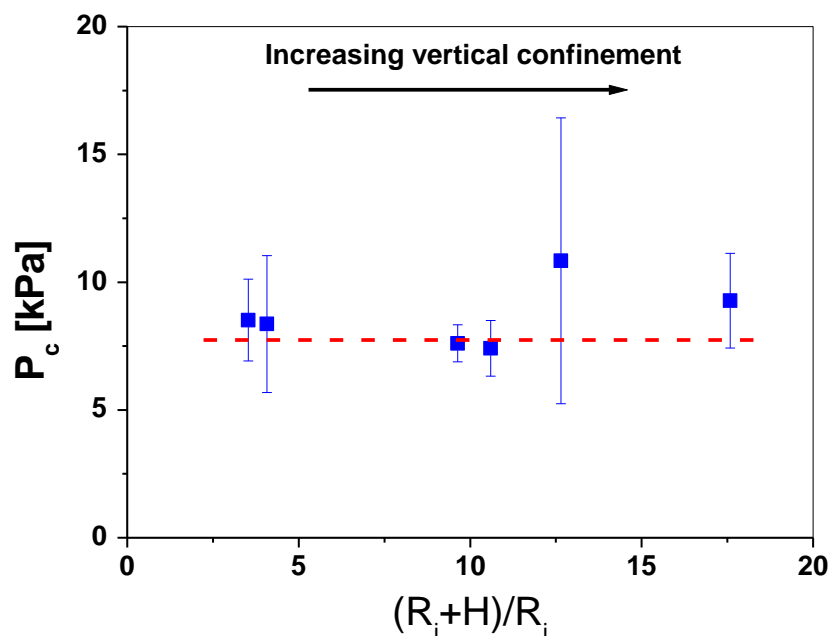


Figure 5.11 Vertical confinement of 10% w/v gelatin in PBS cast in a polystyrene 96 well plate. .
The dashed line shown is used as a guide to the eye

5.5.3 Spheroid investigation

The growth of the spheroids was monitored by light microscopy over a number of days, figure 5.12. After 24 hours, the cells formed loose, asymmetric clusters, figure 5.12. By day 2 more defined spheroids with an average diameter of $209 \pm 10 \mu\text{m}$ ($n = 60$) were observed, figure 5.13.

Due to the limited diffusion of oxygen, in most tissues cells are located no further than 100 to 200 μm from the nearest capillary (Jain et al. 2005), similarly, unless positioned within 100 to 200 μm from the nearest capillary, the cells of laboratory grown implants do not survive (Rouwkema et al. 2008). In spheroids, a necrotic core develops, due to hypoxia (Shimizu et al. 1996), when the spheroid grows large and the interior cells are located beyond the diffusion limit of $\sim 200 \mu\text{m}$ from the rim of the spheroid (Grimes et al. 2014; Groebe & Mueller-Klieser 1996). At day 8, 36% of the spheroids developed

outgrowths figure 5.12, consistent with a breach of the diffusion limit and possible ejection of the necrotic core (Wong et al. 2012). Therefore, the spheroids were harvested after seven days when the spheroids were large, (figure 5.12), but before the diffusion limit was breached, thus ensuring that the spheroids were a periconfluent mass of hypermotile, cells without a necrotic core (Alessandri et al. 2013).

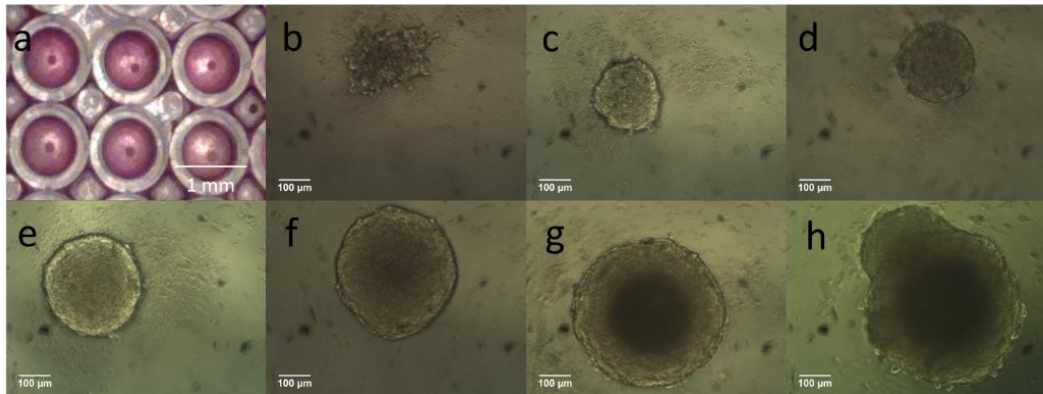


Figure 5.12 HEK 293T/17 spheroids grown using overlay method (1% agarose). Growth was monitored over eight days. (a) overview of cell in section of a 96 well plate, scale bar 1 mm, (b-h) day 1 – day 8, scale bar 100 µm. A grid, of known dimensions, was used to convert length in pixels to length in mm (3,157 pixels = 1 mm using a 10 x lens).

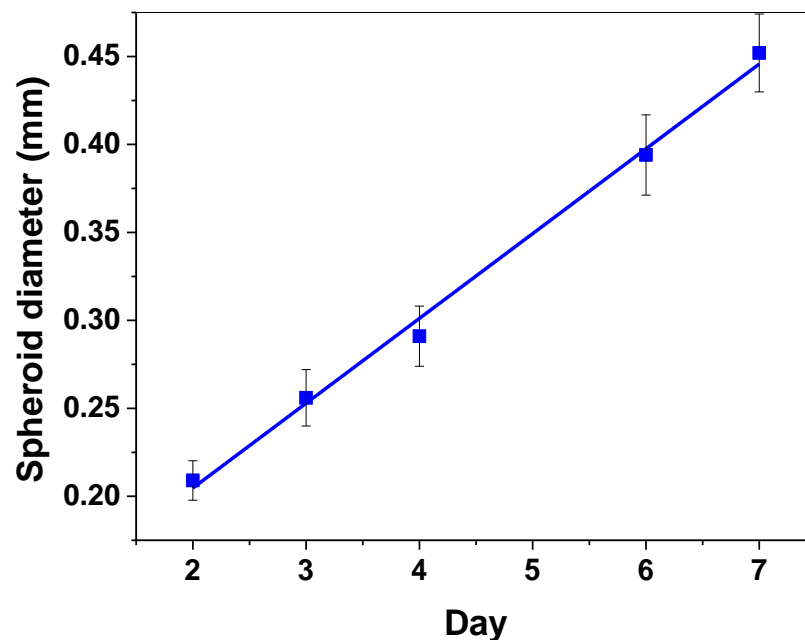


Figure 5.13 Growth curve for HEK 293T/17 spheroids grown using an overlay method (1% agarose) seeded at 1.5×10^3 cells/ well; 60 replicates per point. Growth rate $\sim 50 \mu\text{m}/\text{day}$

5.5.3.1 Mechanical properties of spheroids

Three needle diameters were selected for cavitation rheology measurements; 5 μm , 10 μm and 30 μm . At 37 $^{\circ}\text{C}$, the critical pressure required to form a bubble (air into liquid) at the tip of these needle diameters ranges from 4.6 to 28 kPa. Given that the elastic moduli of some cell types have been measured at ~ 100 Pa (table 5.1), water was selected as the cavitation medium to reduce the interfacial tension contribution to the critical pressure (there is a minimal surface tension difference between water and the medium in which the cells are bathed, CGM or bovine calf serum (figure 5.5)). The control experiments performed on gelatin indicate that the elastic modulus is measured consistently when $D_n/D_c < 0.43$. The cavitation rheology measurements are summarised in table 5.3, figure 5.14 and figure 5.16.

Table 5.3 Cavitation rheology of HEK 293T/17 spheroids on day 7.

	Needle diameter		
	5 μm	10 μm	30 μm
Number of replicates	25	28	23
Minimum C_p (kPa)	0.047	0.014	0.013
Maximum C_p (kPa)	0.742	0.417	0.259
Relative frequency (0-0.15 kPa)	0.28	0.89	0.95
Relative frequency (0.15-0.25 kPa)	0.32	0.04	0.0
Relative frequency (0.25-0.50 kPa)	0.28	0.07	0.05
Relative frequency (0.5-0.80 kPa)	0.12	0.0	0.0

5.5.3.2 What length-scales are being measured?

To consider what part of the spheroid is being probed by CR measurements at each needle diameter, it is important to consider the dimensions of the needles when compared to the components of the cell spheroid. HEK293 cells have an average diameter of ~ 15 μm (Dietmair et al. 2012). The inside diameter of the needles used during cavitation rheology are 30 μm , 10 μm and 5 μm ; the outside diameter to inside diameter ratio for these needles is 1.33:1. The 30 μm needle is much larger (2x) than the cell diameter, thus the needle is too large to probe the mechanics of a single cell, figure 5.15. Therefore, it is likely that any deformation that occurs upon bubble formation will be due to disruption of cell-cell contacts (rather than by deformation of individual cell structures). Hence, the material properties of cells around the local area of the needle tip and any associated adhesion molecules within the cell membranes should be reflected in the elastic modulus measured at this needle diameter, figure 5.15a.

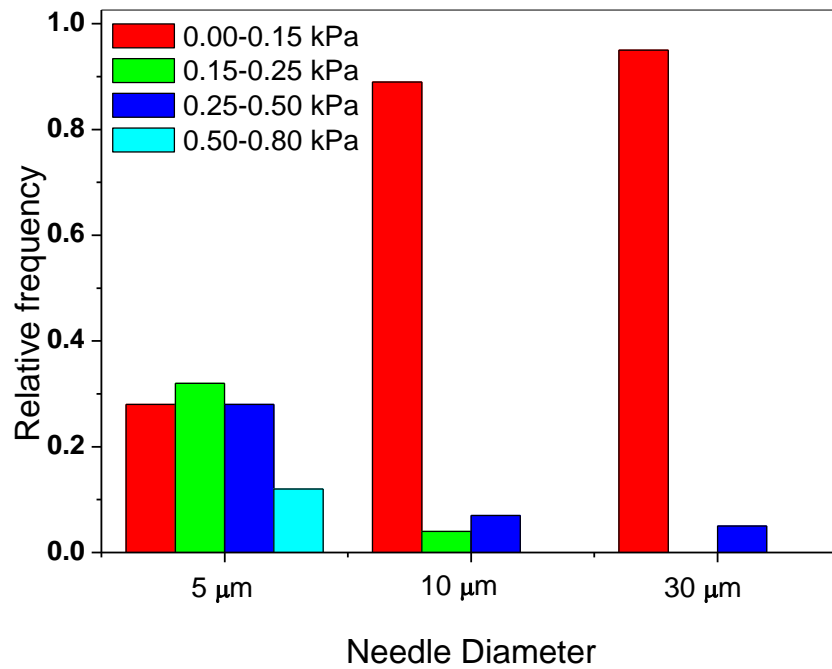


Figure 5.14 Range of critical pressure values for HEK 293T/17 spheroids on day 7 and the relative frequency of critical pressures.

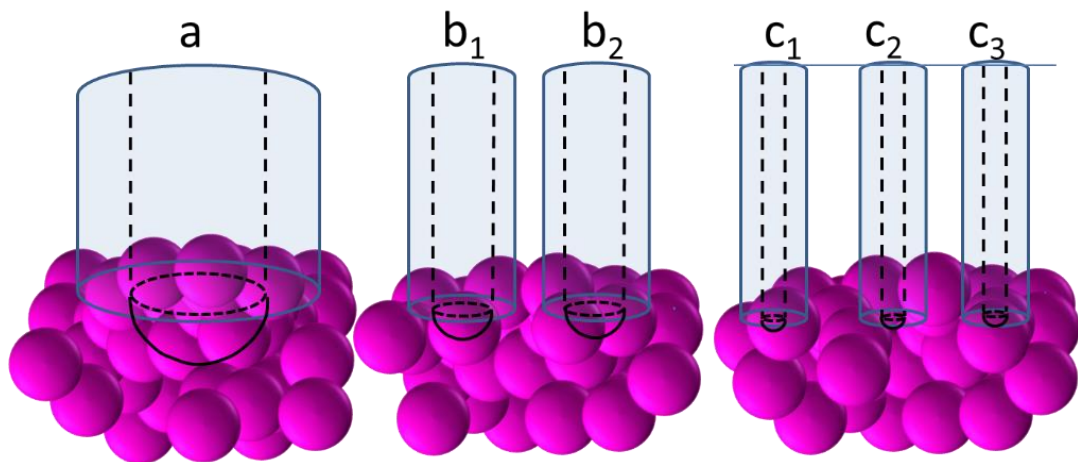


Figure 5.15 Schematic (to scale) of needles inserted into cell spheroids to illustrate the relative sizes of the needles and the cell spheroid structures; diameter of needle a) 30 μm , b) 10 μm and c) 5 μm .

The 10 μm needle is similar to the cell diameter, however, when the outside diameter is considered this needle is also too large to penetrate a single cell (and keep it in-tact), figure 5.15b₂. Again, for this needle size, it is the local extracellular environment

and any cell-cell contacts that are the most likely structures to be probed by CR measurements at this length-scale, figure 5.15.

In principle, the 5 μm needle is sufficiently small to penetrate a single cell within the spheroid and enter the cytoplasm, even when the exterior diameter is accounted for. Therefore, for a 5 μm needle, the material properties of the extracellular space and local cell-cell contacts, in addition to measurements inside a cell (albeit with lower frequency) are possible, figure 5.15.

For all three needle diameters the most likely mechanism by which deformation will occur upon bubble formation will be due to the disruption of the contacts between cells (rather than the individual structures within a single cell). Thus, it is the material properties of the adhesion molecules located within the cell membranes, which mediate cell-cell contacts, which are measured in the majority of cases. This is consistent with the data, which indicates that for the vast majority of measurements, the critical pressure falls between 0 to 0.50 kPa. This is consistent with previously measured Young's moduli (using indentation and tensile deformations) for soft biological tissues (including spinal cord, breast, brain and sclera), (McKee et al. 2011; Pachenari et al. 2014; Guevorkian et al. 2010).

Figure 5.14 indicates that critical pressures exceeding 0.5 kPa (0.61, 0.66 and 0.74 kPa) occur with low probability and only for measurements made with a 5 μm needle. Measurement of elasticity of the cytoplasm range between 0.5 and 2.4 kPa (Slomka et al. 2011; Caille et al. 2002) and this would suggest that the 5 μm needle diameter measurements are indeed measuring elasticities within a single cell. However, the sample size ($n = 25$) is not sufficient to fully discriminate between the various contributions to the elastic modulus at this length scale. Further studies, with an increased sample size, will be required.

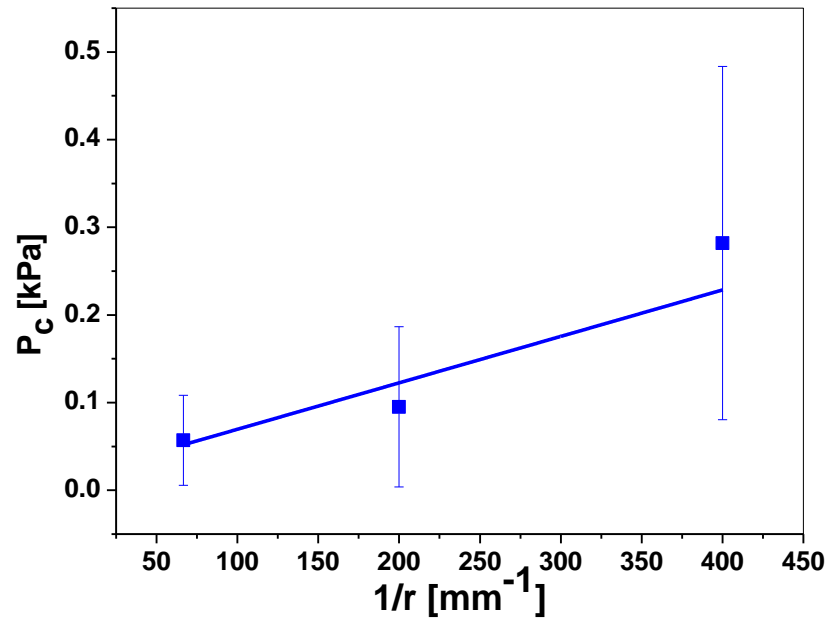


Figure 5.16 The elastic modulus (E) and interfacial tension (γ) of HEKT/17 spheroids on day 7 $E=19.9$ Pa, (γ) 2.95×10^{-4} mNm $^{-1}$.

5.5.3.3 Interpretation of the data

The pressure required to grow a cavity in a viscoelastic network is the sum of both the interfacial energy and the elastic restoring energy of the network. A plot of critical pressure against $1/r$ yields the interfacial tension as the slope and the intercept is $5/6E$. The interfacial tension was measured at 2.95×10^{-4} mNm $^{-1}$ and the elastic modulus of the spheroids was determined to be 19.9 Pa, figure 5.16.

Interfacial tension provides cells and tissues with apparent mechanical stiffness with which they resist mechanical stress. Interfacial tension values for individual cells (cortical tension) have been reported to range between 10^{-3} and 10^{-5} mNm $^{-1}$ (Hochmuth 2000; Peukes & Betz 2014; Evans & Yeung 1989; Chaigne et al. 2015; Cartagena-Rivera et al. 2015) while tissue interfacial tensions have been measured at ~ 1.6 to 20 mNm $^{-1}$ (Foty et al. 1996; Guevorkian et al. 2010; Mgharbel et al. 2009; Manning et al. 2010). The interfacial tension measured here was 2.95×10^{-4} mNm $^{-1}$ which is consistent with a measurement of cortical tension of the cells local to the needle rather than the bulk tissue interfacial tension. The interfacial energy contributes minimally to the critical pressure at the length-scales probed ($30 \mu\text{m} = 3.95 \times 10^{-5}$ Pa, $10 \mu\text{m} = 1.18 \times 10^{-4}$ Pa and $5 \mu\text{m} =$

2.37×10^{-4} Pa). Therefore, at these length-scales the elastic modulus is the major contributor to the critical pressure in these measurements.

Since the “thickshell” limit was approached during these experiments [$15 < (R_i+H)/R_i < 91$, where R_i is the needle radius and H is the radius of the spheroid] the modified CR equation was used to determine the elastic moduli for each needle diameter, following the methodology of Solomon and co-workers (Pavlovsky et al. 2014). Since the interfacial tension contribution is small i.e. $\frac{2\gamma}{r} \approx 0$, then:

$$P_c = \frac{5E}{6} \left[\frac{6a}{5} \left(\frac{R_i + H}{R_i} \right)^b + 1 \right] \quad (\text{Equation 5.3})$$

The parenthetical contribution was calculated for each needle size, table 5.4. This contribution was within the overall error for this data. The local elastic moduli at 30 μm , 10 μm and 5 μm needle diameters was therefore determined to be 39 Pa, 73 Pa and 227 Pa, respectively.

Measuring the elastic modulus (for each needle radius) provides a means of determining the energy associated with the formation of the cavity at each length scale. This value may then be compared to the known biophysical properties of cell-cell adhesion molecules (mostly cadherins), which by hydrophobic interactions form attachments between the cells of the spheroid (see 1.8.2).

Table 5.4 Calculations of the parenthetical contribution to the modified CR equation for different needle sizes

Parameter	value
a	-0.8558
b	-0.6547
H (half spheroid diameter)	225 μm
$\left[\frac{6a}{5} \left(\frac{R_{15} + H}{R_{15}} \right)^b + 1 \right]$	0.83
$\left[\frac{6a}{5} \left(\frac{R_5 + H}{R_5} \right)^b + 1 \right]$	0.92
$\left[\frac{6a}{5} \left(\frac{R_{2.5} + H}{R_{2.5}} \right)^b + 1 \right]$	0.97

The volume of the cavity formed, at the tip of the needle, is that of a hemisphere with the same radius as the internal radius of the needle and cavity formation is known to be rapid, figure 5.17.

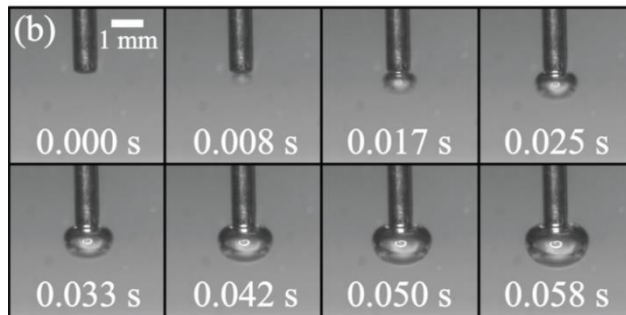


Figure 5.17 Frame-by-frame images of cavitation event 4% poly(ethylene oxide) using a needle with an internal radius of 0.084 mm, captured at 120 fps; modified from (Pavlovsky et al. 2014)

The work of forming a bubble (W_c) is related to the pressure of the medium (P_m) and the volume of the bubble (V_c) by;

$$W_c = P_m \times V_c \quad (\text{Equation 5.4})$$

For each needle diameter, the energy associated with the formation of a cavity was determined, table 5.5

Table 5.5 Calculation of the work of cavity formation.

Needle radius (m)	Cavity volume (m³)	Critical pressure (Pa = Nm⁻²)	Work of cavity formation (Nm = J)
2.5 x 10 ⁻⁶	3.9 x 10 ⁻¹⁷	227	7.4 x 10 ⁻¹⁵
5 x 10 ⁻⁶	2.6 x 10 ⁻¹⁶	73	1.9 x 10 ⁻¹⁴
15 x 10 ⁻⁶	7.1 x 10 ⁻¹⁵	39	2.8 x 10 ⁻¹³

The contribution of cell-cell adhesion molecules to the elastic restoring energy must be considered. Cadherins are an important family of proteins that mediate cell-cell adhesion. The adhesion process is a hydrophobic interaction and involves the insertion of an amino-terminal tryptophan residue from one strand into a hydrophobic pocket on the neighbouring strand. The energy associated with the formation of a cadherin-cadherin bond has been measured as 6.5 kcal mol⁻¹ [4.52 x 10⁻²⁰ joules/bond] (Katsamba et al. 2009), table 5.7.

Total cadherin expression levels of have been reported at between 2.4 x 10⁴ and 15.8 x 10⁴ cadherins per cell for L929 cells (Duguay et al. 2003) which have a smaller diameter (~10 µm) than HEK cells (~15 µm). This value translates to a minimum overall density of cadherin monomers of 76 µm⁻², Table 5.6. This corresponds to a total cadherin bond energy of 2.4 x 10⁻¹⁵ joules per cell. When the work of cavity formation was divided by the cadherin bond energy per cell, the energy associated with the formation of the cavity was found to be equivalent to the disruption cadherin bonds on a surface area equivalent to ~3 cells for a 5 µm needle, ~8 cells for a 10 µm needle and ~115 cells for a 30 µm needle, table 5.7.

Table 5.6 Calculation of cadherin bond energy per cell

Parameter	Value	Units
L929 cell cadherin density	2.40E+04	/cell
Surface area of L929 cell (4πr ²), (r = 5 µm)	314	um ²
Surface area of HEK cell (r = 7.5 µm)	706.5	um ²
HEK cell cadherin density	5.40E+04	/cell
HEK cell cadherin denstiy	7.64E+01	/um ²
Cadherin bond energy	4.52E-20	joules/bond

Cadherin bond energy	2.44E-15	joules/cell
----------------------	----------	-------------

A cascade of cell-cell dissociation events between the cells within the vicinity of the cavity must necessarily occur to facilitate the formation of a cavity. The area affected by such dissociations occur, should increase with the volume of the cavity, which is scaled to the radius of the needle. The cavities formed by the 5 μm and the 10 μm needles occupy a small fraction of the volume of a HEK cell, x 0.02 and x 0.15, respectively. Although the cavity volume is smaller than a cell, the cell adhesion molecules on many cells around the cavitation zone the must undoubtedly be forced to disassociate to accommodate the bubble, figure 5.15. The cavity formed by a 30 μm needle has a volume x 4 that of HEK cell and cell adhesion molecules equivalent to those on many more cells must disassociate to accommodate such a relatively large bubble. Total disrupted cell surface areas equivalent to 3 cells, 8 cells and 115 cells for 5, 10 and 30 μm needles, respectively, are considered physically reasonable.

Table 5.7 Calculations for cadherin energy associated with cavitation

Parameter	Value	Unit
Cadherin bond energy	6.5	kcal mol ⁻¹
Conversion factor	4,184	joules/kcal
Avogadro's number	6.02×10^{23}	
Cadherin bond energy	4.52×10^{-20}	kcal/bond
Diameter of HEK cell	15	μm
Surface area of HEK cell	706.5	μm^2
Cadherin density	76	/ μm^2
Cadherin density	53,694	/cell
Cadherin bond energy	2.4×10^{-15}	joules/cell
Cavity energy (5 μm needle)	7.4×10^{-15}	joules
Cavity energy (10 μm needle)	1.9×10^{-14}	joules
Cavity energy (15 μm needle)	2.8×10^{-13}	joules
Adhesion energy equivalents (5 μm needle)	~ 3	cells
Adhesion energy equivalents (10 μm needle)	~8	cells
Adhesion energy equivalents (30 μm needle)	~115	cells

During the testing of the autocalibration of the sensor, it was observed that as the needle radius decreased the overall drop in pressure associated with the formation of the bubble also decreased, figure 5.18. From visual observation, when air is used as the cavitation medium in water, the bubble did not remain at the tip of the needle and continue to grow, rather the bubble detached from the needle tip floated upwards. Thus, as the

needle diameter decreased the volume of the bubble prior to dissociation was increasingly small and this volume is minute compared to the total volume of the system thus only very small changes in pressure are recorded during bubble formation. When the bubble dissociates the pressure of the system is less than the critical pressure and surface tension restores the water surface at the needle tip. If the syringe pump was run continuously this results in a cycling of the system pressure over a narrow range of pressures.

A similar phenomena was observed during the cavitation of the spheroids, figure 5.18. If the syringe pump was run continuously a cycling of the system pressure was also observed. The surface tension contribution to the critical pressures (calculated from the bulk surface tension value, Figure 5.16, [$30\ \mu\text{m} = 3.95 \times 10^{-5}\ \text{Pa}$, $10\ \mu\text{m} = 1.18 \times 10^{-4}\ \text{Pa}$ and $5\ \mu\text{m} = 2.37 \times 10^{-4}\ \text{Pa}$]) are not sufficient to account for this effect which must therefore originate in the elastic contribution to the critical pressure. A mechanism involving the rapid cycle of “unzipping” and “re-zipping” of the cadherin-cadherin contacts may explain this CR response. Upon the formation of the cavity the cadherin bonds dissociate. There is minimal surface tension between the water in the cavity and the culture medium in which the cells are bathed. The water freely diffuses and the cadherin bonds reform which restores the surface at the tip of the needle. Since bubble formation is rapid, < 1 second, an elastic response is consistent with previous studies using fibroblasts (Thoumine & Ott 1997).

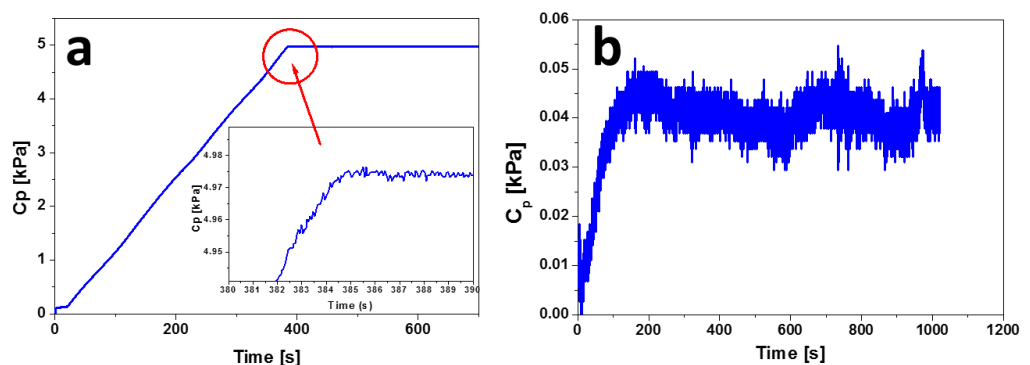


Figure 5.18 The cycling of pressure during a CR experiment; a) using air as the cavitating medium into water, $R_i = 38\ \mu\text{m}$, b) using water as the cavitating medium into HEK293 spheroids, $R_i = 5\ \mu\text{m}$.

5.6 Conclusions

A High Accuracy Silicon Ceramic series of pressure sensors by Honeywell was chosen to replace the Omega sensors for cavitation rheology measurements. These sensors have digital output options which reduces the noise-to-signal ratio and are a suitable for CR due to the pressure range available and their ability to accommodate either air or water as the cavitating medium.

For measurements to take place, spheroids must be examined in cell culture medium are not “fixed” in place, such that it is necessary to “trap” the spheroid against the side of the container in order to successfully penetrate the spheroid. Gelatin was used to investigate the “thickshell” boundary as a method to determine whether such confinement had an effect on the measurement of the elastic modulus using CR. Using the premise that a 1-D confinement effect will only be observed if the growth of the bubble within a trapped spheroid is beyond the “thickshell” limit, confinement experiments were performed to determine the “thickshell” limit. For these gelatin confinement studies, neither a horizontal nor a vertical confinement effect was not observed and these results may indicate the limits of the “thickshell” boundary may depend on the material being studied since Solomon and co-workers observed a “thickshell” effect for weaker PEO gels for similar needle to sample height ratios.

Cavitation rheology was extended to determine the elastic modulus and interfacial tensions of small volumes of biological soft matter. For spheroids formed from HEK293 cells, at 7 days, the interfacial tension at length-scales $< 30 \mu\text{m}$ was found to be dominated by the cortical tension of the cells local to the insertion point. The contribution of cell-cell adhesion to the elastic restoring energy was also examined. It was found that the mechanical response could be related quantitatively to the disruption of cell-cell adhesion molecules during the formation of the cavity. A cascade of cadherin-cadherin dissociation events occurs to facilitate the formation of the cavity with a total disrupted cell surface areas equivalent to 3 cells, 8 cells and 115 cells for 5, 10 and 30 μm needles.

The process involved is largely elastic. When the syringe pump was run continuously a cycling of the system pressure over a narrow range of pressures was

observed. Surface tension contribution to the critical pressures were not sufficient to account for this effect which must therefore originate in the reversible association of the cell-cell contacts. It is envisaged that the cadherin bonds undergo a rapid cycle of “unzipping” to accommodate the cavity and “re-zipping” to restore the surface at the needle tip.

In oncology, changes in cortical tension and cell-cell adhesion are indicators of the transition from healthy to malignant cells. This study indicates that cavitation rheology may provide a useful addition to the oncologists’ toolbox.

Final conclusions

This work focuses on the self-organisation of biological soft matter systems at different length-scales. In chapter 3, the molecular-level interactions that govern the aggregation process following thermal denaturation of lysozyme were investigated. Using novel analysis, it was possible to quantify the degree to which protein is lost to irreversible aggregation and show that an increase in the melt transition temperature does not necessarily confer an increase in reversibility. It was shown that there was considerable overlap between the T_m values where reversible and non-reversible thermal denaturation occurred. Indeed, at the highest and lowest T_m no refolding was observed whereas at intermediate values refolding occurred. Furthermore, similar T_m values had different proportions of refolded protein. In chapter 4, the model proteins BSA and gelatin, were used to assess if the self-organisation behaviour of proteins could be used to generate a novel biomaterial. Thorough control of the solution conditions and kinetics ensured that the inter-species attraction between the two protein systems were weak compared to the intra-protein attraction, leading to bigel formation composed of two discrete but interpenetrating networks. The protein bigel was shown to have an elastic modulus four times greater than the combined elastic moduli of the parent gels. Furthermore, the elastic response was maintained over several deformation cycles and the gel is both thermo- and chemo-responsive. Chapter 5 explores self-association at the cellular length scale. Here an attempt is made to relate the mechanical behaviour of tissues to cell-cell self-organisation. Cavitation rheology was used to show that for spheroids formed from HEK293 cells the interfacial tension was dominated by cortical tension at length-scales $< 30 \mu\text{m}$. It was found that the elastic modulus could be related quantitatively to the disruption of cell-cell adhesion molecules which facilitates the formation of the cavity. A cascade of cadherin-cadherin dissociation events, totalling a disrupted surface are equivalent to 3, 8 and 117 cells was calculated for 5, 10 and 30 μm needles, respectively, was calculate. Furthermore, the process involved was shown to be largely elastic and a mechanism involving a rapid cycle of “unzipping” and “re-zipping” the cadherin bonds was proposed to account for this elasticity.

References

- Abbott, A., 2003. Cell culture: biology's new dimension. *Nature*, 424(6951), pp.870–2.
- Aguzzi, A. & O'Connor, T., 2010. Protein aggregation diseases: pathogenicity and therapeutic perspectives. *Nat Rev Drug Discov*, 9(3), pp.237–248.
- Alessandri, K. et al., 2013. Cellular capsules as a tool for multicellular spheroid production and for investigating the mechanics of tumor progression in vitro. *Proceedings of the National Academy of Sciences of the United States of America*, 110(37), pp.14843–8.
- Algaer, E.A. & van der Vegt, N.F.A., 2011. Hofmeister ion interactions with model amide compounds. *The journal of physical chemistry. B*, 115(46), pp.13781–7.
- Amiel, D. et al., 2009. The Effect of Immobilization on Collagen Turnover in Connective Tissue: A Biochemical-Biomechanical Correlation. *Acta Orthopaedica Scandinavica*.
- Amin, S. et al., 2014. Protein aggregation, particle formation, characterization & rheology. *Current Opinion in Colloid & Interface Science*, 19(5), pp.438–449.
- Anderson, J.M. & Van Itallie, C.M., 2009. Physiology and function of the tight junction. *Cold Spring Harbor perspectives in biology*, 1(2), p.a002584.
- Asherie, N., Lomakin, A. & Benedek, G.B., 1996. Phase Diagram of Colloidal Solutions. *Physical Review Letters*, 77(23), pp.4832–4835.
- Athanasίου, K.A. et al., 2013. Self-Organization and the Self-Assembling Process in Tissue Engineering. *Annual Review of Biomedical Engineering*, 15(1), pp.115–136.
- Atkins, 2014. *Physical Chemistry Tenth.*, Oxford: OUP Oxford.
- Baker, E.L. et al., 2010. Cancer cell stiffness: integrated roles of three-dimensional matrix stiffness and transforming potential. *Biophysical journal*, 99(7), pp.2048–57.
- Baldwin, R.L., 2007. Energetics of protein folding. *J Mol Biol*, 371(2), pp.283–301.

- Banerjee, A. et al., 2009. The influence of hydrogel modulus on the proliferation and differentiation of encapsulated neural stem cells. *Biomaterials*, 30(27), pp.4695–9.
- Barone, V. & Heisenberg, C.-P., 2012. Cell adhesion in embryo morphogenesis. *Current opinion in cell biology*, 24(1), pp.148–53.
- Bendas, G. & Borsig, L., 2012. Cancer cell adhesion and metastasis: selectins, integrins, and the inhibitory potential of heparins. *International journal of cell biology*, 2012, p.676731.
- Bhattacharjee, A. & Bansal, M., 2005. Collagen structure: the Madras triple helix and the current scenario. *IUBMB Life*, 57(3), pp.161–172.
- Birukov, K.G. et al., 2002. Shear stress-mediated cytoskeletal remodeling and cortactin translocation in pulmonary endothelial cells. *American journal of respiratory cell and molecular biology*, 26(4), pp.453–64.
- Blake, C.C. et al., 1965. Structure of hen egg-white lysozyme. A three-dimensional Fourier synthesis at 2 Angstrom resolution. *Nature*, 206(4986), pp.757–761.
- Blanchoin, L. et al., 2014. Actin dynamics, architecture, and mechanics in cell motility. *Physiological reviews*, 94(1), pp.235–63.
- Blumlein, A. & McManus, J.J., 2015. Bigels formed via spinodal decomposition of unfolded protein. *J. Mater. Chem. B*, 3(17), pp.3429–3435.
- Bose, S. et al., 2010. A semianalytical model to study the effect of cortical tension on cell rolling. *Biophysical journal*, 99(12), pp.3870–9.
- Brangwynne, C.P., 2006. Microtubules can bear enhanced compressive loads in living cells because of lateral reinforcement. *The Journal of Cell Biology*, 173(5), pp.733–741.
- Brasch, J. et al., 2012. Thinking outside the cell: how cadherins drive adhesion. *Trends in cell biology*, 22(6), pp.299–310.
- Brodland, G.W., 2003. New information from cell aggregate compression tests and its implications for theories of cell sorting. *Biorheology*, 40(1-3), pp.273–7.

- Brodland, G.W. & Veldhuis, J.H., 2012. The mechanics of metastasis: insights from a computational model. *PloS one*, 7(9), p.e44281.
- Brown, P.H. et al., 2011. Density contrast sedimentation velocity for the determination of protein partial-specific volumes. *PloS one*, 6(10), p.e26221.
- Bryant, C.M. & McClements, D.J., 1998. Molecular basis of protein functionality with special consideration of cold-set gels derived from heat-denatured whey. *Trends in Food Science & Technology*, 9(4), pp.143–151.
- Buehler, M.J. & Ackbarow, T., 2008. Nanomechanical strength mechanisms of hierarchical biological materials and tissues. *Comput Methods Biomech Biomed Engin*, 11(6), pp.595–607.
- Cadena-Nava, R.D. et al., 2012. Self-assembly of viral capsid protein and RNA molecules of different sizes: requirement for a specific high protein/RNA mass ratio. *Journal of virology*, 86(6), pp.3318–26.
- Caille, N. et al., 2002. Contribution of the nucleus to the mechanical properties of endothelial cells. *Journal of Biomechanics*, 35(2), pp.177–187.
- Cailliez, F. & Lavery, R., 2005. Cadherin mechanics and complexation: the importance of calcium binding. *Biophysical journal*, 89(6), pp.3895–903.
- Campbell, I.D. & Humphries, M.J., 2011. Integrin structure, activation, and interactions. *Cold Spring Harbor perspectives in biology*, 3(3), p.a004994–.
- Canfield, R.E., 1963. The Amino Acid Sequence of Egg White Lysozyme. *J Biol Chem*, 238, pp.2698–2707.
- Cardinaux, F. et al., 2007. Interplay between Spinodal Decomposition and Glass Formation in Proteins Exhibiting Short-Range Attractions. *Physical Review Letters*, 99(11), p.118301.
- Cartagena-Rivera, A.X. et al., 2015. Cortical Actin Tension, Elastic Modulus and Cytosolic Pressure in Fibroblasts Determined using Atomic Force Microscopy. *Biophysical Journal*, 108(2), p.140a.

- Castets, V. et al., 1990. Experimental evidence of a sustained standing Turing-type nonequilibrium chemical pattern. *Physical review letters*, 64(24), pp.2953–2956.
- Cellmer, T. et al., 2007. Protein aggregation in silico. *Trends Biotechnol*, 25(6), pp.254–261.
- Di Cera, E., 2009. Serine proteases. *IUBMB life*, 61(5), pp.510–5.
- Černý, J. & Hobza, P., 2007. Non-covalent interactions in biomacromolecules. *Physical Chemistry Chemical Physics*, 9(39), p.5291.
- Chaigne, A. et al., 2015. A narrow window of cortical tension guides asymmetric spindle positioning in the mouse oocyte. *Nature communications*, 6, p.6027.
- Chambon, F., 1987. Linear Viscoelasticity at the Gel Point of a Crosslinking PDMS with Imbalanced Stoichiometry. *Journal of Rheology*, 31(8), p.683.
- Chandrasekaran, S., 2012. Gather Round: In vitro tumor spheroids as improved models of in vivo tumors. *Journal of Bioengineering & Biomedical Science*, 02(04).
- Chang, S.-W. & Buehler, M.J., 2014. Molecular biomechanics of collagen molecules. *Materials Today*, 17(2), pp.70–76.
- Charras, G.T. et al., 2005. Non-equilibration of hydrostatic pressure in blebbing cells. *Nature*, 435(7040), pp.365–9.
- Chaudhuri, O., Parekh, S.H. & Fletcher, D.A., 2007. Reversible stress softening of actin networks. *Nature*, 445(7125), pp.295–8.
- Chen, B. et al., 2014. The WAVE regulatory complex links diverse receptors to the actin cytoskeleton. *Cell*, 156(1-2), pp.195–207.
- Chi, E. et al., 2003. Physical Stability of Proteins in Aqueous Solution: Mechanism and Driving Forces in Nonnative Protein Aggregation. *Pharmaceutical Research*, 20(9), pp.1325–1336.
- Chi, E.Y. et al., 2003. Physical stability of proteins in aqueous solution: mechanism and driving forces in nonnative protein aggregation. *Pharmaceutical Research*, 20(9), pp.1325–1336.

- Chin, M.S. et al., 2013. Cavitation rheology as a potential method for in vivo assessment of skin biomechanics. *Plastic and reconstructive surgery*, 131(2), p.303e–305e.
- Cicuta, P. & Donald, A.M., 2007. Microrheology: a review of the method and applications. *Soft Matter*, 3(12), p.1449.
- Cooper, A., 1999. Thermodynamic analysis of biomolecular interactions. *Current Opinion in Chemical Biology*, 3(5), pp.557–563.
- Cooper, A., Nutley, M.A. & Wadwood, A., 2000. Differential Scanning Microcalorimetry. In *Protein-Ligand Interactions: hydrodynamics and calorimetry*. Oxford New York: Oxford University Press, pp. 287–318.
- Cooper, A., Nutley, M.A. & Wadwood, A., 2001. Differential Scanning Microcalorimetry. In S. Harding & B. Choudhary, eds. *Protein-Ligand Interactions; A Practical Approach*. Oxford University Press.
- Costa, K.D., Sim, A.J. & Yin, F.C.-P., 2006. Non-Hertzian approach to analyzing mechanical properties of endothelial cells probed by atomic force microscopy. *Journal of biomechanical engineering*, 128(2), pp.176–84.
- Costantini, L. & Snapp, E., 2013. Probing endoplasmic reticulum dynamics using fluorescence imaging and photobleaching techniques. *Current protocols in cell biology / editorial board, Juan S. Bonifacino ... [et al.]*, 60, p.Unit 21.7.
- Cross, S.E. et al., 2007. Nanomechanical analysis of cells from cancer patients. *Nature nanotechnology*, 2(12), pp.780–3.
- Cui, J. et al., 2011. Cavitation rheology of the eye lens. *Soft Matter*, 7(17), p.7827.
- Daanoun, A., Tejero, C.F. & Baus, M., 1994. van der Waals theory for solids. *Physical Review E*, 50(4), pp.2913–2924.
- Daniels, B.R. et al., 2010. Differences in the microrheology of human embryonic stem cells and human induced pluripotent stem cells. *Biophysical journal*, 99(11), pp.3563–70.
- David, R. et al., 2014. Tissue cohesion and the mechanics of cell rearrangement.

Development (Cambridge, England), 141(19), pp.3672–82.

- Deguchi, S. et al., 2005. Flow-induced hardening of endothelial nucleus as an intracellular stress-bearing organelle. *Journal of biomechanics*, 38(9), pp.1751–9.
- Desai, B. V, Harmon, R.M. & Green, K.J., 2009. Desmosomes at a glance. *Journal of cell science*, 122(Pt 24), pp.4401–7.
- DeToma, A.S. et al., 2012. Misfolded proteins in Alzheimer's disease and type II diabetes. *Chemical Society reviews*, 41(2), pp.608–21.
- Dietmair, S. et al., 2012. A multi-omics analysis of recombinant protein production in Hek293 cells. *PloS one*, 7(8), p.e43394.
- Dinsmore, A.D. & Weitz, D.A., 2002. Direct imaging of three-dimensional structure and topology of colloidal gels. *Journal of Physics: Condensed Matter*, 14(33), pp.7581–7597.
- Djabourov, M., 1988. Architecture of gelatin gels. *Contemporary Physics*, 29(3), pp.273–297.
- Dokukin, M.E., Guz, N. V & Sokolov, I., 2013. Quantitative study of the elastic modulus of loosely attached cells in AFM indentation experiments. *Biophysical journal*, 104(10), pp.2123–31.
- Du, H., Wickramasinghe, R. & Qian, X., 2010. Effects of salt on the lower critical solution temperature of poly (N-isopropylacrylamide). *The journal of physical chemistry. B*, 114(49), pp.16594–604.
- Duguay, D., Foty, R.A. & Steinberg, M.S., 2003. Cadherin-mediated cell adhesion and tissue segregation: qualitative and quantitative determinants. *Developmental Biology*, 253(2), pp.309–323.
- Dumetz, A.C. et al., 2008. Protein phase behavior in aqueous solutions: crystallization, liquid-liquid phase separation, gels, and aggregates. *Biophysical journal*, 94(2), pp.570–83.
- Eleswarapu, S. V, Responde, D.J. & Athanasiou, K.A., 2011. Tensile properties, collagen

content, and crosslinks in connective tissues of the immature knee joint. *PloS one*, 6(10), p.e26178.

Epstein, Irving, R. & Pojman, John, A., 1998. *An introduction to Nonlinear Chemical Dynamics: Oscillations, Waves, Patterns and Chaos*, Oxford: Oxford University Press.

Escudero, D. et al., 2010. Cooperativity effects between non-covalent interactions: Are they important for Z-DNA stability? *Chemical Physics Letters*, 485(1-3), pp.221–225.

Evans, E. & Yeung, A., 1989. Apparent viscosity and cortical tension of blood granulocytes determined by micropipet aspiration. *Biophysical journal*, 56(1), pp.151–60.

Fan, Z. et al., 2014. Theranostic nanomedicine for cancer detection and treatment. *Journal of food and drug analysis*, 22(1), pp.3–17.

Feneberg, W., Aepfelbacher, M. & Sackmann, E., 2004. Microviscoelasticity of the apical cell surface of human umbilical vein endothelial cells (HUVEC) within confluent monolayers. *Biophysical journal*, 87(2), pp.1338–50.

Fennema, E. et al., 2013. Spheroid culture as a tool for creating 3D complex tissues. *Trends in biotechnology*, 31(2), pp.108–15.

Fischer-Friedrich, E. et al., 2014. Quantification of surface tension and internal pressure generated by single mitotic cells. *Scientific reports*, 4, p.6213.

Fletcher, D.A. & Mullins, R.D., 2010. Cell mechanics and the cytoskeleton. *Nature*, 463(7280), pp.485–492.

Flory, P.J., 1941. Molecular Size Distribution in Three Dimensional Polymers. I. Gelation1. *Journal of the American Chemical Society*, 63(11), pp.3083–3090.

Foty, R.A. et al., 1996. Surface tensions of embryonic tissues predict their mutual envelopment behavior. *Development (Cambridge, England)*, 122(5), pp.1611–20.

Foty, R.A. & Steinberg, M.S., 2005. The differential adhesion hypothesis: a direct

- evaluation. *Developmental Biology*, 278(1), pp.255–263.
- Frantz, C., Stewart, K.M. & Weaver, V.M., 2010. The extracellular matrix at a glance. *Journal of cell science*, 123(Pt 24), pp.4195–200.
- Fung, Y.C., 2013. *Biomechanics: Mechanical Properties of Living Tissues*, Springer Science & Business Media.
- García De La Torre, J., Huertas, M.L. & Carrasco, B., 2000. Calculation of hydrodynamic properties of globular proteins from their atomic-level structure. *Biophysical journal*, 78(2), pp.719–30.
- Gardel, M.L. et al., 2004. Elastic behavior of cross-linked and bundled actin networks. *Science (New York, N.Y.)*, 304(5675), pp.1301–5.
- Gardner, R.L., Surani, M.A. & Solter, D., 2003. Epigenesis versus preformation during mammalian development. Introduction. *Philosophical transactions of the Royal Society of London. Series B, Biological sciences*, 358(1436), pp.1313–5.
- Ge, S. et al., 1998. Bovine serum albumin adsorption onto immobilized organotrichlorosilane surface: influence of the phase separation on protein adsorption patterns. *J Biomater Sci Polym Ed*, 9(2), pp.131–150.
- Gebbink, M.F.B.G. et al., 2005. Amyloids--a functional coat for microorganisms. *Nature reviews. Microbiology*, 3(4), pp.333–41.
- Gelatin Manufacturers Institute of America, I., 2013. *Standard Testing Methods for Edible Gelatin*,
- de Gennes, P.-G., 1992. Soft Matter (Nobel Lecture). *Angewandte Chemie International Edition in English*, 31(7), pp.842–845.
- Gent, A.N., 2005. Elastic instabilities in rubber. *International Journal of Non-Linear Mechanics*, 40(2-3), pp.165–175.
- Gent, A.N. & Lindley, P.B., 1959. Internal Rupture of Bonded Rubber Cylinders in Tension. *Proceedings of the Royal Society A: Mathematical, Physical and Engineering Sciences*, 249(1257), pp.195–205.

- Ghahghaei, A. & Faridi, N., 2009. Review: structure of amyloid fibril in diseases. *Journal of Biomedical Science and Engineering*, 02(05), pp.345–358.
- Gibaud, T. & Schurtenberger, P., 2009. A closer look at arrested spinodal decomposition in protein solutions. *Journal of physics. Condensed matter : an Institute of Physics journal*, 21(32), p.322201.
- Gittes, F. et al., 1993. Flexural rigidity of microtubules and actin filaments measured from thermal fluctuations in shape. *The Journal of cell biology*, 120(4), pp.923–34.
- Glade, N., Demongeot, J. & Tabony, J., 2002. Comparison of reaction-diffusion simulations with experiment in self-organised microtubule solutions. *Comptes rendus biologiques*, 325(4), pp.283–94.
- Goldschmidt, L. et al., 2010. Identifying the amyloids, proteins capable of forming amyloid-like fibrils. *Proceedings of the National Academy of Sciences of the United States of America*, 107(8), pp.3487–92.
- Golmohammadi, R. et al., 1993. The refined structure of bacteriophage MS2 at 2.8 Å resolution. *Journal of molecular biology*, 234(3), pp.620–39.
- Gradišar, H. & Jerala, R., 2014. Self-assembled bionanostructures: proteins following the lead of DNA nanostructures. *Journal of Nanobiotechnology*, 12(1), p.4.
- Graham, F.L. & van der Eb, A.J., 1973. A new technique for the assay of infectivity of human adenovirus 5 DNA. *Virology*, 52(2), pp.456–467.
- Graner, F., 1993. Can Surface Adhesion Drive Cell-rearrangement? Part I: Biological Cell-sorting. *Journal of Theoretical Biology*, 164(4), pp.455–476.
- Grimes, D.R. et al., 2014. A method for estimating the oxygen consumption rate in multicellular tumour spheroids. *Journal of the Royal Society, Interface / the Royal Society*, 11(92), p.20131124.
- Groebe, K. & Mueller-Klieser, W., 1996. On the relation between size of necrosis and diameter of tumor spheroids. *International journal of radiation oncology, biology, physics*, 34(2), pp.395–401.

- De Groot, A.S. & Scott, D.W., 2007. Immunogenicity of protein therapeutics. *Trends in immunology*, 28(11), pp.482–490.
- Guevorkian, K. et al., 2010. Aspiration of biological viscoelastic drops. *Physical review letters*, 104(21), p.218101.
- Haraguchi, K. & Takehisa, T., 2002. Nanocomposite Hydrogels: A Unique Organic–Inorganic Network Structure with Extraordinary Mechanical, Optical, and Swelling/De-swelling Properties. *Advanced Materials*, 14(16), p.1120.
- Harris, A.K., 1976. Is Cell sorting caused by differences in the work of intercellular adhesion? A critique of the Steinberg hypothesis. *Journal of theoretical biology*, 61(2), pp.267–85.
- Havea, P., Carr, A.J. & Creamer, L.K., 2004. The roles of disulphide and non-covalent bonding in the functional properties of heat-induced whey protein gels. *J Dairy Res*, 71(3), pp.330–339.
- Heinen, M., 2011. *Charged Colloids and Proteins: Structure, Diffusion, and Rheology*, Forschungszentrum Jülich.
- Herant, M., Heinrich, V. & Dembo, M., 2005. Mechanics of neutrophil phagocytosis: behavior of the cortical tension. *Journal of cell science*, 118(Pt 9), pp.1789–97.
- Heskins, M. & Guillet, J.E., 1968. Solution Properties of Poly(N-isopropylacrylamide). *Journal of Macromolecular Science: Part A - Chemistry*, 2(8), pp.1441–1455.
- Hochmuth, R.M., 2000. Micropipette aspiration of living cells. *Journal of biomechanics*, 33(1), pp.15–22.
- Hoffman, B.D. & Crocker, J.C., 2009. Cell mechanics: dissecting the physical responses of cells to force. *Annual review of biomedical engineering*, 11, pp.259–88.
- Hofmeister, F., 1888. Zur Lehre von der Wirkung der Salze. *Naunyn-Schmiedeberg's Archives of Pharmacology*, 24(4), pp.247–260.
- Hsiao, A.Y. et al., 2009. Microfluidic system for formation of PC-3 prostate cancer co-culture spheroids. *Biomaterials*, 30(16), pp.3020–7.

- Huttenlocher, A. & Horwitz, A.R., 2011. Integrins in cell migration. *Cold Spring Harbor perspectives in biology*, 3(9), p.a005074.
- Isnard, R.N. et al., 1989. Pulsatile diameter and elastic modulus of the aortic arch in essential hypertension: a noninvasive study. *Journal of the American College of Cardiology*, 13(2), pp.399–405.
- Jackson, W.M. & Brandts, J.F., 1970. Thermodynamics of protein denaturation. Calorimetric study of the reversible denaturation of chymotrypsinogen and conclusions regarding the accuracy of the two-state approximation. *Biochemistry*, 9(11), pp.2294–2301.
- Jain, R.K. et al., 2005. Engineering vascularized tissue. *Nature biotechnology*, 23(7), pp.821–3.
- James, S. & McManus, J.J., 2012. Thermal and solution stability of lysozyme in the presence of sucrose, glucose, and trehalose. *The journal of physical chemistry. B*, 116(34), pp.10182–8.
- Jefferson, J.J., Leung, C.L. & Liem, R.K.H., 2004. Plakins: goliaths that link cell junctions and the cytoskeleton. *Nature reviews. Molecular cell biology*, 5(7), pp.542–53.
- Johnson, C.M., 2013. Differential scanning calorimetry as a tool for protein folding and stability. *Archives of biochemistry and biophysics*, 531(1-2), pp.100–9.
- Jones, R.A.L., 2002. *Soft Condensed Matter*, OUP Oxford.
- K. Abraham Vaynberg, † et al., 1999. Gelatin Adsorption at the Air/Water Interface As Investigated by X-ray Reflectivity.
- Kamerzell, T.J. et al., 2011. Protein-excipient interactions: mechanisms and biophysical characterization applied to protein formulation development. *Adv Drug Deliv Rev*, 63(13), pp.1118–1159.
- Karsenti, E., 2008. Self-organization in cell biology: a brief history. *Nature reviews. Molecular cell biology*, 9(3), pp.255–62.

- Katen, S. & Zlotnick, A., 2009. The thermodynamics of virus capsid assembly. *Methods in enzymology*, 455, pp.395–417.
- Katsamba, P. et al., 2009. Linking molecular affinity and cellular specificity in cadherin-mediated adhesion. *Proceedings of the National Academy of Sciences of the United States of America*, 106(28), pp.11594–9.
- Kelly, S.M., Jess, T.J. & Price, N.C., 2005. How to study proteins by circular dichroism. *Biochimica et biophysica acta*, 1751(2), pp.119–39.
- Kim, J.A. et al., 2013. High-throughput generation of spheroids using magnetic nanoparticles for three-dimensional cell culture. *Biomaterials*, 34(34), pp.8555–8563.
- Kim, S.A. et al., 2011. Calcium-dependent dynamics of cadherin interactions at cell-cell junctions. *Proceedings of the National Academy of Sciences of the United States of America*, 108(24), pp.9857–62.
- Kleman, M. & Laverntovich, O.D., 2007. *Soft Matter Physics: An Introduction*, Springer Science & Business Media.
- Koenderink, G.H. et al., 2009. An active biopolymer network controlled by molecular motors. *Proceedings of the National Academy of Sciences of the United States of America*, 106(36), pp.15192–7.
- Koláčná, L. et al., 2007. Biochemical and biophysical aspects of collagen nanostructure in the extracellular matrix. *Physiological research / Academia Scientiarum Bohemoslovaca*, 56 Suppl 1, pp.S51–60.
- Kontomaris, S. V. et al., 2012. Mechanical properties of collagen fibrils on thin films by Atomic Force Microscopy nanoindentation. In *2012 IEEE 12th International Conference on Bioinformatics & Bioengineering (BIBE)*. IEEE, pp. 608–613.
- Krieg, M. et al., 2008. Tensile forces govern germ-layer organization in zebrafish. *Nature cell biology*, 10(4), pp.429–36.
- Kroy, K., Cates, M.E. & Poon, W.C.K., 2004. Cluster mode-coupling approach to weak gelation in attractive colloids. *Physical review letters*, 92(14), p.148302.

- Kumari, A. & Dorai, K., 2013. Identifying secondary structures in proteins using NMR chemical shift 3D correlation maps. *Journal of Molecular Structure*, 1041, pp.200–212.
- Kundu, S. & Crosby, A.J., 2009. Cavitation and fracture behavior of polyacrylamide hydrogels. *Soft Matter*, 5(20), pp.3963–3968.
- Kurachi, Y. & North, A., 2004. Ion channels: their structure, function and control - an overview. *The Journal of Physiology*, 554(2), pp.245–247.
- LaCroix, A.S. et al., 2013. Relationship between tendon stiffness and failure: a metaanalysis. *Journal of applied physiology (Bethesda, Md. : 1985)*, 115(1), pp.43–51.
- Lakes, R., 2009. *Viscoelastic Materials*, Cambridge: Cambridge University Press.
- Lakowicz, J., 2006. *Principles of Fluorescence Spectroscopy* 3rd Editio., Plenum.
- Lecuit, T. & Lenne, P.-F., 2007. Cell surface mechanics and the control of cell shape, tissue patterns and morphogenesis. *Nature reviews. Molecular cell biology*, 8(8), pp.633–44.
- Lee, C., Wacklin, H. & Bain, C.D., 2009. Changes in molecular composition and packing during lipidmembrane reconstitution from phospholipid–surfactant micelles. *Soft Matter*, 5(3), pp.568–575.
- Leheny, R.L., 2012. XPCS: Nanoscale motion and rheology. *Current Opinion in Colloid & Interface Science*, 17(1), pp.3–12.
- Lesniak, A. et al., 2012. Effects of the presence or absence of a protein corona on silica nanoparticle uptake and impact on cells. *ACS nano*, 6(7), pp.5845–57.
- Li, J. et al., 2010. 3D PLGA Scaffolds Improve Differentiation and Function of Bone Marrow Mesenchymal Stem Cell–Derived Hepatocytes. *Stem Cells and Development*, 19(9), pp.1427–1436.
- Lillie, M.A. & Gosline, J.M., 2002. The viscoelastic basis for the tensile strength of elastin. *International Journal of Biological Macromolecules*, 30(2), pp.119–127.

- Liu, Y. et al., 2011. Lysozyme protein solution with an intermediate range order structure. *J Phys Chem B*, 115(22), pp.7238–7247.
- Lodish, H. et al., 2000. Noncovalent Bonds.
- Logue, J.S. et al., 2015. Erk regulation of actin capping and bundling by Eps8 promotes cortex tension and leader bleb-based migration. *eLife*, 4, p.e08314.
- Lu, P.J. et al., 2008. Gelation of particles with short-range attraction. *Nature*, 453(7194), pp.499–503.
- Lu, P.J. & Weitz, D.A., 2013. Colloidal Particles: Crystals, Glasses, and Gels. *Annual Review of Condensed Matter Physics*, 4(1), pp.217–233.
- Luo, J.J. et al., 2011. Denaturation behaviors of two-state and non-two-state proteins examined by an interruption-incubation protocol. *J Phys Chem B*, 115(28), pp.8901–8909.
- MacKintosh, F., Käs, J. & Janmey, P., 1995. Elasticity of semiflexible biopolymer networks. *Physical review letters*, 75(24), pp.4425–4428.
- Maeda, E. et al., 2014. Significant increase in Young's modulus of ATDC5 cells during chondrogenic differentiation induced by PAMPS/PDMAAm double-network gel: comparison with induction by insulin. *Journal of biomechanics*, 47(13), pp.3408–14.
- Mahmood, T.A. et al., 2004. Adhesion-mediated signal transduction in human articular chondrocytes: the influence of biomaterial chemistry and tenascin-C. *Experimental Cell Research*, 301(2), pp.179–188.
- Maître, J.-L. & Heisenberg, C.-P., 2013. Three Functions of Cadherins in Cell Adhesion. *Current Biology*, 23(14), pp.R626–R633.
- Manning, G.S., 2006. The persistence length of DNA is reached from the persistence length of its null isomer through an internal electrostatic stretching force. *Biophysical journal*, 91(10), pp.3607–16.
- Manning, M.L. et al., 2010. Coaction of intercellular adhesion and cortical tension

specifies tissue surface tension. *Proceedings of the National Academy of Sciences of the United States of America*, 107(28), pp.12517–22.

Mansel, B. et al., 2013. *Rheology - New Concepts, Applications and Methods* R. Durairaj, ed., InTech.

Von Der Mark, K. et al., 1977. Relationship between cell shape and type of collagen synthesised as chondrocytes lose their cartilage phenotype in culture. *Nature*, 267(5611), pp.531–532.

Marturano, J.E. et al., 2013. Characterization of mechanical and biochemical properties of developing embryonic tendon. *Proceedings of the National Academy of Sciences of the United States of America*, 110(16), pp.6370–5.

Mathur, A.B., Reichert, W.M. & Truskey, G.A., 2007. Flow and high affinity binding affect the elastic modulus of the nucleus, cell body and the stress fibers of endothelial cells. *Annals of biomedical engineering*, 35(7), pp.1120–30.

McGowan, D.P. et al., 2000. Amyloid-like inclusions in Huntington's disease. *Neuroscience*, 100(4), pp.677–80.

McKee, C.T. et al., 2011. Indentation versus tensile measurements of Young's modulus for soft biological tissues. *Tissue engineering. Part B, Reviews*, 17(3), pp.155–64.

McManus, J.J. et al., 2007. Altered phase diagram due to a single point mutation in human gammaD-crystallin. *Proceedings of the National Academy of Sciences of the United States of America*, 104(43), pp.16856–61.

McUmbler, A.C., Randolph, T.W. & Schwartz, D.K., 2015. Electrostatic Interactions Influence Protein Adsorption (but Not Desorption) at the Silica–Aqueous Interface. *The Journal of Physical Chemistry Letters*, pp.2583–2587.

Menard, K., 2008. *Dynamic Mechanical Analysis: A Practical Introduction* Second., CRC Press.

Merrifield, C.J., 2016. Actin puts the squeeze on *Drosophila* glue secretion. *Nature cell biology*, 18(2), pp.142–144.

- Meşe, G., Richard, G. & White, T.W., 2007. Gap junctions: basic structure and function. *The Journal of investigative dermatology*, 127(11), pp.2516–24.
- Metzger, W. et al., 2011. The liquid overlay technique is the key to formation of co-culture spheroids consisting of primary osteoblasts, fibroblasts and endothelial cells. *Cytotherapy*, 13(8), pp.1000–12.
- Mgharbel, A., Delanoë-Ayari, H. & Rieu, J.-P., 2009. Measuring accurately liquid and tissue surface tension with a compression plate tensiometer. *HFSP journal*, 3(3), pp.213–21.
- Di Michele, L. et al., 2014. Aggregation dynamics, structure, and mechanical properties of bigels. *Soft Matter*, 10(20), pp.3633–3648.
- Mitragotri, S., Burke, P.A. & Langer, R., 2014. Overcoming the challenges in administering biopharmaceuticals: formulation and delivery strategies. *Nature reviews. Drug discovery*, 13(9), pp.655–72.
- Miyamoto, S. & Kollman, P.A., 1993. What determines the strength of noncovalent association of ligands to proteins in aqueous solution? *Proceedings of the National Academy of Sciences of the United States of America*, 90(18), pp.8402–6.
- Miyazaki, H. & Hayashi, K., 1999. Atomic force microscopic measurement of the mechanical properties of intact endothelial cells in fresh arteries. *Medical & Biological Engineering & Computing*, 37(4), pp.530–536.
- Moeendarbary, E. et al., 2013. The cytoplasm of living cells behaves as a poroelastic material. *Nature Materials*, 12(3), pp.253–261.
- Monnard, P.-A. & Deamer, D.W., 2002. Membrane self-assembly processes: steps toward the first cellular life. *The Anatomical record*, 268(3), pp.196–207.
- Morrow, T. & Felcone, L.H., 2004. Defining the difference: What Makes Biologics Unique. *Biotechnology healthcare*, 1(4), pp.24–9.
- Mouw, J.K., Ou, G. & Weaver, V.M., 2014. Extracellular matrix assembly: a multiscale deconstruction. *Nature reviews. Molecular cell biology*, 15(12), pp.771–785.

- Muiznieks, L.D. & Keeley, F.W., 2013. Molecular assembly and mechanical properties of the extracellular matrix: A fibrous protein perspective. *Biochimica et biophysica acta*, 1832(7), pp.866–75.
- Murphy, B.E. & Marvin, M., 1974. Interaction of gelatin with stereospecific binding proteins and its enhancement of competitive binding assays. *Journal of clinical pathology*, 27(9), pp.687–92.
- Muschol, M. & Rosenberger, F., 1997. Liquid–liquid phase separation in supersaturated lysozyme solutions and associated precipitate formation/crystallization. *The Journal of Chemical Physics*, 107(6), p.1953.
- Neudecker, P. et al., 2012. Structure of an intermediate state in protein folding and aggregation. *Science*, 336(6079), pp.362–366.
- Ninomiya, H. & Winklbauer, R., 2008. Epithelial coating controls mesenchymal shape change through tissue-positioning effects and reduction of surface-minimizing tension. *Nature cell biology*, 10(1), pp.61–9.
- Nogales, E. et al., 1999. High-resolution model of the microtubule. *Cell*, 96(1), pp.79–88.
- Nordestgaard, B.G. & Rostgaard, J., 1985. Critical-point drying versus freeze drying for scanning electron microscopy: a quantitative and qualitative study on isolated hepatocytes. *Journal of Microscopy*, 137(2), pp.189–207.
- Nwaneshiudu, A. et al., 2012. Introduction to confocal microscopy. *The Journal of investigative dermatology*, 132(12), p.e3.
- Ogashara, K. & Hamaguchi, K., 1967. Structure of Lysozyme: XII. Effect of pH on the Stability of Lysozyme. *Journal of Biochemistry*, 61(2), pp.199–210.
- Okumura, Y. & Ito, K., 2001. The Polyrotaxane Gel: A Topological Gel by Figure-of-Eight Cross-links. *Advanced Materials*, 13(7), pp.485–487.
- Pace, C., 1990. Measuring and increasing protein stability. *Trends in Biotechnology*, 8, pp.93–98.

- Pachenari, M. et al., 2014. Mechanical properties of cancer cytoskeleton depend on actin filaments to microtubules content: investigating different grades of colon cancer cell lines. *Journal of biomechanics*, 47(2), pp.373–9.
- Pavlovsky, L. et al., 2014. Elasticity of microscale volumes of viscoelastic soft matter by cavitation rheometry. *Applied Physics Letters*, 105(11), p.114105.
- Pelgrom, M.J.M., 2010. *Analog-to-Digital Conversion*, Dordrecht: Springer Netherlands.
- Peukes, J. & Betz, T., 2014. Direct measurement of the cortical tension during the growth of membrane blebs. *Biophysical journal*, 107(8), pp.1810–20.
- Philo, J.S. & Arakawa, T., 2009. Mechanisms of protein aggregation. *Curr Pharm Biotechnol*, 10(4), pp.348–351.
- Pollock, C.M. & Shadwick, R.E., 1994. Relationship between body mass and biomechanical properties of limb tendons in adult mammals. *The American journal of physiology*, 266(3 Pt 2), pp.R1016–21.
- Prasad, V., Semwogerere, D. & Weeks, E.R., 2007. Confocal microscopy of colloids. *Journal of Physics: Condensed Matter*, 19(11), p.113102.
- Prigogine, I., 1967. On Symmetry-Breaking Instabilities in Dissipative Systems. *The Journal of Chemical Physics*, 46(9), p.3542.
- Prigogine, I., Nicolis, G. & Babloyantz, A., 1974. Nonequilibrium problems in biological phenomena. *Annals of the New York Academy of Sciences*, 231(1), pp.99–105.
- Rahaman, H. et al., 2015. Heterogeneity of equilibrium molten globule state of cytochrome c induced by weak salt denaturants under physiological condition. *PLoS one*, 10(4), p.e0120465.
- Rambaran, R.N. & Serpell, L.C., 2008. Amyloid fibrils: abnormal protein assembly. *Prion*, 2(3), pp.112–7.
- Rastogi, R.P., 2008. *Introduction to Non-equilibrium Physical Chemistry*, Elsevier.
- Rawicz, W. et al., 2000. Effect of chain length and unsaturation on elasticity of lipid bilayers. *Biophysical journal*, 79(1), pp.328–39.

- Reece, J. et al., 2009. *Cambell Biology* 8th ed. B. Wilbur, ed., New York: Pearson Education, Inc.
- Reisler, E. & Eisenberg, H., 1970. Studies on the viscosity of solutions of bovine liver glutamate dehydrogenase and on related hydrodynamic models; effect of toluene on enzyme association. *Biopolymers*, 9(8), pp.877–89.
- Rho, J.Y., Ashman, R.B. & Turner, C.H., 1993. Young's modulus of trabecular and cortical bone material: Ultrasonic and microtensile measurements. *Journal of Biomechanics*, 26(2), pp.111–119.
- Robert, D. et al., 2012. Magnetic nanomanipulations inside living cells compared with passive tracking of nanoprobe to get consensus for intracellular mechanics. *Physical review. E, Statistical, nonlinear, and soft matter physics*, 85(1 Pt 1), p.011905.
- Rodier, F. & Campisi, J., 2011. Four faces of cellular senescence. *The Journal of cell biology*, 192(4), pp.547–56.
- Rossmann, M.G. & Johnson, J.E., 1989. Icosahedral RNA virus structure. *Annual review of biochemistry*, 58, pp.533–73.
- Rouwkema, J., Rivron, N.C. & van Blitterswijk, C.A., 2008. Vascularization in tissue engineering. *Trends in biotechnology*, 26(8), pp.434–41.
- Royall, C.P. et al., 2015. Probing Colloidal Gels at Multiple Length Scales: The Role of Hydrodynamics. *Physical review letters*, 114(25), p.258302.
- Ruzicka, B. et al., 2011. Observation of empty liquids and equilibrium gels in a colloidal clay. *Nature materials*, 10(1), pp.56–60.
- Saarikangas, J., Zhao, H. & Lappalainen, P., 2010. Regulation of the actin cytoskeleton-plasma membrane interplay by phosphoinositides. *Physiological reviews*, 90(1), pp.259–89.
- Salveti, G. et al., 2002. The Endothermic Effects during Denaturation of Lysozyme by Temperature Modulated Calorimetry and an Intermediate Reaction Equilibrium. *The Journal of Physical Chemistry B*, 106(23), pp.6081–6087.

- Sasahara, K. et al., 2007. Heat-induced Conversion of β 2-Microglobulin and Hen Egg-white Lysozyme into Amyloid Fibrils. *Journal of Molecular Biology*, 372(4), pp.981–991.
- Sasahara, K. & Goto, Y., 2012. Application and use of differential scanning calorimetry in studies of thermal fluctuation associated with amyloid fibril formation. *Biophysical Reviews*, 5(3), pp.259–269.
- Sato, H. et al., 2004. Kinetic study on the elastic change of vascular endothelial cells on collagen matrices by atomic force microscopy. *Colloids and surfaces. B, Biointerfaces*, 34(2), pp.141–6.
- Sato, M. et al., 1990. Application of the micropipette technique to the measurement of cultured porcine aortic endothelial cell viscoelastic properties. *Journal of biomechanical engineering*, 112(3), pp.263–8.
- Sato, M. et al., 2000. Local mechanical properties measured by atomic force microscopy for cultured bovine endothelial cells exposed to shear stress. *Journal of biomechanics*, 33(1), pp.127–35.
- Schiele, N.R. et al., 2015. Actin cytoskeleton contributes to the elastic modulus of embryonic tendon during early development. *Journal of orthopaedic research : official publication of the Orthopaedic Research Society*, 33(6), pp.874–81.
- Schooley, A.M. et al., 2012. β 1 integrin is required for anchorage-independent growth and invasion of tumor cells in a context dependent manner. *Cancer letters*, 316(2), pp.157–67.
- Schrot, S. et al., 2005. Influence of hydrocortisone on the mechanical properties of the cerebral endothelium in vitro. *Biophysical journal*, 89(6), pp.3904–10.
- Schuler, B. & Eaton, W.A., 2008. Protein folding studied by single-molecule FRET. *Current opinion in structural biology*, 18(1), pp.16–26.
- Sedger, L.M. & McDermott, M.F., 2014. TNF and TNF-receptors: From mediators of cell death and inflammation to therapeutic giants - past, present and future. *Cytokine & growth factor reviews*, 25(4), pp.453–72.

- Sheu, S.-Y. et al., 2003. Energetics of hydrogen bonds in peptides. *Proceedings of the National Academy of Sciences of the United States of America*, 100(22), pp.12683–7.
- Shimizu, S. et al., 1996. Induction of apoptosis as well as necrosis by hypoxia and predominant prevention of apoptosis by Bcl-2 and Bcl-XL. *Cancer research*, 56(9), pp.2161–6.
- Shoulders, M.D. & Raines, R.T., 2009. Collagen structure and stability. *Annual review of biochemistry*, 78, pp.929–58.
- Slomka, N., Oomens, C.W.J. & Gefen, A., 2011. Evaluating the effective shear modulus of the cytoplasm in cultured myoblasts subjected to compression using an inverse finite element method. *Journal of the mechanical behavior of biomedical materials*, 4(7), pp.1559–66.
- Sola-Penna, M. & Meyer-Fernandes, J.R., 1998. Stabilization against thermal inactivation promoted by sugars on enzyme structure and function: Why is trehalose more effective than other sugars? *Archives of Biochemistry and Biophysics*, 360(1), pp.10–14.
- Sõmera, M., Sarmiento, C. & Truve, E., 2015. Overview on Sobemoviruses and a Proposal for the Creation of the Family Sobemoviridae. *Viruses*, 7(6), pp.3076–115.
- Sonmez, M. et al., 2013. The effect of alcohols on red blood cell mechanical properties and membrane fluidity depends on their molecular size. *PloS one*, 8(9), p.e76579.
- Spitz, F. & Furlong, E.E.M., 2012. Transcription factors: from enhancer binding to developmental control. *Nature reviews. Genetics*, 13(9), pp.613–26.
- Steinberg, M.S., 1963. Reconstruction of tissues by dissociated cells. Some morphogenetic tissue movements and the sorting out of embryonic cells may have a common explanation. *Science (New York, N.Y.)*, 141(3579), pp.401–8.
- Steiner, R.F., 1964. Structural transitions of lysozyme. *Biochimica et Biophysica Acta (BBA) - Specialized Section on Biophysical Subjects*, 79(1), pp.51–63.
- Stewart, M.P. et al., 2011. Hydrostatic pressure and the actomyosin cortex drive mitotic

- cell rounding. *Nature*, 469(7329), pp.226–30.
- Stirbat, T.V. et al., 2013. Fine tuning of tissues' viscosity and surface tension through contractility suggests a new role for α -catenin. *PloS one*, 8(2), p.e52554.
- Storm, C. et al., 2005. Nonlinear elasticity in biological gels. *Nature*, 435(7039), pp.191–4.
- Stratman, A.N., Davis, M.J. & Davis, G.E., 2011. VEGF and FGF prime vascular tube morphogenesis and sprouting directed by hematopoietic stem cell cytokines. *Blood*, 117(14), pp.3709–19.
- Strnad, P. et al., 2016. Simple Epithelial Keratins. *Methods in enzymology*, 568, pp.351–88.
- Sturtevant, J.M., 2003. Some Applications of Calorimetry in Biochemistry and Biology.
- Sugakov, V., 1998. *Lectures in Synergetics*, London: World Scientific Publishing Co. Pte. Ltd.
- Sugiyama, M. et al., 2010. SAXS and SANS observations of abnormal aggregation of human alpha-crystallin. *Chemistry & biodiversity*, 7(6), pp.1380–8.
- Sun, D.P., Liao, D.I. & Remington, S.J., 1989. Electrostatic fields in the active sites of lysozymes. *Proceedings of the National Academy of Sciences*, 86(14), pp.5361–5365.
- Sun, J.Y. et al., 2012. Highly stretchable and tough hydrogels. *Nature*, 489(7414), pp.133–136.
- Sun, J.-Y. et al., 2012. Highly stretchable and tough hydrogels. *Nature*, 489(7414), pp.133–136.
- Swaminathan, R. et al., 2011. Lysozyme: a model protein for amyloid research. *Adv Protein Chem Struct Biol*, 84, pp.63–111.
- Swaminathan, V. et al., 2011. Mechanical stiffness grades metastatic potential in patient tumor cells and in cancer cell lines. *Cancer research*, 71(15), pp.5075–80.

- Takeichi, M., 2014. Dynamic contacts: rearranging adherens junctions to drive epithelial remodelling. *Nature reviews. Molecular cell biology*, 15(6), pp.397–410.
- Tanaka, H., 2013. Importance of many-body orientational correlations in the physical description of liquids. *Faraday Discussions*, 167, p.9.
- Tekin, H. et al., 2010. Stimuli-responsive microwells for formation and retrieval of cell aggregates. *Lab on a Chip*, 10(18), p.2411.
- Tharman, R., Claessens, M.M.A.E. & Bausch, A.R., 2007. Viscoelasticity of Isotropically Cross-Linked Actin Networks. *Physical Review Letters*, 98(8), p.088103.
- Theret, D.P. et al., 1988. The application of a homogeneous half-space model in the analysis of endothelial cell micropipette measurements. *Journal of biomechanical engineering*, 110(3), pp.190–9.
- Thiriet, M., 2011. Extracellular Matrix. In *Cell and Tissue Organization in the Circulatory and Venilatory Systems*. New: Springer New York, pp. 485–519.
- Thiruvengadathan, R. et al., 2013. Nanomaterial processing using self-assembly-bottom-up chemical and biological approaches. *Reports on progress in physics. Physical Society (Great Britain)*, 76(6), p.066501.
- Thoumine, O. & Ott, A., 1997. Time scale dependent viscoelastic and contractile regimes in fibroblasts probed by microplate manipulation. *J. Cell Sci.*, 110(17), pp.2109–2116.
- Thusius, D., Dessen, P. & Jallon, J.M., 1975. Mechanisms of bovine liver glutamate dehydrogenase self-association. I. Kinetic evidence for a random association of polymer chains. *Journal of molecular biology*, 92(3), pp.413–32.
- Tibbitt, M.W. & Anseth, K.S., 2009. Hydrogels as extracellular matrix mimics for 3D cell culture. *Biotechnology and bioengineering*, 103(4), pp.655–63.
- Truscott, R.J.W., 2005. Age-related nuclear cataract-oxidation is the key. *Experimental eye research*, 80(5), pp.709–25.

- Tsang, S.K. et al., 2000. Stabilization of poliovirus by capsid-binding antiviral drugs is due to entropic effects. *Journal of molecular biology*, 296(2), pp.335–40.
- Ungrin, M.D. et al., 2008. Reproducible, Ultra High-Throughput Formation of Multicellular Organization from Single Cell Suspension-Derived Human Embryonic Stem Cell Aggregates P. Callaerts, ed. *PLoS ONE*, 3(2), p.e1565.
- Valadez-Pérez, N.E. et al., 2013. Dynamical arrest in adhesive hard-sphere dispersions driven by rigidity percolation. *Physical review. E, Statistical, nonlinear, and soft matter physics*, 88(6), p.060302.
- Varrato, F. et al., 2012. Arrested demixing opens route to bigels. *Proceedings of the National Academy of Sciences*.
- Vasita, R. & Katti, D.S., 2012. Structural and functional characterization of proteins adsorbed on hydrophilized polylactide-co-glycolide microfibers. *Int J Nanomedicine*, 7, pp.61–71.
- Velev, O.D., Kaler, E.W. & Lenhoff, A.M., 1998. Protein interactions in solution characterized by light and neutron scattering: Comparison of lysozyme and chymotrypsinogen. *Biophysical Journal*, 75(6), pp.2682–2697.
- Van Vlierberghe, S., Dubruel, P. & Schacht, E., 2011. Biopolymer-based hydrogels as scaffolds for tissue engineering applications: a review. *Biomacromolecules*, 12(5), pp.1387–408.
- Wagner, B. et al., 2006. Cytoskeletal polymer networks: the molecular structure of cross-linkers determines macroscopic properties. *Proceedings of the National Academy of Sciences of the United States of America*, 103(38), pp.13974–8.
- Watters, D.A. et al., 1985. Mechanical properties of the rat colon: the effect of age, sex and different conditions of storage. *Quarterly journal of experimental physiology (Cambridge, England)*, 70(1), pp.151–62.
- Waudby, C.A. et al., 2013. Protein folding on the ribosome studied using NMR spectroscopy. *Progress in nuclear magnetic resonance spectroscopy*, 74, pp.57–75.
- Weinber, 2013. *The Biology of Cancer* 2nd ed., Garland Science.

- Weiner, O.D. et al., 2007. An actin-based wave generator organizes cell motility. *PLoS biology*, 5(9), p.e221.
- Weiss, W.F. th, Young, T.M. & Roberts, C.J., 2009. Principles, approaches, and challenges for predicting protein aggregation rates and shelf life. *J Pharm Sci*, 98(4), pp.1246–1277.
- Weiswald, L.-B., Bellet, D. & Dangles-Marie, V., 2015. Spherical Cancer Models in Tumor Biology. *Neoplasia (New York, N.Y.)*, 17(1), pp.1–15.
- Weitz, D. et al., 1985. Limits of the fractal dimension for irreversible kinetic aggregation of gold colloids. *Physical review letters*, 54(13), pp.1416–1419.
- Wenger, M.P.E. et al., 2007. Mechanical properties of collagen fibrils. *Biophysical journal*, 93(4), pp.1255–63.
- Wickstead, B. & Gull, K., 2011. The evolution of the cytoskeleton. *The Journal of cell biology*, 194(4), pp.513–25.
- Wong, C. et al., 2012. Human neuroendocrine tumor cell lines as a three-dimensional model for the study of human neuroendocrine tumor therapy. *Journal of visualized experiments : JoVE*, (66), p.e4218.
- Xu, W. et al., 2012. Cell stiffness is a biomarker of the metastatic potential of ovarian cancer cells. *PloS one*, 7(10), p.e46609.
- Xu, Y., Strickland, E.C. & Fitzgerald, M.C., 2014. Thermodynamic analysis of protein folding and stability using a tryptophan modification protocol. *Analytical chemistry*, 86(14), pp.7041–8.
- Yamada, K.M. & Cukierman, E., 2007. Modeling tissue morphogenesis and cancer in 3D. *Cell*, 130(4), pp.601–10.
- Zaccarelli, E., 2007. Colloidal gels: equilibrium and non-equilibrium routes. *Journal of Physics: Condensed Matter*, 19(32), p.323101.
- Zeng, D. et al., 2010. Young's modulus of elasticity of Schlemm's canal endothelial cells. *Biomechanics and modeling in mechanobiology*, 9(1), pp.19–33.

- Zhang, X. et al., 2014. Rational design of multifunctional hetero-hexameric proteins for hydrogel formation and controlled delivery of bioactive molecules. *Advanced healthcare materials*, 3(11), pp.1804–11.
- Zhang, Z., Chen, X. & Xu, J., 2015. Entry effects of droplet in a micro confinement: Implications for deformation-based circulating tumor cell microfiltration. *Biomicrofluidics*, 9(2), p.024108.
- Zhanhua, C. et al., 2005. Protein subunit interfaces: heterodimers versus homodimers. *Bioinformatics*, 1(2), pp.28–39.
- Zhao, X. et al., 2015. Discrimination Between Cervical Cancer Cells and Normal Cervical Cells Based on Longitudinal Elasticity Using Atomic Force Microscopy. *Nanoscale research letters*, 10(1), p.482.
- Zhu, J. & Marchant, R.E., 2011. Design properties of hydrogel tissue-engineering scaffolds. *Expert Rev Med Devices*, 8(5), pp.607–626.
- Ziemann, F., Rädler, J. & Sackmann, E., 1994. Local measurements of viscoelastic moduli of entangled actin networks using an oscillating magnetic bead micro-rheometer. *Biophysical journal*, 66(6), pp.2210–6.
- Zimberlin, J.A. et al., 2007. Cavitation rheology for soft materials. *Soft Matter*, 3(6), p.763.
- Zimberlin, J.A., McManus, J.J. & Crosby, A.J., 2010. Cavitation rheology of the vitreous: mechanical properties of biological tissue. *Soft Matter*, 6(15), p.3632.

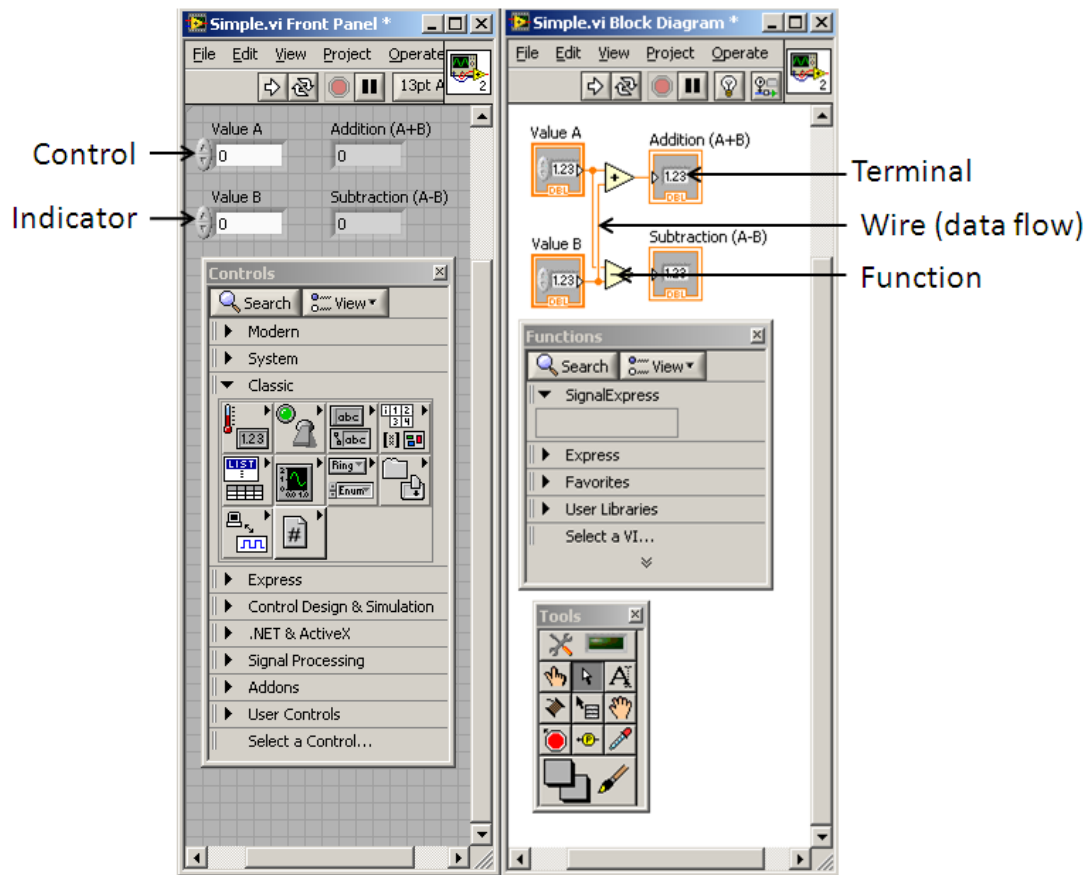
Appendix: Integration and automation of syringe pump

I. Aim

To improve the responsiveness of cavitation rheology automation of the syringe pump pressurisation system was integrated into the LabView control program. The original cavitation rheology equipment consisted of a data acquisition system (pressure transducer, computer and LabVIEW software) a syringe pump and needle. The syringe pump, used to control the pressure during a cavitation rheology experiment, was heretofore manually controlled by the operator. A new LabVIEW programme was written to integrate the operation of the pump and the data acquisition system. The software was programmed to automatically adjust the pump's actions in response to key pressure values during a cavitation rheology experiment.

II. Brief outline of programming in LabView

LabVIEW (from National Instruments), Laboratory Virtual Instrument Engineering Workbench, is a visual programming language widely used for data acquisition and instrument control. Each LabVIEW program is called a virtual instrument (VI) and consists of three components: a block diagram, a front panel and a connector panel. The connector panel is used to represent the VI in the block diagram of another VI. LabVIEW is programmed using icons instead of lines of texts to create the VI. The front panel, the user interface, is coded/built using graphical representations of controls and indicators. Controls are inputs, modified by the user to supply information to the VI whereas the indicators display outputs. The block diagram (back panel) contains the graphical source code i.e. code is added using graphical representation of functions. Objects placed on the front panel appear as terminals on the block diagram. The block diagram also contains structures and functions that perform operations on controls and supply data to the indicators. Controls, indicators, structures and functions are known as nodes and are connected to each other using wires, which represent the flow of data. Appendix Figure 1 shows the front and back panel of a simple VI that adds and subtracts two numbers.



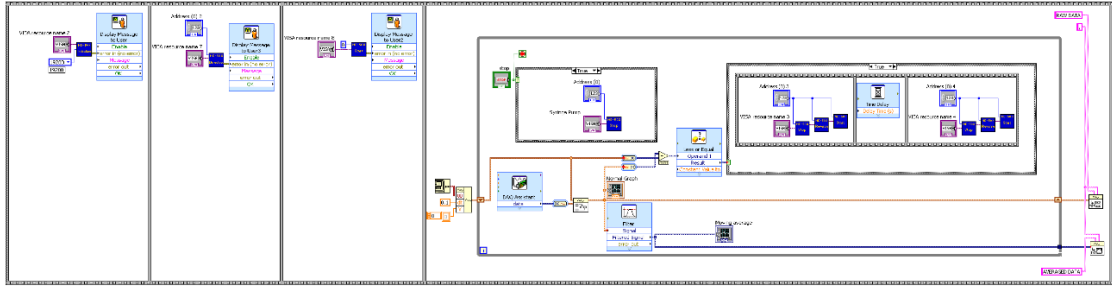
Appendix Figure 1 LabVIEW front and back panels for a simple VI which adds and subtracts two numbers..

A VI should consist of three main phases; initialization of the hardware, the main application and shut down, where the data are written to files. LabVIEW communicates with instruments (such as the pressure sensor) via an instrument driver. There are libraries of instrument drivers available which eliminate the need to programme a driver VI for many instruments. The New Era Pump Systems NE-50X LabVIEW Plug and Play Instrument Driver was downloaded from the New Instruments website.

III. Software development

I. Block diagram – Frames 1, 2 & 3

In the block diagram, a flat sequence structure was inserted to set the order operations (sub-diagrams/frames) within the VI were executed. A flat sequence structure executes left to right when all the data values within a frame is available. Four frames were added to the sequence structure, appendix figure 2.



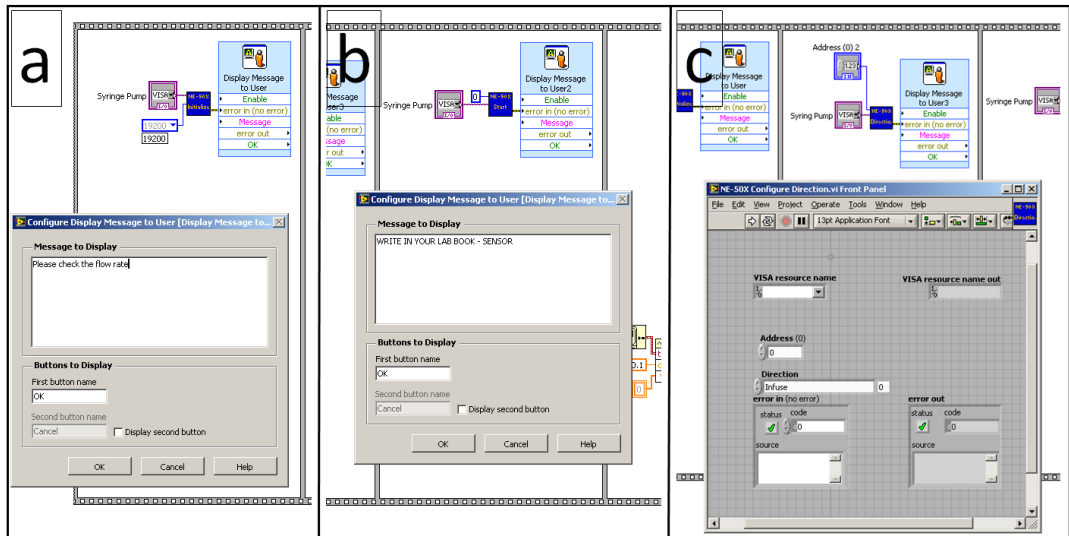
Appendix Figure 2 Complete block diagram showing the flat sequence structure with four frames.

The first three frames initialise, set the direction of and start the pump (appendix figure 3-a,b and c, respectively). The syringe pump is represented on the block diagram by a VISA (Virtual Instrument Software Architecture). A VISA is a standard in/out Application Programming Interface (API) for instrumentation programming. In the first frame (appendix figure 3-a) an initialise VI was selected from the palette of VIs previously downloaded as part of the instrument driver. The initialise VI was connected to the pump VISA; which identifies the particular pump to be activated as there may be several pumps used for more complicated applications. A baud rate function was wired to the appropriate input and the baud rate was set to 9600. The baud rate is the rate at which data bits are transferred to and from the pump. Also included in this frame is an express VI which displays a message to the user. Express VIs are pre-programmed, commonly required VIs which are available in the functions palate. The VI is used here to remind the user to check rate which has been set manually on the pump. This VI is not essential to the programme, but reminds the user to record the flow rate in their experimental. The execution of the programme is paused until the user responds by clicking an ‘OK’ button which appears on the front panel.

In the second frame a direction VI was selected from the palette of VIs previously downloaded as part of the instrument driver which was connected to the pump visa (appendix figure 3-b). The address was set to “0” and the direction set to “infuse” as per the driver instruction manual. A user message was also included to remind the user to check syringe had an adequate supply of medium.

In the third frame a start VI was selected from the palette of VIs previously downloaded as part of the instrument driver which was connected to the pump visa

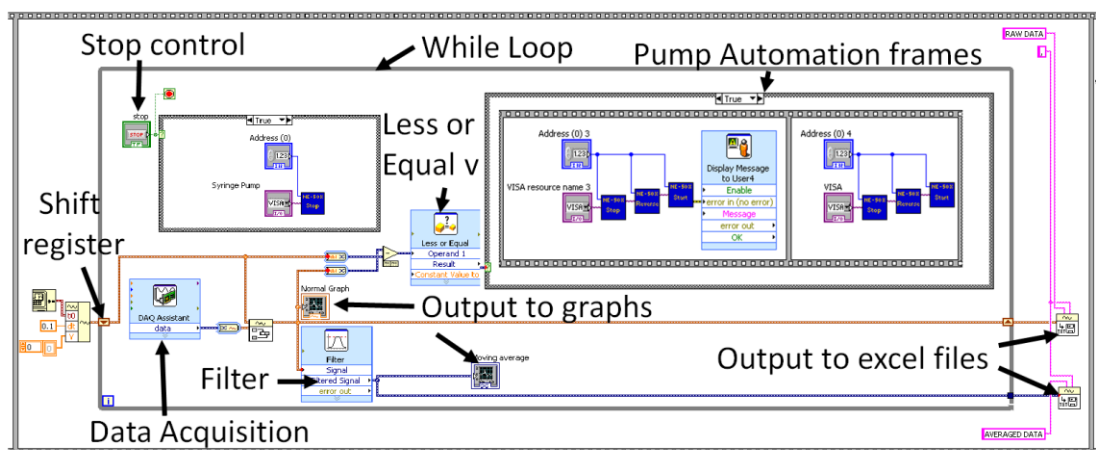
(appendix figure 3-c). The address was set to “0” and a user message was also included to remind the user to make note of the sensor which was selected for the experiment.



Appendix Figure 3 Frame 1, 2 & 3 of VI. a) The syringe pump is initialised in frame 1 b) The flow direction is set in frame two and c) the pump is started in frame 3.

II. Block diagram – Frame 4

The fourth frame contained the bulk of the programme and integrated the voltage values from the pressure sensor with the operations of the pump. Appendix Figure 4 shows the major components of this frame.



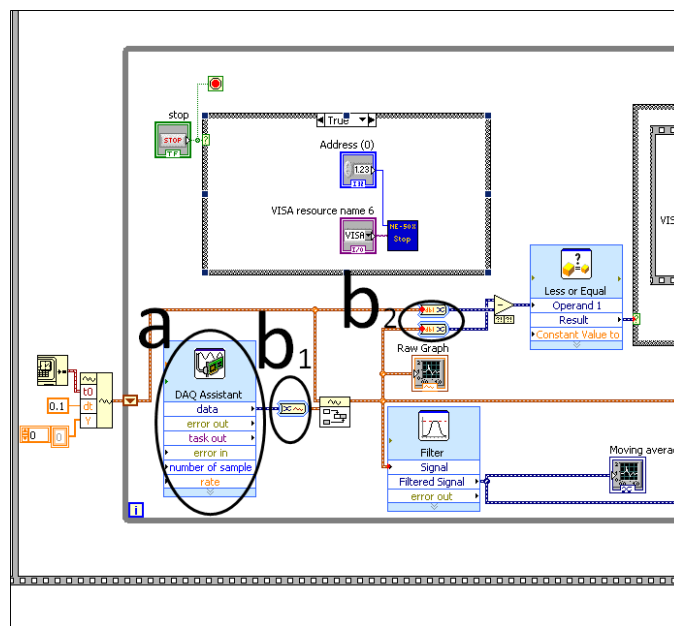
Appendix Figure 4 Frame 4 of VI indicating the major components of the frame.

A while loop was used to repeatedly run the code within frame four. A Boolean button, a stop control, was added to the front panel which was then dragged inside the while loop on the block diagram. This conditional terminal was set to Stop if True (i.e. the code within the loop stops running). The output from this terminal was also connected to the syringe pump visa. Therefore the data collection and the pump stopped simultaneously when the user engaged the Stop control on the front panel. A shift register was used to include a time stamp with each data point and pass the data values from each iteration through the loop to the next iteration.

The programme within the loop was designed to detect signals from the pressure sensor (omega PX26 series is piezoresistive bridge device). In addition, the programme displays the data, writes those data to an excel file in a comma delineated format and operates the pump in response to key pressure values. When pressure is applied a voltage is output which is proportional to the pressure. The signal (voltage) was read by the computer via a Peripheral Component Interconnect (PCI) device with multiple in/out slots. The voltage was detected at pin 68 and pin 67 was grounded. This device (and therefore the pressure sensor) was represented in the block diagram as a Signal Express function; a DAQ (Data AcQuisition) assistant, appendix figure 5-a. During the creation of this express task the pressure sensor was detected and selected and the settings used were; acquire signal, analog input, voltage and channels 68 and 67. The DAQ was then configured to a signal input range from 10 to -1 volts, the acquisition mode was set to N samples (i.e. the number of samples is specified by the Samples to Read setting. Samples to Read was set to 2 and the rate was set to 100 Hz.

In LabVIEW every object and wire is associated with data type. The data can be readily converted from one type to another using a converter function which allows the flow of data between objects with different data type outputs and inputs. Two types of data type converters were selected from the signal manipulation palate for use within this programme which allowed the flow of data between the objects, appendix figure 5-b₁ and b₂. The different data types are reflected in the colour of the wiring. Dynamic data is depicted as blue whereas numeric, Boolean, waveform and array data types are depicted as orange, appendix figure 5.

An operator was added to the block diagram to append to the data from the previous iteration (2 samples at a rate of 100 Hz) to the data from the current iteration. The appended data is sent for processing to four separate operators, see appendix figure 4. Firstly, a “raw data” graph was added to the front panel to into which the appended data was wired. This allowed the user to view the data in real-time as the experiment proceeded. Secondly, the appended data was sent to an Export Waveform to Spreadsheet file VI. The delimiter was set to comma and when the programme ends the prompt for this VI was set to remind the user that these are the raw data and second prompt was used to instruct the user to choose the file to which to write. The third sink for the appended data was a filter VI. The filtering type was set to smoothing and a moving average and a half-width of 20 was selected. The signal was thus processed to remove some of the noise inherently associated with data that has been converted from analog to digital; the voltage output from the pressure sensor is analog whereas the output from the DAQ is digital. There were two outputs from the filter. The first output from the smoothed data was sent to a “Moving average” graph which has previously been added to the front panel and the second output was sent to an Export Waveform to Spreadsheet file vi which was configured as above with the exception that the prompt reminded the user that these were filtered data. Thus both the raw and smoothed data were captured and recorded. The fourth output from the appended data file was sent to a Less or Equal VI.



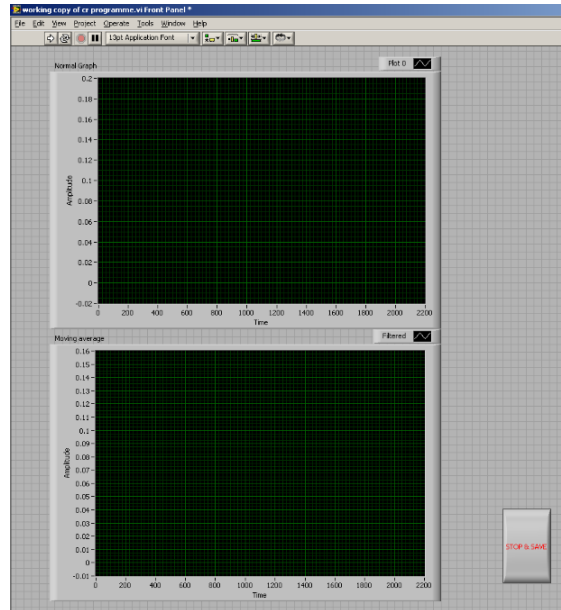
Appendix Figure 5 Frame 4 of VI indicating (a) the DAQ (b) two data converter types and different data types depicted as blue and orange.

The Less or Equal VI subtracts two values ($x-y$) and compares the result to a less than or equal to value constant set by the programmer. Here, the x input is wired to the output from the appended data and the y input is wired to the data output from the previous iteration and the constant was set to -0.05 . The sum of the appended value (x) minus the previous iteration value is calculated and compared to -0.05 . The VI is programmed to issue a True signal if the value is less than or equal to -0.05 and a False signal if the sum does not meet these criteria. Therefore, if the voltage (and therefore pressure) has decreased since the previous iteration by a value ≥ 0.5 the programme issues a true command to the next sequence in the VI, which automates the operation of the syringe pump.

The Pump Automation frames, see appendix figure 4, were set to respond to a True signal from the Less Than or Equal operator, i.e. if the pressure dropped between the current iteration and the previous iteration these frames are activated. The first frame issues a command to stop the pump, reverse the flow direction (i.e. change from infuse to withdraw) and restart the pump. An express VI which displays a message to the user was added. The VI is used here instruct the user to “Hit OK when the pressure has returned to baseline”. The second frame does not activate until the user clicks the “OK” button. The second frame issues a command to stop the pump, reverse the pump flow direction (i.e. change from withdraw to infuse) and restart the pump. In summary, when the critical pressure, C_p , is reached the pump stops infusing and begins to withdraw until the user indicates that the pressure has dropped to the baseline value, then the pump stops withdrawing and begins to infuse again.

III. Front Panel

The front panel, user interface, of the VI contained two graphs for viewing the data as the experiment progressed, appendix figure 6. One graph displayed the raw data feed from the sensor, the second the smoothed data to which a moving average filter had been applied. A “Stop and Save” Boolean was also added which terminated the programme and saved the data to comma delimited excel files. The programme was run from a forward arrow on the toolbar.



Appendix Figure 6 Front panel of VI showing graphs to view the data and stop Boolean.

IV. Conclusion

An original LabVIEW programme was written to integrate the operation of the of cavitation rheology syringe pump pressurisation system with the data output from the pressure sensor. The new programme automatically responds to the rapid pressure drop during a cavitation or fracture event.